

UNCLASSIFIED

AD NUMBER

AD920703

LIMITATION CHANGES

TO:

Approved for public release; distribution is unlimited.

FROM:

Distribution authorized to U.S. Gov't. agencies only; Test and Evaluation; JUL 1974. Other requests shall be referred to Armament Development Test Center, Eglin AFB, FL 32542.

AUTHORITY

ADTC ltr 5 Jun 1979

THIS PAGE IS UNCLASSIFIED

AEDC-TR-74-58
AFATL-TR-74-99

cy 2

JUL 1974
MAR 15 1976



STATIC STABILITY AND CONTROL EFFECTIVENESS OF THE MK-84 MODULAR GUIDED GLIDE BOMB II AT TRANSONIC MACH NUMBERS

This document has been approved for public release
and its distribution is unlimited. *Per TAB
No. 80-3*

J. A. Webb
ARO, Inc.

PROPULSION WIND TUNNEL FACILITY
ARNOLD ENGINEERING DEVELOPMENT CENTER
AIR FORCE SYSTEMS COMMAND
ARNOLD AIR FORCE STATION, TENNESSEE 37389

July 1974

Final Report for Period February 7-19, 1974

~~Distribution limited to U.S. Government agencies only; this report contains information on test and evaluation of military hardware; July 1974; other requests for this document must be referred to Armament Development Test Center (SDTT), Eglin AFB, FL 32542.~~

Property of U. S. Air Force
AEDC LIBRARY
F40600-74-C-0001

Prepared for

ARMAMENT DEVELOPMENT TEST CENTER (SDTT)
EGLIN AFB, FLORIDA 32542

NOTICES

When U. S. Government drawings specifications, or other data are used for any purpose other than a definitely related Government procurement operation, the Government thereby incurs no responsibility nor any obligation whatsoever, and the fact that the Government may have formulated, furnished, or in any way supplied the said drawings, specifications, or other data, is not to be regarded by implication or otherwise, or in any manner licensing the holder or any other person or corporation, or conveying any rights or permission to manufacture, use, or sell any patented invention that may in any way be related thereto.

Qualified users may obtain copies of this report from the Defense Documentation Center.

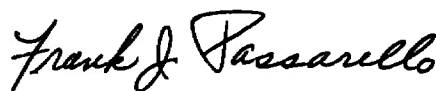
References to named commercial products in this report are not to be considered in any sense as an endorsement of the product by the United States Air Force or the Government.

APPROVAL STATEMENT

This technical report has been reviewed and is approved.



LAMAR R. KISSLING
Lt Colonel, USAF
Chief Air Force Test Director, PWT
Directorate of Test



FRANK J. PASSARELLO
Colonel, USAF
Director of Test

UNCLASSIFIED

SECURITY CLASSIFICATION OF THIS PAGE (When Data Entered)

REPORT DOCUMENTATION PAGE		READ INSTRUCTIONS BEFORE COMPLETING FORM
1. REPORT NUMBER AEDC-TR-74-58 AFATL-TR-74-99	2. GOVT ACCESSION NO.	3. RECIPIENT'S CATALOG NUMBER
4. TITLE (and Subtitle) STATIC STABILITY AND CONTROL EFFECTIVENESS OF THE MK-84 MODULAR GUIDED GLIDE BOMB II AT TRANSONIC MACH NUMBERS		5. TYPE OF REPORT & PERIOD COVERED Final Report, February 7 to 19, 1974
		6. PERFORMING ORG. REPORT NUMBER
7. AUTHOR(s) J. A. Webb, ARO, Inc.		8. CONTRACT OR GRANT NUMBER(s)
9. PERFORMING ORGANIZATION NAME AND ADDRESS Arnold Engineering Development Center Arnold Air Force Station, TN 37389		10. PROGRAM ELEMENT, PROJECT, TASK AREA & WORK UNIT NUMBERS Program Element 63741
11. CONTROLLING OFFICE NAME AND ADDRESS Armament Development Test Center (SDTT) Eglin AFB, FL 32542		12. REPORT DATE July 1974
		13. NUMBER OF PAGES 132
14. MONITORING AGENCY NAME & ADDRESS (if different from Controlling Office)		15. SECURITY CLASS. (of this report) UNCLASSIFIED
		15a. DECLASSIFICATION/DOWNGRADING SCHEDULE N/A
16. DISTRIBUTION STATEMENT (of this Report) Distribution limited to U.S. Government agencies only; this report contains information on test and evaluation of military hardware; July 1974; other requests for this document must be referred to Armament Development Test Center (SDTT), Eglin AFB, FL 32542.		
17. DISTRIBUTION STATEMENT (of the abstract entered in Block 20, if different from Report)		
18. SUPPLEMENTARY NOTES Available in DDC.		
19. KEY WORDS (Continue on reverse side if necessary and identify by block number) MK-84 bomb Modular Guided Glide Bomb (MGGB) static stability transonic flow		
20. ABSTRACT (Continue on reverse side if necessary and identify by block number) Wind tunnel tests were conducted to determine the static sta- bility and control effectiveness of the MK-84 Modular Guided Glide Bomb II (MGGB II). A 0.20-scale model of the MK-84 MGGB II was tested at Mach numbers from 0.5 to 1.3 at angles of attack from -12 to 8 deg and sideslip angles from -6 to 14 deg. Aerodynamic coefficients are presented to show the longitudinal, directional, and lateral static stability and control characteristics of the MK-84 MGGB II configuration.		

UNCLASSIFIED

PREFACE

The work reported herein was conducted by the Arnold Engineering Development Center (AEDC), Air Force Systems Command (AFSC), and sponsored by the Armament Development Test Center (ADTC/SDTT), Air Force Systems Command (AFSC), under Program Element 63741F. ADTC Project Monitors were Capt. F. Wheeler and Mr. M. Bouffard. The results presented were obtained by ARO, Inc. (a subsidiary of Sverdrup & Parcel and Associates, Inc.), contract operator of AEDC, AFSC, Arnold Air Force Station, Tennessee. The test was conducted from February 7 through 19, 1974, under ARO Project No. PA454. The manuscript (ARO Control No. ARO-PWT-TR-74-42) was submitted for publication on May 20, 1974.

CONTENTS

	<u>Page</u>
1.0 INTRODUCTION	7
2.0 APPARATUS	
2.1 Test Facility	7
2.2 Test Article	8
2.3 Instrumentation	8
3.0 TEST DESCRIPTION	
3.1 Test Procedures and Conditions	9
3.2 Data Corrections	9
3.3 Precision of Measurements	9
4.0 RESULTS AND DISCUSSION	
4.1 General	10
4.2 Model Buildup	10
4.3 Canard and Wing Sweep Angle Effects	10
4.4 Control Effectiveness	11
4.5 Control Surface Hinge Moments	13
4.6 Calibration of Vane-Type Angle-of-Attack Indicator	13
5.0 CONCLUSIONS	13
REFERENCES	14

ILLUSTRATIONS

Figure

1. Dimensional Sketch of MK-84 MGGB II, Configuration B2S1W2T5L1C2	15
2. Photographs of Model and Installation, Configuration B2S1W2T5L1C4	16
3. Dimensional Sketch of the Strongback (S1)	18
4. Dimensional Sketch of the Wing (W2)	19
5. Photograph of the Wing Showing Swaybrace Slots and Boundary-Layer Transition Grit	20
6. Dimensional Sketch of the Tail Fin and Flap	21
7. Photograph of Tail Fin and Flap (T5)	22
8. Photographs of the Canard Configurations	23
9. Dimensional Sketches of the C2(C3) and C4 Canards	24
10. Photograph of the Two C4 and the C2(C3) Canards	25
11. Dimensional Sketch of the Vane-Type Angle-of-Attack Indicator	26
12. Orientation of Model Forces and Moments	27
13. Orientation of Control Surface Deflections	28

<u>Figure</u>	<u>Page</u>
14. Lift, Drag, and Pitching-Moment Coefficients for Configurations B2C2, B2T5C2, B2S1W2L1C2, and B2S1W2T5L1C2	29
15. Lift-to-Drag Ratio for Configurations B2C2, B2T5C2, B2S1W2L1C2, and B2S1W2T5L1C2	35
16. Crosswind-Force, Yawing-Moment, and Rolling-Moment Coefficients for Configurations B2S1W2L1, B2S1W2T5L1, B2S1W2L1C2, and B2S1W2T5L1C2	38
17. Effect of Canards C2, C3, and C4 on the Crosswind-Force, Yawing-Moment, and Rolling-Moment Coefficients, $\alpha = 0$	44
18. Effect of Canards C2, C3, and C4 on the Crosswind-Force, Yawing-Moment, and Rolling-Moment Coefficients, $\alpha = 5$ deg	48
19. Effect of Canards C2, C3, and C4 on the Crosswind-Force, Yawing-Moment, and Rolling-Moment Coefficients, $\alpha = -10$ deg	51
20. Effect of Wing Sweep Angle on the Lift, Drag, and Pitching-Moment Coefficients of the MK-84 MGGB II Configuration	54
21. Effect of the Wing Sweep Angle on the Lift-to-Drag Ratio of the MK-84 MGGB II Configuration	64
22. Effect of the Wing Sweep Angle on the Rolling-Moment Coefficient of the MK-84 MGGB II Configuration	69
23. Effect of the Wing Sweep Angle on the Crosswind-Force, Yawing-Moment, and Rolling-Moment Coefficients of the MK-84 MGGB II Configuration, $\alpha = -5$ deg .	74
24. Effect of the Wing Sweep Angle on the Crosswind-Force, Yawing-Moment, and Rolling-Moment Coefficients of the MK-84 MGGB II Configuration, $\alpha = 0$. .	80
25. Effect of the Wing Sweep Angle on the Crosswind-Force, Yawing-Moment, and Rolling-Moment Coefficients of the MK-84 MGGB II Configuration, $\alpha = 5$ deg	90
26. Effect of Pitch Control Deflections on the Lift, Drag, and Pitching-Moment Coefficients of the MK-84 MGGB II Configuration	96
27. Effectiveness of the Flap Control Surfaces in Producing Lift at Zero Angle of Attack	102
28. Pitch Effectiveness of the Flap Control Surfaces at Zero Angle of Attack . . .	103
29. Longitudinal Load Factor per Degree of Pitch Control Deflection (δQ) versus Mach Number	104
30. Effect of Yaw Control Deflections on the Crosswind-Force, Yawing-Moment, and Rolling-Moment Coefficients of the MK-84 MGGB II Configuration . . .	105
31. Effectiveness of the Flap Control Surfaces in Producing Crosswind Force at Zero Sideslip Angle	111
32. Yaw Effectiveness of the Flap Control Surfaces at Zero Angle of Attack . . .	112
33. Lateral Load Factor per Degree of Yaw Control Deflection (δR) versus Mach Number	113

<u>Figure</u>	<u>Page</u>
34. Effect of Roll Control Deflections on the Rolling-Moment Coefficients of the MK-84 MGGB II Configuration	114
35. Roll Effectiveness of the Flap Control Surfaces at Zero Angle of Attack . . .	117
36. Control Surface Hinge-Moment Coefficients versus Angle of Attack for Different Control Deflection Angles	118
37. Vane Calibration Data, α versus α_s , Comparing Configurations B2, B2C2, B2T5C2, B2S1W2T5L1, and B2S1W2T5L1C2	124

TABLES

1. Summary of Test Conditions and Flap Control Surface Deflections	127
2. Uncertainties in Aerodynamic and Hinge-Moment Coefficients	128
3. Precision of Flap Control Surface Deflection Angle Settings	128

NOMENCLATURE	129
------------------------	-----

1.0 INTRODUCTION

Wind tunnel tests were conducted in the Aerodynamic Wind Tunnel (4T), Propulsion Wind Tunnel Facility (PWT) to determine the static stability and control effectiveness of the MK-84 Modular Guided Glide Bomb II (MGGB II). The MK-84 MGGB II is comprised of a MK-84 bomb, Range Extension System (RES), a KMU-353X guidance and control kit, and a vertical canard located on the nose of the vehicle for enhanced maneuverability in the yaw plane. The MK-84 MGGB II is similar to basic MGGB configurations which were previously tested in Tunnel 4T and in the Propulsion Wind Tunnel (16T) and documented in Refs. 1 through 4.

The MGGB series is a high-speed air-launched glide weapon system that has evolved from the MK-84 Homing Optical Bombing System (HOBOS). Following aircraft release, the wings from the RES are deployed to provide lifting surfaces for range extension. Tail control surfaces (flaps) are used to provide aerodynamic control of the vehicle in pitch, yaw, and roll.

The MK-84 MGGB II, a modification of the MGGB Mark II (Ref. 4) has improved tail and flap control surfaces. Also, the forward fuselage has been elongated and the nose section modified to allow the addition of a distance-measuring equipment (DME) guidance module. The location of the vane-type angle-of-attack sensor was also changed from the location used during the tests cited in Ref. 4.

The tests were conducted to determine the aerodynamic characteristics of the basic MK-84 MGGB II configuration and to evaluate the effect of two alternate vertical canard configurations on the lateral-directional characteristics. Also, flap hinge moments were determined for several deflection angles and a calibration was determined for the angle-of-attack sensor. Data were obtained at Mach numbers from 0.5 to 1.3 at angles of attack from -12 to 8 deg and angles of sideslip from -6 to 14 deg.

2.0 APPARATUS

2.1 TEST FACILITY

Tunnel 4T is a closed-loop, continuous flow, variable density tunnel in which the Mach number can be varied from 0.1 to 1.3. At all Mach numbers, the stagnation pressure can be varied from 300 to 3700 psfa. The test section is 4 ft square and 12.5 ft long with perforated, variable porosity (0.5- to 10-percent open) walls. It is completely enclosed in a plenum chamber from which the air can be evacuated, allowing part of the tunnel airflow to be removed through the perforated walls of the test section. A more thorough description of the tunnel may be found in Ref. 5.

2.2 TEST ARTICLE

The test article was a 0.20-scale model of the MK-84 MGGB II modular guided glide bomb. Dimensions of the MK-84 MGGB II model configuration are shown in Fig. 1. Photographs of the model and test installation are shown in Fig. 2. The basic MK-84 MGGB II configuration consists of a MK-84 bomb, a KMU-353X guidance and control kit, and RES. The components are identified on the model in Fig. 1. The model RES consisted of a strongback and two wings. The strongback shown in Fig. 3 was mounted to the bomb section and supported the wings. The wing shown in Fig. 4 was modified to include slots which provide clearance for pylon swaybraces when the MK-84 MGGB II (wings folded) is attached to an aircraft. A photograph of the left model wing with the swaybrace slots and boundary-layer transition grit is shown in Fig. 5. When deployed, the wings had a sweep angle of 30 deg, an incidence angle of 3 deg, and a dihedral angle of -10 deg. The sweep angle was 88 deg with the wings folded. The rear section of the KMU-353X guidance and control kit included four tail fins and flap control surfaces. The details and dimensions of a tail fin and flap control surface are shown in Fig. 6, and a photograph is presented in Fig. 7. Three of the movable flap control surfaces were attached to strain-gage balances to measure flap hinge moments.

Three canard configurations shown in Fig. 8 were tested on the basic MK-84 MGGB II. The details and dimensions of the canards are shown in Fig. 9, and a photograph is presented in Fig. 10. The C2 and C3 canard configurations used the same canard, which was 2.0 in. in height. Configuration C2 was mounted on the lower fuselage surface, whereas C3 was mounted on the upper fuselage surface. The C4 configuration consisted of two canards 0.8 in. in height and mounted on the upper and lower fuselage surfaces. The majority of the test was conducted with the C2 canard.

A vane-type angle-of-attack indicator was tested on the MK-84 MGGB II model and is shown in a dimensional sketch in Fig. 11. The vane can be seen in the photograph shown in Fig. 8, and its location on the model is given in Fig. 1. The vane was mounted on a gimbaled shaft which allowed the vane to remain aligned with the local flow around the model.

2.3 INSTRUMENTATION

Aerodynamic forces and moments acting on the model were measured using a six-component, moment-type, internal strain-gage balance. Two-component, moment-type, strain-gage balances were used to measure hinge moments on three of the tail fin control surfaces. The vane-type angle-of-attack indicator used a potentiometer to measure the angle of rotation of the vane shaft with respect to the fuselage centerline. Base pressure was measured at one location in the plane of the model base using a 5-psid transducer.

3.0 TEST DESCRIPTION

3.1 TEST PROCEDURES AND CONDITIONS

Model forces and moments were obtained at angles of attack and angles of sideslip using two model positioning procedures as follows:

1. The model angle of attack was varied while Mach number, roll angle ($\beta = 0$), and flap deflection were held constant.
2. The model pitch angle and roll angle were both varied yielding a variation of the sideslip angle at a constant angle of attack relative to the free-stream velocity vector. Again Mach number and flap deflection were held constant.

Force and moment data were obtained with and without flap deflections at Mach numbers from 0.5 to 1.3 by both procedures. Data were obtained for angles of attack from -12 to 8 deg using procedure 1 and for sideslip angles from -6 to 14 deg using procedure 2. Boundary-layer transition on the wings was fixed with a 0.1-in.-wide band of No. 120 grit (0.005-in. diameter) located 0.30 in. aft of the wing leading edges.

The tunnel stagnation pressure was varied from 1000 to 1200 psf, and the tunnel stagnation temperature was varied from 100 to 125°F. The resulting Reynolds number variation was from 1.3 to 2.5×10^6 per foot.

The data are presented in the wind axis system. The orientation of the axis system, control surface numbering, and deflection sign convention are shown in Fig. 12. A summary of the control deflections used and test conditions is shown in Table 1.

3.2 DATA CORRECTIONS

Correction for the components of model weight, normally termed static tares, was made in order to calculate the net aerodynamic forces and moments. The angle of attack was corrected for sting and balance deflections caused by the aerodynamic loads. The model was tested both upright and inverted to obtain the necessary data to correct for tunnel flow angularity and model-balance misalignment.

3.3 PRECISION OF MEASUREMENTS

The uncertainties of the data presented which can be attributed to errors in the balance measurements and tunnel conditions were determined for a confidence level of 95 percent, and the values are presented in Table 2. The precision in setting Mach number was ± 0.002 . The Mach number variation in the test section occupied by the model was

no greater than ± 0.005 for Mach numbers up to 0.95 and ± 0.01 for Mach numbers greater than 1.0. The uncertainty in the angle of attack and angle of sideslip was ± 0.1 deg, and the precision of the flap settings is shown in Table 3.

4.0 RESULTS AND DISCUSSION

4.1 GENERAL

The measured force and moment data were reduced to coefficient form in the wind-axis system as shown in Fig 12. With the wings extended the moment reference was at MS 15.745 on the bomb centerline. For the wings-folded configuration ($\lambda_w = 88$ deg), the moment reference point was at MS 15.962 on the bomb centerline. The deflections of the flap control surfaces for pitch, yaw, and roll control are illustrated in Fig. 13. The majority of the test data presented in this report are machine plotted and faired from point to point with straight lines.

4.2 MODEL BUILDUP

The aerodynamic coefficients for various buildup stages of the MK-84 MGGB II configuration (model without canard, wings, hardback, tail fins, etc.) are shown in Figs. 14 through 16.

The addition of canard C2 to configurations B2 or B2T5 had no appreciable effect on the longitudinal characteristics of the configurations; therefore, model buildup data without canard C2 are not presented. The C2 canard did affect the lateral-directional characteristics of the MK-84 MGGB II (Fig. 16). The magnitude of the crosswind-force coefficient, C_c , was increased for increasing magnitudes of sideslip angle by the addition of the canard, and the directional stability was decreased. The addition of the canard produced a negative increment in the rolling-moment coefficient, $C_{l,w}$ (Fig. 16) for positive sideslip angles and a positive increment in $C_{l,w}$ for negative sideslip angles, which repeats the trends of a previous test (Ref. 4).

4.3 CANARD AND WING SWEEP ANGLE EFFECTS

The lateral-directional characteristics of the basic MK-84 MGGB II configuration without a canard and with the three canard configurations (C2, C3, and C4) are shown in Figs. 17 through 19 for angles of attack of 0 (Fig. 17), 5 deg (Fig. 18), and -10 deg (Fig. 19). The directional stability of the model was reduced by the addition of the canards. The C2 canard generally produced the largest decrease in directional stability and resulted in a directionally unstable or neutrally stable vehicle at large sideslip angles for $M_\infty = 0.5$ and 0.9 at $\alpha = -10$ deg (Fig. 19). The C2 canard tended in general to

reduce the magnitude of the induced rolling-moment coefficient obtained when increasing sideslip angle at all angles of attack. At 0- and 5-deg angles of attack (Figs. 17 and 18), the C3 canard increased the magnitude of the rolling-moment coefficient, C_{l_w} , with increasing sideslip angle. The C4 canard had no appreciable effect on C_{l_w} for moderate sideslip angles at all angles of attack. Based on the data presented in Figs. 17 through 19, the C2 canard configuration was chosen as the most effective canard for the MK-84 MGGB II configuration.

The aerodynamic coefficients for the MK-84 MGGB II with wings open ($\lambda_w = 30$ deg) and wings folded ($\lambda_w = 88$ deg) are shown in Figs. 20 through 25. The longitudinal stability (Fig. 20) was greater for the wings-folded configuration than for the wings-open configuration. The wings-open configuration was close to neutrally stable at $M_\infty = 0.5$, but the stability increased with Mach number. The lift-to-drag ratio (Fig. 21) for the wings-open configuration reached a maximum value of approximately 9.4 at $M_\infty = 0.7$. The rolling-moment coefficient, C_{l_w} (Fig. 22) was negligible for the wings-folded configuration, but became substantial when the wings were opened. Comparison of the C_{l_w} data for the wings-open and -closed configurations show large values of C_{l_w} for the wings-open configuration. These increments were probably due to some asymmetry in the model wings.

The lateral-directional characteristics (Figs. 23 through 25) show that the directional stability was somewhat increased for the wings-open configuration and in general increased with increasing angle of attack. The wings-open configuration possessed unstable dihedral effects in that positive sideslip angles produced positive rolling-moment coefficients for all Mach numbers at $\alpha = 0$ and 5 deg (Figs. 24 and 25). At $M_\infty < 0.85$ for $\alpha = 0$ and 5 deg, the wings-open configuration displayed unstable as well as stable dihedral effects, depending on the Mach number and sideslip angle.

4.4 CONTROL EFFECTIVENESS

The longitudinal aerodynamic coefficients for pitch control deflections, δQ , are shown in Fig. 26. At Mach numbers less than 0.95, the vehicle is essentially neutrally stable for all values of the flap deflection. The stability of the vehicle increases with Mach number.

The variation of the lift increment parameter, $C_{L_{\delta Q}}$, and the pitch control effectiveness, $C_{m_{w_{\delta Q}}}$, with Mach number are shown in Figs. 27 and 28, respectively. The changes in the lift coefficient per degree of pitch control deflection, $C_{L_{\delta Q}}$ (Fig. 27), indicate that the lift control effectiveness decreased with increasing magnitude of control deflection, as expected, and that a $\delta Q = 10$ -deg was more effective than a $\delta Q = -10$ -deg deflection. For the $\delta Q = -5$ deg deflection, $C_{L_{\delta Q}}$ indicated that at $M_\infty = 0.5$ and 1.1 wing-fin interference or possibly other aerodynamic phenomena caused a loss in

lift control effectiveness, which resulted in control deflections of $\delta Q = \pm 10$ deg being more effective than $\delta Q = -5$ deg in lift. In general, $C_{m,w\delta Q}$ (Fig. 28) decreased with increasing magnitudes of negative pitch control deflections. However, at $M_\infty = 0.5$ and 0.95 , a $\delta Q = 10$ -deg deflection was more effective than a $\delta Q = -5$ -deg deflection. A large increase in $C_{m,w\delta Q}$ occurred at $M_\infty > 0.85$ for $\delta Q = -15$ -deg deflections, whereas δQ deflections of lesser magnitude tended to become less effective at $M_\infty > 0.85$.

The longitudinal load factor per degree of pitch deflection, $n_z/\delta Q$, is shown in Fig. 29. The values of $n_z/\delta Q$ were calculated using linear analysis in the angle-of-attack range from $\alpha = -2$ to 2 deg. These data indicate that for a dynamic pressure of 778 psf (critical design value) a MK-84 MGGB II configuration weighing 2650 lb could obtain longitudinal load factors as high as 12 at $M_\infty = 0.75$ with a $\delta Q = -5$ deg.

The lateral-directional coefficients for several yaw control deflections, δR , are shown in Fig. 30. Increasing δR to 10 and 15 deg tended to reduce the directional stability of the MK-84 MGGB II configuration. In fact, for $\delta R = 15$ deg at $M_\infty = 0.5$, the vehicle was neutrally stable for the lower values of β . However, the directional stability increased with Mach number, and the $\delta R = 15$ deg deflection resulted in a stable condition at $M_\infty > 0.5$. The crosswind-force parameter, $C_{c\delta R}$, and yaw control effectiveness, $C_{n,w\delta R}$, both evaluated at zero angle of attack, are shown in Figs. 31 and 32, respectively. $C_{c\delta R}$ and $C_{n,w\delta R}$ decreased with increasing control deflection angles, as expected.

The directional load factor per degree of control deflection ($n_y/\delta R$) is shown in Fig. 33 for the MK-84 MGGB II with the three canard configurations for several values of δR . The values of $n_y/\delta R$ were calculated using linear analysis in the sideslip angle range from $\beta = -2$ to 2 deg. These data indicate that the C2 canard configuration consistently produced higher load factors at any given Mach number and δR control deflection than either the C3 or C4 canard configurations. With the C2 canard configuration, a MK-84 MGGB II weighing 2650 lb and flying at a dynamic pressure of 778 psf could obtain a lateral load factor of 1.45 at $M_\infty = 0.75$ and $\delta R = 5$ deg.

The rolling-moment coefficients for negative roll control deflections, δP , are shown in Fig. 34. The variation of $C_{l,w}$ with α became very nonlinear at $M_\infty = 0.85$ for $\alpha > 4$ deg; however, sufficient roll control was available to offset the $C_{l,w}$ attributable to angle of attack at $\beta = 0$ deg. The roll control effectiveness, $C_{l,w\delta P}$, is shown in Fig. 35 for $\alpha = \beta = 0$. $C_{l,w\delta P}$ decreased with increasing magnitudes of δR for all values of δR except at $M_\infty = 0.5$. In this instance $\delta R = -5$ and -10 deg produced the same value for $C_{l,w\delta P}$.

4.5 CONTROL SURFACE HINGE MOMENTS

Control surface hinge moments are presented in Fig. 36. The hinge moments, in general, were opposing in that the hinge moment was opposite in direction to the actuator torque required to deflect the flaps from the undeflected position. This is very obvious at $M_\infty \geq 0.95$ in Fig. 36. There was little increase in the hinge-moment coefficients as a result of the 5-deg control surface deflections ($\delta P = -5$ deg) at $M_\infty \leq 0.85$; however, the increase was substantial at $M_\infty \geq 0.95$ and, for fin No. 2, reached a value corresponding to a full-scale actuator torque of 178 in.-lb for a flight condition of $q_{FS} = 778$ psf at $M_\infty = 0.95$ and $\alpha = 0$. The maximum hinge-moment coefficient obtained occurred on fin No. 1 for a $\delta Q = -10$ deg at $M_\infty = 0.95$ and would correspond to a full-scale actuator torque of 350 in.-lb at $q = 778$ psf.

4.6 CALIBRATION OF VANE-TYPE ANGLE-OF-ATTACK INDICATOR

The vane-type angle-of-attack calibration data for several buildup configurations are shown in Fig. 37. The addition of the RES (wing, strongback, and launch lugs) caused a slight offset in the zero intercept of the vane angle of attack, α_v , with the model angle of attack, α . The addition of the RES also resulted in a decrease in the slope of the α versus α_v curve, which remained relatively constant with Mach number.

5.0 CONCLUSIONS

The static stability and control effectiveness characteristics of a 0.20-scale model of the MK-84 MGGB II were obtained at Mach numbers from 0.5 to 1.3 at angles of attack from -12 to 8 deg and sideslip angles from -6 to 14 deg. The effects of canard configuration variations, wing sweep angle, and control deflections were investigated. Also, control surface hinge moments and the influence of configuration buildup on the vane-type angle-of-attack sensor were determined. The following conclusions were reached:

1. The longitudinal stability margin was close to zero at Mach number 0.5, but increased with Mach number. The stability was greater with the wings folded than with the wings open. Longitudinal load factors as high as 12 (dynamic pressures of 778 psf) were produced by the MK-84 MGGB II at Mach number 0.75 and a pitch control deflection of -5 deg.
2. The directional stability of the vehicle was reduced by the addition of the canards, and the C2 canard resulted in an unstable configuration at Mach numbers 0.5 and 0.9 for large sideslip angles at an angle of attack of -10 deg. The C2 canard consistently produced higher directional load factors at any given Mach number and yaw control deflection than either the C3

or C4 canards. Directional load factors as high as 1.45 (dynamic pressure of 778 psf) were produced by the configuration with the C2 canard at Mach number 0.75 for a yaw control deflection of 5 deg. The wings-open configuration had unstable dihedral effects for Mach numbers 0.85 through 1.3.

3. In general, the flap hinge moments opposed the applied torques.
4. The addition of the range extension system (RES) caused a slight offset in the zero intercept of the vane-type angle-of-attack calibration curve.

REFERENCES

1. Gomillion, G. R. "Results of a 0.25-Scale Modular Guided Glide Bomb at Transonic Mach Numbers." (U) AEDC-TR-71-168 (AFATL-TR-71-103) (AD517266L), September 1971. Confidential Report.
2. MacLanahan, D. A., Jr. "Calibration of Angle-of-Attack and Dynamic Pressure Sensors on the Modular Guided Glide Bomb at Transonic Mach Numbers." AEDC-TR-72-124 (AFATL-TR-72-171) (AD902886L), September 1972.
3. Smith, D. K. "Static Stability and Control Effectiveness of the MK-84 HOBOS and the Modular Guided Glide Bomb at Transonic Speeds." AEDC-TR-73-101 (AFATL-TR-73-126) (AD911338L), June 1973.
4. Smith, D. K. "Static Stability and Control Effectiveness of the Modular Guided Glide Bomb (MGGB) Mark II Munition at Transonic Speed." AEDC-TR-73-178 (AFATL-TR-73-209) (AD754276), October 1973.
5. Test Facilities Handbook (Tenth Edition). "Propulsion Wind Tunnel Facility, Vol. 4." Arnold Engineering Development Center, May 1974.

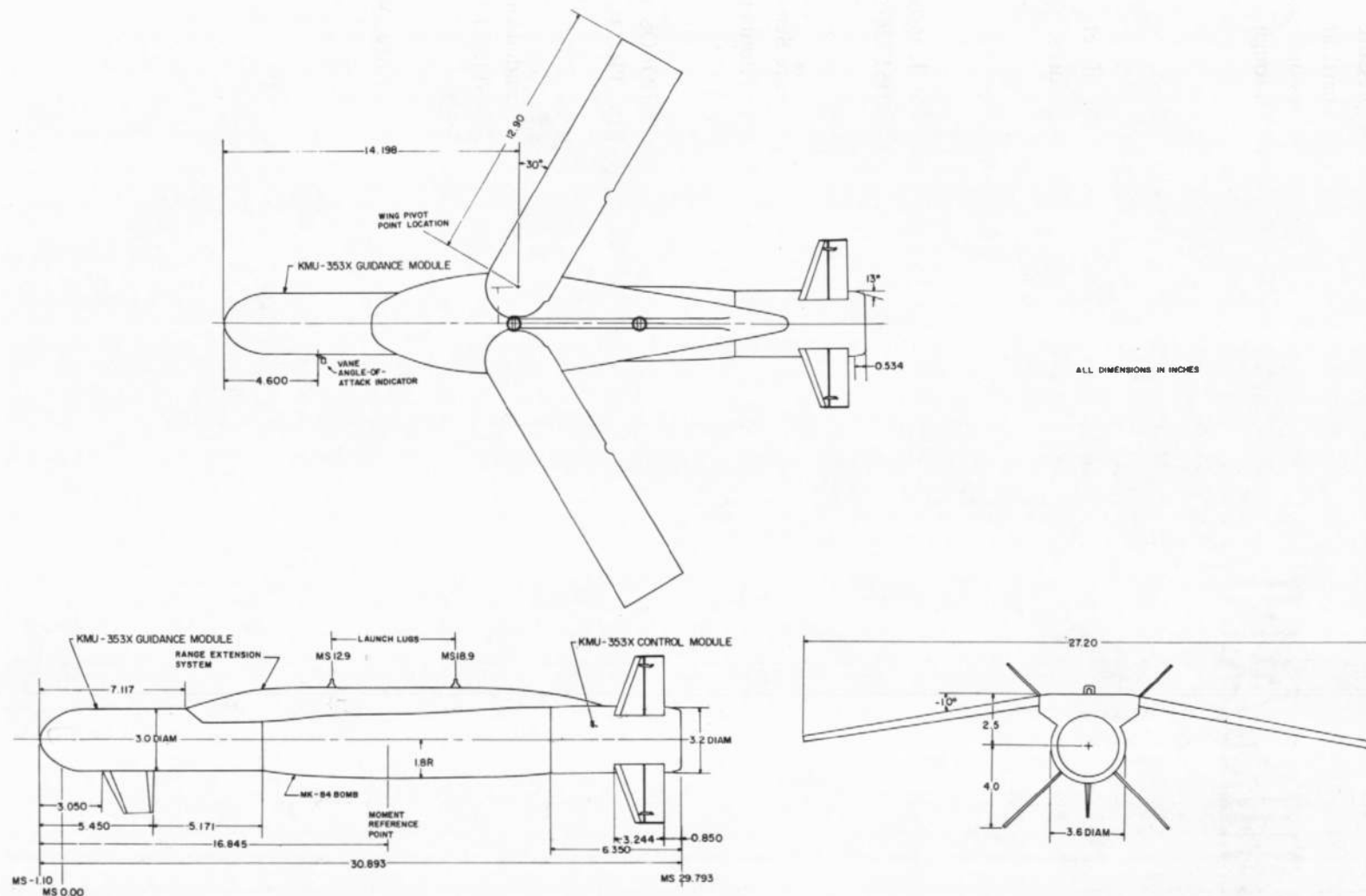
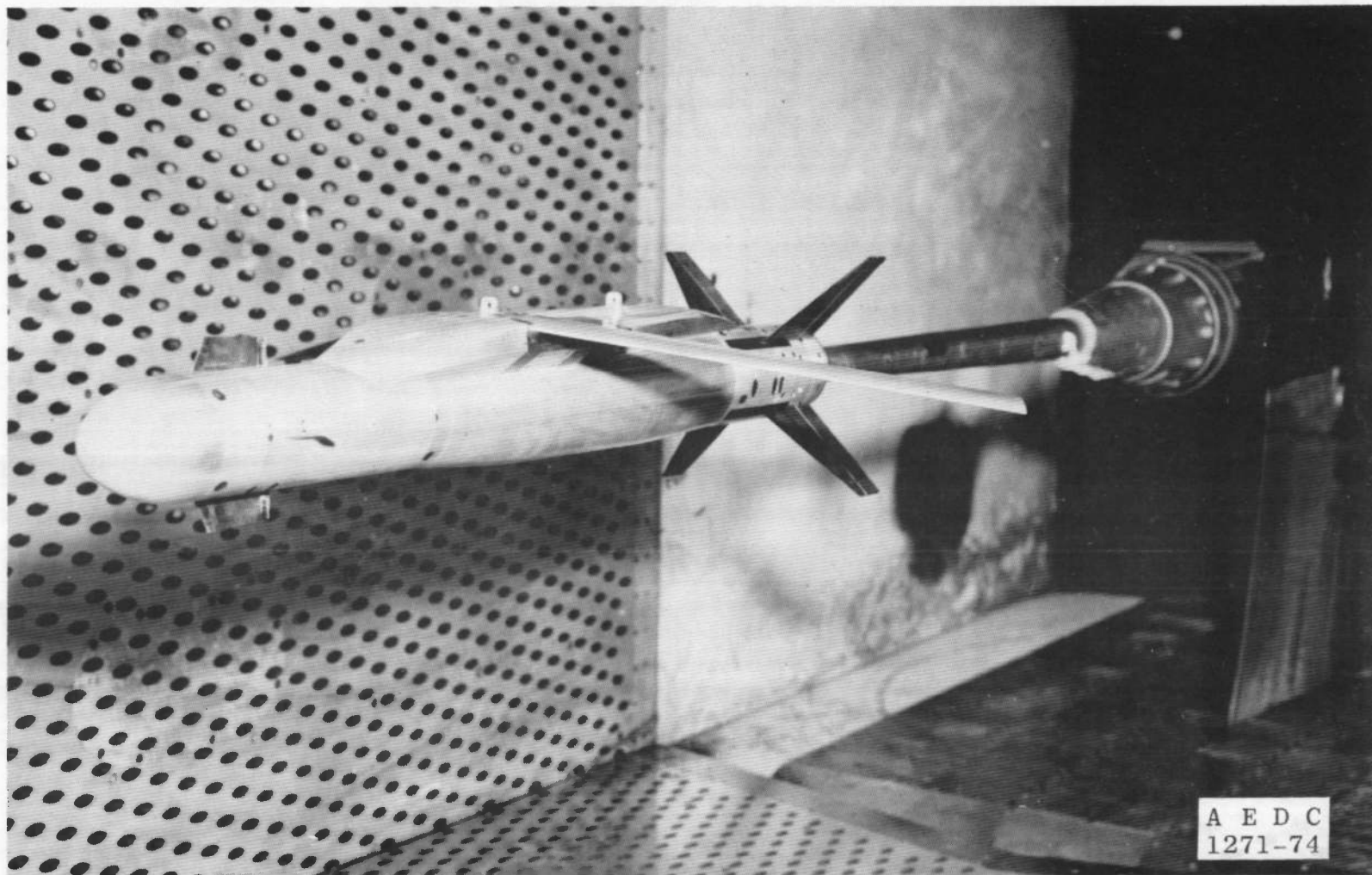
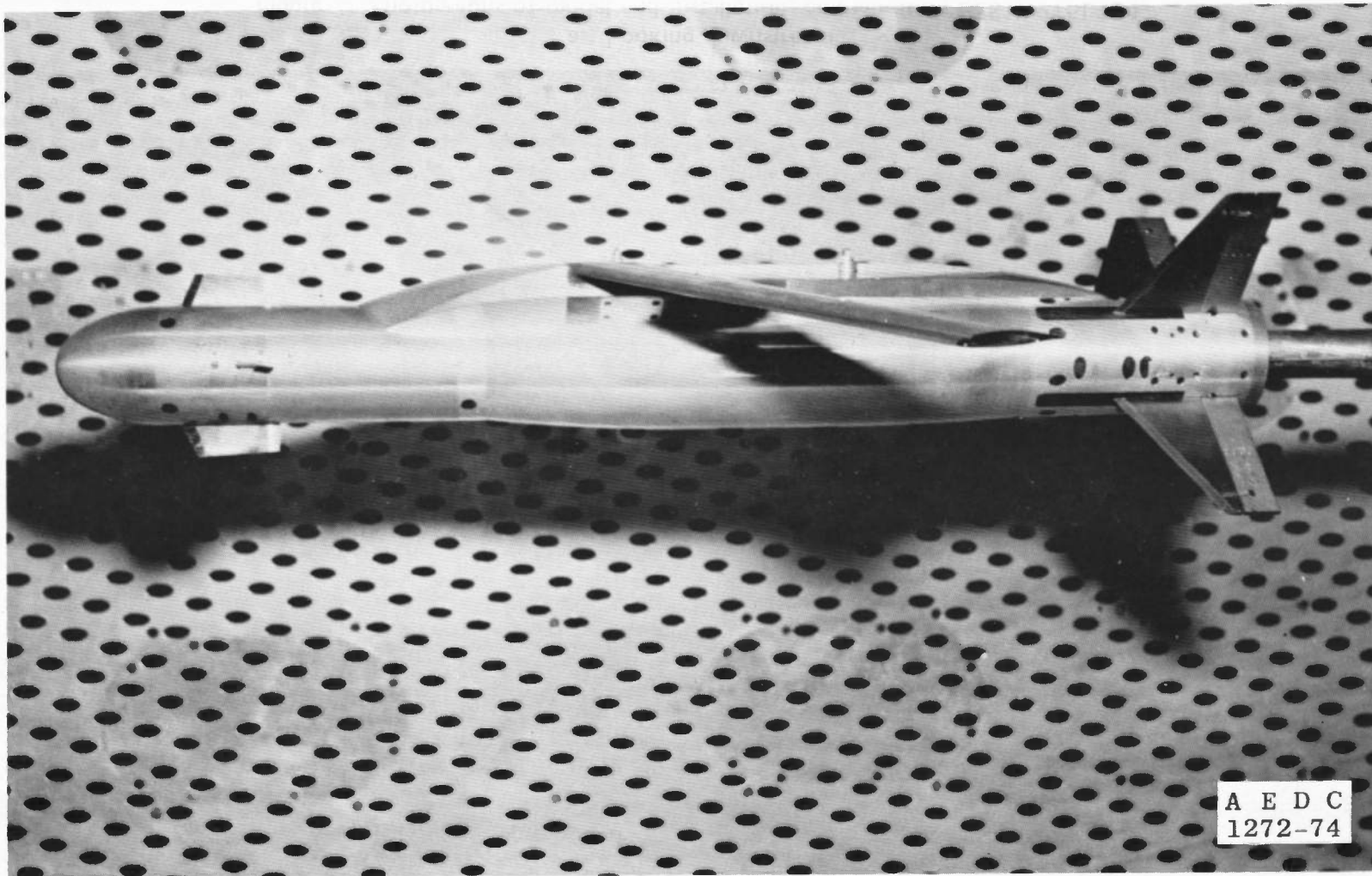


Figure 1. Dimensional sketch of MK-84 MGGB II, configuration B2S1W2T5L1C2.



a. Looking downstream

Figure 2. Photographs of model and installation, configuration B2S1W2T5L1C4.



b. Side view
Figure 2. Concluded.

A E D C
1272-74

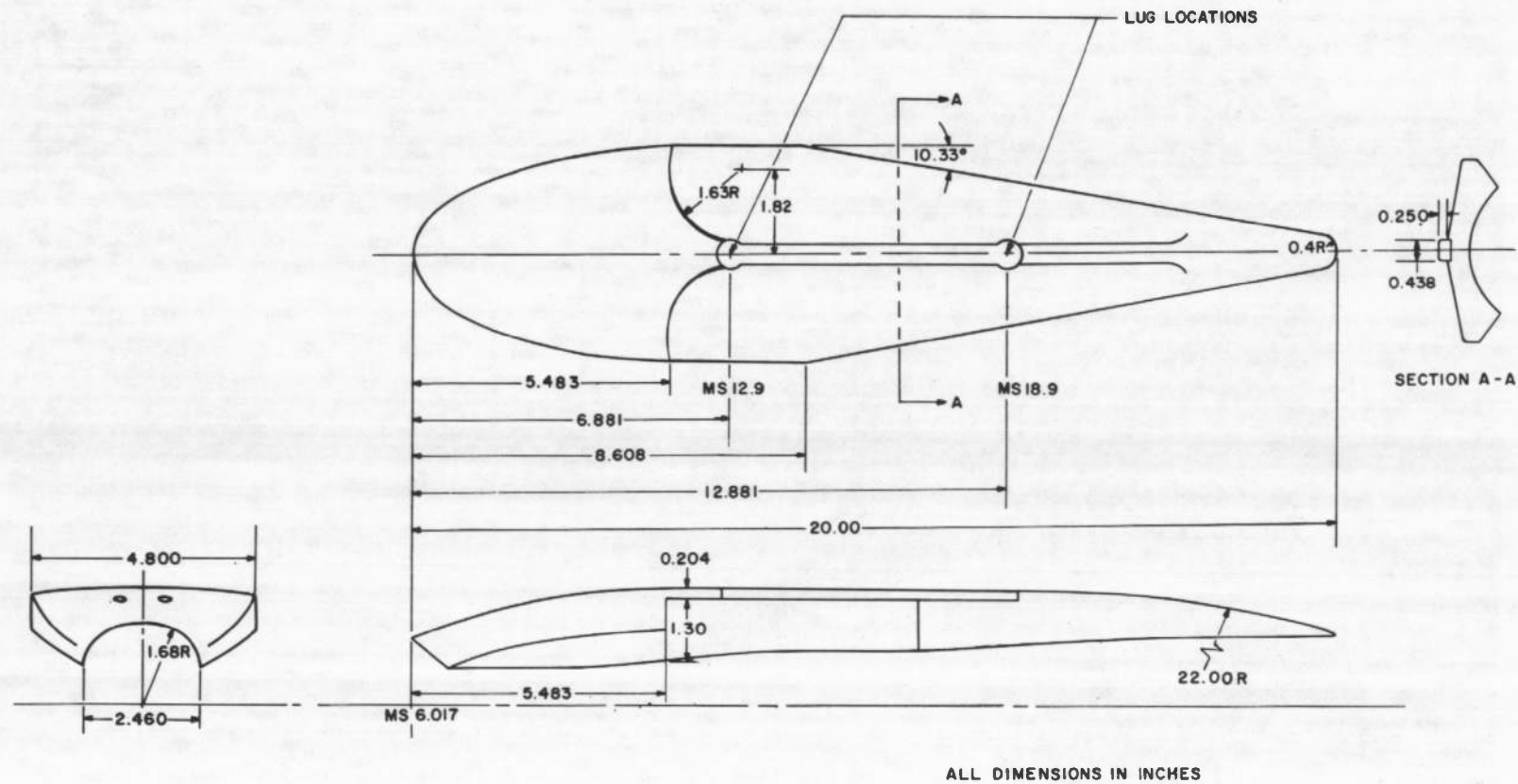


Figure 3. Dimensional sketch of the strongback (S1).

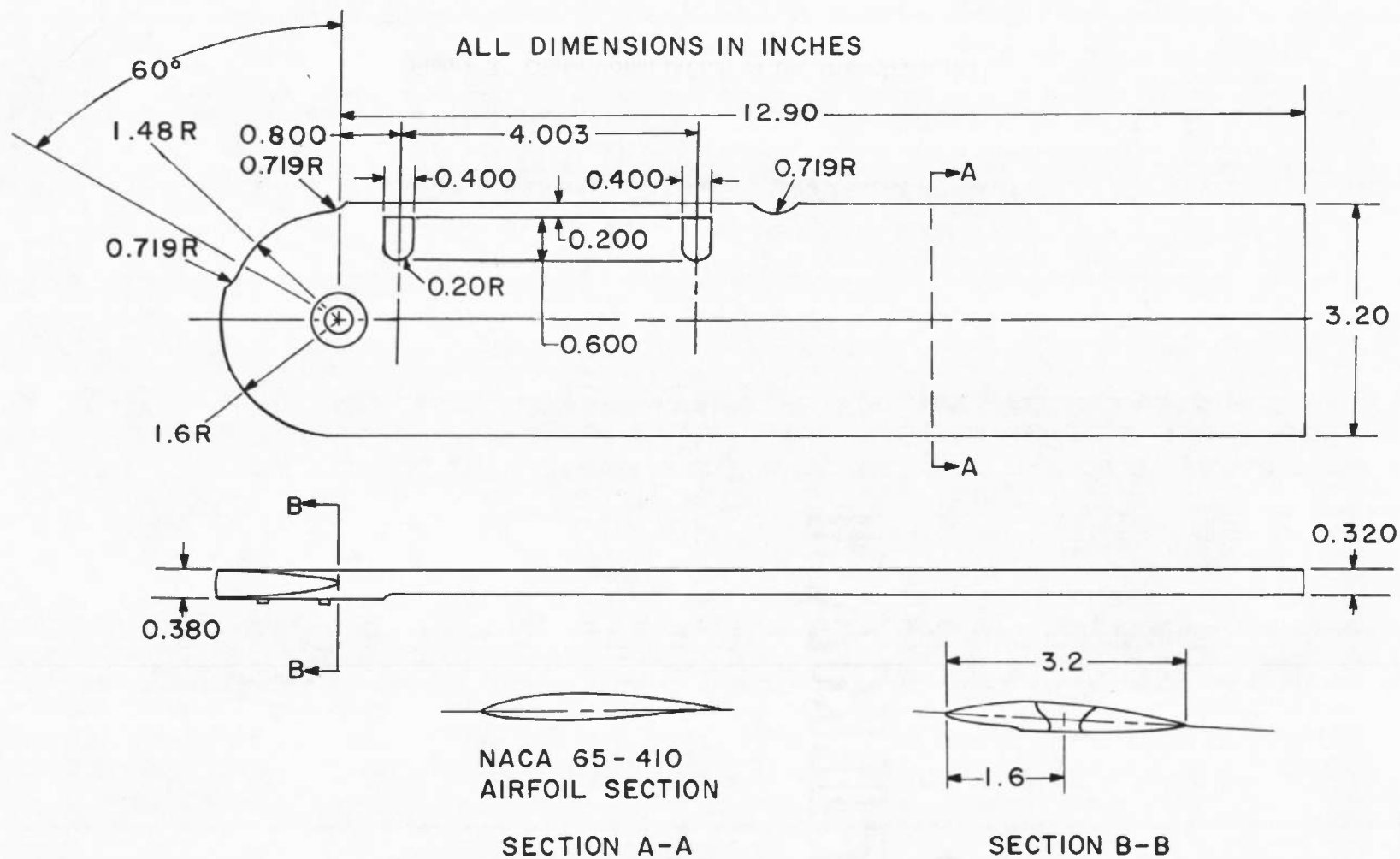


Figure 4. Dimensional sketch of the wing (W2).

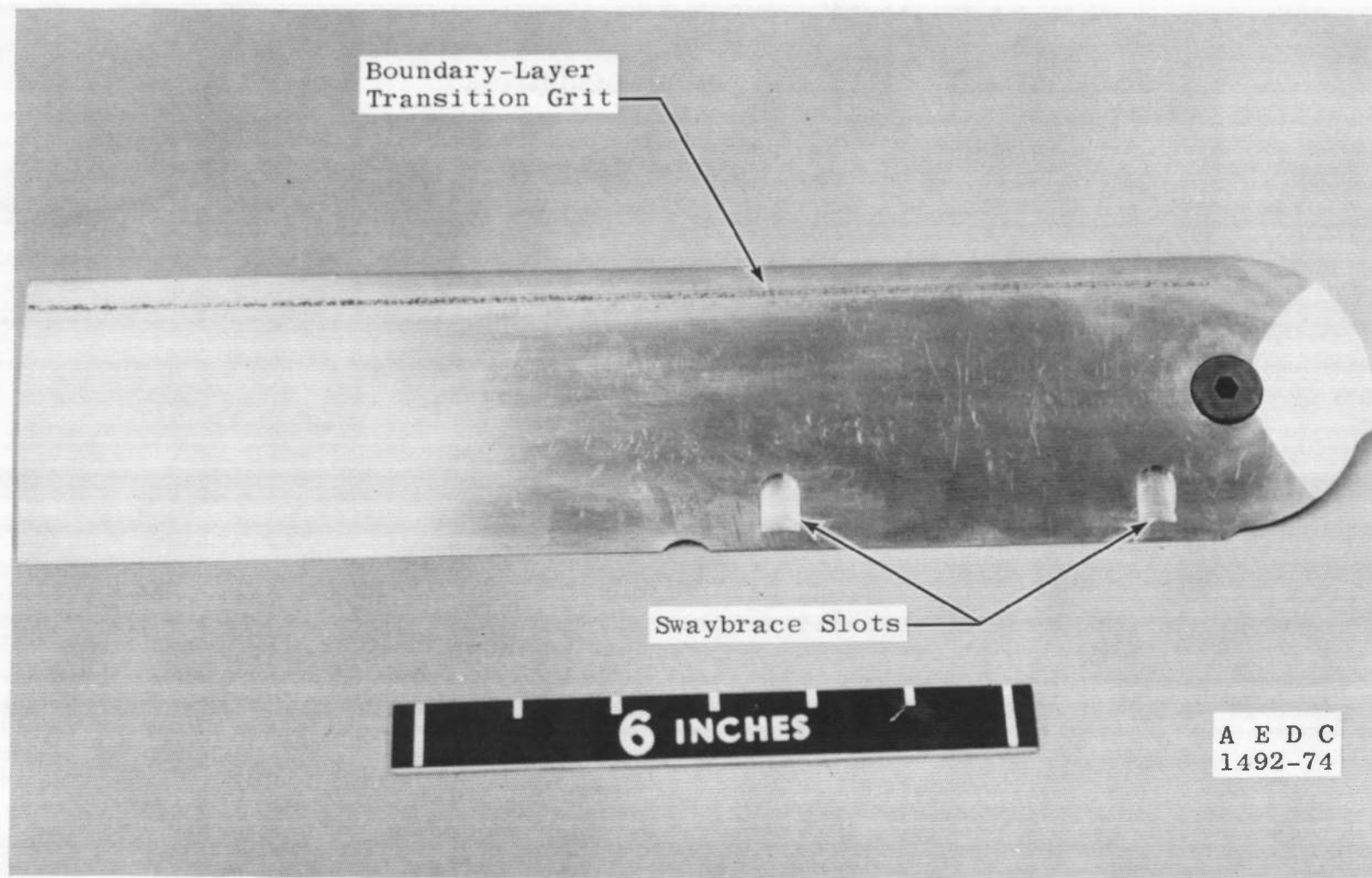


Figure 5. Photograph of the wing showing swaybrace slots and boundary-layer transition grit.

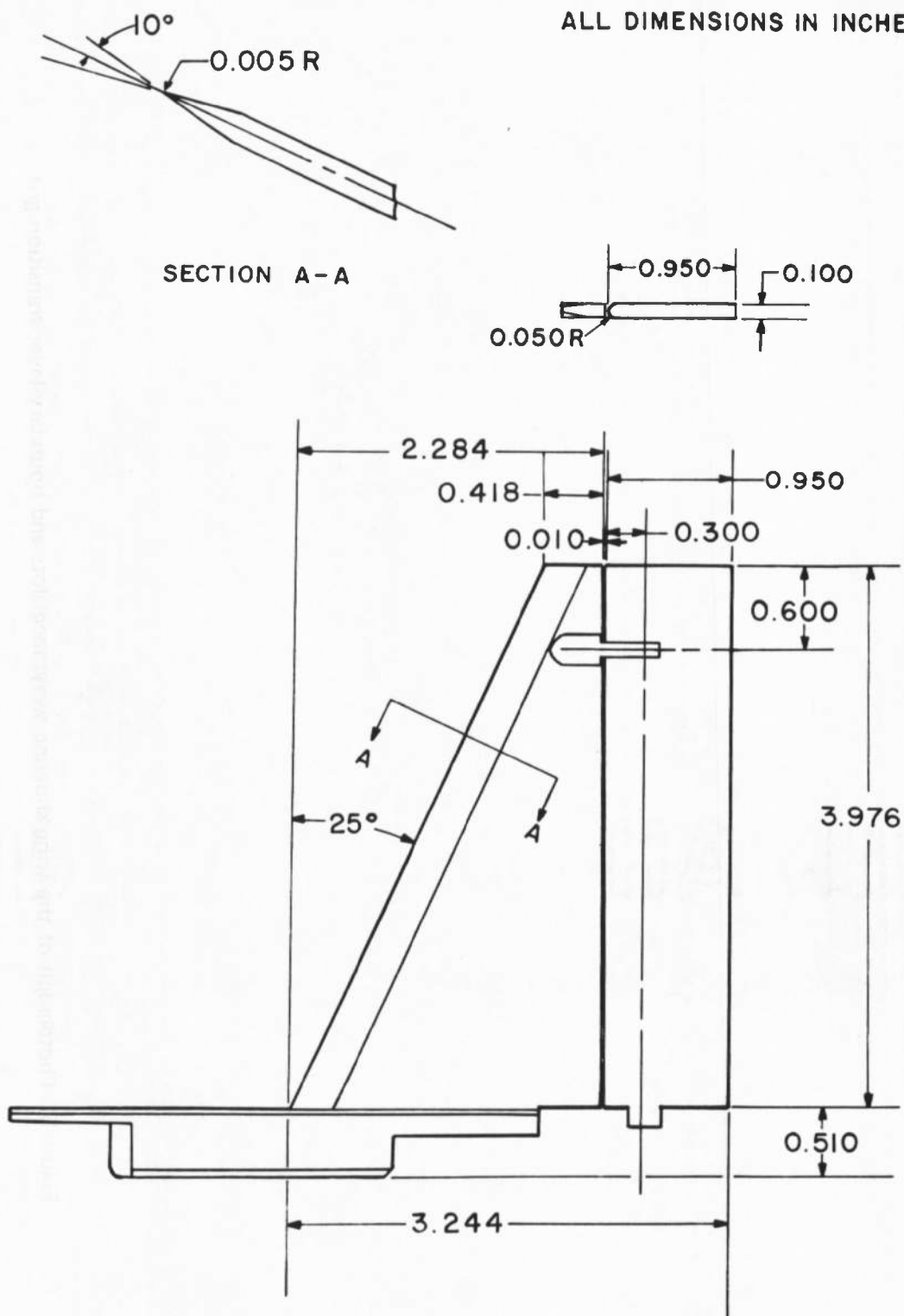


Figure 6. Dimensional sketch of the tail fin and flap.

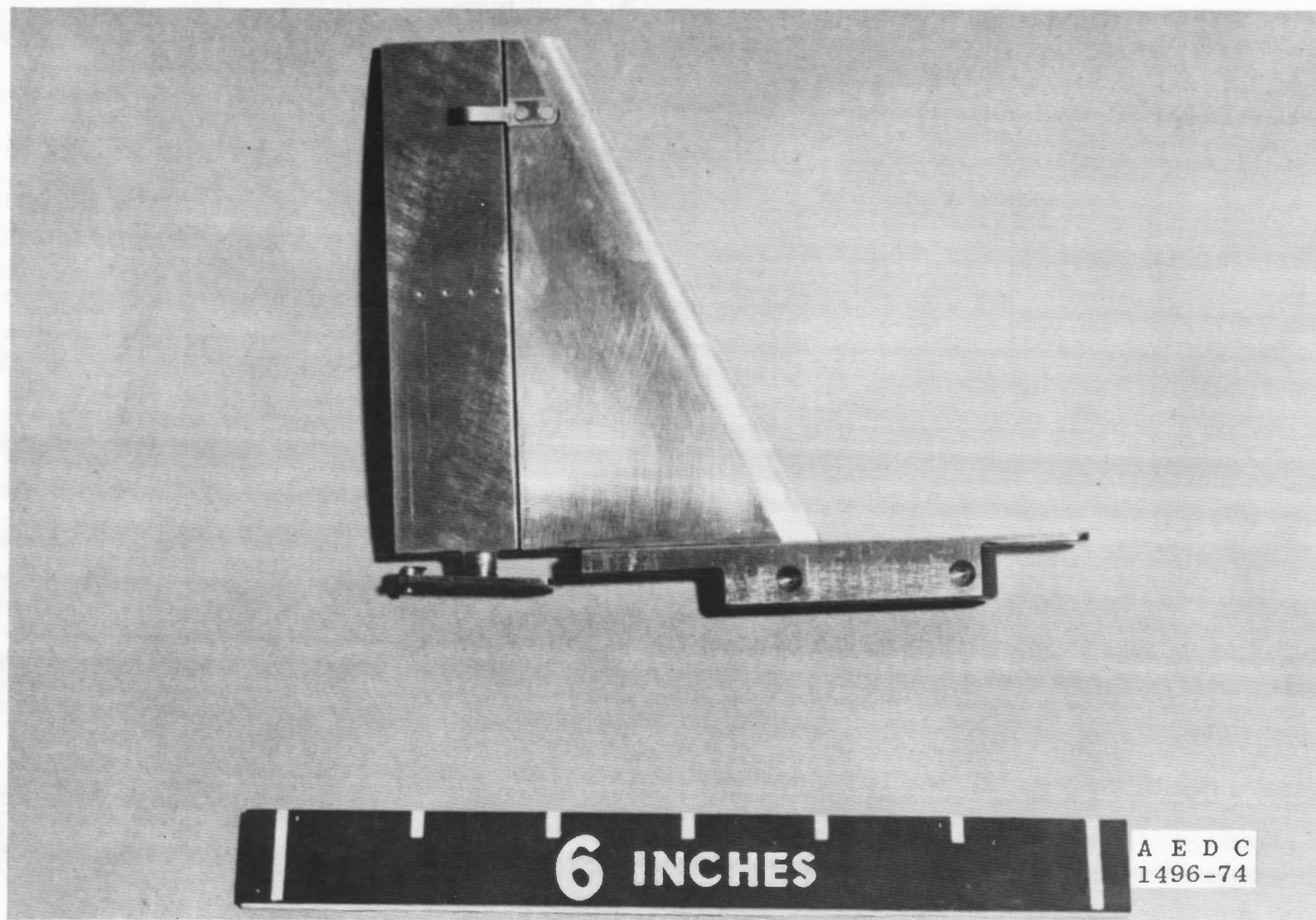
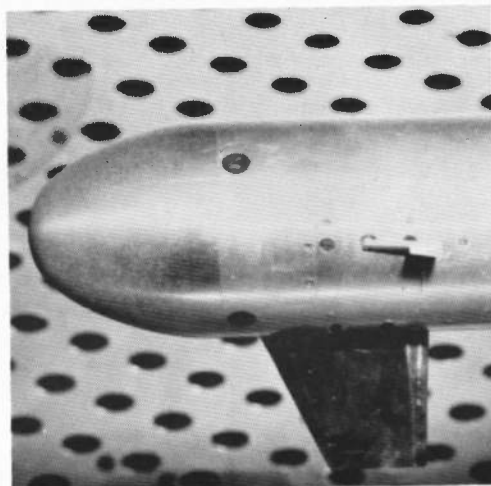
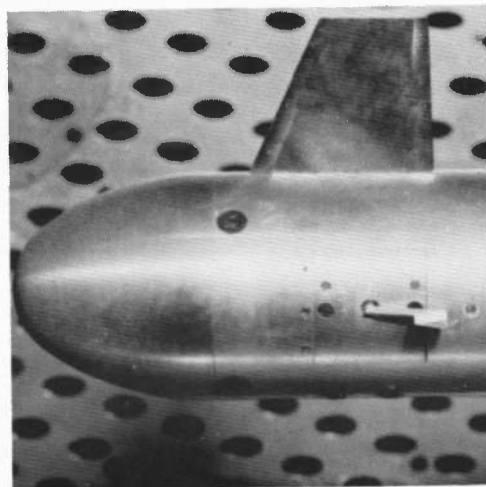


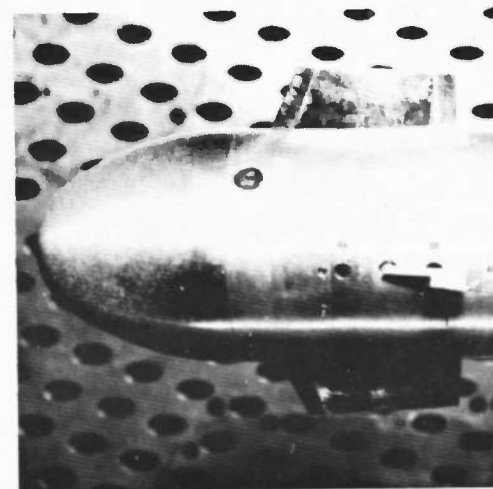
Figure 7. Photograph of tail fin and flap (T5).



a. Canard configuration C2

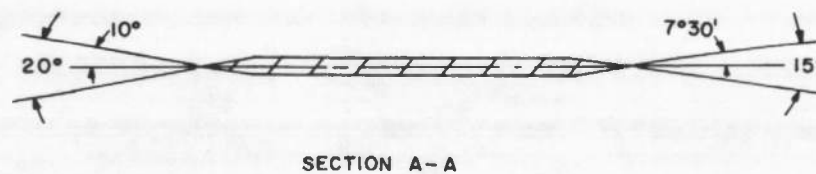
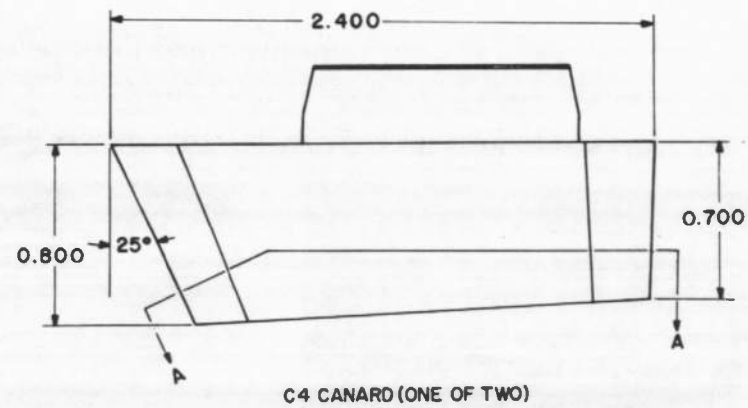
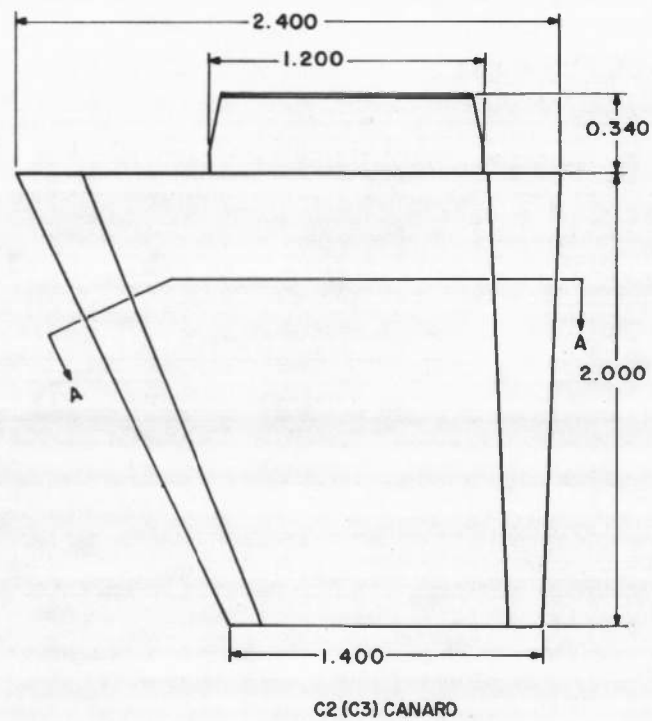


b. Canard configuration C3



c. Canard configuration C4

Figure 8. Photographs of the canard configurations.



ALL DIMENSIONS IN INCHES

Figure 9. Dimensional sketches of the C2(C3) and C4 canards.

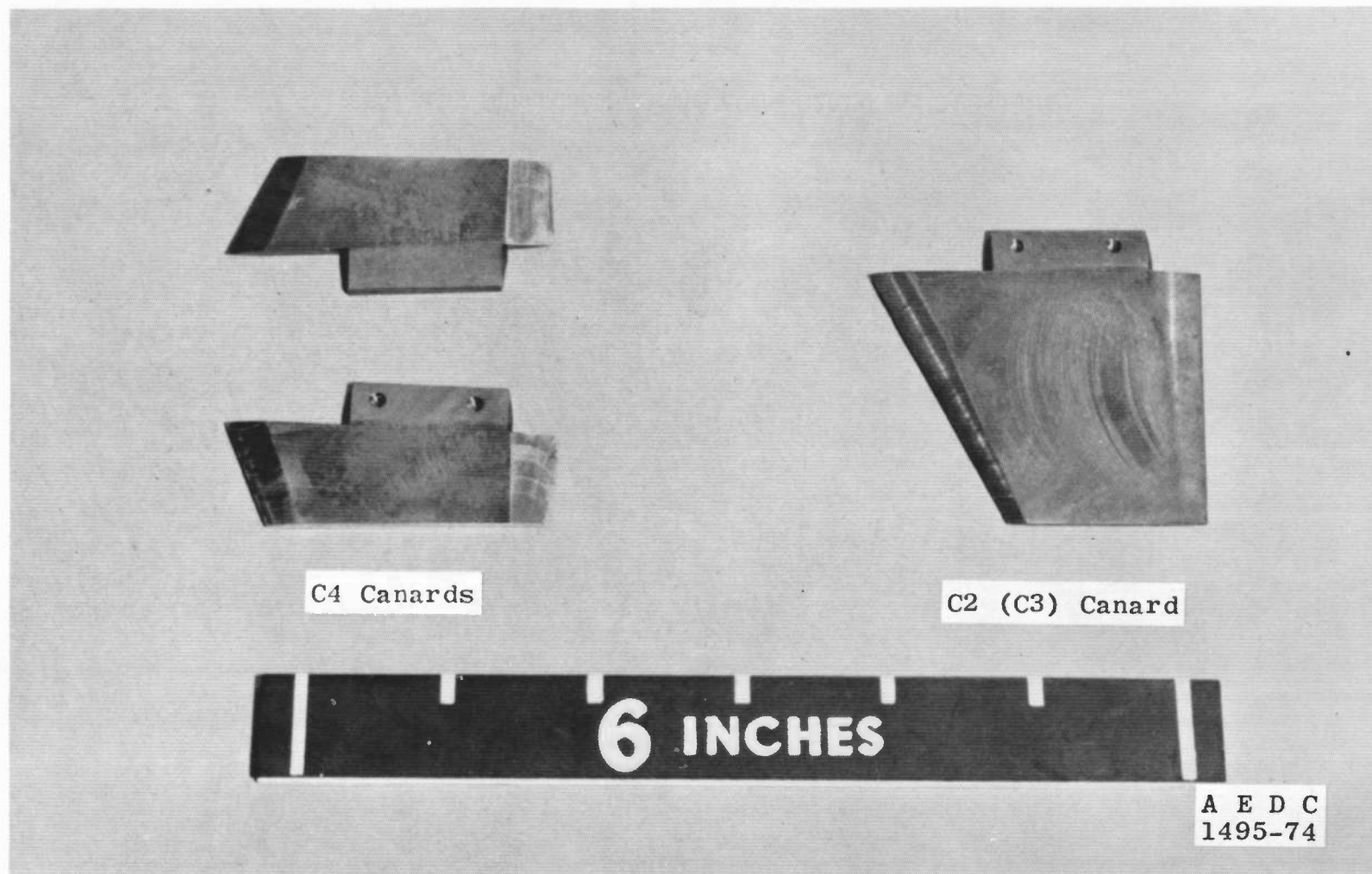
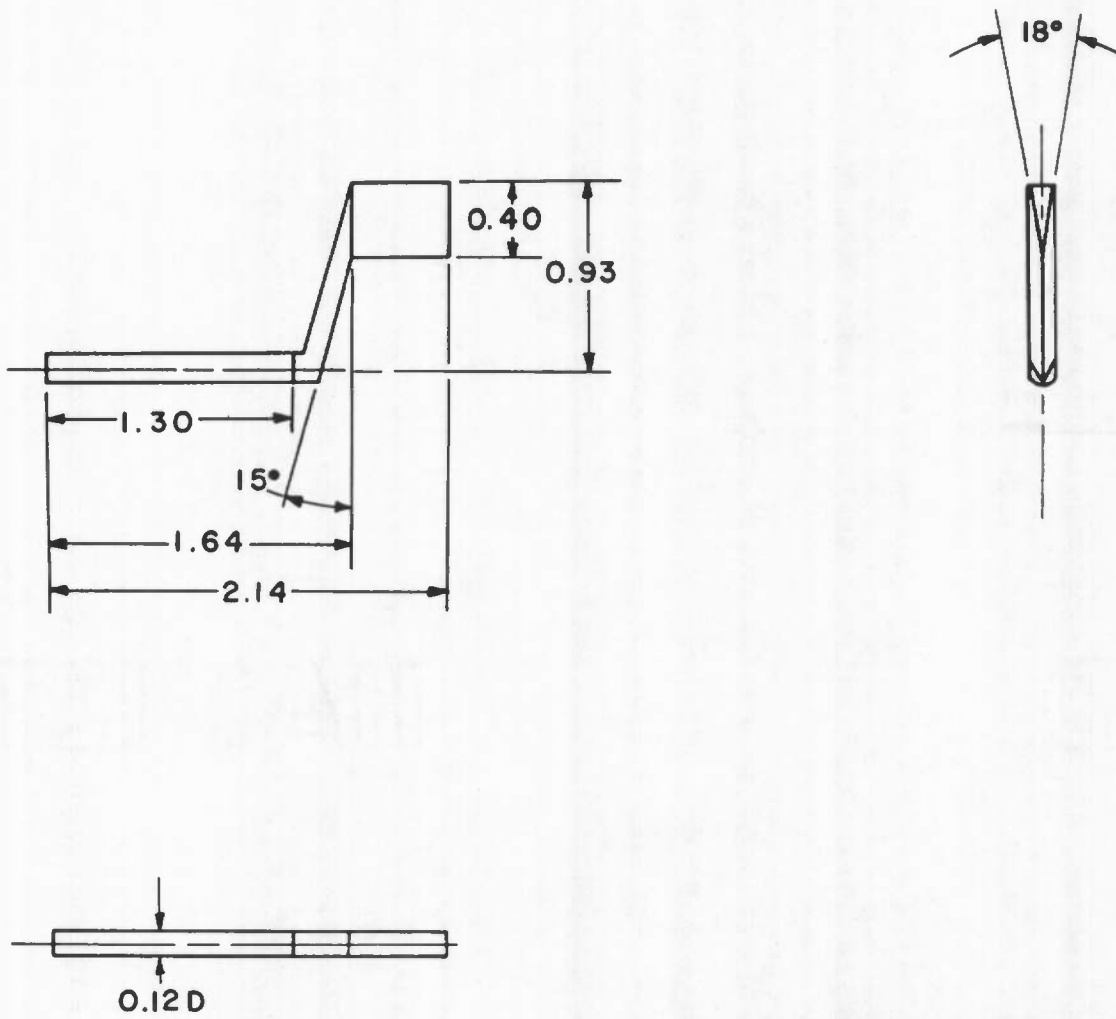


Figure 10. Photograph of the two C4 and the C2(C3) canards.



ALL DIMENSIONS IN INCHES

Figure 11. Dimensional sketch of the vane-type angle-of-attack indicator.

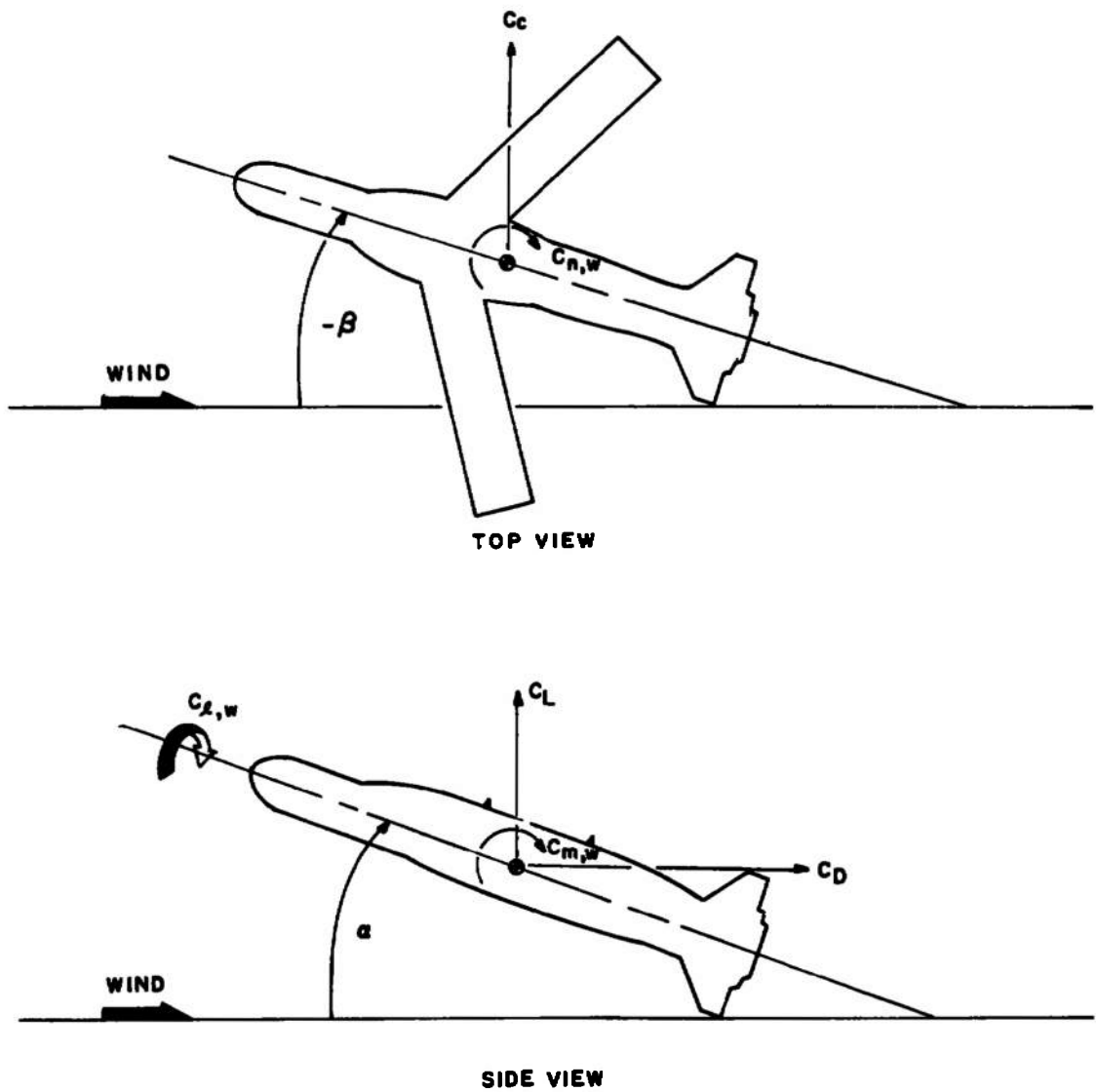


Figure 12. Orientation of model forces and moments.

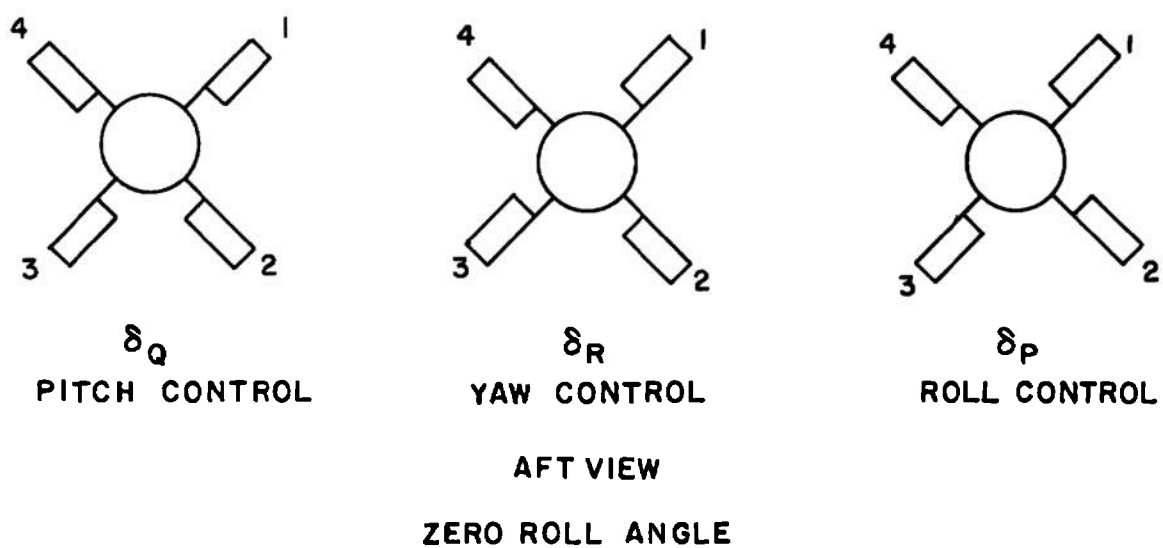
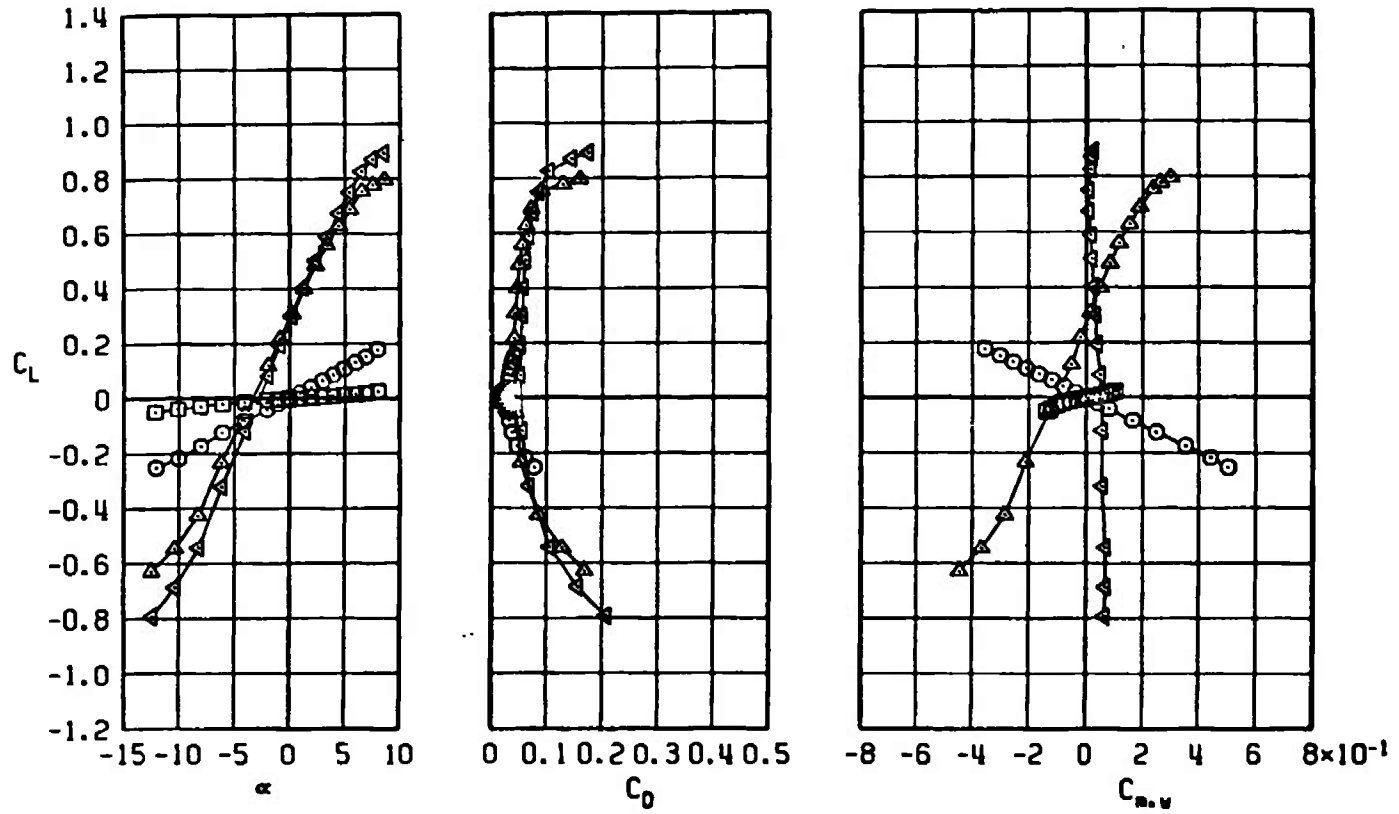


Figure 13. Orientation of control surface deflections.

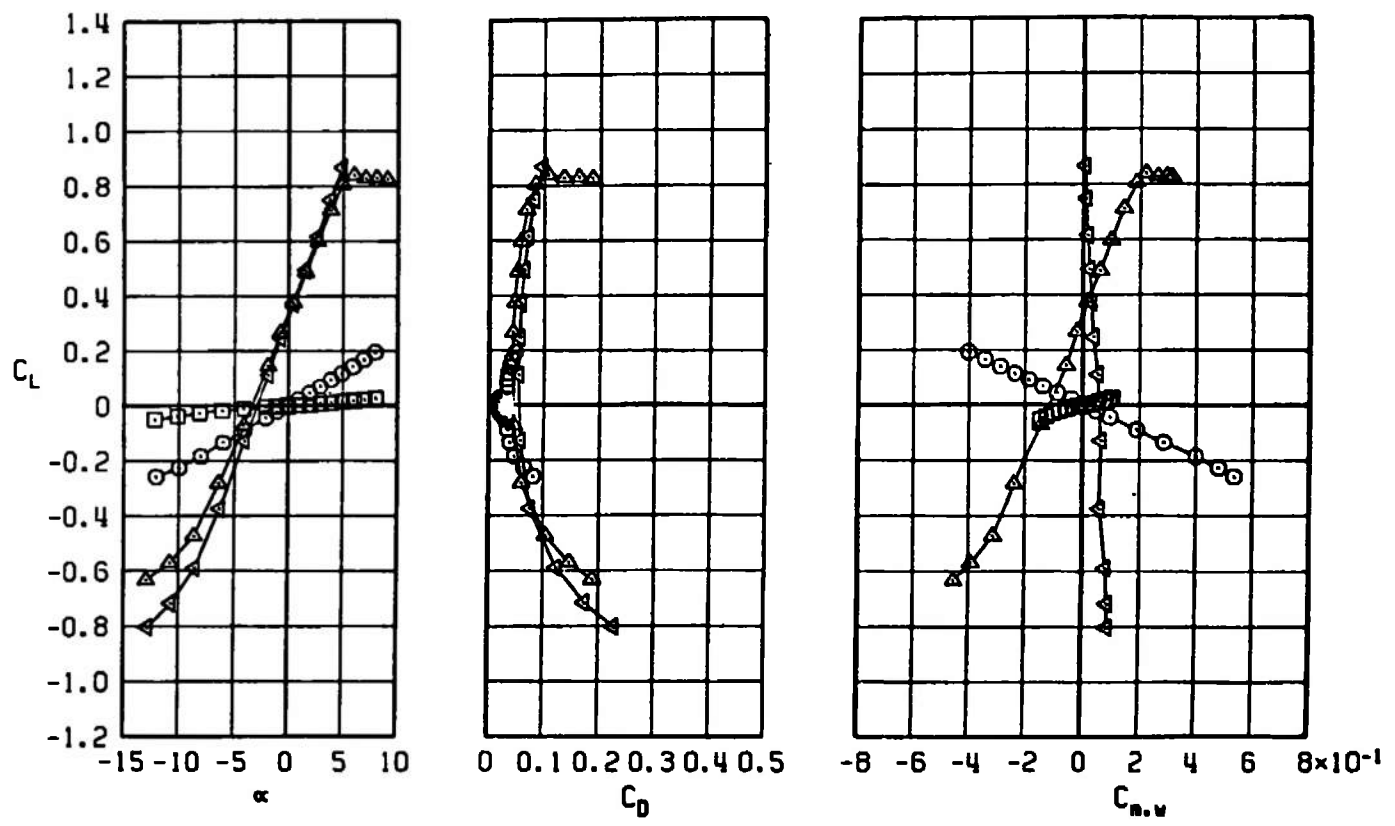
SYMBOL	CONFIG	M_∞	λ_∞	δP	δQ	δR
□	B2C2	0.50	-	-	-	-
○	B2T5C2	0.50	-	0	0	0
△	B2S1W2L1C2	0.50	30	-	-	-
◄	B2S1W2T5L1C2	0.50	30	0	0	0



a. $M_\infty = 0.50$

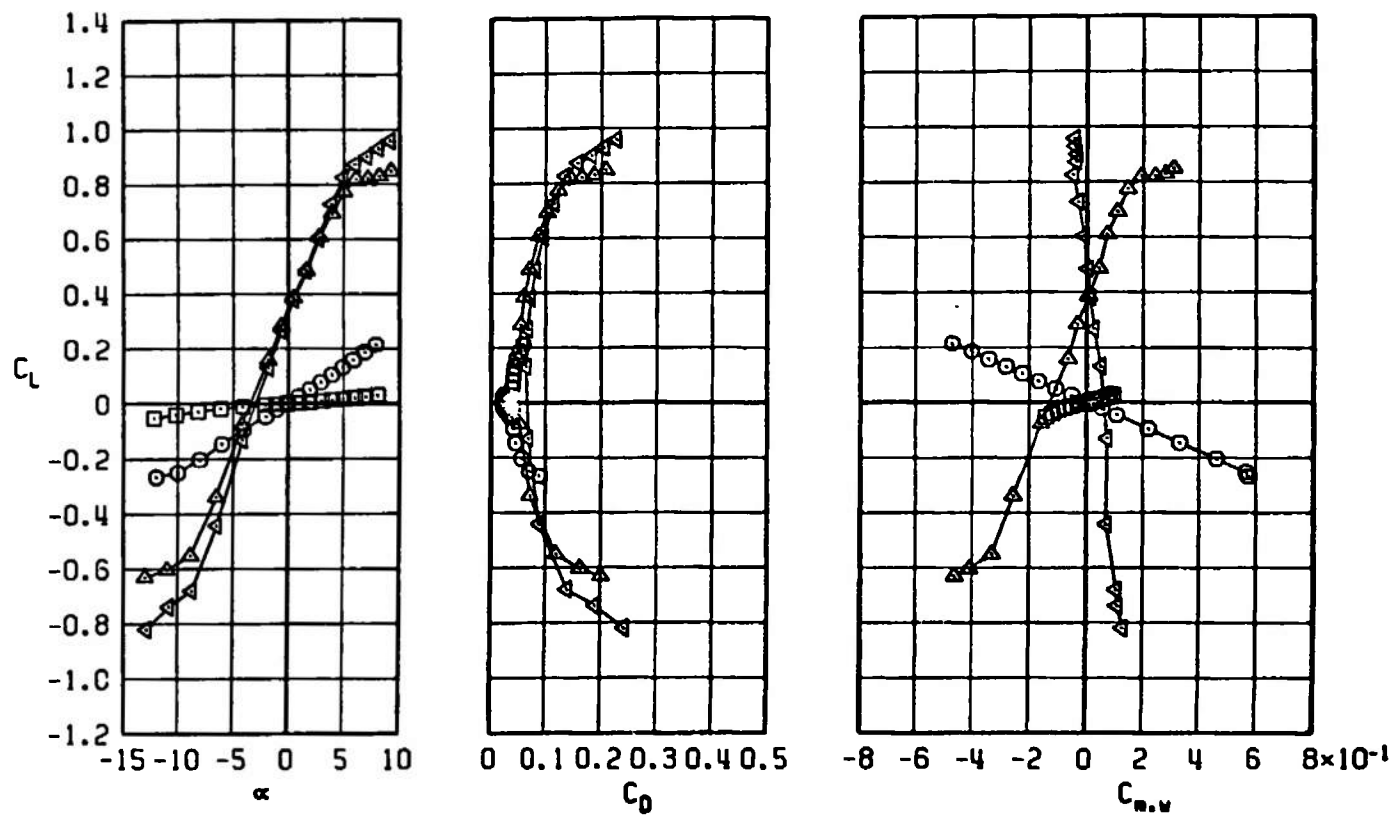
Figure 14. Lift, drag, and pitching-moment coefficients for configurations B2C2, B2T5C2, B2S1W2L1C2, and B2S1W2T5L1C2.

SYMBOL	CONFIG	M_∞	λ_H	δP	δQ	δR
□	B2C2	0.75	-	-	-	-
○	B2T5C2	0.75	-	0	0	0
△	B2S1W2L1C2	0.75	30	-	-	-
◄	B2S1W2T5L1C2	0.75	30	0	0	0



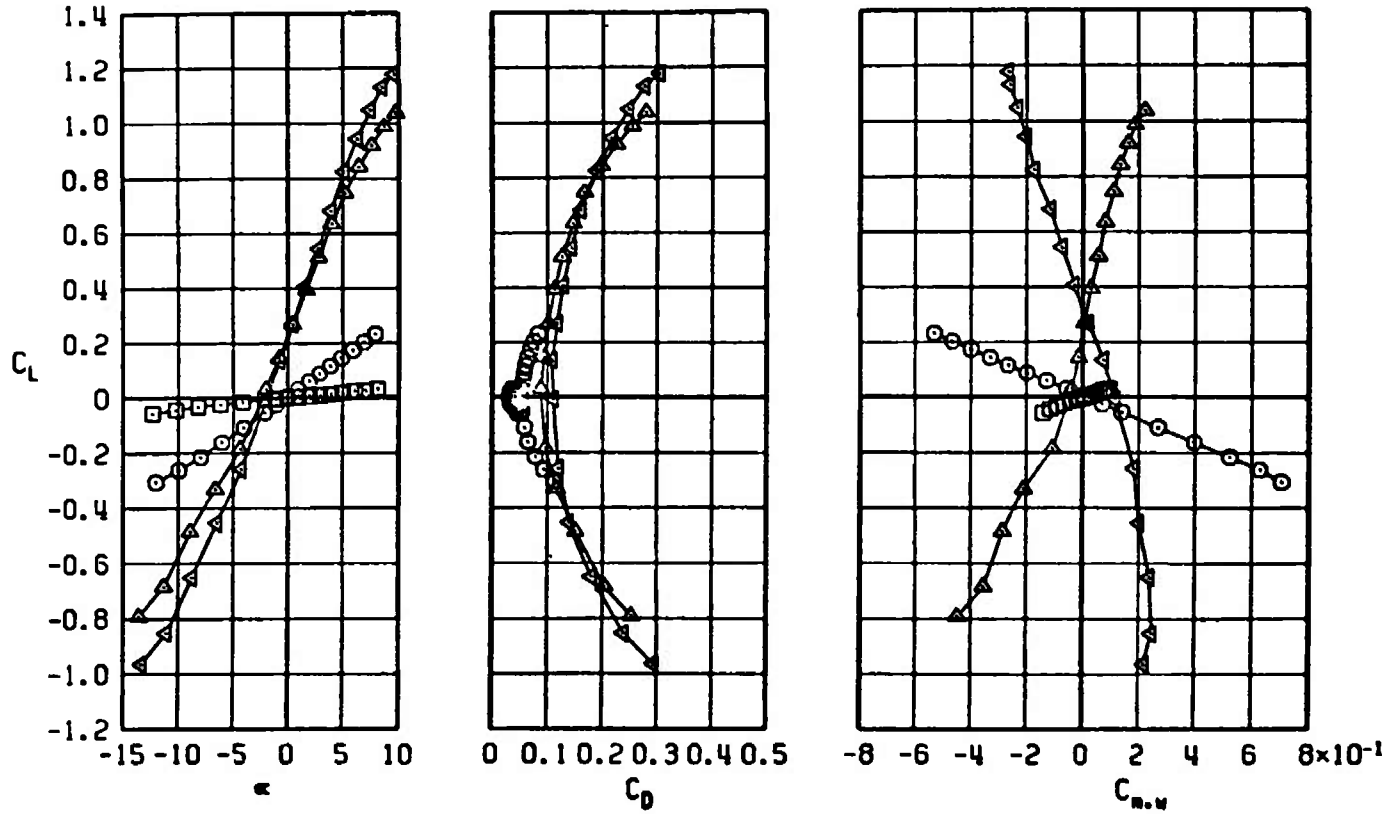
b. $M_\infty = 0.75$
Figure 14. Continued.

SYMBOL	CONFIG	M_∞	λ_H	δP	δQ	δR
□	B2C2	0.85	-	-	-	-
○	B2T5C2	0.85	-	0	0	0
△	B2S1W2L1C2	0.85	30	-	-	-
◄	B2S1W2T5L1C2	0.85	30	0	0	0



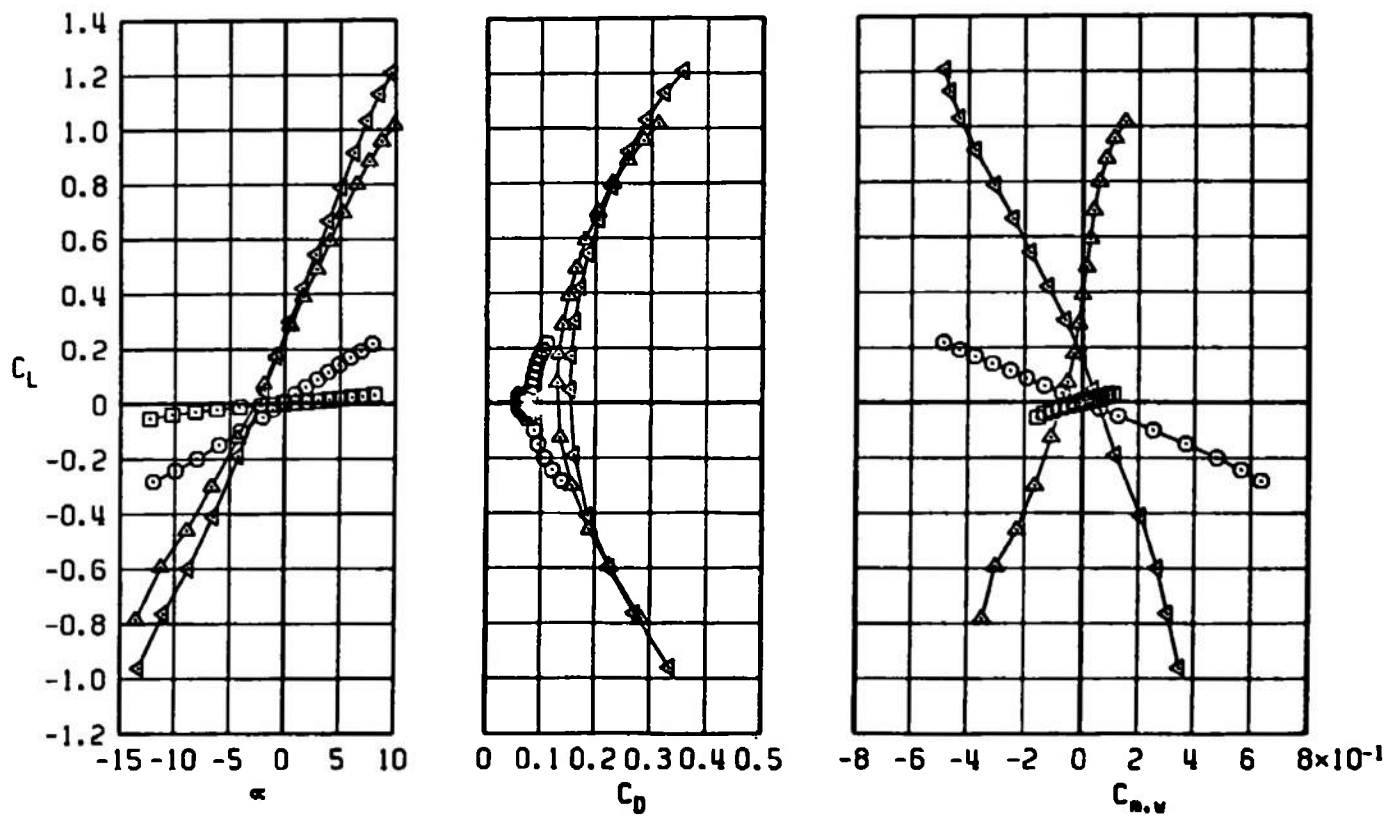
c. $M_\infty = 0.85$
Figure 14. Continued.

SYMBOL	CONFIG	M_∞	λ_H	δP	δQ	δR
□	B2C2	0.95	-	-	-	-
○	B2T5C2	0.95	-	0	0	0
△	B2S1W2L1C2	0.95	30	-	-	-
◀	B2S1W2T5L1C2	0.95	30	0	0	0



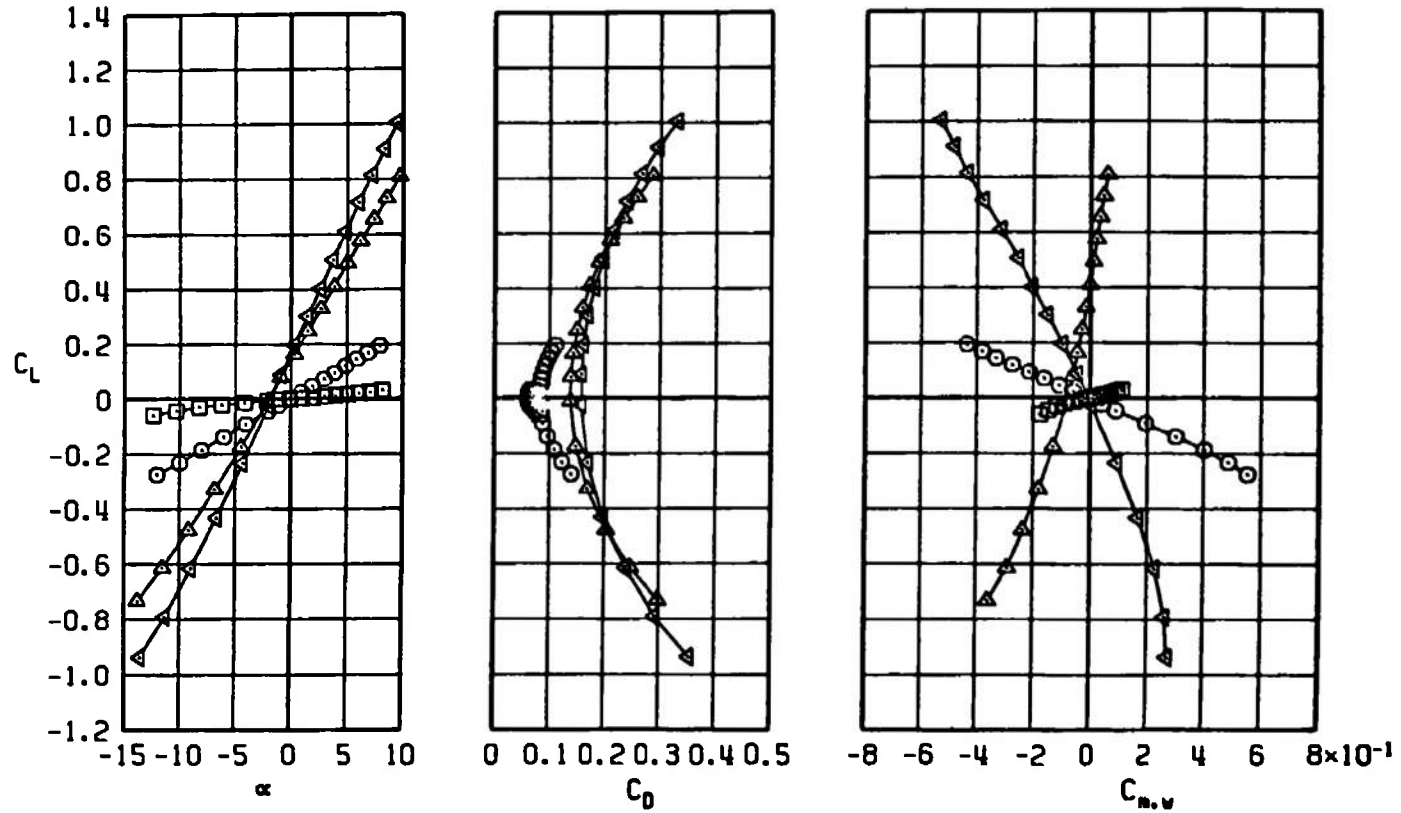
d. $M_\infty = 0.95$
Figure 14. Continued.

SYMBOL	CONFIG	M_∞	λ_M	δP	δQ	δR
□	B2C2	1.10	-	-	-	-
○	B2T5C2	1.10	-	0	0	0
△	B2S1W2L1C2	1.10	30	-	-	-
◁	B2S1W2T5L1C2	1.10	30	0	0	0



e. $M_\infty = 1.10$
Figure 14. Continued.

SYMBOL	CONFIG	M_∞	λ_N	δP	δQ	δR
□	B2C2	1.30	-	-	-	-
○	B2T5C2	1.30	-	0	0	0
△	B2S1W2L1C2	1.30	30	-	-	-
◀	B2S1W2T5L1C2	1.30	30	0	0	0



f. $M_\infty = 1.30$
Figure 14. Concluded.

SYMBOL	CONFIG	λ_w	ϕ_P	ϕ_Q	ϕ_R
□	B2C2	-	-	-	-
○	B2T5C2	-	0	0	0
△	B2S1W2L1C2	30	-	-	-
◀	B2S1W2T5L1C2	30	0	0	0

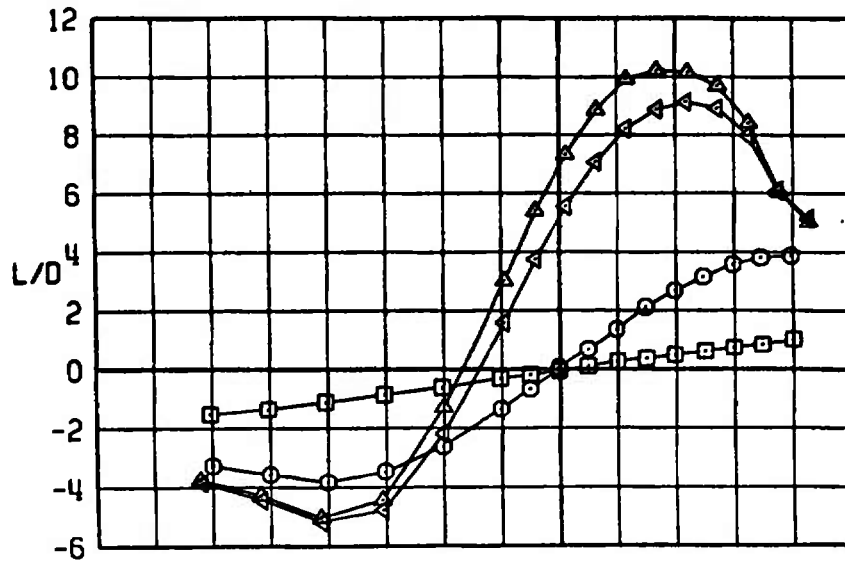
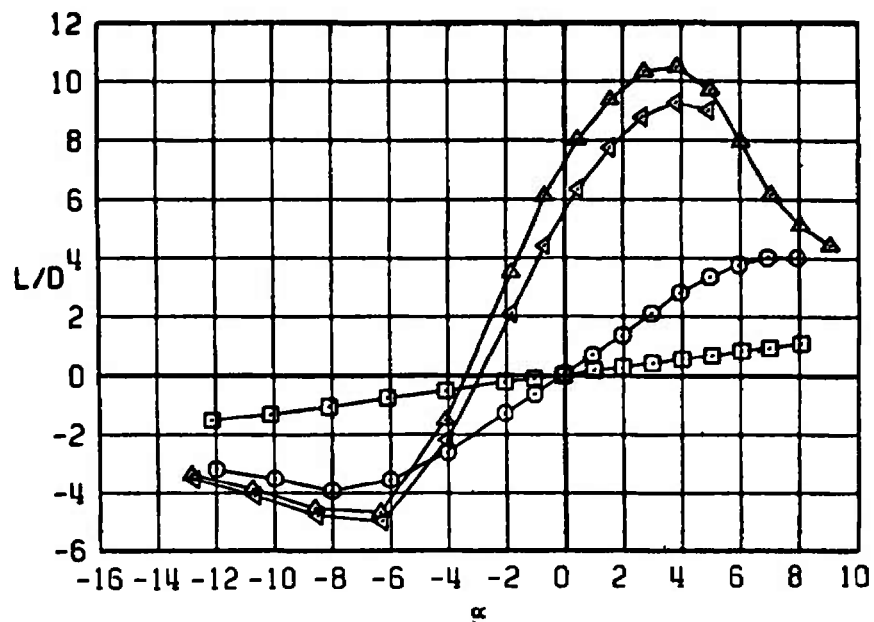
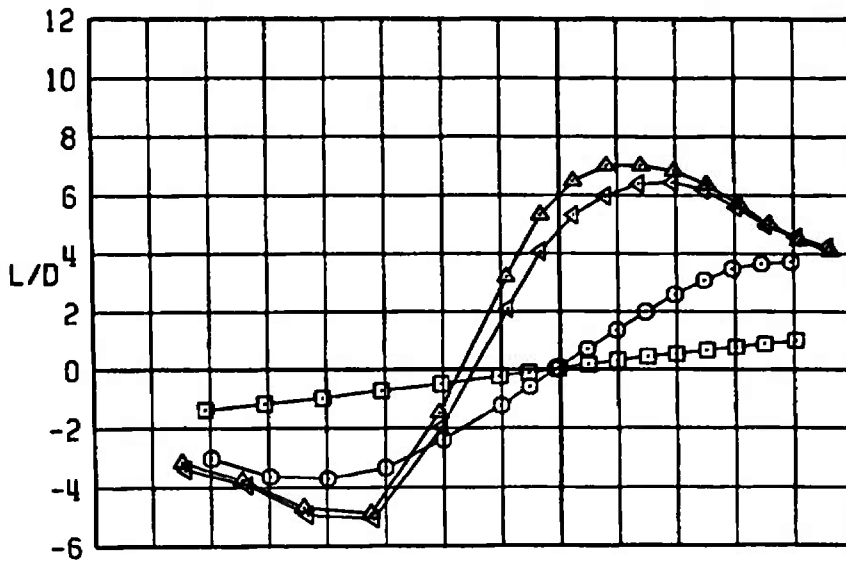
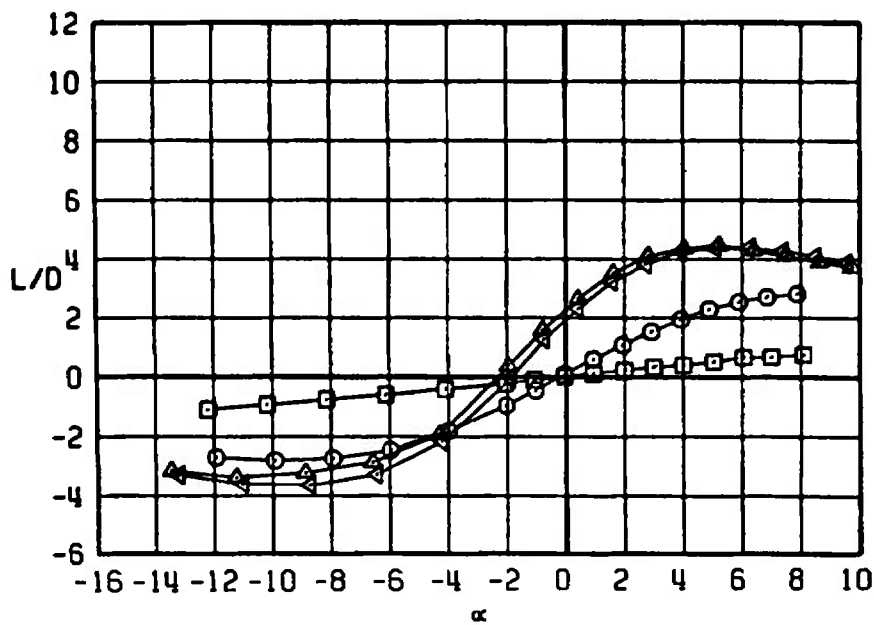
 $M_\infty = 0.50$  $M_\infty = 0.75$ a. $M_\infty = 0.50$ and 0.75

Figure 15. Lift-to-drag ratio for configurations B2C2, B2T5C2, B2S1W2L1C2, and B2S1W2T5L1C2.

SYMBOL	CONFIG	λ_M	ϕ_P	ϕ_Q	ϕ_R
□	B2C2	-	-	-	-
○	B2T5C2	-	0	0	0
△	B2S1W2L1C2	30	-	-	-
◄	B2S1W2T5L1C2	30	0	0	0

 $M_\infty = 0.85$  $M_\infty = 0.95$ 

b. $M_\infty = 0.85$ and 0.95
Figure 15. Continued.

SYMBOL	CONFIG	λ_H	ϕ_P	ϕ_Q	ϕ_R
□	B2C2	-	-	-	-
○	B2T5C2	-	0	0	0
△	B2S1W2L1C2	30	-	-	-
◁	B2S1W2T5L1C2	30	0	0	0

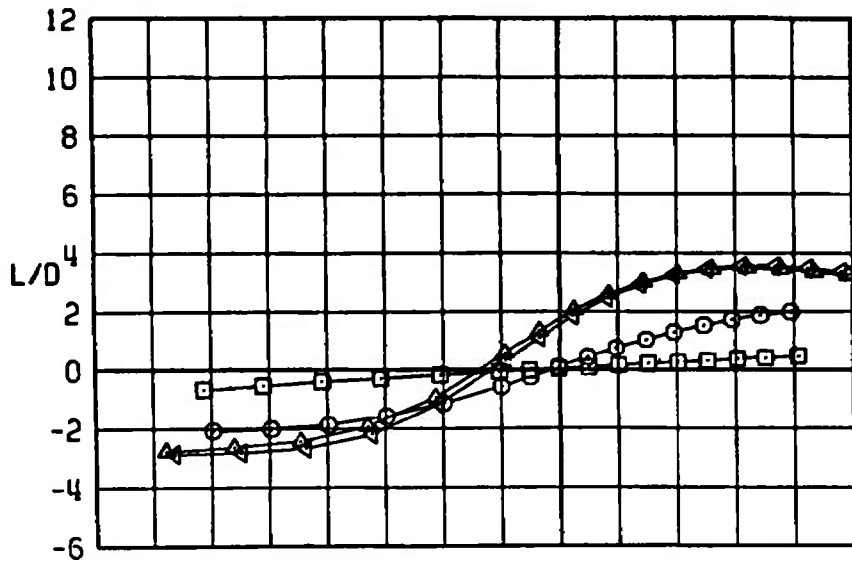
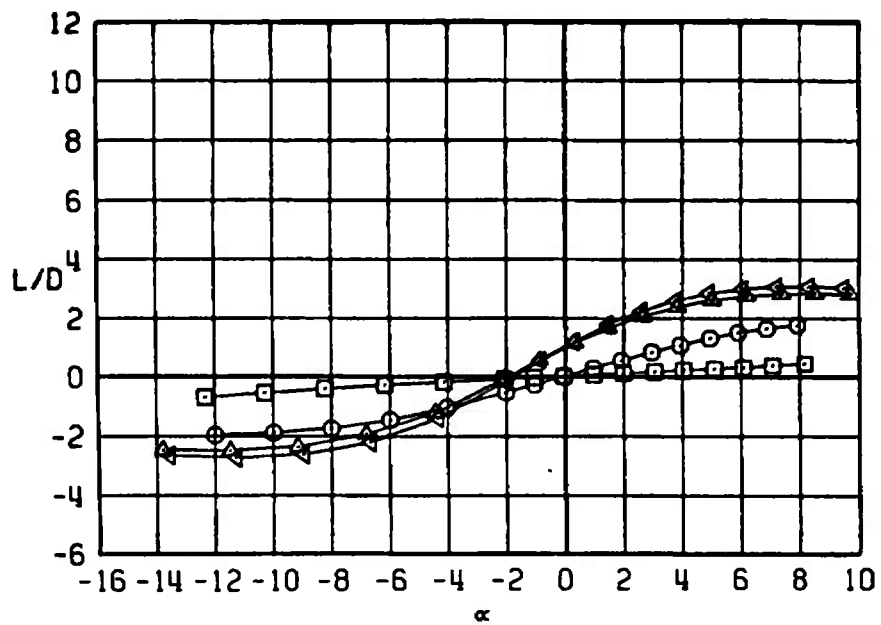
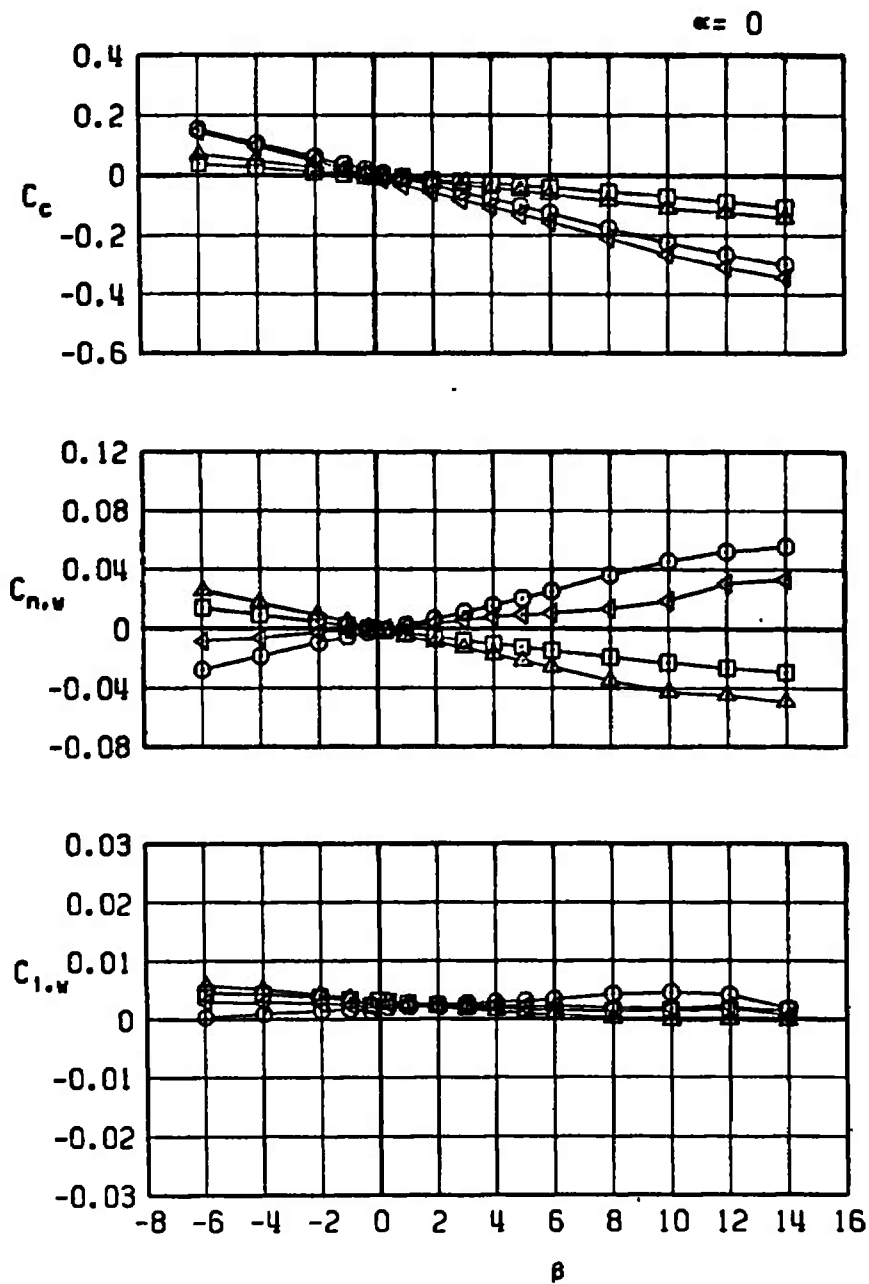
 $M_\infty = 1.10$  $M_\infty = 1.30$ c. $M_\infty = 1.10$ and 1.30

Figure 15. Concluded.

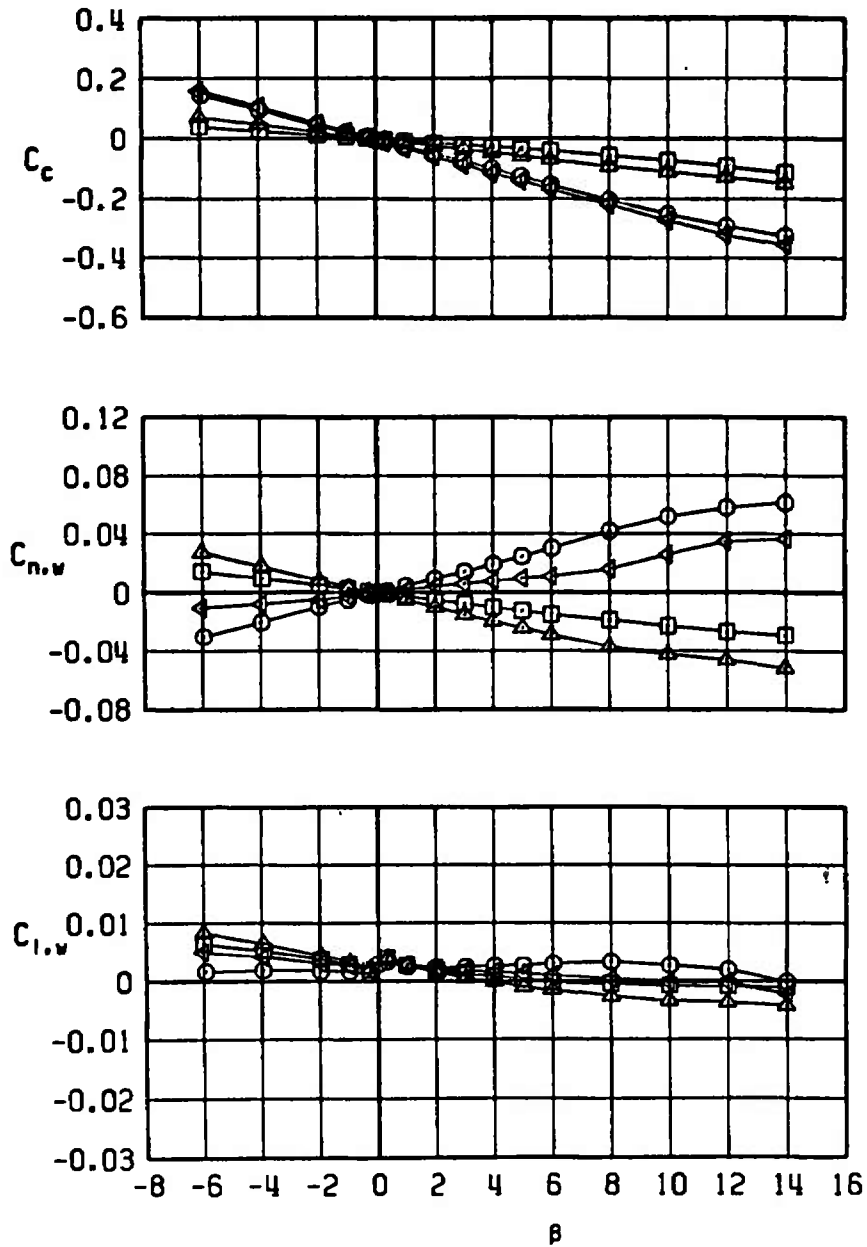
SYMBOL	CONFIG	M_∞	λ_W	ϕ_P	ϕ_Q	ϕ_R
□	B2S1W2L1	0.50	30	0	0	0
○	B2S1W2T5L1	0.50	30	0	0	0
△	B2S1W2L1C2	0.50	30	0	0	0
◁	B2S1W2T5L1C2	0.50	30	0	0	0



a. $M_\infty = 0.50$

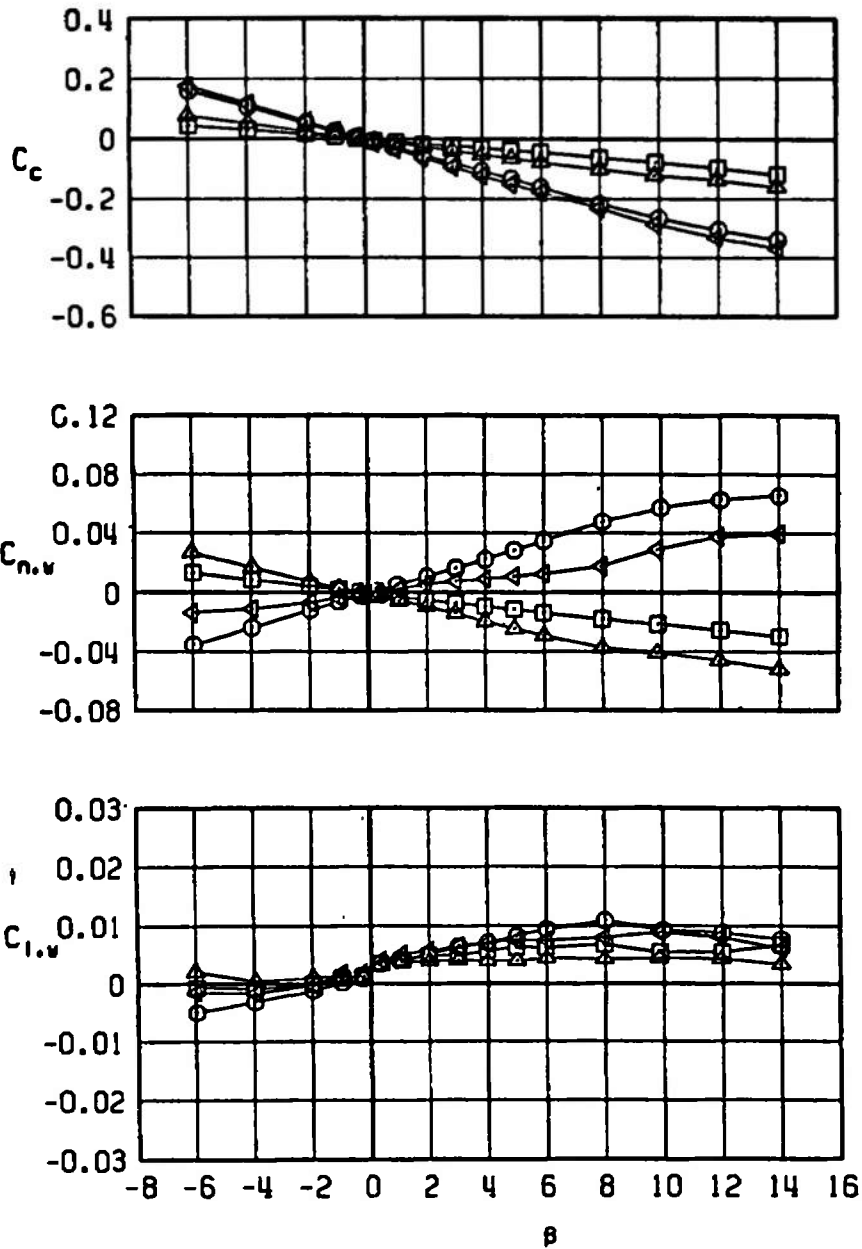
Figure 16. Crosswind-force, yawing-moment, and rolling-moment coefficients for configurations B2S1W2L1, B2S1W2T5L1, B2S1W2L1C2, and B2S1W2T5L1C2.

SYMBOL	CONFIG	M_∞	λ_M	δP	δQ	δR
□	B2S1W2L1	0.75	30	0	0	0
○	B2S1W2T5L1	0.75	30	0	0	0
△	B2S1W2L1C2	0.75	30	0	0	0
◄	B2S1W2T5L1C2	0.75	30	0	0	0

 $\alpha = 0$ 

b. $M_\infty = 0.75$
Figure 16. Continued.

SYMBOL	CONFIG	M_∞	λ_M	δP	δQ	δR
□	B2S1W2L1	0.85	30	0	0	0
○	B2S1W2T5L1	0.85	30	0	0	0
△	B2S1W2L1C2	0.85	30	0	0	0
◁	B2S1W2T5L1C2	0.85	30	0	0	0

 $\alpha = 0$ 

c. $M_\infty = 0.85$
Figure 16. Continued.

SYMBOL	CONFIG	M_∞	λ_M	ϕ_P	ϕ_Q	ϕ_R
□	B2S1W2L1	0.95	30	0	0	0
○	B2S1W2T5L1	0.95	30	0	0	0
△	B2S1W2L1C2	0.95	30	0	0	0
◀	B2S1W2T5L1C2	0.95	30	0	0	0

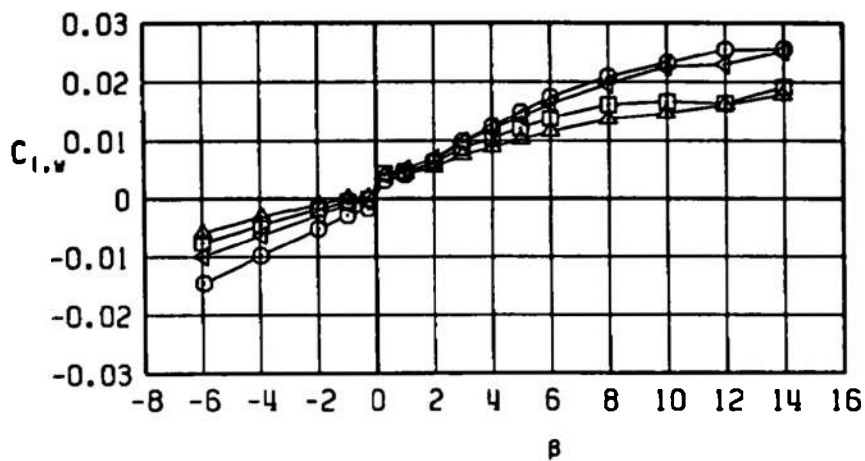
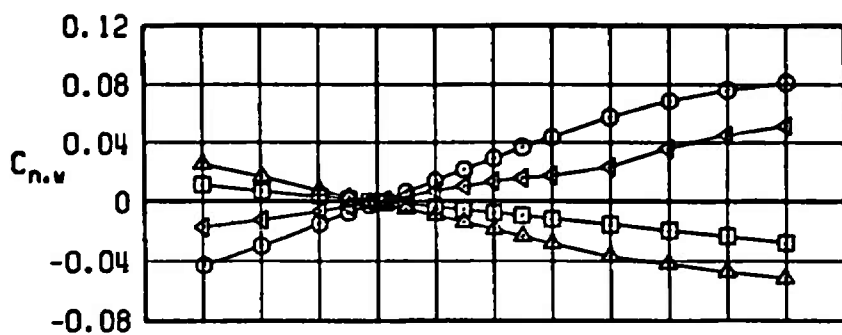
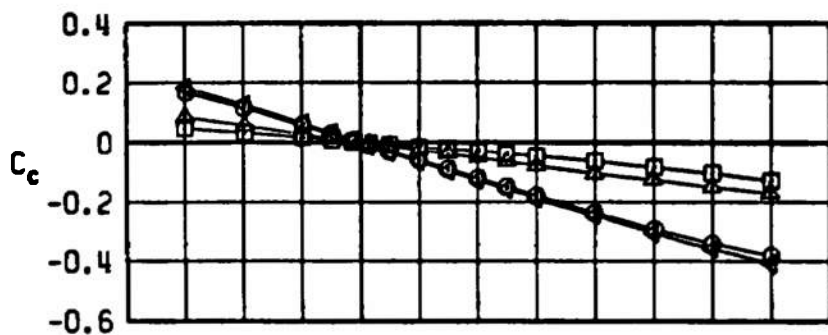
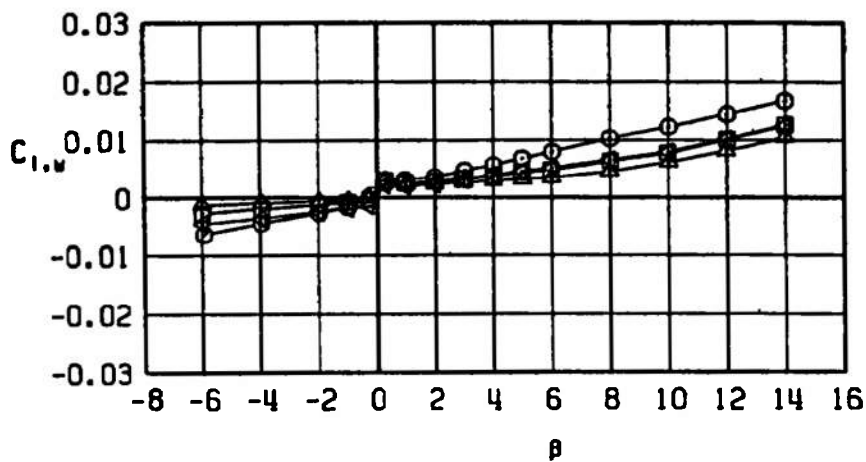
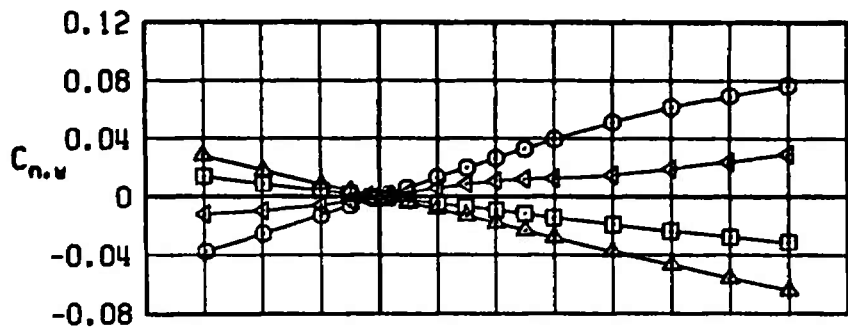
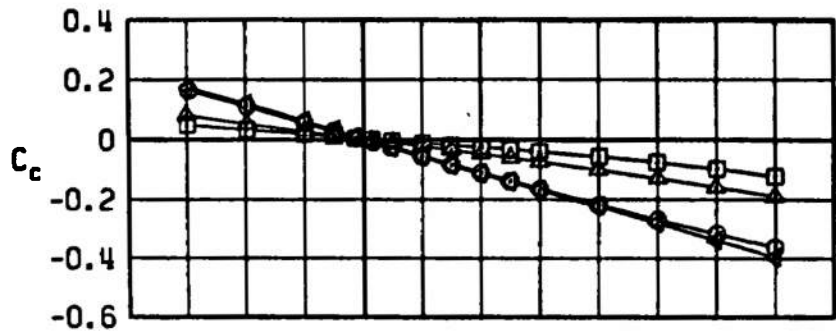
 $\alpha = 0$ d. $M_\infty = 0.95$

Figure 16. Continued.

SYMBOL	CONFIG	M_∞	λ_M	δP	δQ	δR
□	B2S1W2L1	1.10	30	0	0	0
○	B2S1W2T5L1	1.10	30	0	0	0
△	B2S1W2L1C2	1.10	30	0	0	0
◄	B2S1W2T5L1C2	1.10	30	0	0	0

 $\alpha = 0$ 

e. $M_\infty = 1.10$
Figure 16. Continued.

SYMBOL	CONFIG	M_∞	λ_H	δP	δQ	δR
□	B2S1W2L1	1.30	30	0	0	0
○	B2S1W2T5L1	1.30	30	0	0	0
△	B2S1W2L1C2	1.30	30	0	0	0
◀	B2S1W2T5L1C2	1.30	30	0	0	0

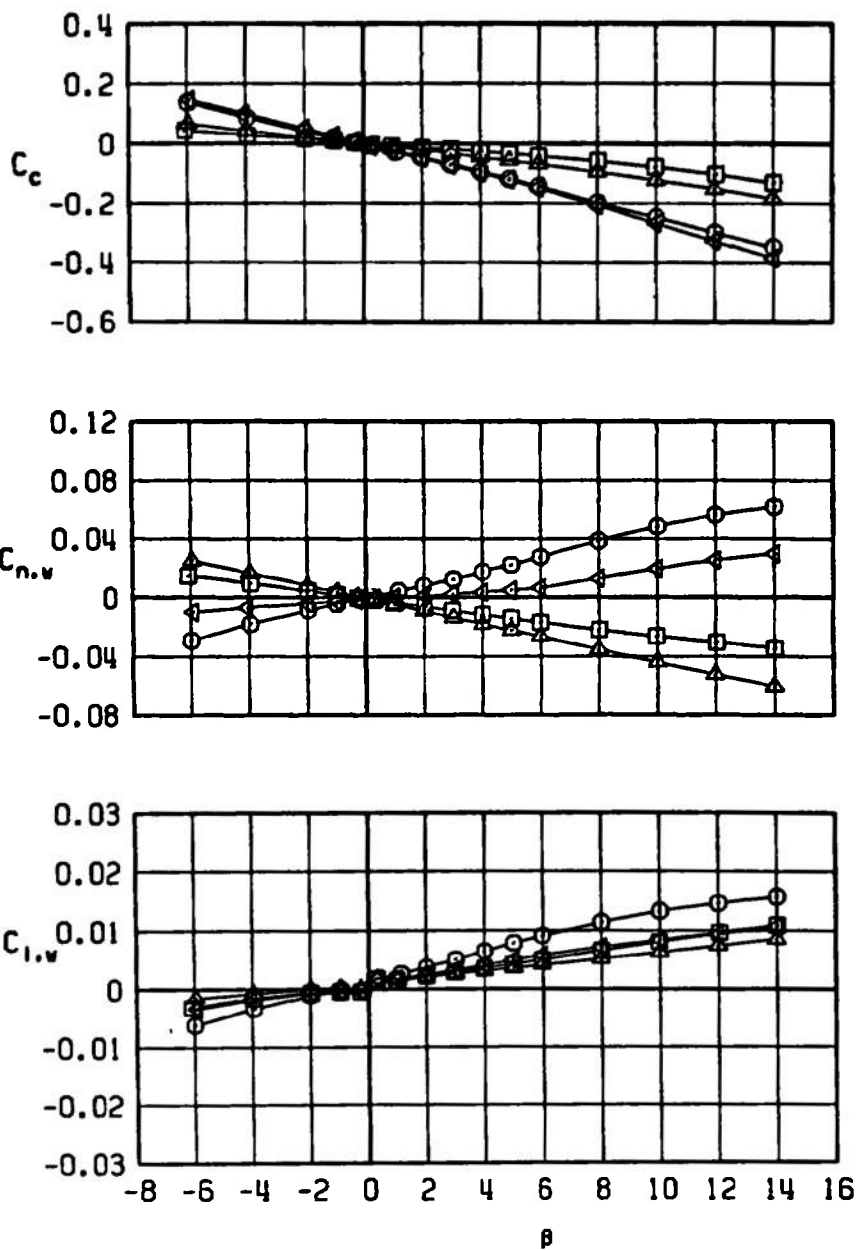
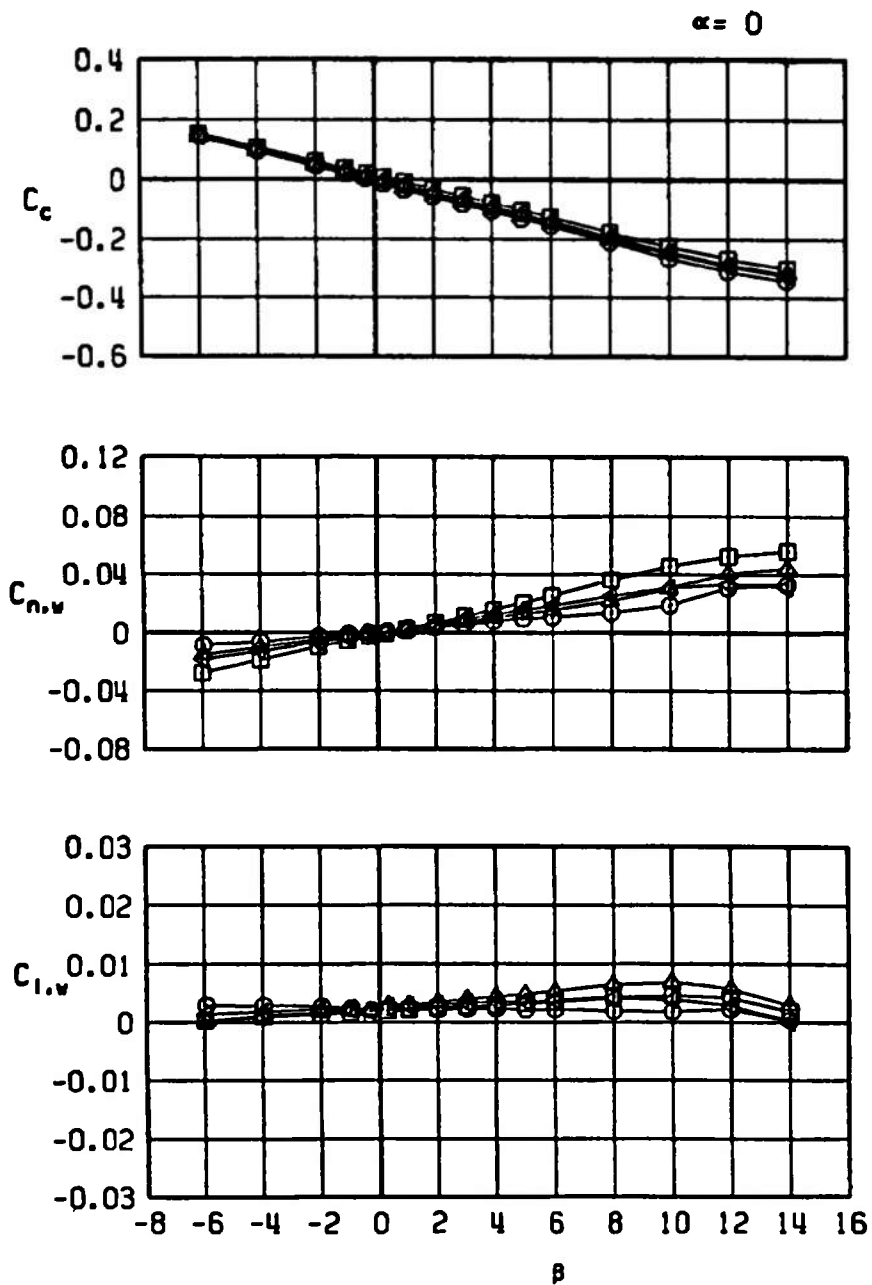
 $\alpha = 0$ f. $M_\infty = 1.30$

Figure 16. Concluded.

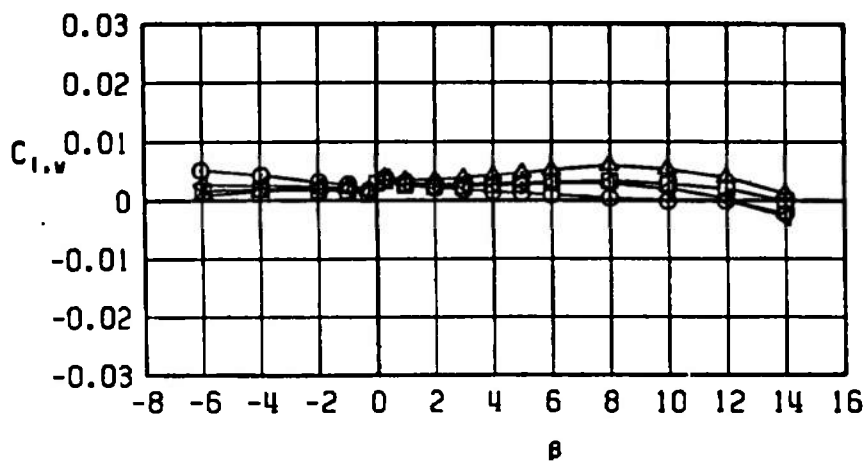
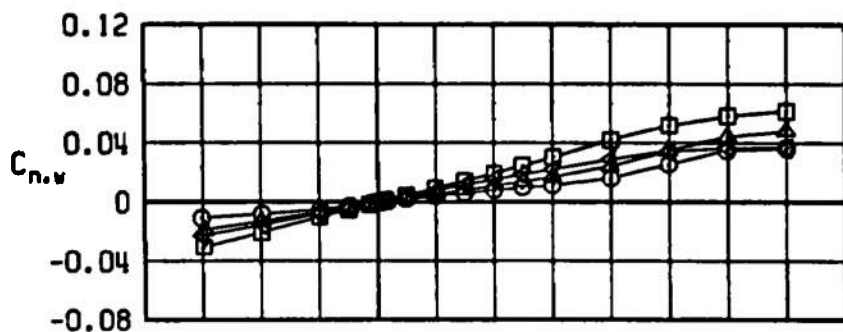
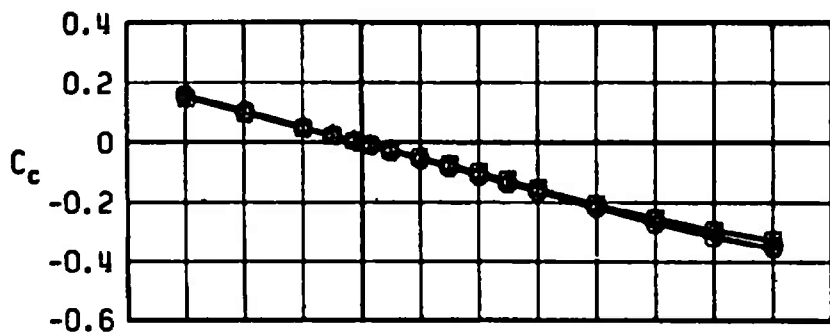
SYMBOL	CONFIG	M_∞	λ_M	δP	δQ	δR
□	B2S1W2T5L1	0.50	30	0	0	0
○	B2S1W2T5L1C2	0.50	30	0	0	0
△	B2S1W2T5L1C3	0.50	30	0	0	0
◁	B2S1W2T5L1C4	0.50	30	0	0	0



a. $M_\infty = 0.50$

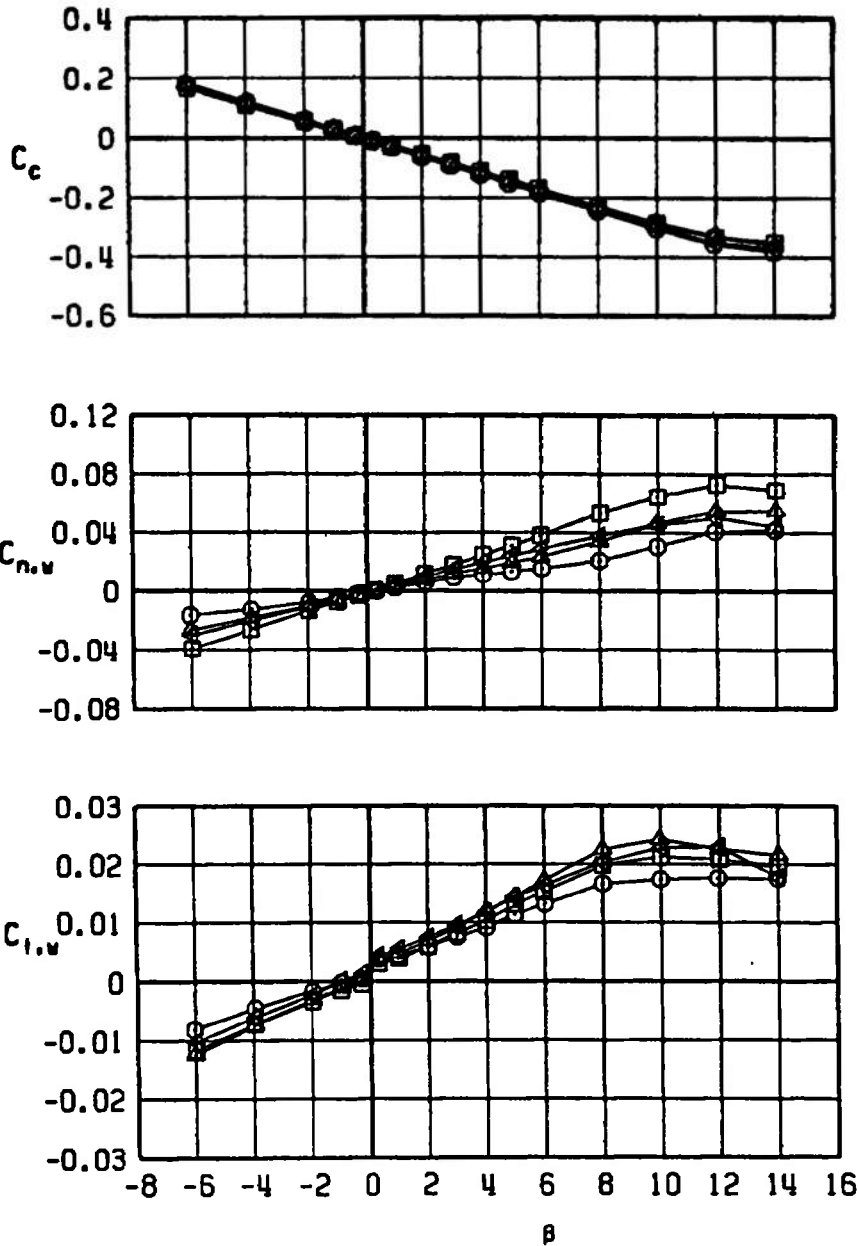
Figure 17. Effect of canards C2, C3, and C4 on the crosswind-force, yawing-moment, and rolling-moment coefficients, $\alpha = 0$.

SYMBOL	CONFIG	M_∞	λ_M	δP	δQ	δR
□	B2S1W2T5L1	0.75	30	0	0	0
○	B2S1W2T5L1C2	0.75	30	0	0	0
△	B2S1W2T5L1C3	0.75	30	0	0	0
◀	B2S1W2T5L1C4	0.75	30	0	0	0

 $\alpha = 0$ 

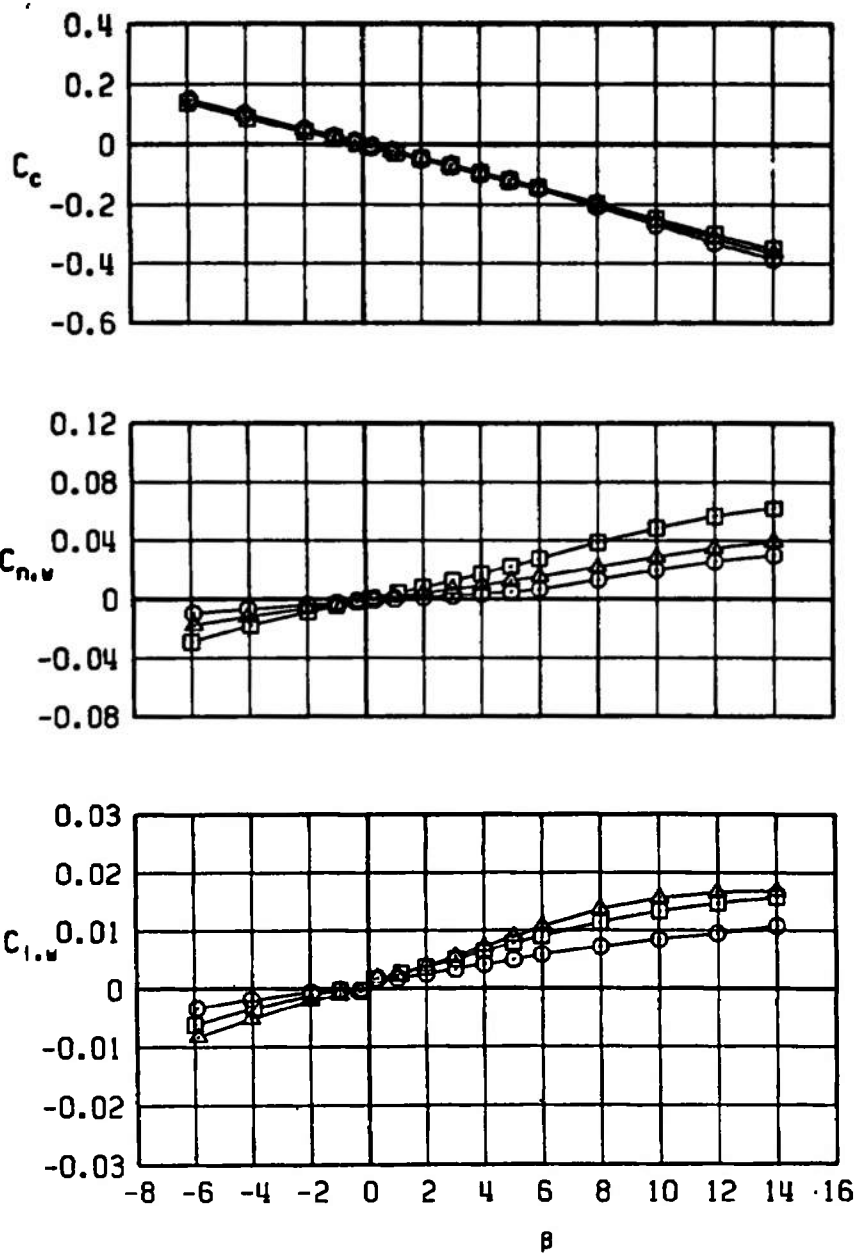
b. $M_\infty = 0.75$
Figure 17. Continued.

SYMBOL	CONFIG	M_∞	λ_M	ϕ_P	ϕ_Q	ϕ_R
□	B2S1W2T5L1	0.90	30	0	0	0
○	B2S1W2T5L1C2	0.90	30	0	0	0
△	B2S1W2T5L1C3	0.90	30	0	0	0
◀	B2S1W2T5L1C4	0.90	30	0	0	0

 $\alpha = 0$ 

c. $M_\infty = 0.90$
Figure 17. Continued.

SYMBOL	CONFIG	M_∞	λ_W	δP	δQ	δR
□	B2S1W2T5L1	1.30	30	0	0	0
○	B2S1W2T5L1C2	1.30	30	0	0	0
△	B2S1W2T5L1C3	1.30	30	0	0	0

 $\alpha = 0$ 

d. $M_\infty = 1.30$
Figure 17. Concluded.

SYMBOL	CONFIG	M_∞	λ_M	δP	δQ	δR
□	B2S1W2T5L1	0.50	30	0	0	0
○	B2S1W2T5L1C2	0.50	30	0	0	0
△	B2S1W2T5L1C3	0.50	30	0	0	0
◀	B2S1W2T5L1C4	0.50	30	0	0	0

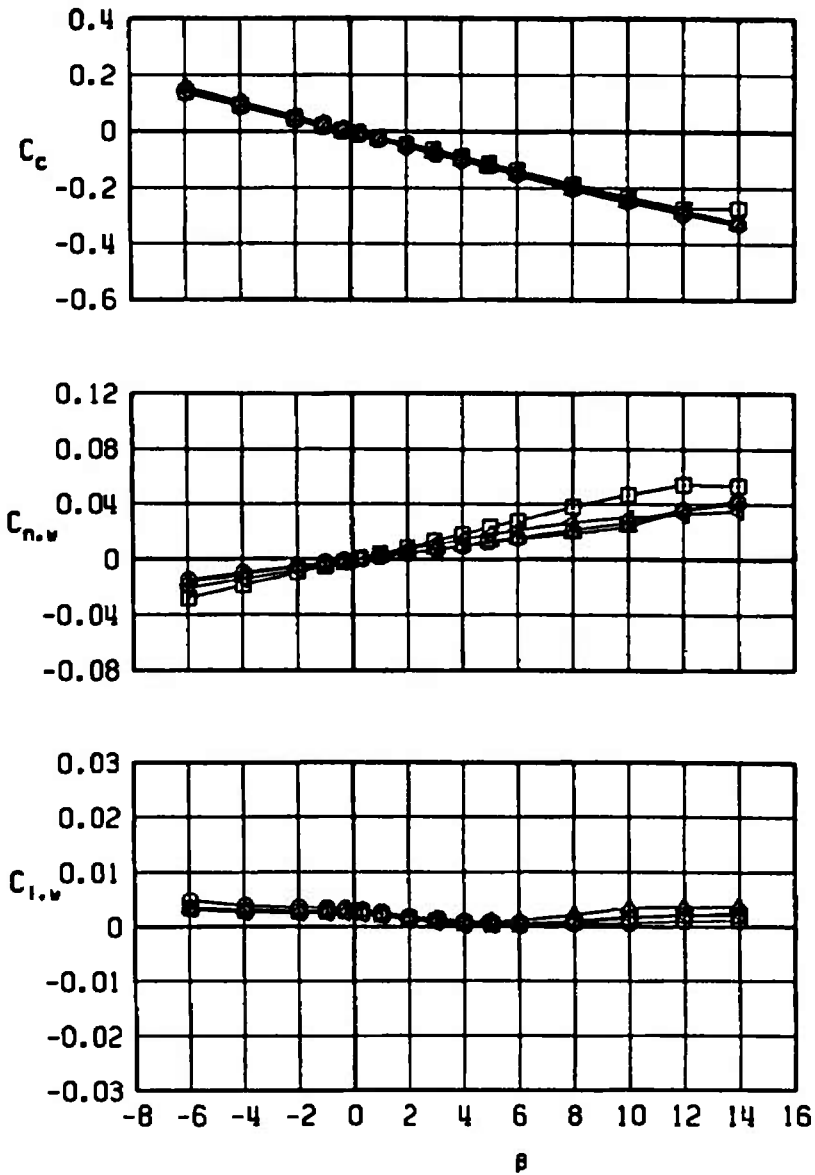
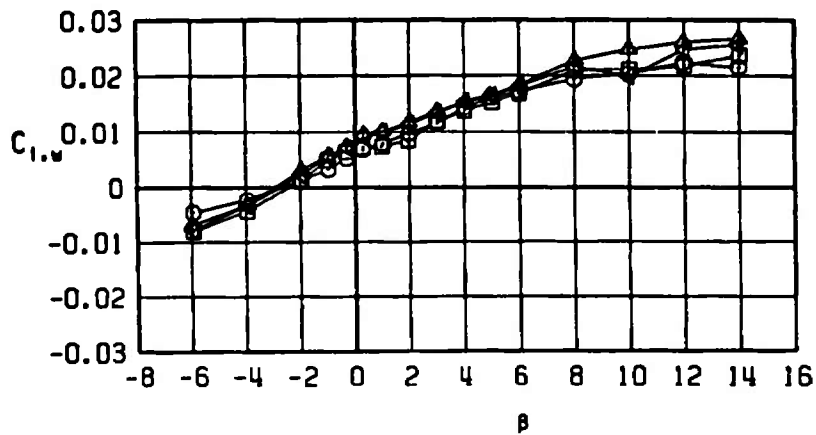
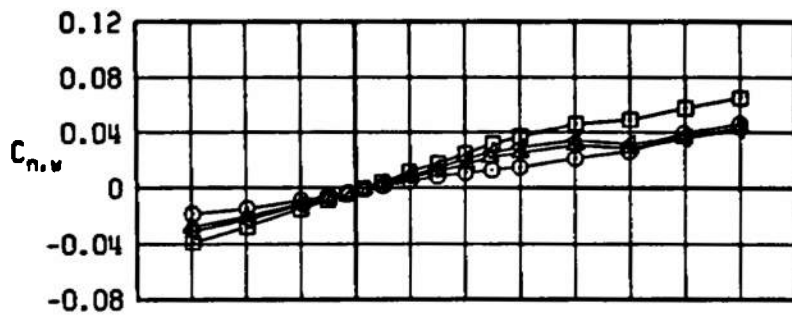
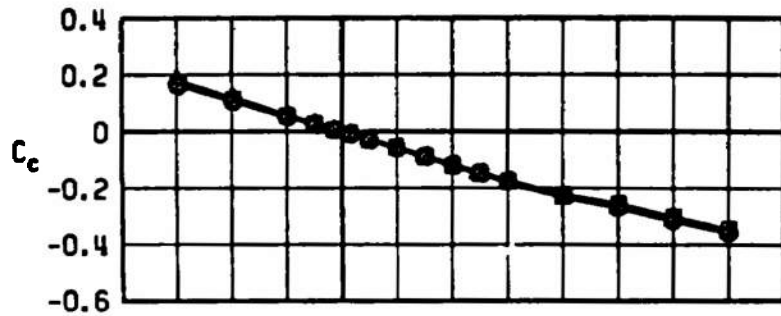
 $\alpha = 5$ a. $M_\infty = 0.50$

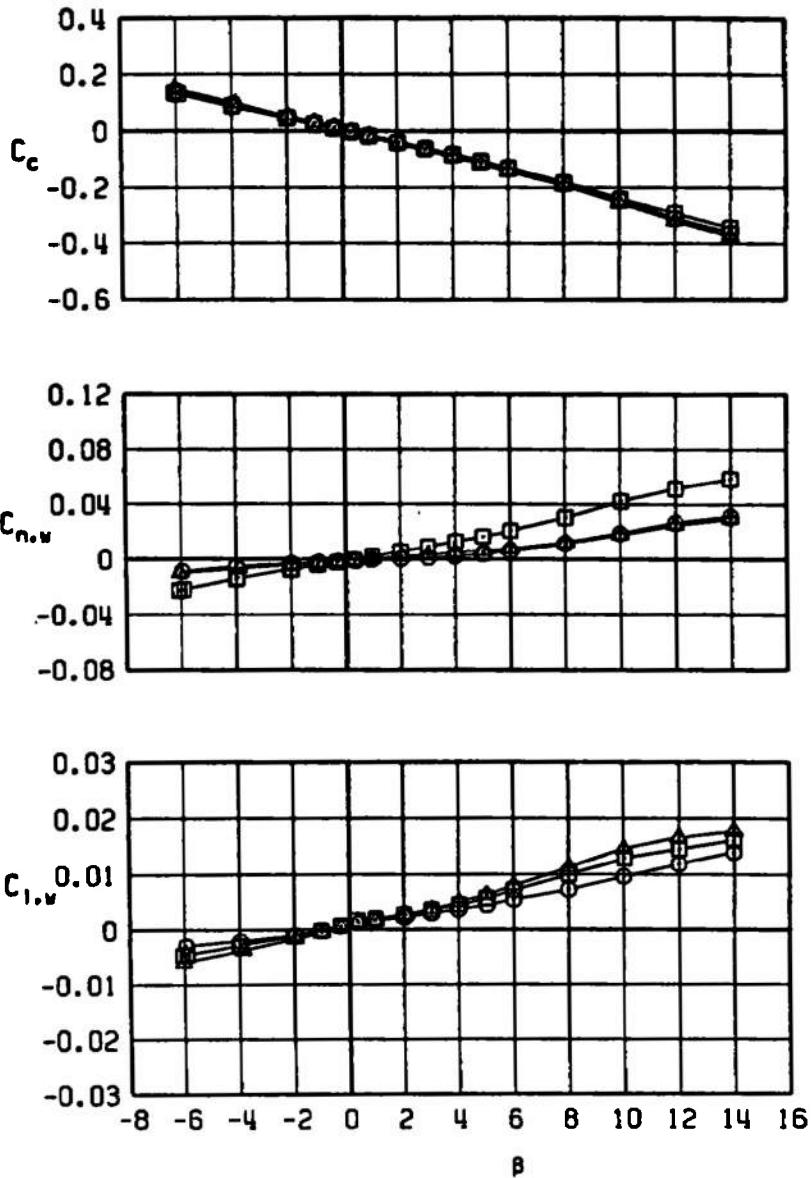
Figure 18. Effect of canards C2, C3, and C4 on the crosswind-force, yawing-moment, and rolling-moment coefficients, $\alpha = 5$ deg.

SYMBOL	CONFIG	M_∞	λ_w	δP	δQ	δR
□	B2S1W2T5L1	0.90	30	0	0	0
○	B2S1W2T5L1C2	0.90	30	0	0	0
△	B2S1W2T5L1C3	0.90	30	0	0	0
◀	B2S1W2T5L1C4	0.90	30	0	0	0

 $\alpha = 5$ 

b. $M_\infty = 0.90$
Figure 18. Continued.

SYMBOL	CONFIG	M_∞	λ_M	δP	δQ	δR
□	B2S1W2T5L1	1.30	30	0	0	0
○	B2S1W2T5L1C2	1.30	30	0	0	0
△	B2S1W2T5L1C3	1.30	30	0	0	0

 $\alpha = 5$ 

c. $M_\infty = 1.30$
Figure 18. Concluded.

SYMBOL	CONFIG	M_∞	λ_M	ϕ_P	ϕ_Q	ϕ_R
□	B2S1W2T5L1	0.50	30	0	0	0
○	B2S1W2T5L1C2	0.50	30	0	0	0
△	B2S1W2T5L1C3	0.50	30	0	0	0
◀	B2S1W2T5L1C4	0.50	30	0	0	0

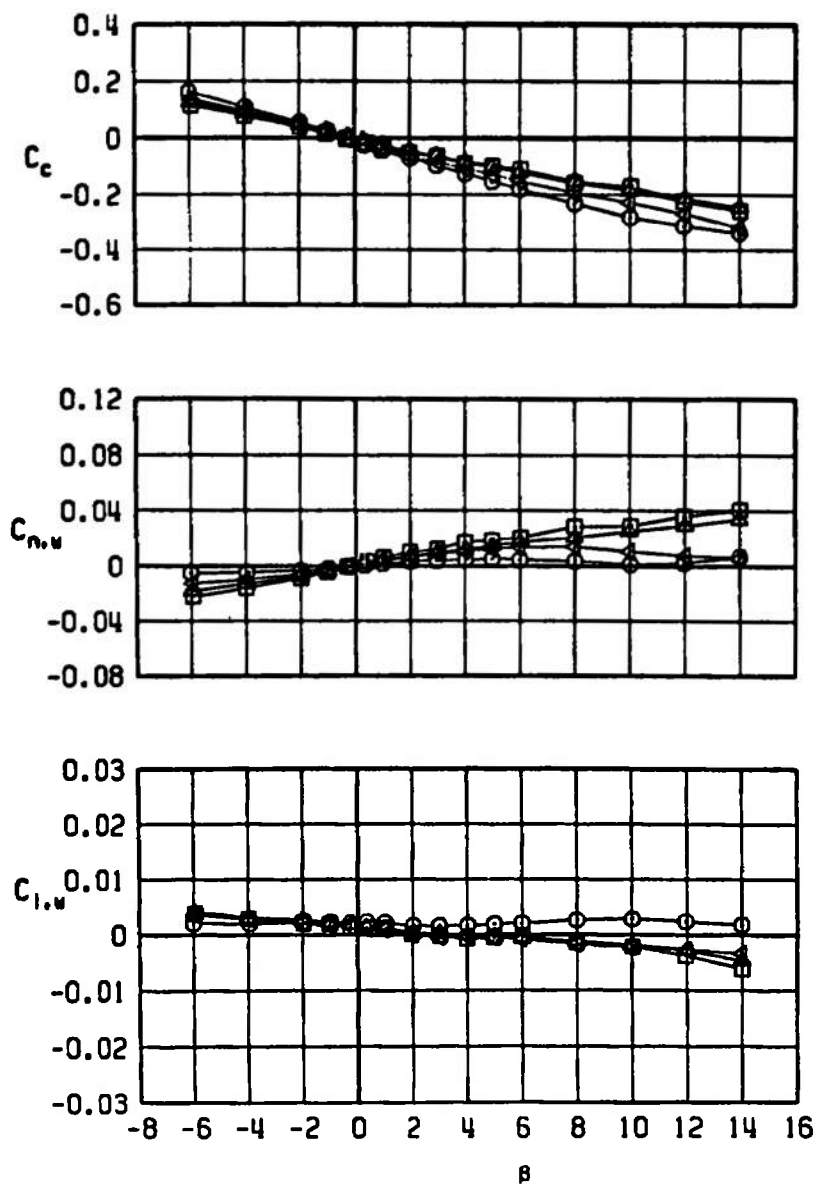
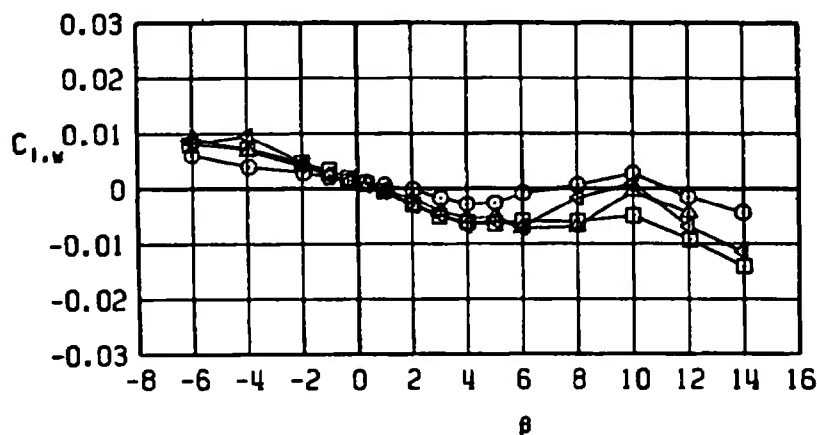
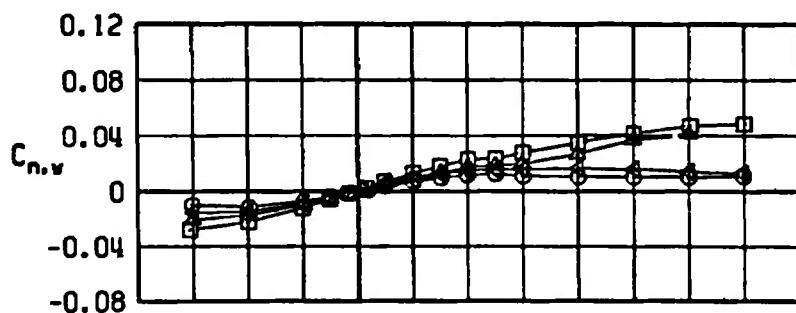
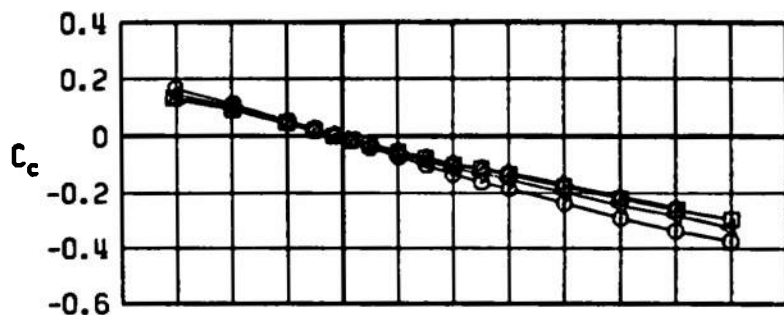
 $\alpha = -10$ a. $M_\infty = 0.50$

Figure 19. Effect of canards C2, C3, and C4 on the crosswind-force, yawing-moment, and rolling-moment coefficients, $\alpha = -10$ deg.

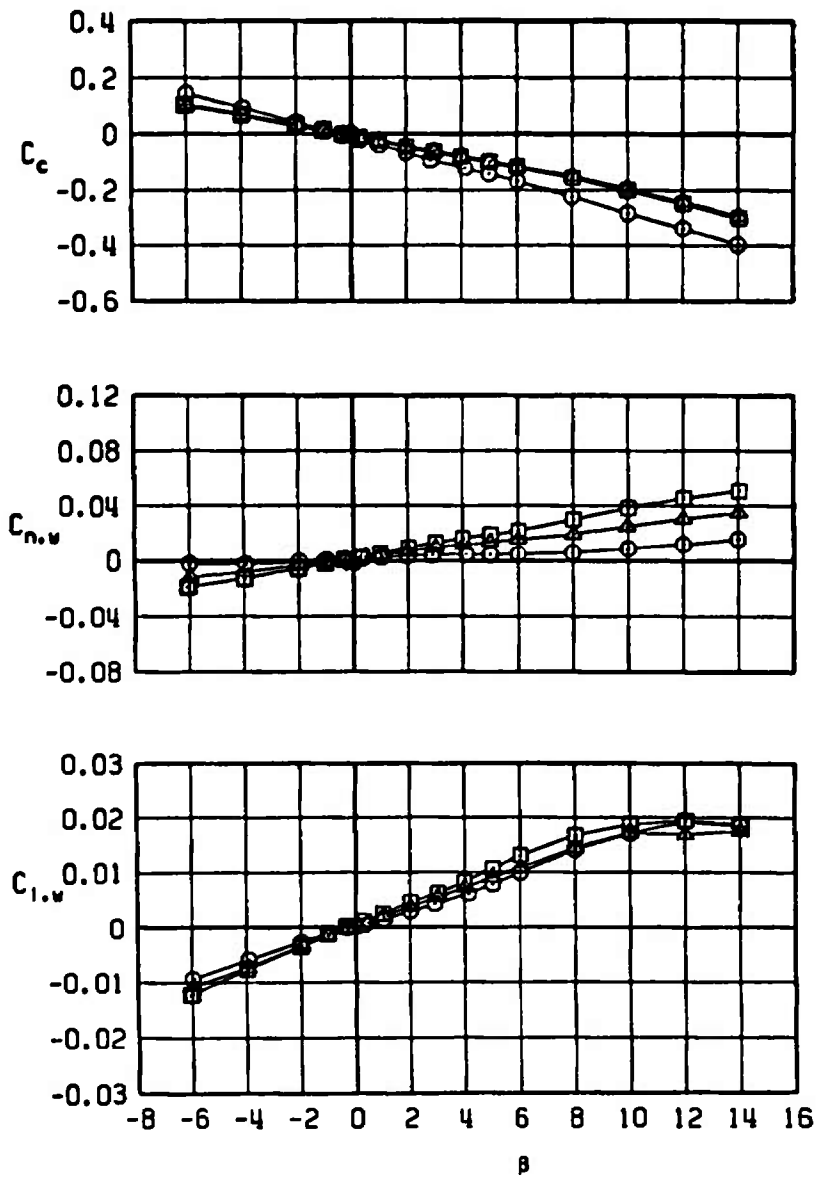
SYMBOL	CONFIG	M_∞	λ_M	δP	δQ	δR
□	B2S1W2T5L1	0.90	30	0	0	0
○	B2S1W2T5L1C2	0.90	30	0	0	0
△	B2S1W2T5L1C3	0.90	30	0	0	0
◀	B2S1W2T5L1C4	0.90	30	0	0	0

 $\alpha = -10$ 

b. $M_\infty = 0.90$
Figure 19. Continued.

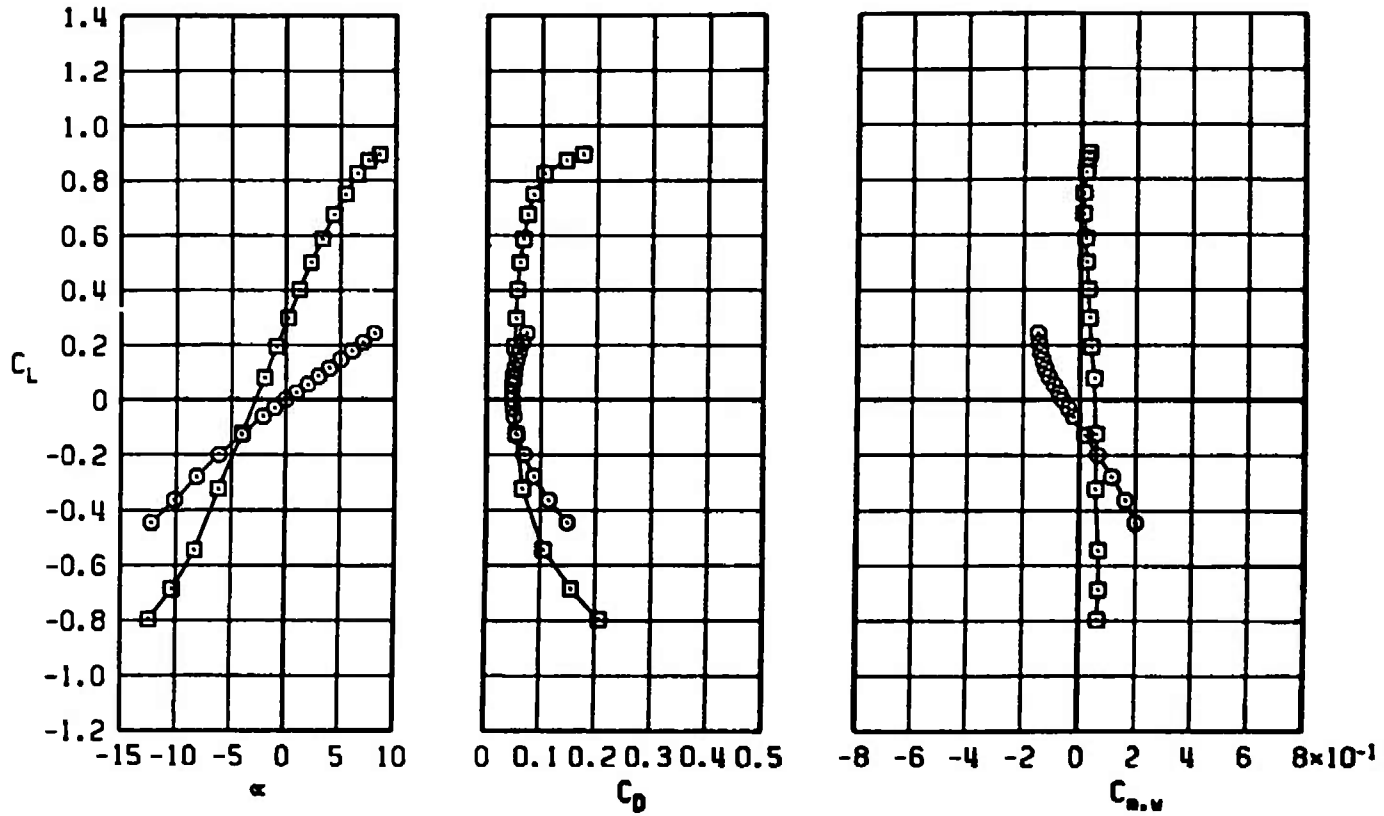
SYMBOL	CONFIG	M_∞	λ_H	δP	δQ	δR
□	B2S1W2T5L1	1.30	30	0	0	0
○	B2S1W2T5L1C2	1.30	30	0	0	0
△	B2S1W2T5L1C3	1.30	30	0	0	0

$\alpha = -10^\circ$



c. $M_\infty = 1.30$
Figure 19. Concluded.

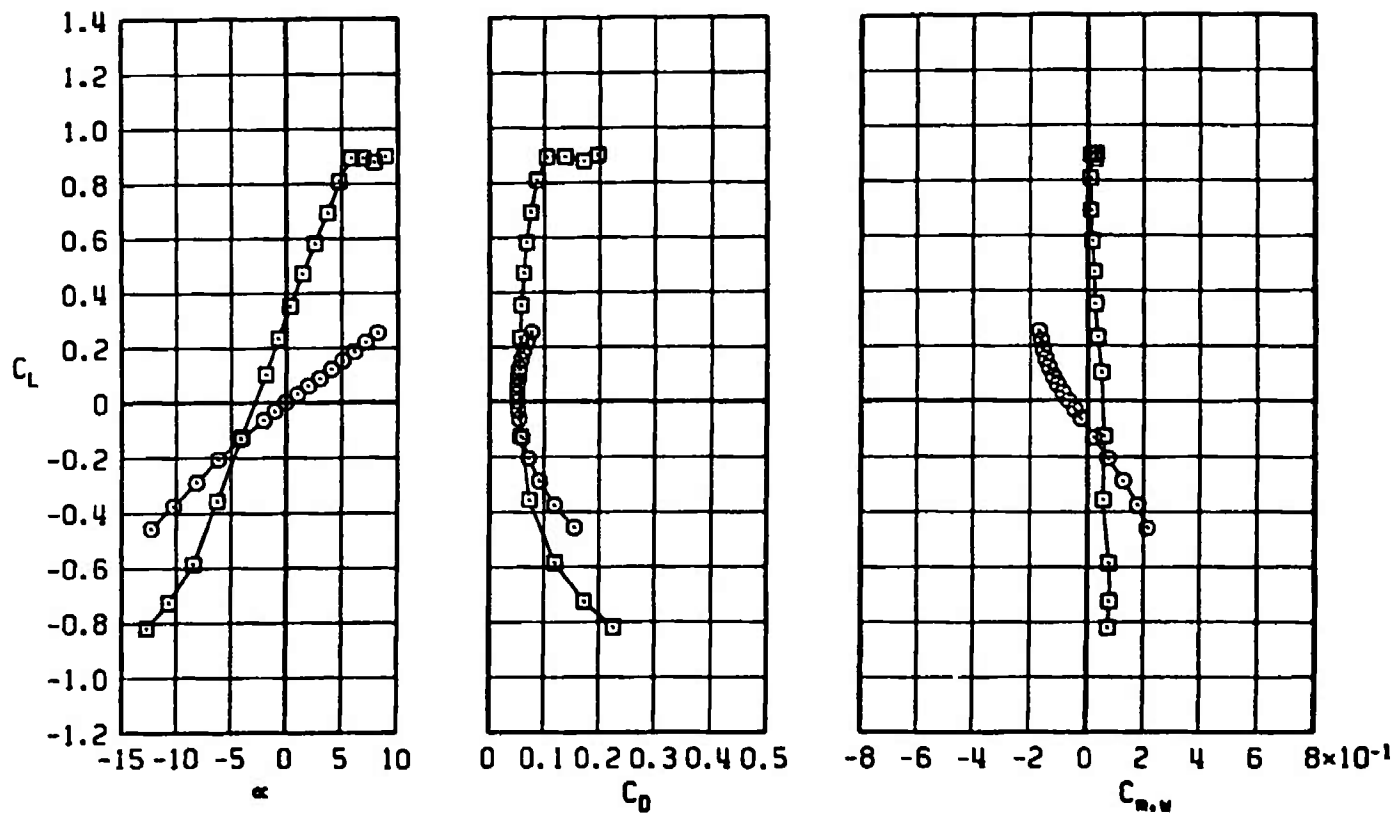
SYMBOL	CONFIG	M_∞	λ_w	δP	δQ	δR
□	B2S1W2T5L1C2	0.50	30	0	0	0
○	B2S1W2T5L1C2	0.50	88	0	0	0



a. $M_\infty = 0.50$

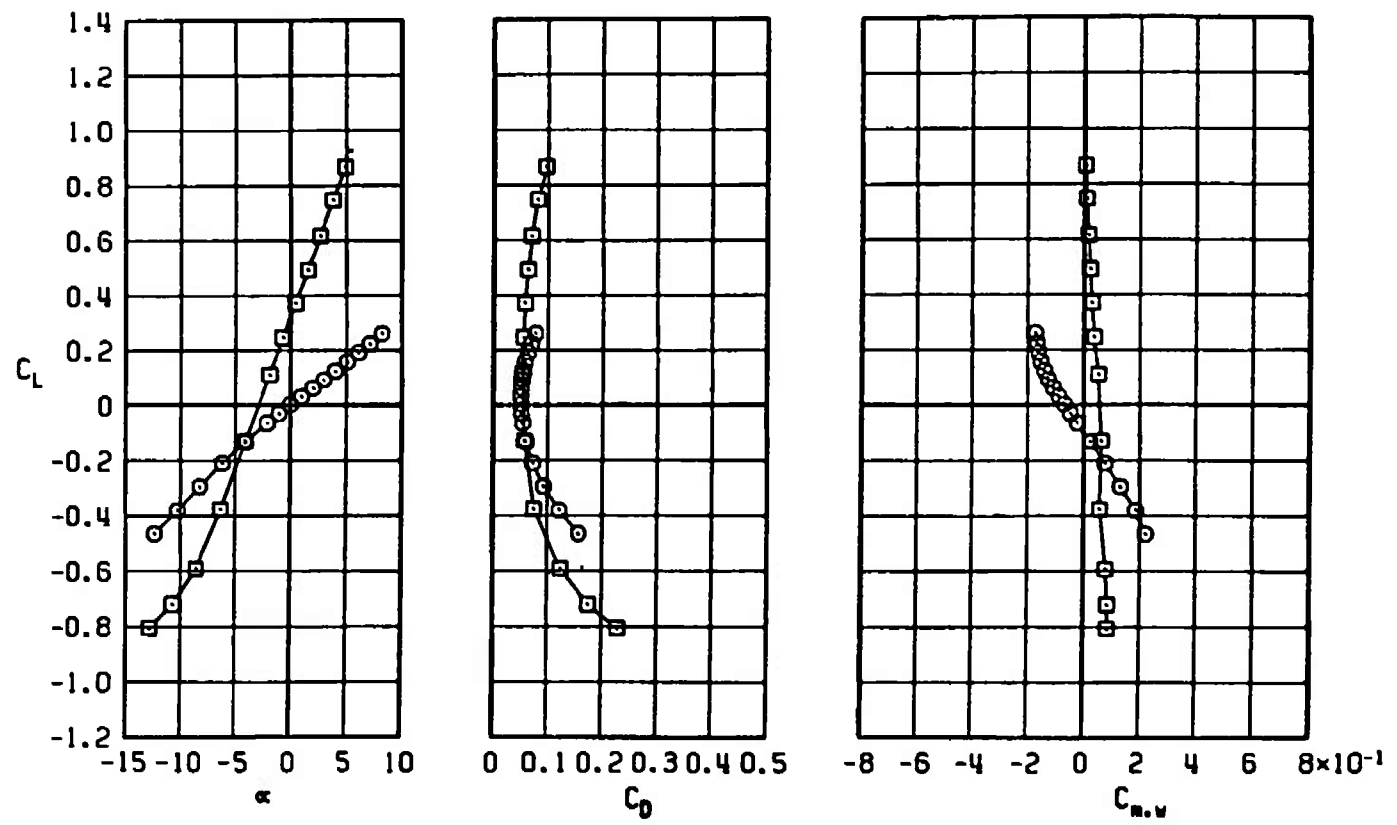
Figure 20. Effect of wing sweep angle on the lift, drag, and pitching-moment coefficients of the MK-84 MGB II configuration.

SYMBOL	CONFIG	M_∞	λ_H	δP	δQ	δR
\square	B2S1W2T5L1C2	0.70	30	0	0	0
\circ	B2S1W2T5L1C2	0.70	88	0	0	0



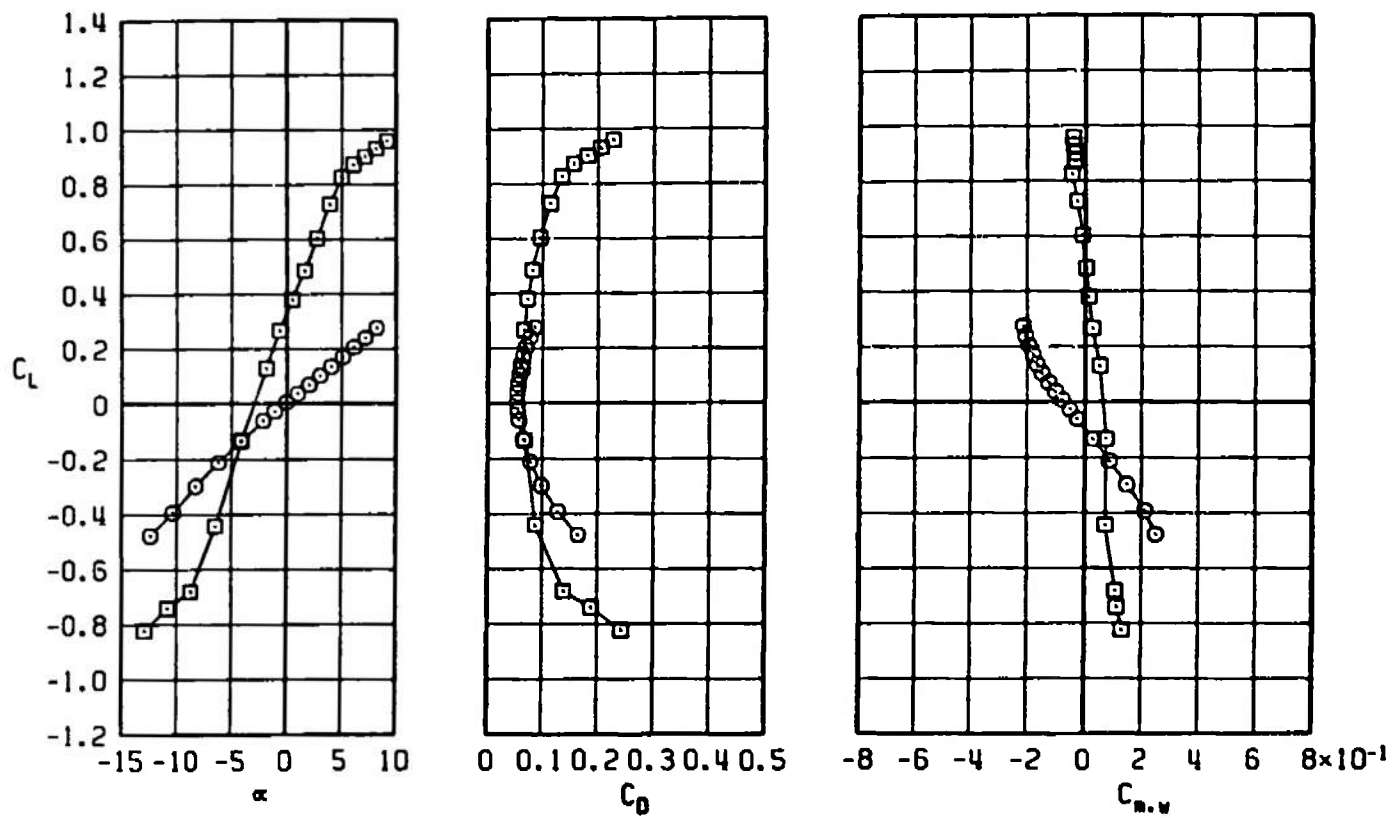
b. $M_\infty = 0.70$
Figure 20. Continued.

SYMBOL	CONFIG	M_∞	λ_M	ϵ_P	ϵ_Q	ϵ_R
□	B2S1W2T5L1C2	0.75	30	0	0	0
○	B2S1W2T5L1C2	0.75	88	0	0	0



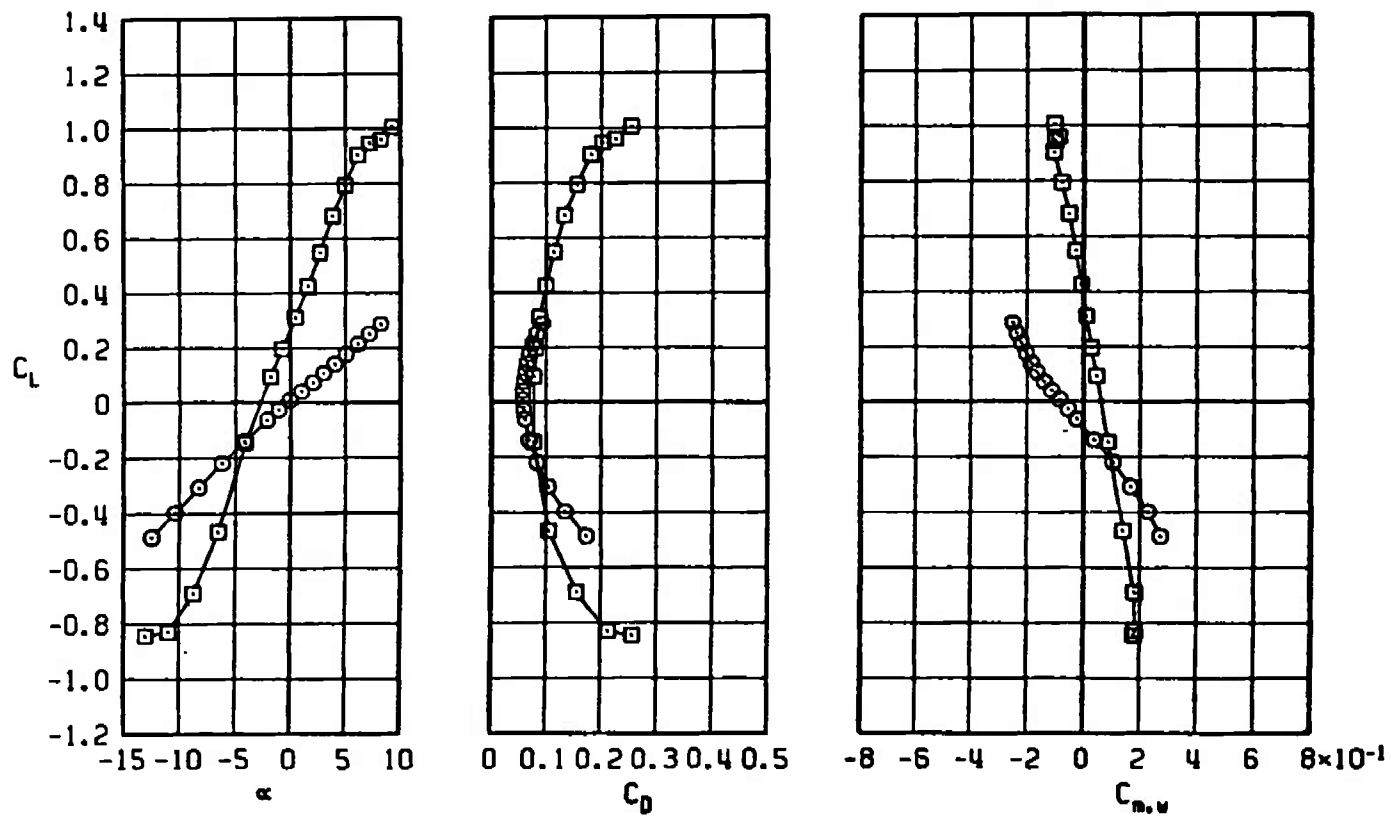
c. $M_\infty = 0.75$
Figure 20. Continued.

SYMBOL	CONFIG	M_∞	λ_M	δP	δQ	δR
\square	B2S1W2T5L1C2	0.85	30	0	0	0
\circ	B2S1W2T5L1C2	0.85	88	0	0	0



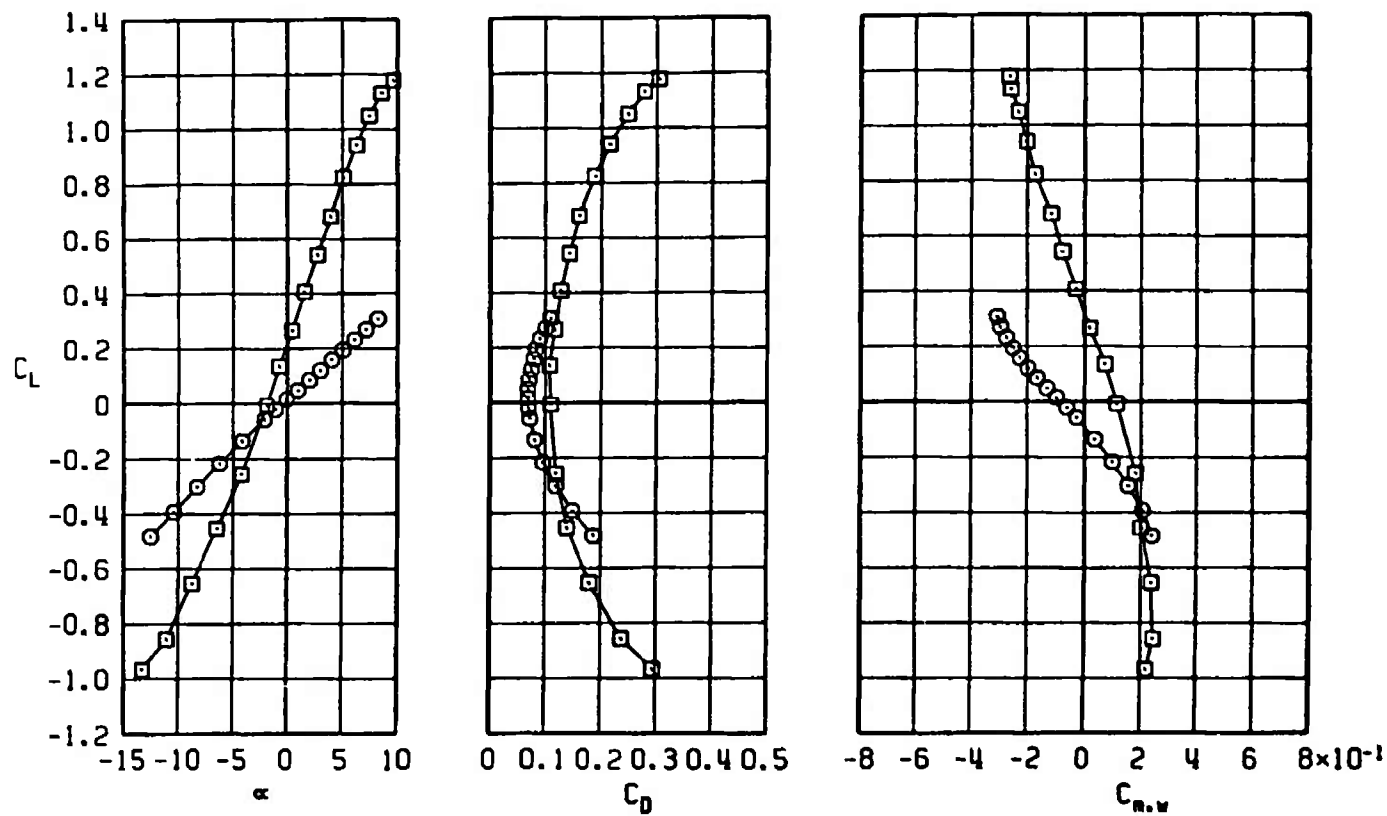
d. $M_\infty = 0.85$
Figure 20. Continued.

SYMBOL	CONFIG	M_∞	λ_N	ϵ_P	ϵ_D	ϵ_R
\square	B2S1W2T5L1C2	0.90	30	0	0	0
\circ	B2S1W2T5L1C2	0.90	88	0	0	0



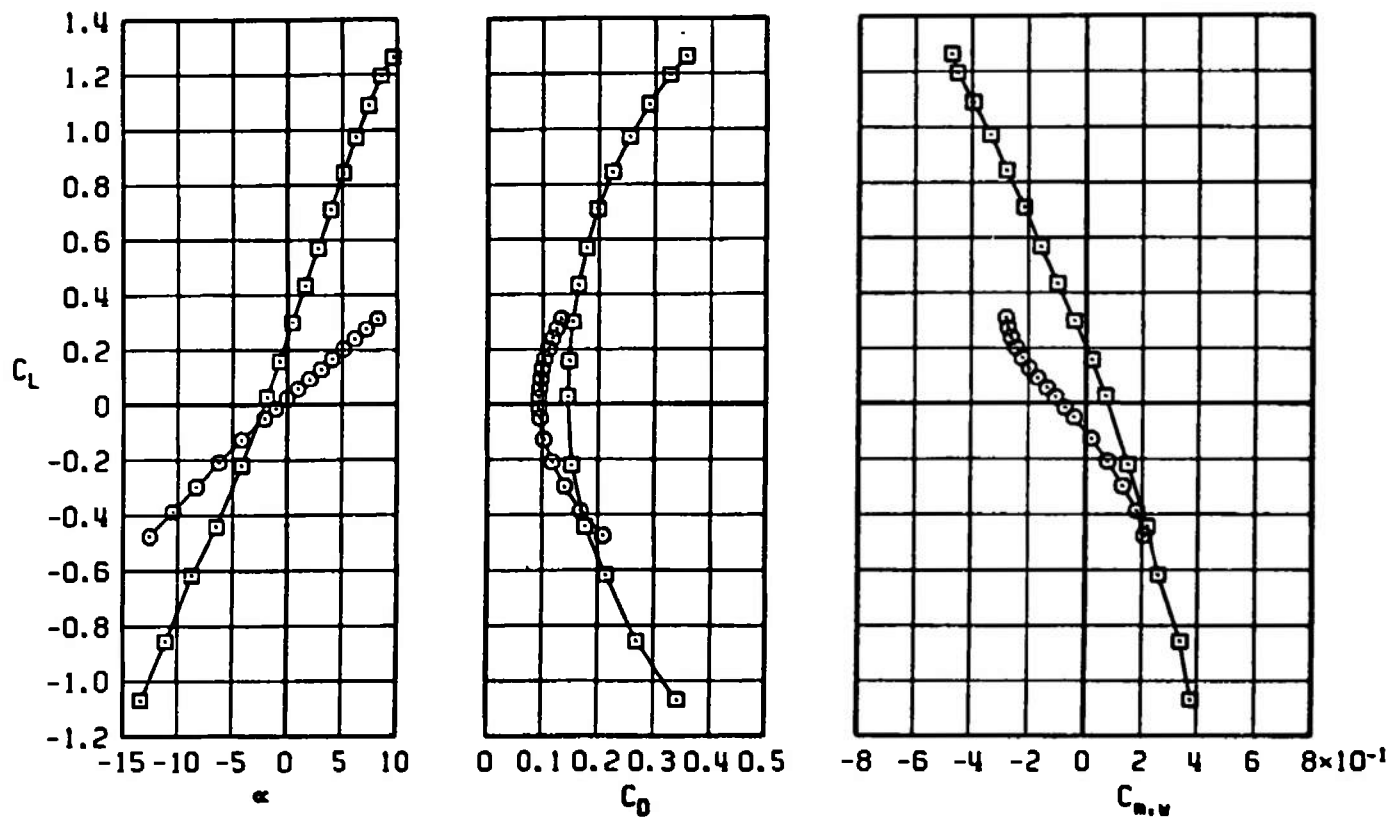
e. $M_\infty = 0.90$
Figure 20. Continued.

SYMBOL	CONFIG	M_∞	λ_M	δP	δQ	δR
\square	B2S1W2T5L1C2	0.95	30	0	0	0
\circ	B2S1W2T5L1C2	0.95	88	0	0	0



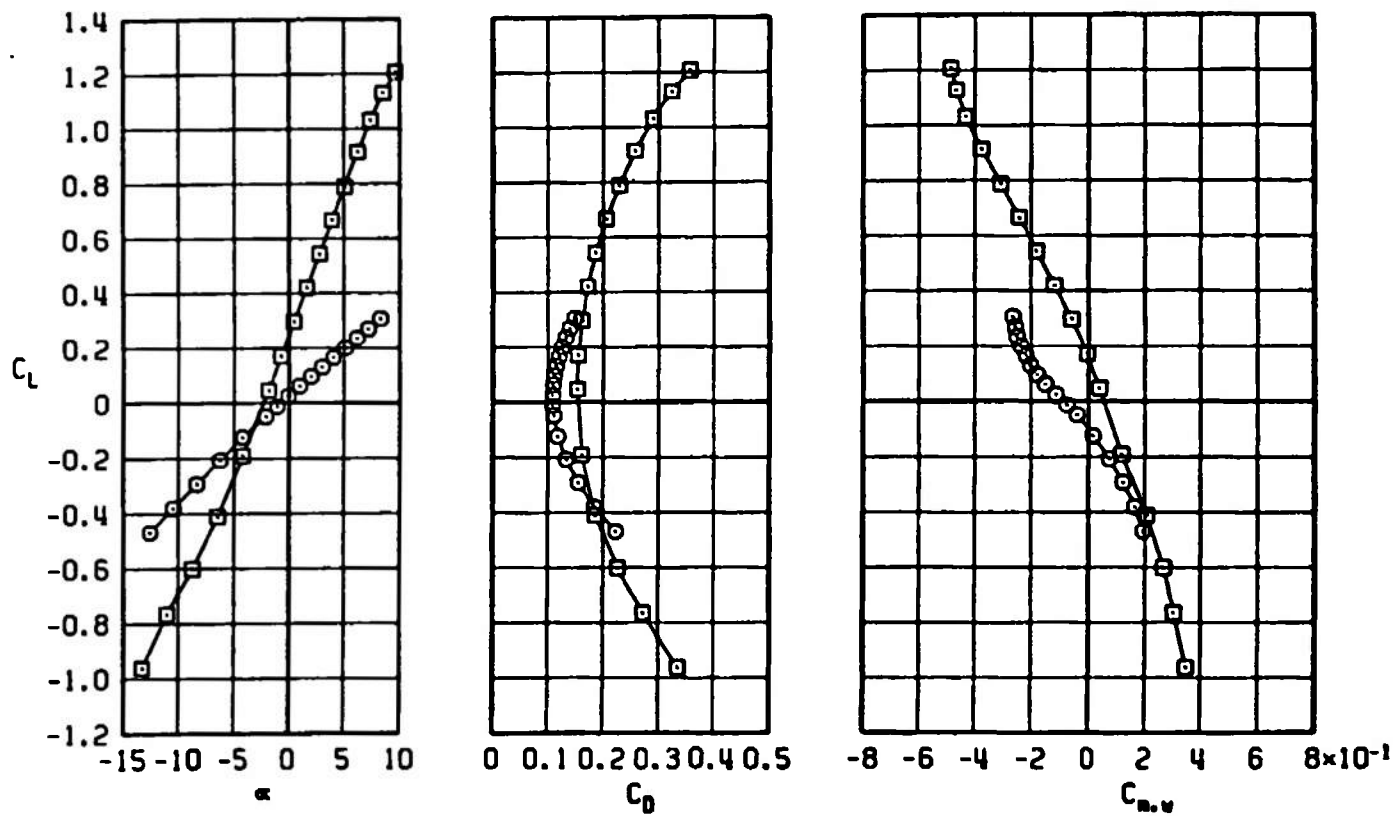
f. $M_\infty = 0.95$
Figure 20. Continued.

SYMBOL	CONFIG	M_∞	λ_H	ϵ_P	ϵ_Q	ϵ_R
\square	B2S1W2T5L1C2	1.00	30	0	0	0
\circ	B2S1W2T5L1C2	1.00	88	0	0	0



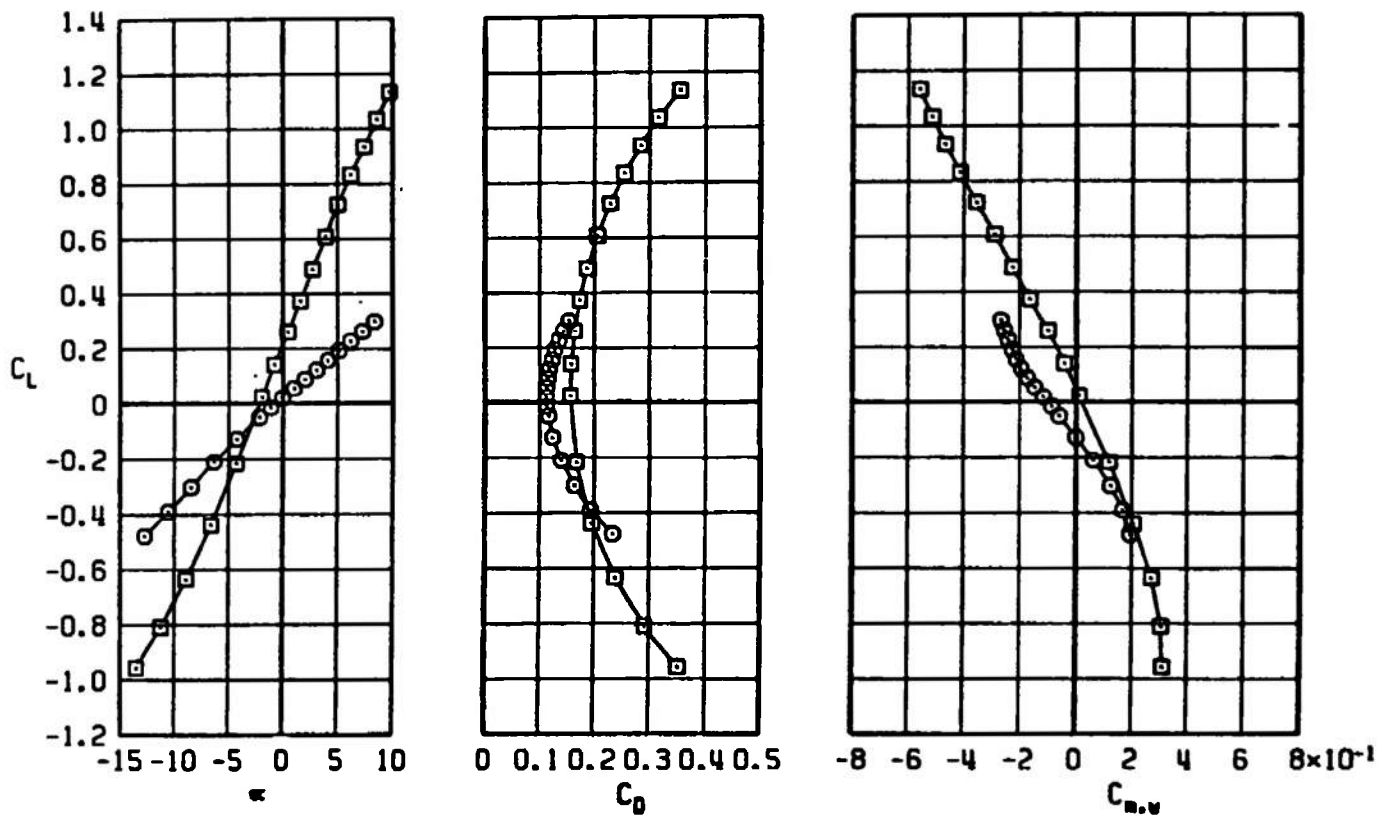
g. $M_\infty = 1.00$
Figure 20. Continued.

SYMBOL	CONFIG	M_∞	λ_∞	δP	δQ	δR
\square	B2S1W2T5L1C2	1.10	30	0	0	0
\circ	B2S1W2T5L1C2	1.10	88	0	0	0



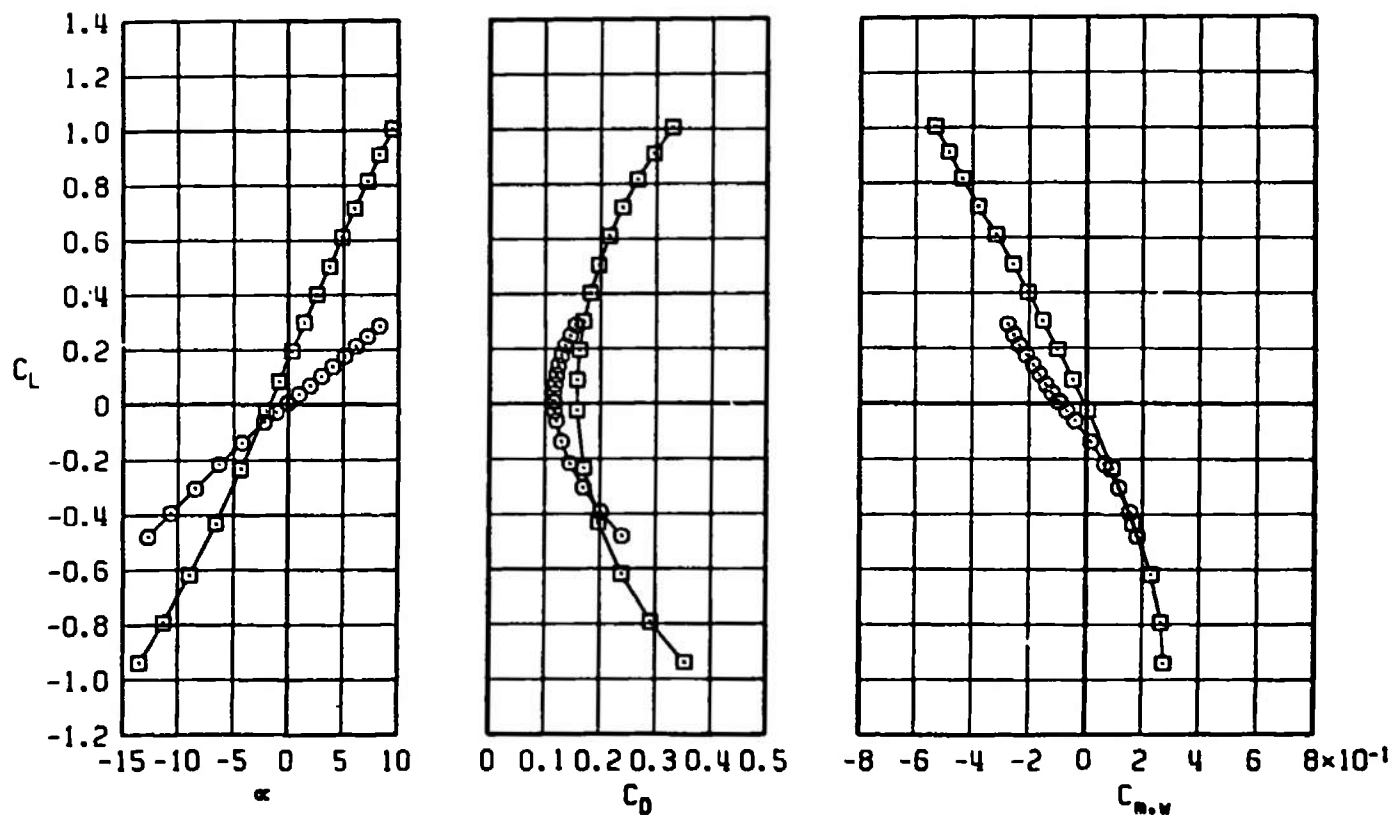
h. $M_\infty = 1.10$
Figure 20. Continued.

SYMBOL	CONFIG	M_∞	λ_w	δP	δQ	δR
\square	B2S1W2T5L1C2	1.20	30	0	0	0
\circ	B2S1W2T5L1C2	1.20	88	0	0	0



i. $M_\infty = 1.20$
Figure 20. Continued.

SYMBOL	CONFIG	M_∞	λ_H	δP	δQ	δR
\square	B2S1W2T5L1C2	1.30	30	0	0	0
\circ	B2S1W2T5L1C2	1.30	88	0	0	0



j. $M_\infty = 1.30$
Figure 20. Concluded.

SYMBOL	CONFIG	λ_M	δP	δQ	δR
□	B2S1W2TSL1C2	30	0	0	0
○	B2S1W2TSL1C2	88	0	0	0

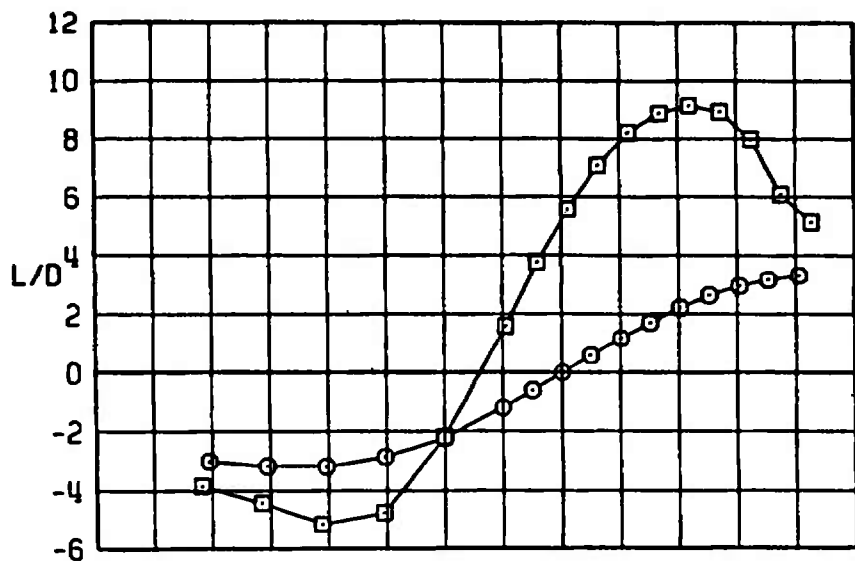
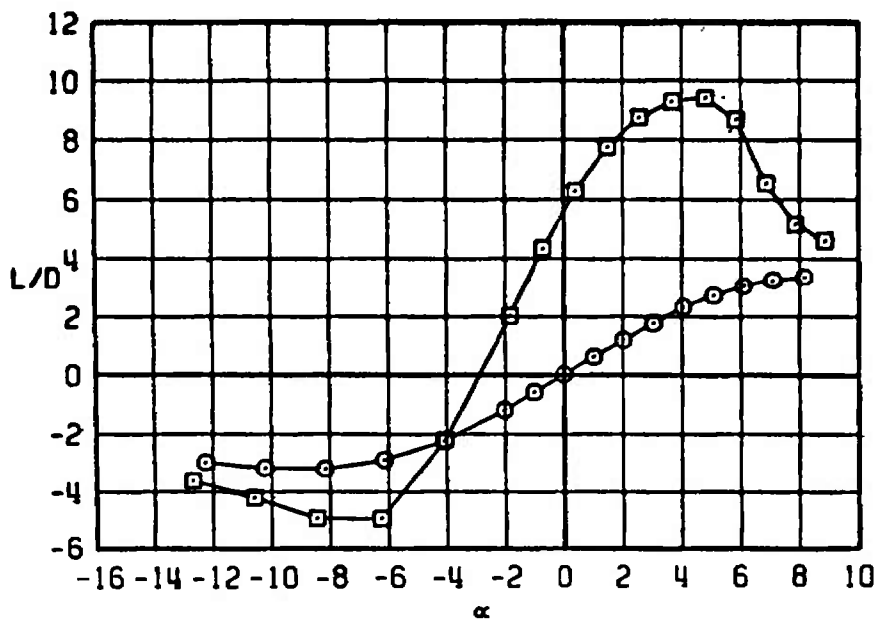
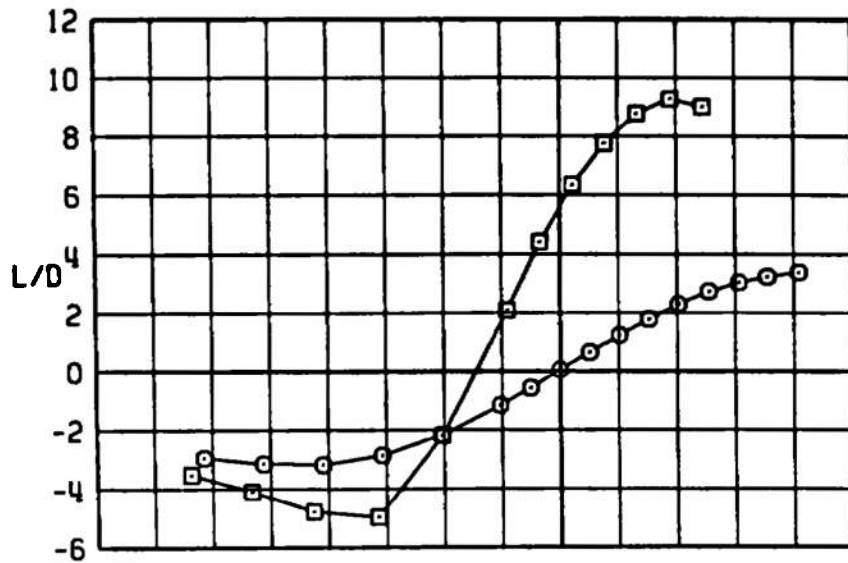
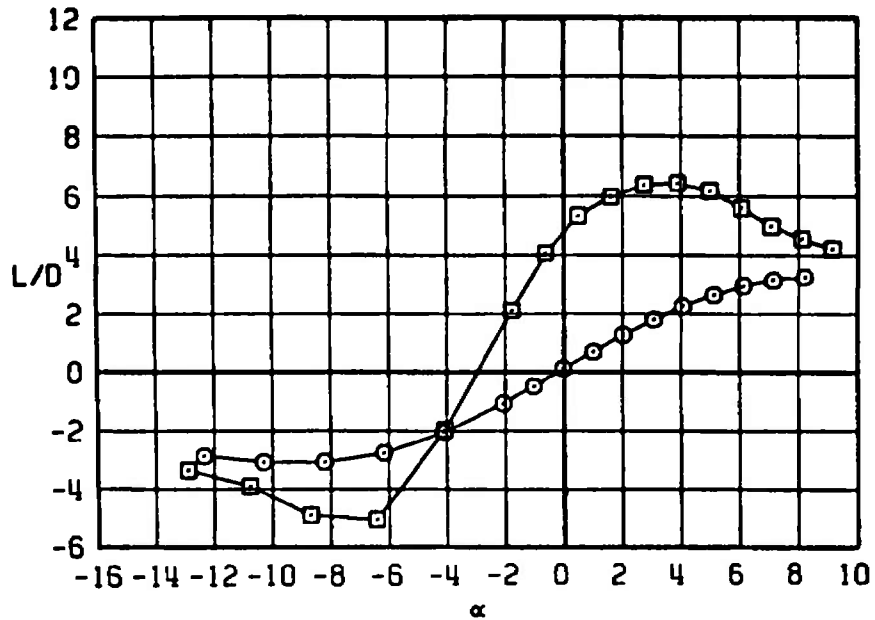
 $M_\infty = 0.50$  $M_\infty = 0.70$ a. $M_\infty = 0.50$ and 0.70

Figure 21. Effect of the wing sweep angle on the lift-to-drag ratio of the MK-84 MGGB II configuration.

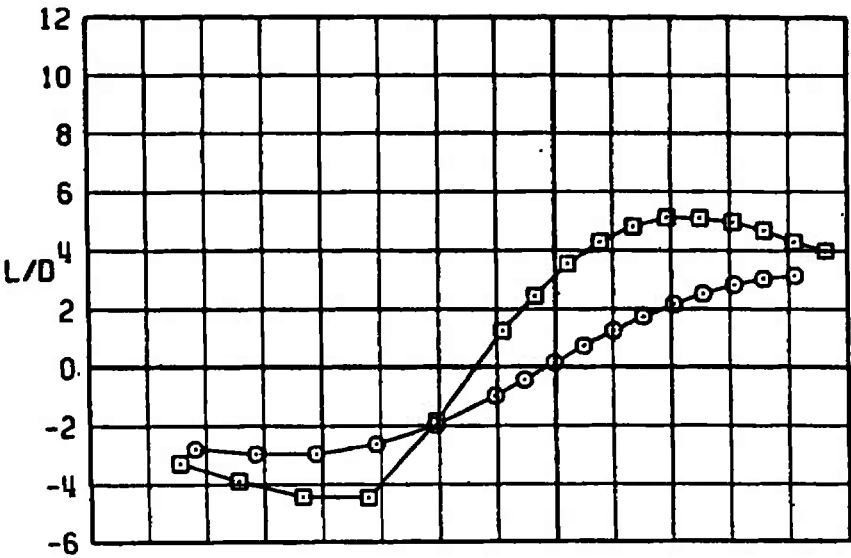
SYMBOL	CONFIG	λ_M	δP	δQ	δR
□	B2S1W2T5L1C2	30	0	0	0
○	B2S1W2T5L1C2	88	0	0	0

 $M_\infty = 0.75$  $M_\infty = 0.85$ 

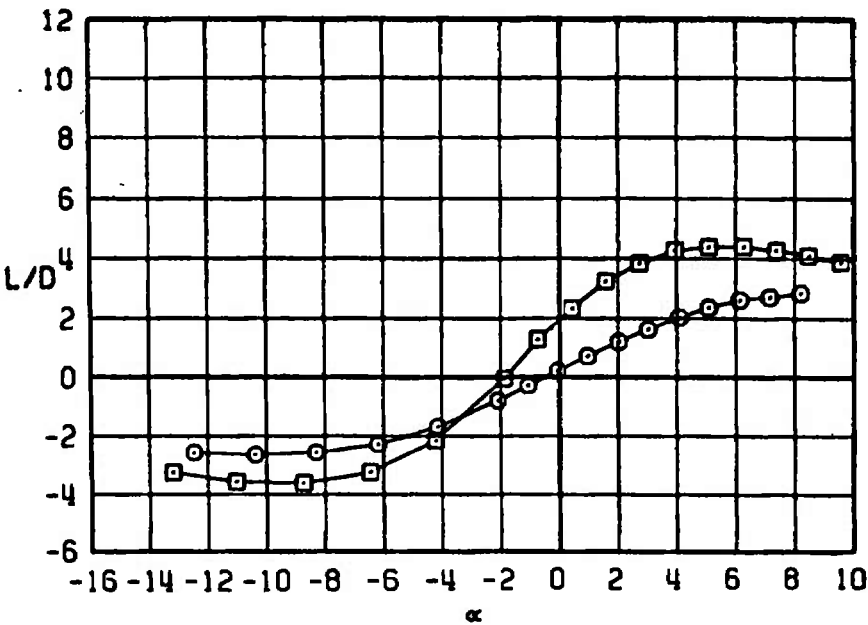
b. $M_\infty = 0.75$ and 0.85
Figure 21. Continued.

SYMBOL	CONFIG	λ_M	ϕ_P	ϕ_Q	ϕ_R
\square	8251W2T5L1C2	30	0	0	0
\circ	8251W2T5L1C2	88	0	0	0

$M_\infty = 0.90$

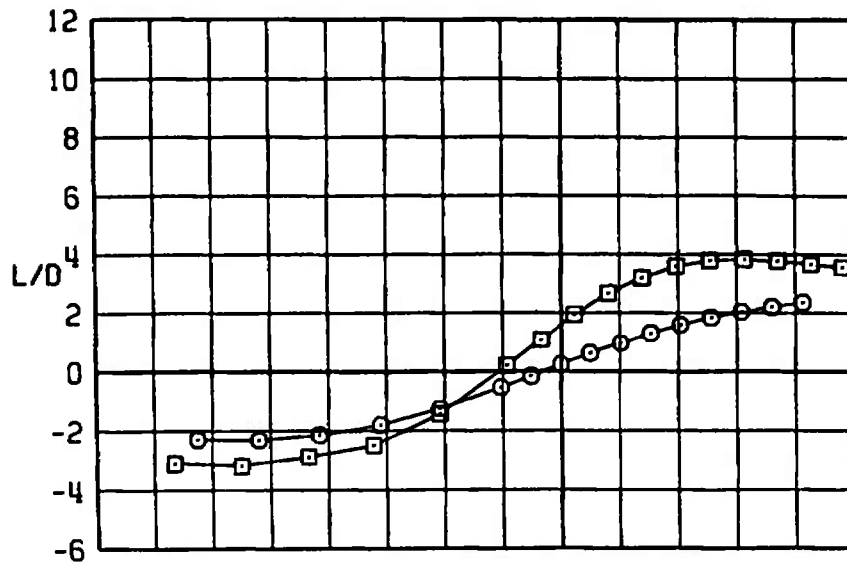
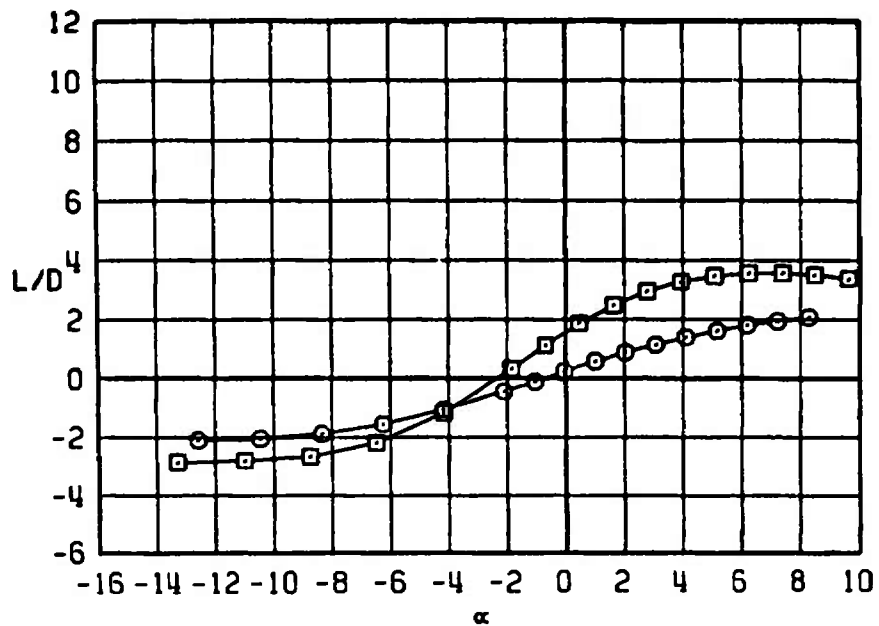


$M_\infty = 0.95$



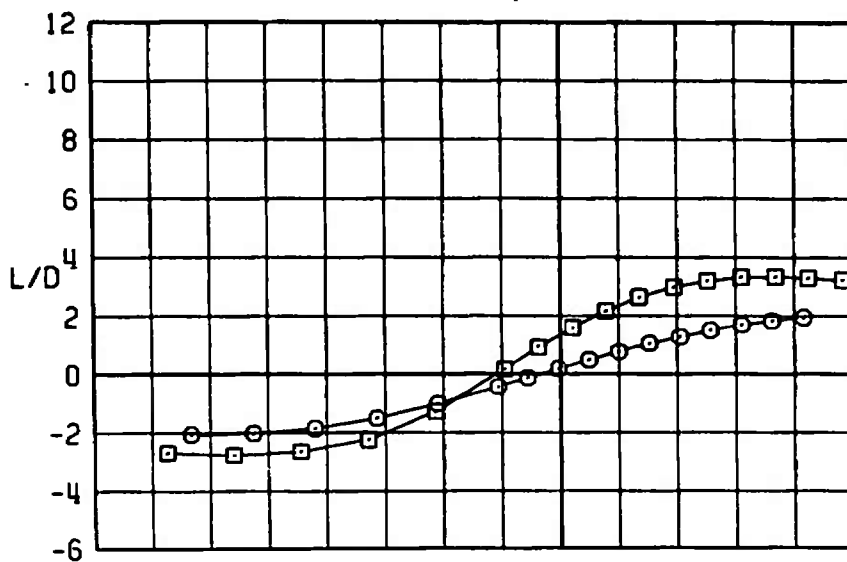
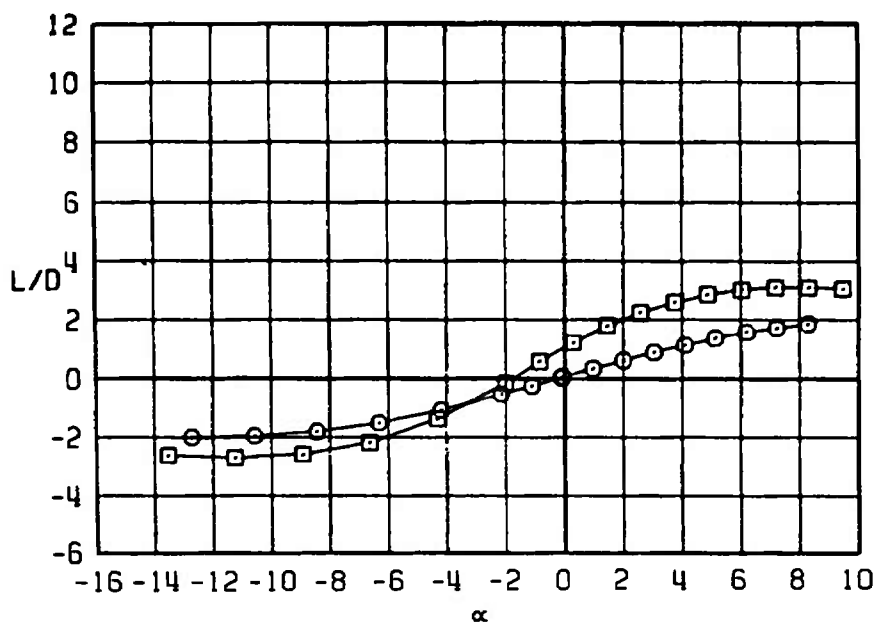
c. $M_\infty = 0.90$ and 0.95
Figure 21. Continued.

SYMBOL	CONFIG	λ_H	δP	δQ	δR
□	B2S1W2T5L1C2	30	0	0	0
○	B2S1W2T5L1C2	88	0	0	0

 $M_\infty = 1.00$  $M_\infty = 1.10$ 

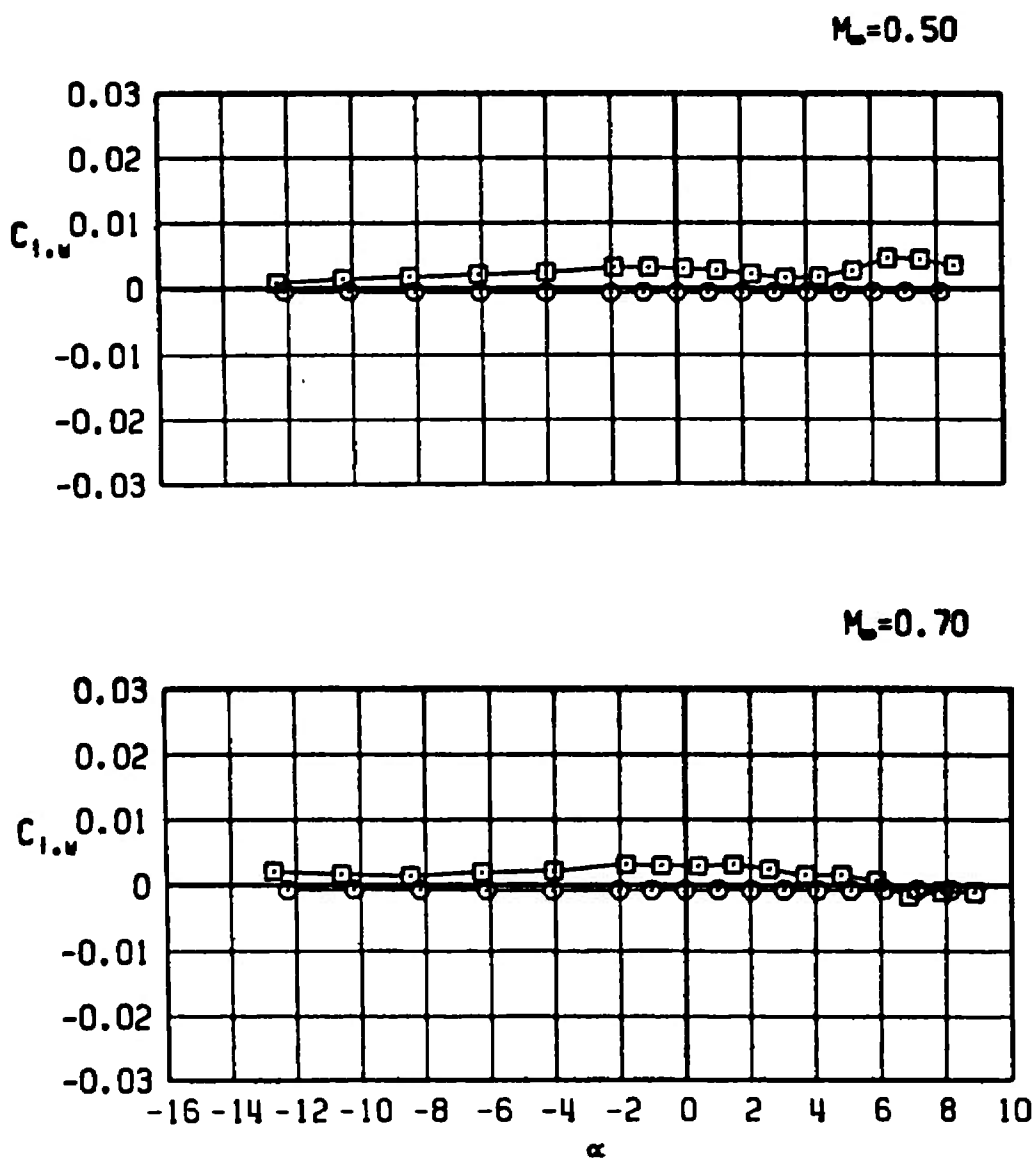
d. $M_\infty = 1.00$ and 1.10
Figure 21. Continued.

SYMBOL	CONFIG	λ_H	δP	δQ	δR
\square	B2S1W2T5L1C2	30	0	0	0
\circ	B2S1W2T5L1C2	88	0	0	0

 $M_\infty = 1.20$  $M_\infty = 1.30$ 

e. $M_\infty = 1.20$ and 1.30
Figure 21. Concluded.

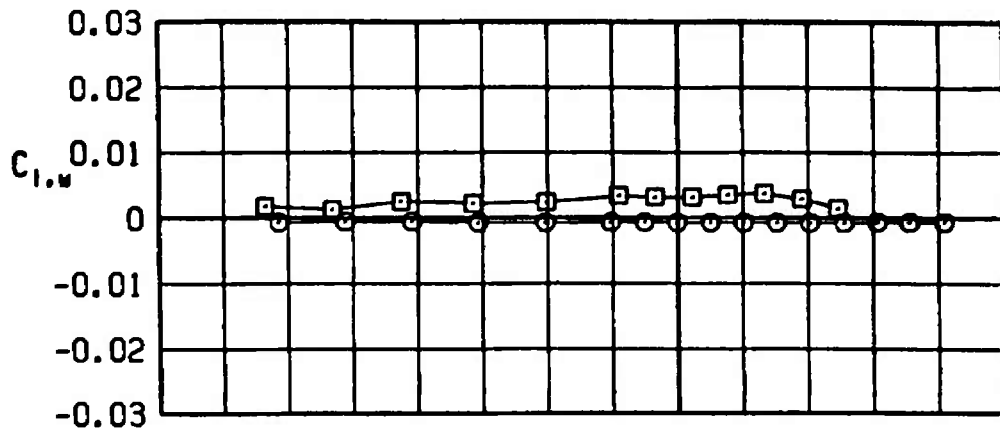
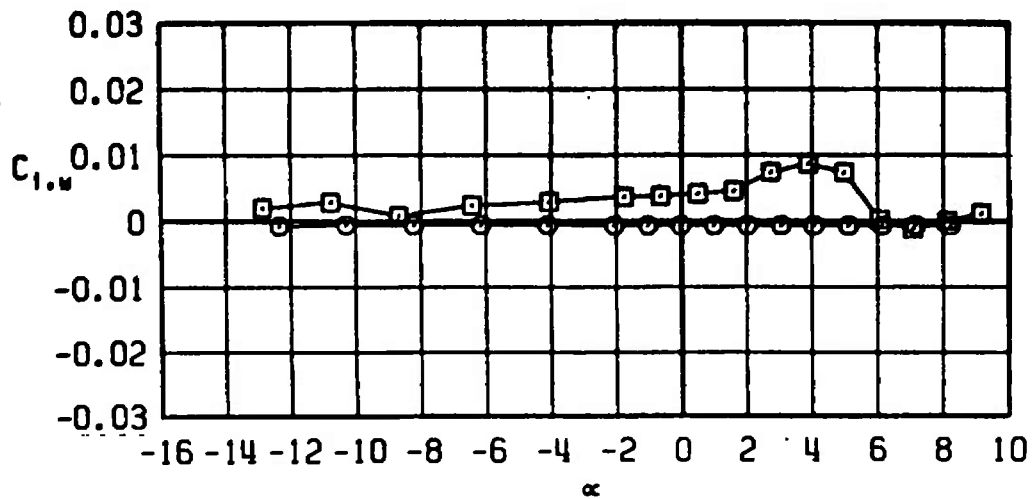
SYMBOL	CONFIG	λ_w	ϕ_P	ϕ_Q	ϕ_R
\square	B2S1W2T5L1C2	30	0	0	0
\circ	B2S1W2T5L1C2	88	0	0	0



a. $M_\infty = 0.50$ and 0.70

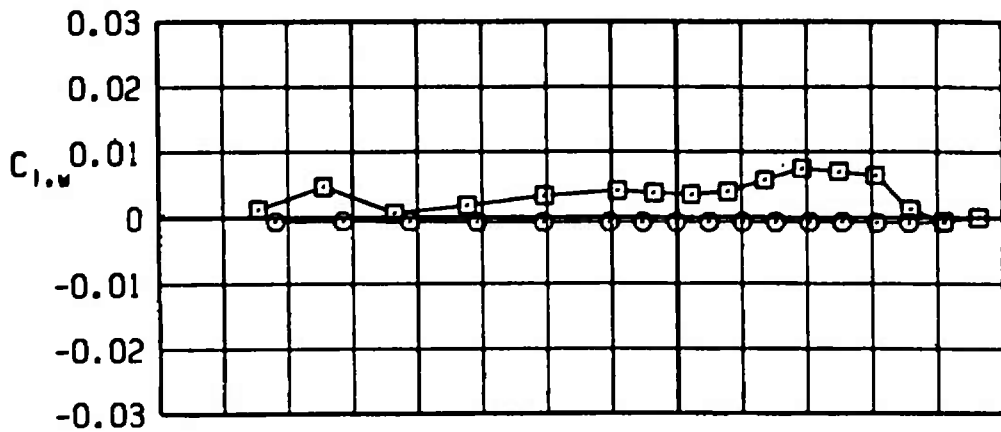
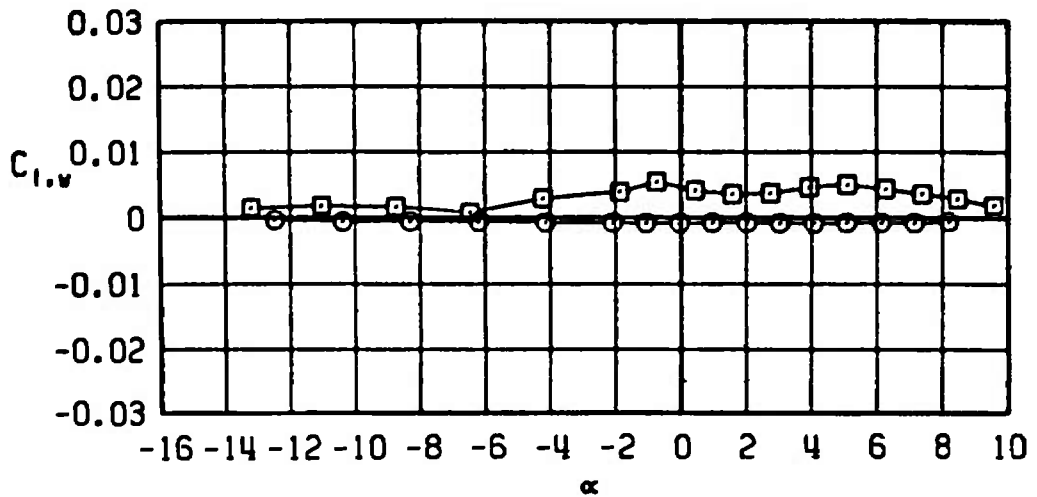
Figure 22. Effect of the wing sweep angle on the rolling-moment coefficient of the MK-84 MGGB II configuration.

SYMBOL.	CONFIG	λ_H	ϕ_P	ϕ_Q	ϕ_R
□	B2S1W2T5L1C2	30	0	0	0
○	B2S1W2T5L1C2	88	0	0	0

 $M_\infty = 0.75$  $M_\infty = 0.85$ 

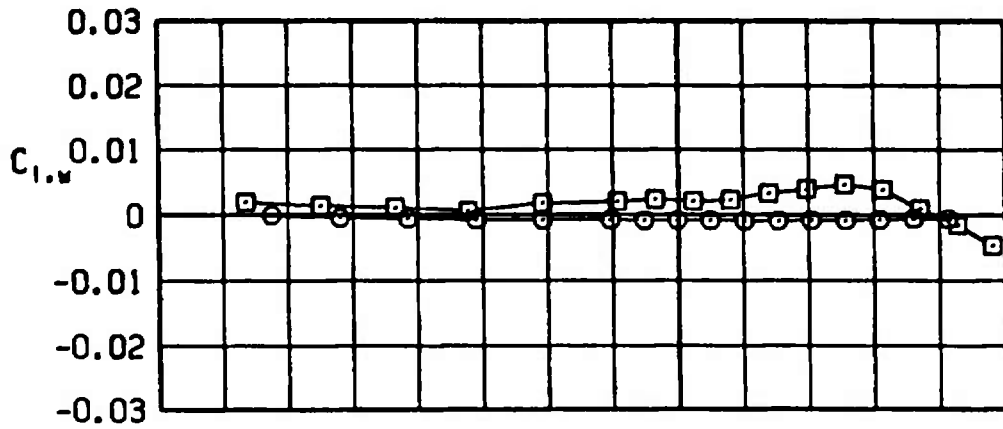
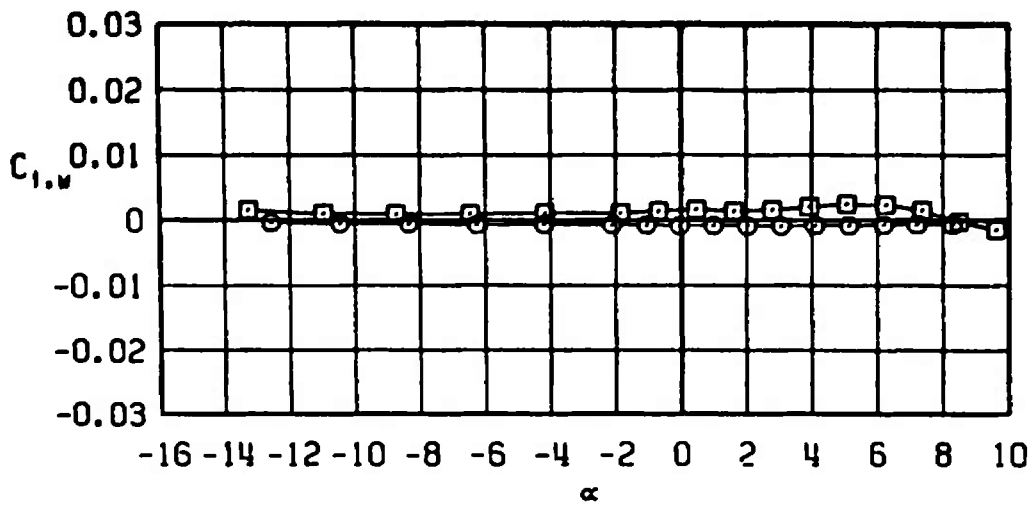
b. $M_\infty = 0.75$ and 0.85
Figure 22. Continued.

SYMBOL	CONFIG	λ_M	δP	δQ	δR
□	B2S1W2T5L1C2	30	0	0	0
○	B2S1W2T5L1C2	88	0	0	0

 $M_\infty = 0.90$  $M_\infty = 0.95$ 

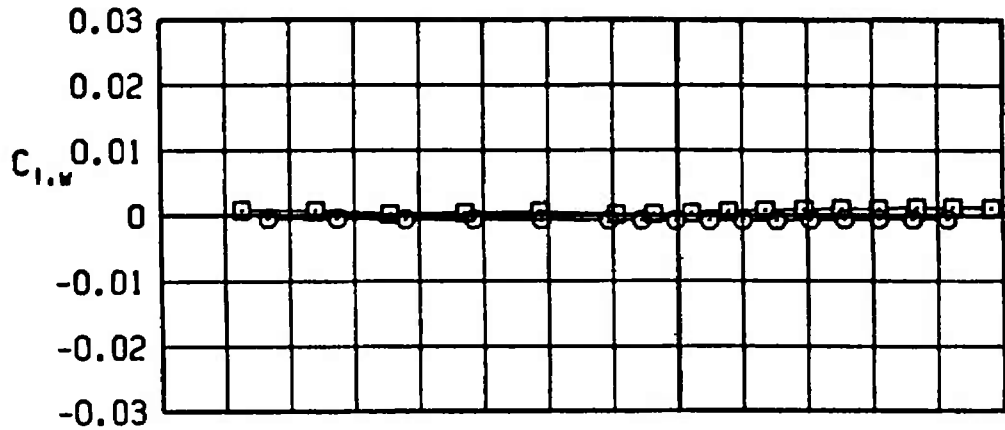
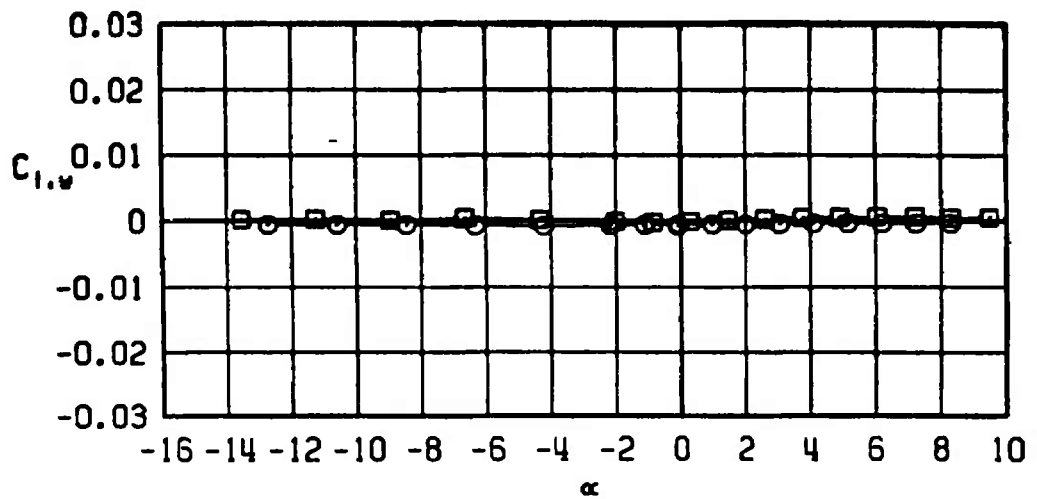
c. $M_\infty = 0.90$ and 0.95
Figure 22. Continued.

SYMBOL	CONFIG	λ_H	ϵ_P	ϵ_Q	ϵ_R
□	B2S1W2T5L1C2	30	0	0	0
○	B2S1W2T5L1C2	88	0	0	0

 $M_\infty = 1.00$  $M_\infty = 1.10$ 

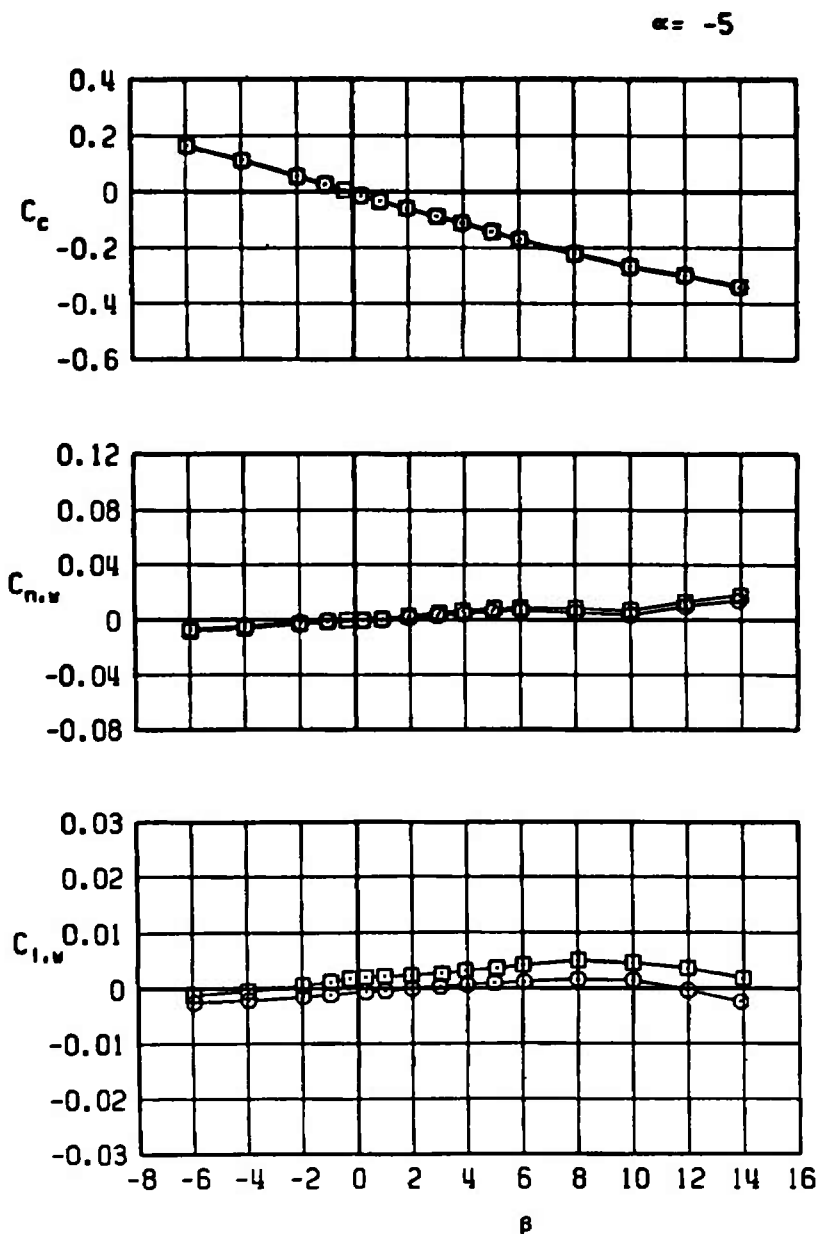
d. $M_\infty = 1.00$ and 1.10
Figure 22. Continued.

SYMBOL	CONFIG	λ_M	ϕ_P	ϕ_Q	ϕ_R
□	B2S1W2T5L1C2	30	0	0	0
○	B2S1W2T5L1C2	88	0	0	0

 $M_\infty = 1.20$  $M_\infty = 1.30$ 

e. $M_\infty = 1.20$ and 1.30
Figure 22. Concluded.

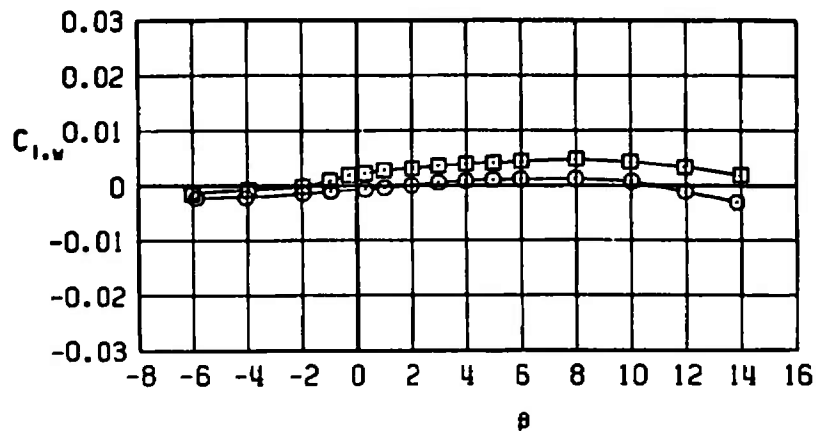
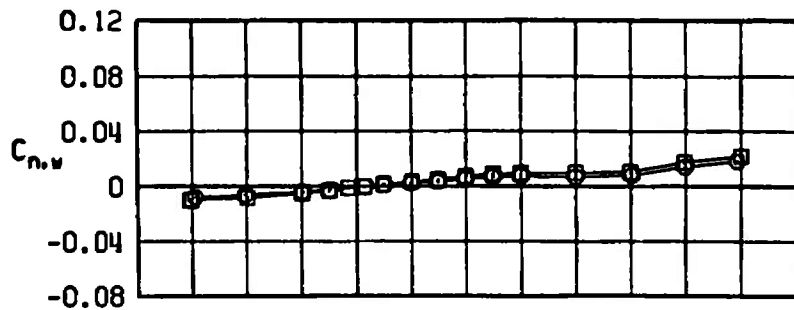
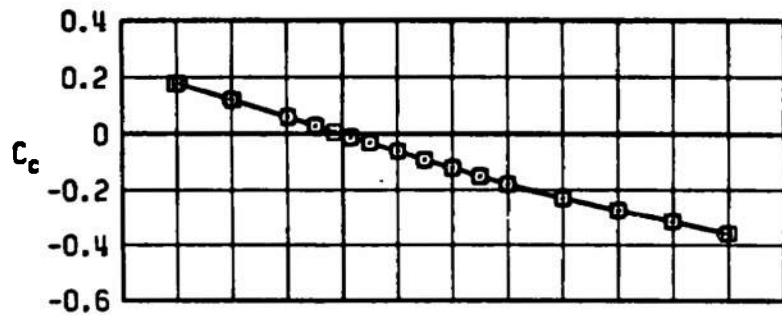
SYMBOL	CONFIG	M_∞	λ_M	δP	δQ	δR
\square	B2S1W2T5L1C2	0.50	30	0	0	0
\circ	B2S1W2T5L1C2	0.50	88	0	0	0



a. $M_\infty = 0.50$

Figure 23. Effect of the wing sweep angle on the crosswind-force, yawing-moment, and rolling-moment coefficients of the MK-84 MGGB II configuration, $\alpha = -5$ deg.

SYMBOL	CONFIG	M_∞	λ_w	$\%P$	$\%Q$	$\%R$
\square	B2S1W2T5L1C2	0.75	30	0	0	0
\circ	B2S1W2T5L1C2	0.75	88	0	0	0

 $\alpha = -5$ 

b. $M_\infty = 0.75$
Figure 23. Continued.

SYMBOL	CONFIG	M_∞	λ_M	δP	δQ	δR
□	B2S1W2T5L1C2	0.85	30	0	0	0
○	B2S1W2T5L1C2	0.85	68	0	0	0

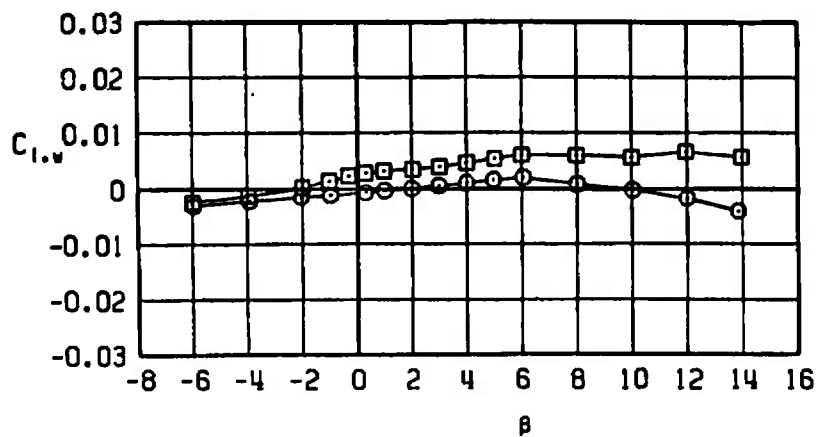
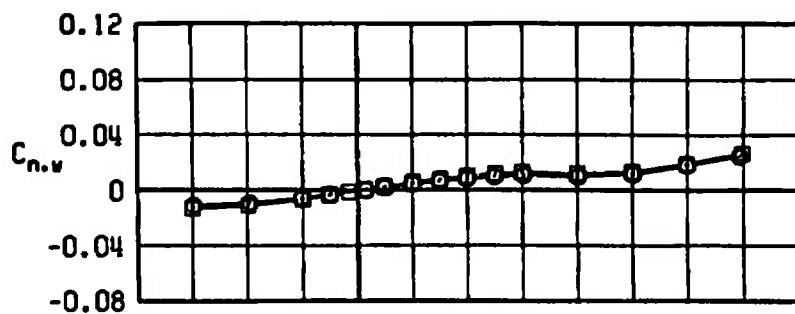
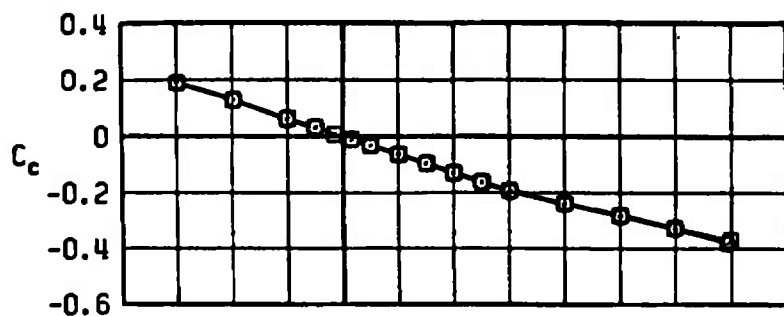
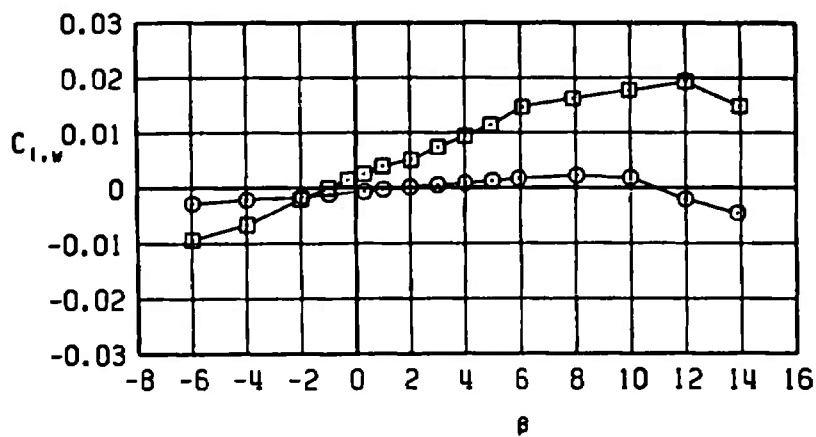
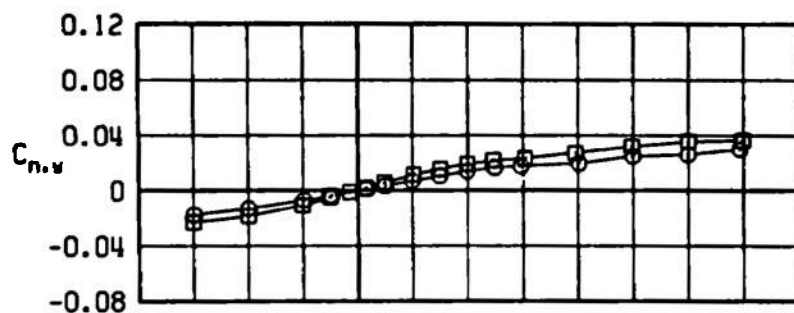
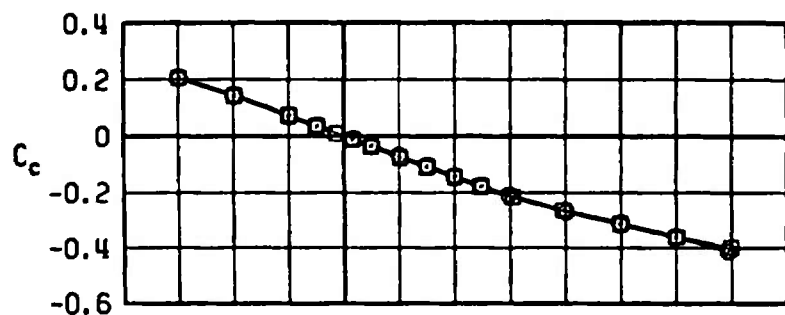
 $\alpha = -5$ c. $M_\infty = 0.85$

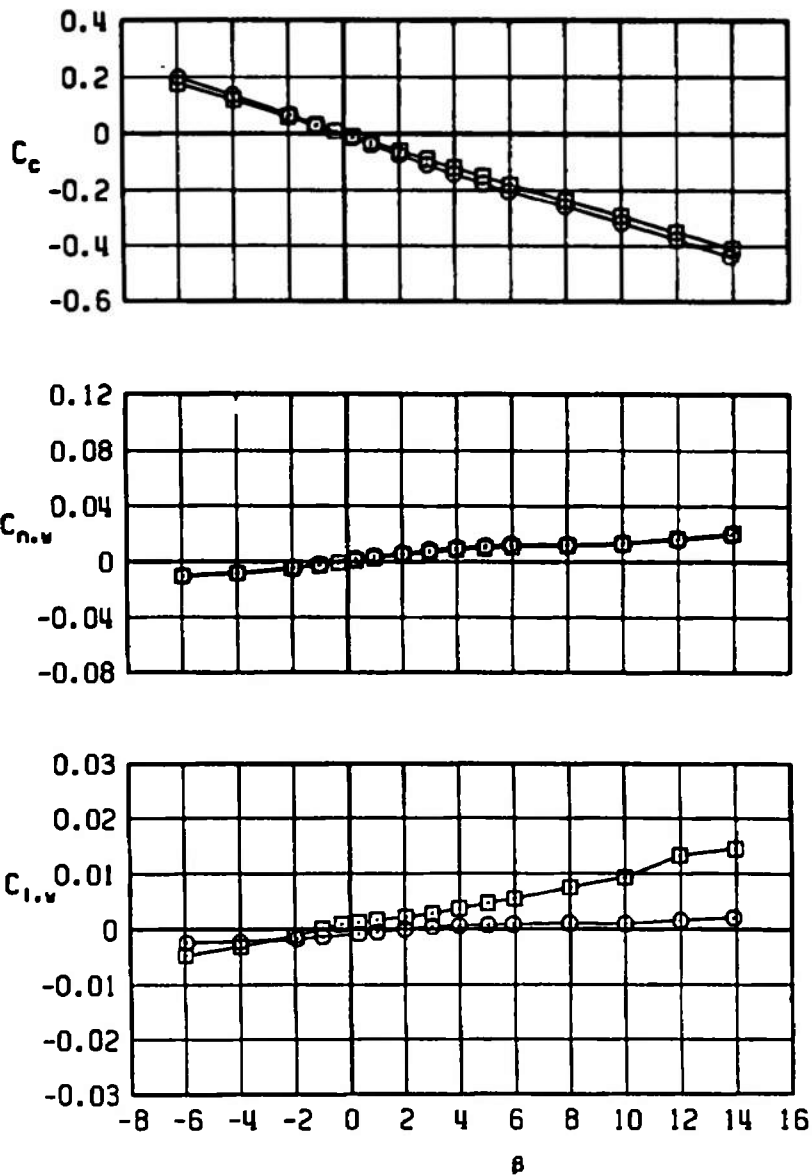
Figure 23. Continued.

SYMBOL	CONFIG	M_∞	λ_H	δP	δQ	δR
\square	B2S1W2T5L1C2	0.95	30	0	0	0
\circ	B2S1W2T5L1C2	0.95	88	0	0	0

 $\alpha = -5$ 

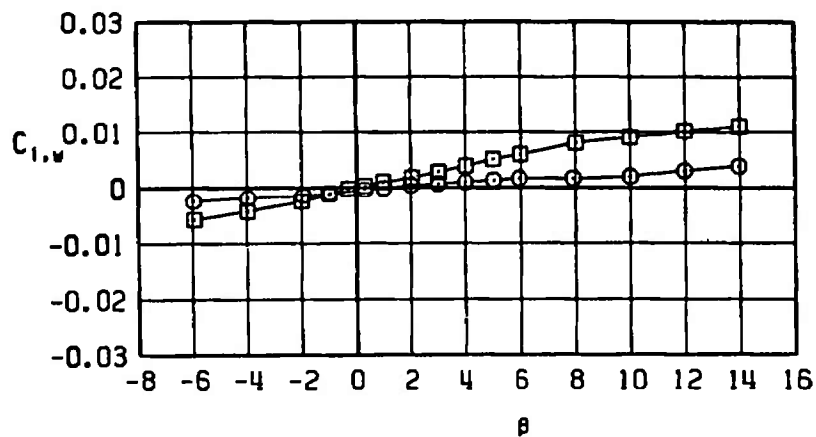
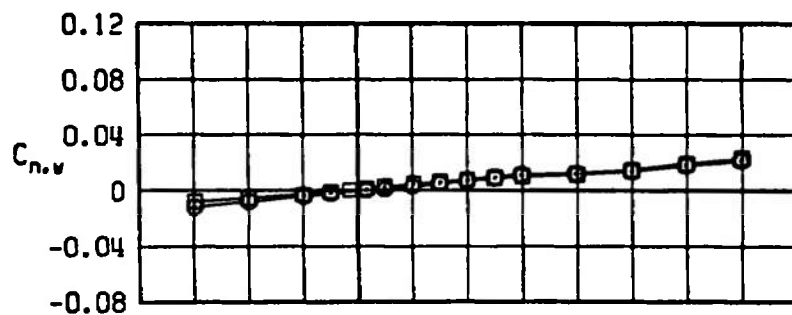
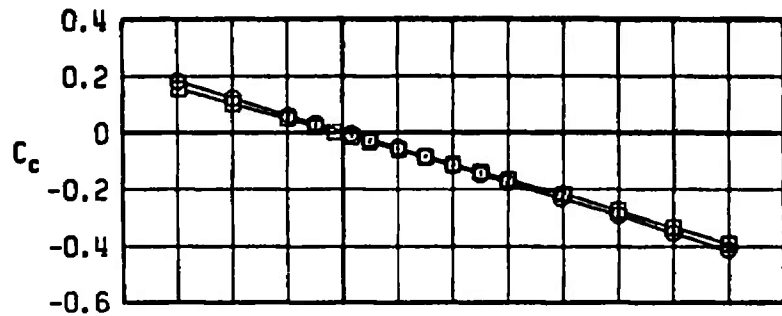
d. $M_\infty = 0.95$
Figure 23. Continued.

SYMBOL	CONFIG	M_∞	λ_N	δP	δQ	δR
□	B2S1W2T5L1C2	1.10	30	0	0	0
○	B2S1W2T5L1C2	1.10	88	0	0	0

 $\alpha = -5$ 

e. $M_\infty = 1.10$
Figure 23. Continued.

SYMBOL	CONFIG	M_∞	λ_M	δP	δQ	δR
\square	B2S1W2T5L1C2	1.30	30	0	0	0
\circ	B2S1W2T5L1C2	1.30	88	0	0	0

 $\alpha = -5$ 

f. $M_\infty = 1.30$
Figure 23. Concluded.

SYMBOL	CONFIG	M_∞	λ_M	δP	δQ	δR
\square	B2S1W2T5L1C2	0.50	30	0	0	0
\circ	B2S1W2T5L1C2	0.50	88	0	0	0

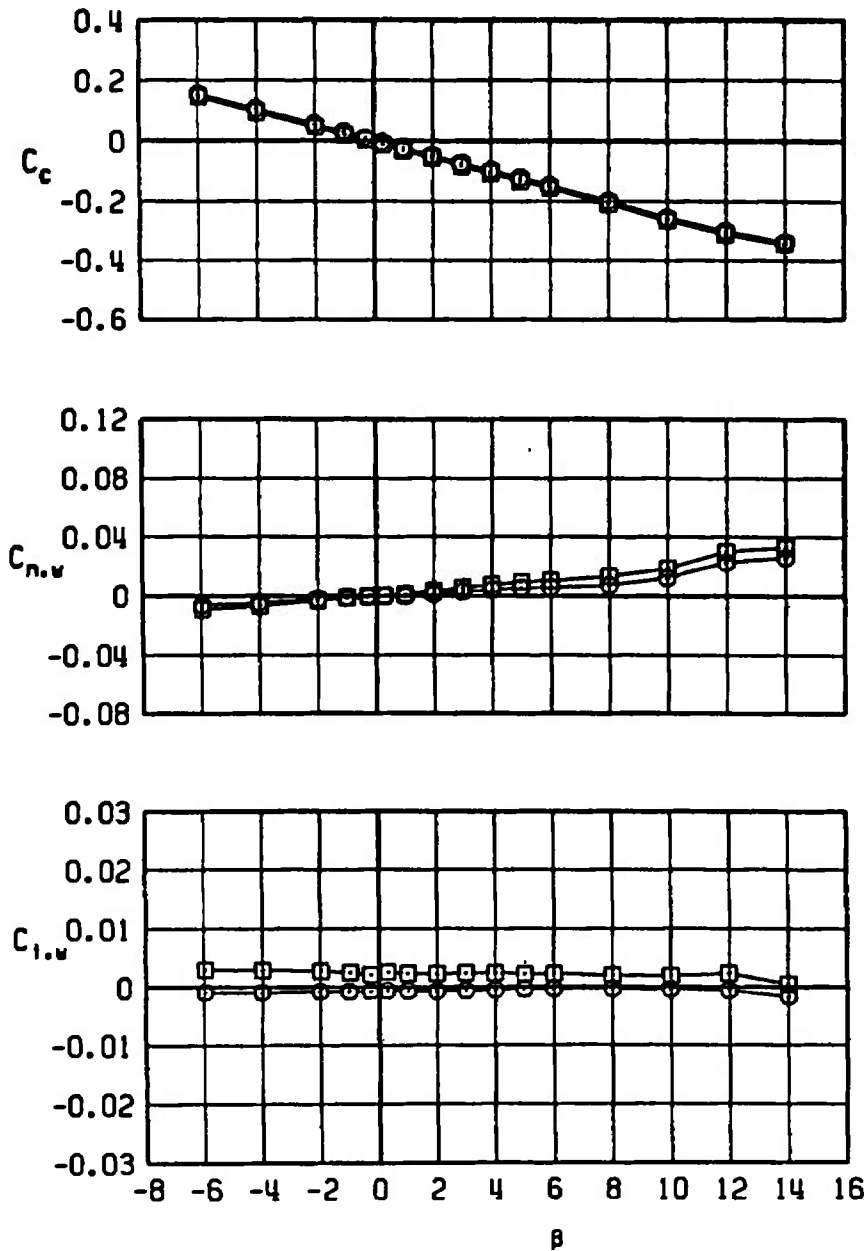
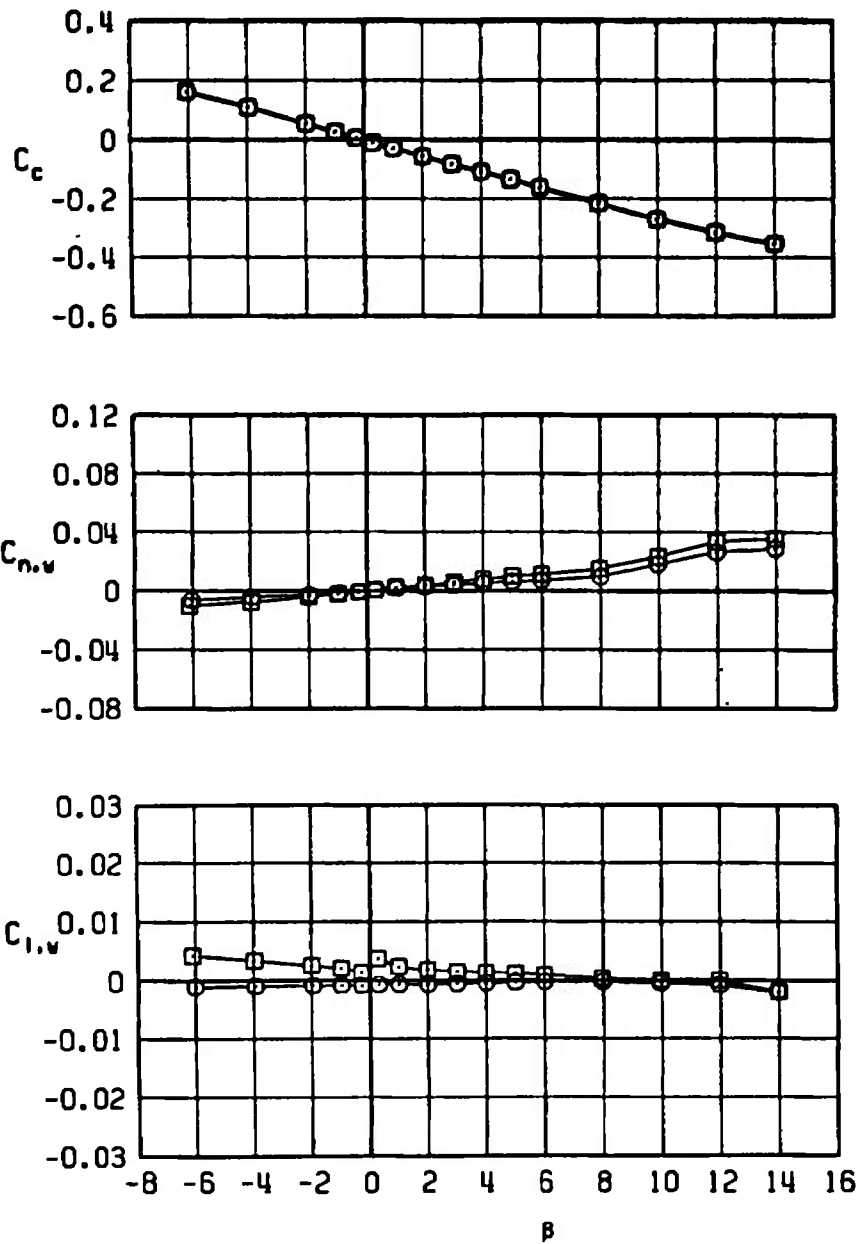
 $\alpha = 0$ a. $M_\infty = 0.50$

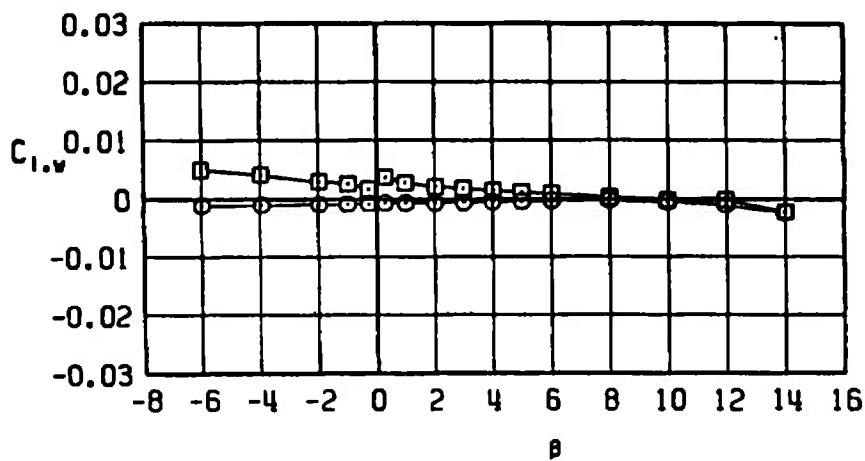
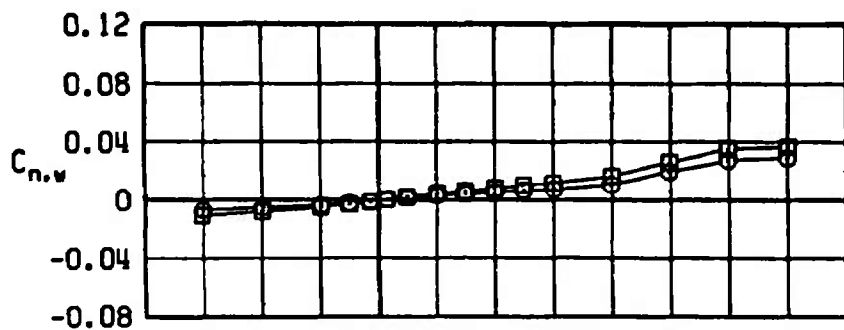
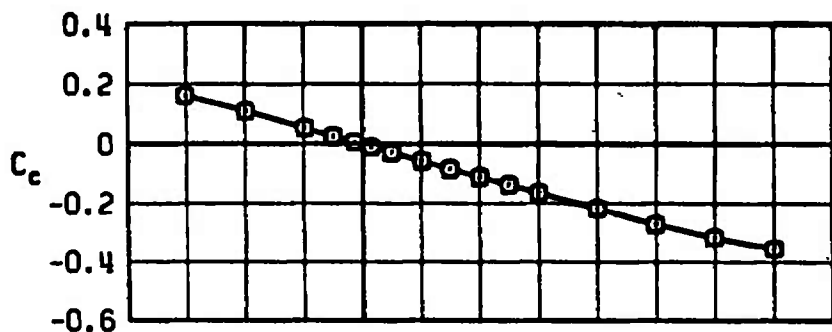
Figure 24. Effect of the wing sweep angle on the crosswind-force, yawing-moment, and rolling-moment coefficients of the MK-84 MGB II configuration, $\alpha = 0$.

SYMBOL	CONFIG	M_∞	λ_∞	δP	δQ	δR
□	B2S1W2T5L1C2	0.70	30	0	0	0
○	B2S1W2T5L1C2	0.70	88	0	0	0

 $\alpha = 0$ 

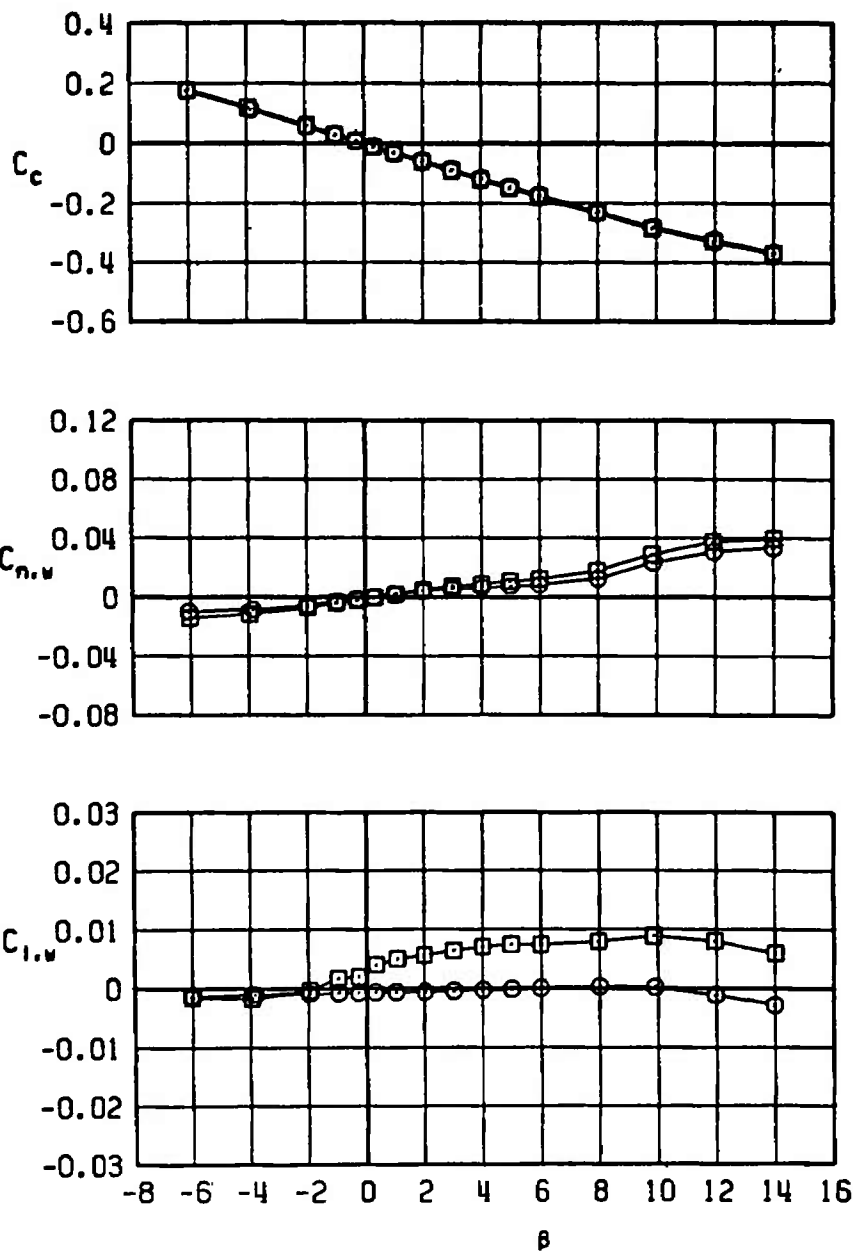
b. $M_\infty = 0.70$
Figure 24. Continued.

SYMBOL	CONFIG	M_∞	λ_H	λ_P	λ_D	λ_R
\square	B2S1W2T5L1C2	0.75	30	0	0	0
\circ	B2S1W2T5L1C2	0.75	88	0	0	0

 $\alpha = 0$ 

c. $M_\infty = 0.75$
Figure 24. Continued.

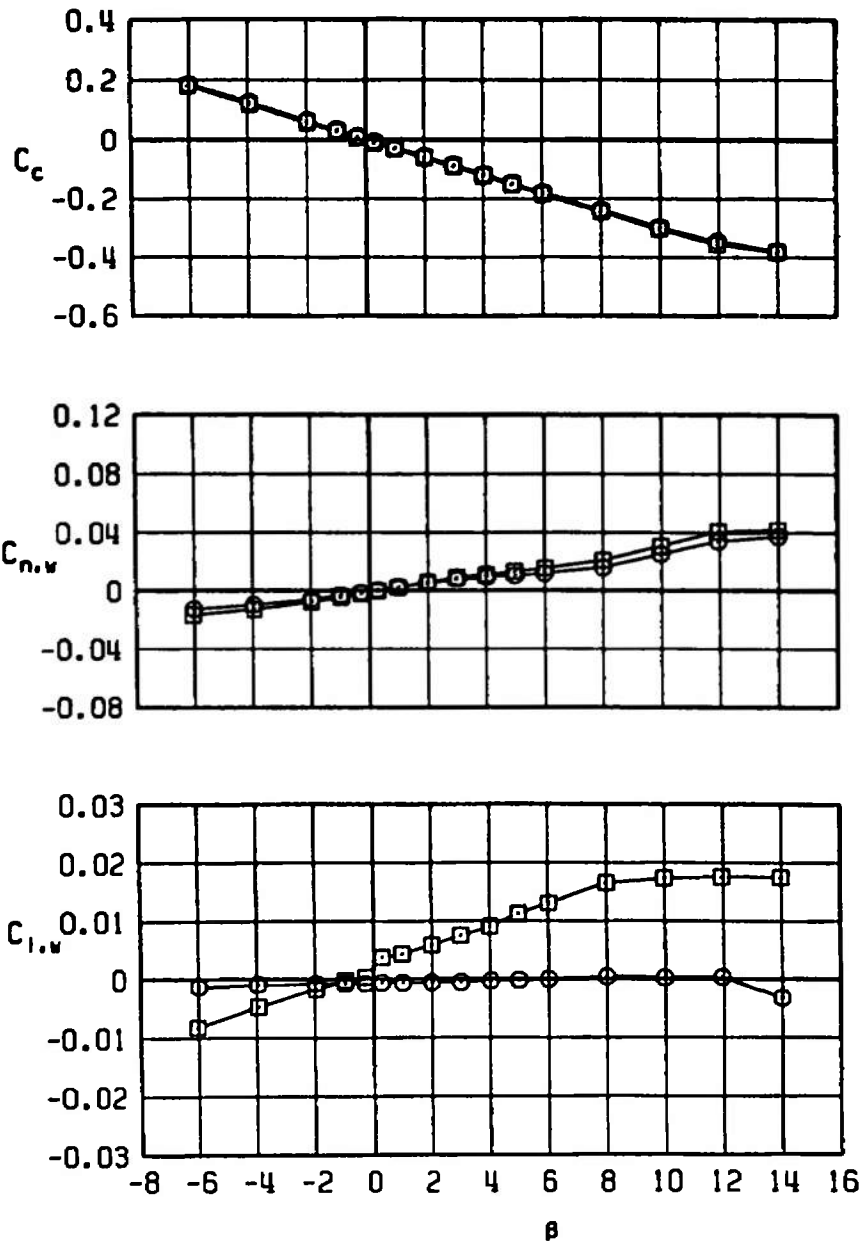
SYMBOL	CONFIG	M_∞	λ_w	δP	δQ	δR
\square	B2S1W2T5L1C2	0.85	30	0	0	0
\circ	B2S1W2T5L1C2	0.85	88	0	0	0

 $\alpha = 0$ 

d. $M_\infty = 0.85$
Figure 24. Continued.

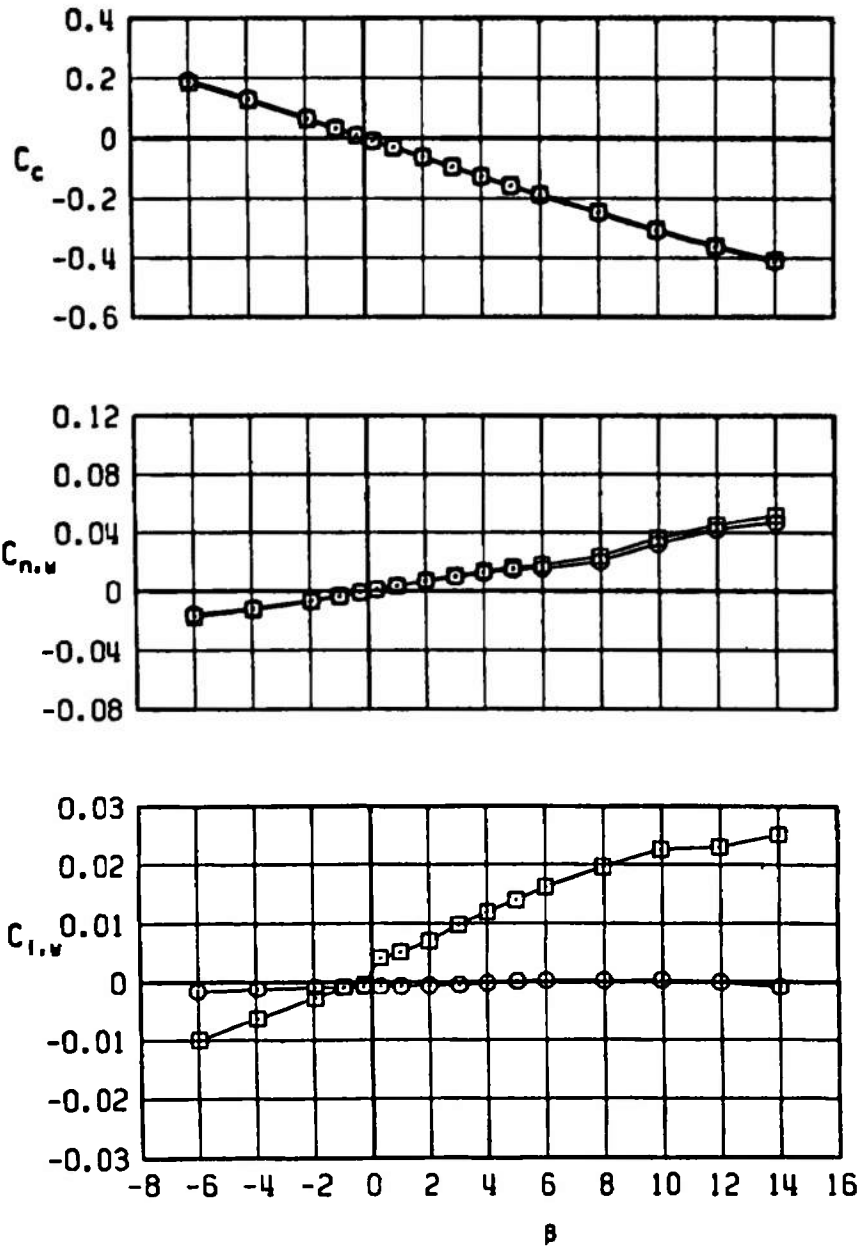
SYMBOL	CONFIG	M_∞	λ_M	δP	δQ	δR
□	B2S1W2T5L1C2	0.90	30	0	0	0
○	B2S1W2T5L1C2	0.90	88	0	0	0

$\alpha = 0$



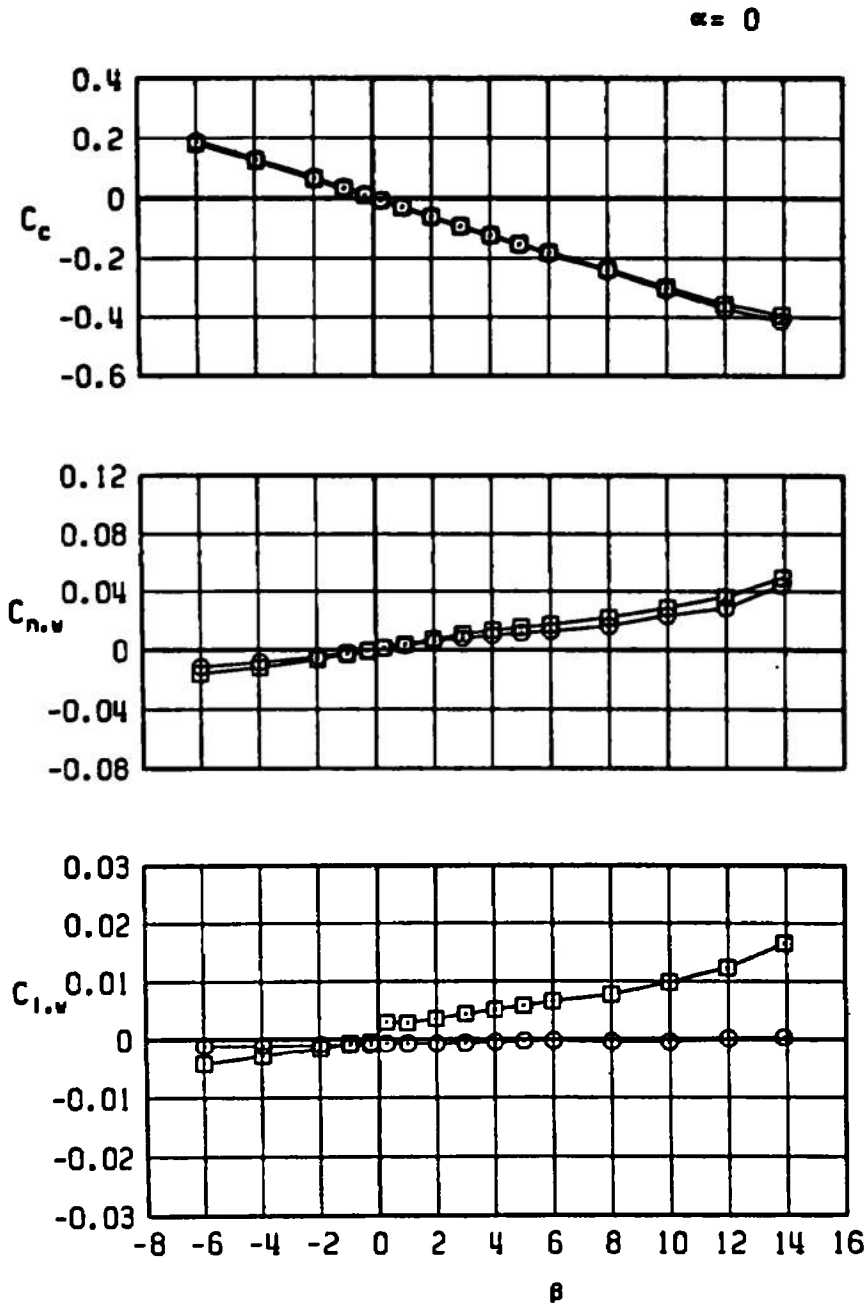
e. $M_\infty = 0.90$
Figure 24. Continued.

SYMBOL	CONFIG	M_∞	λ_w	δP	δQ	δR
\square	B2S1W2T5L1C2	0.95	30	0	0	0
\circ	B2S1W2T5L1C2	0.95	88	0	0	0

 $\alpha = 0$ 

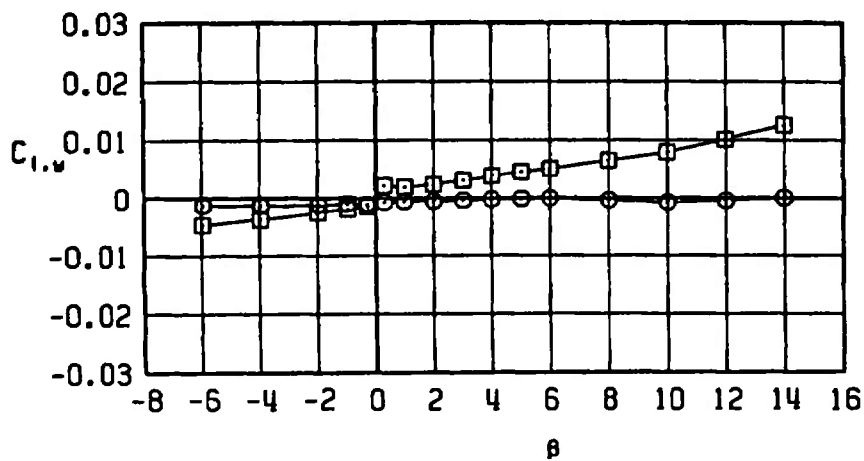
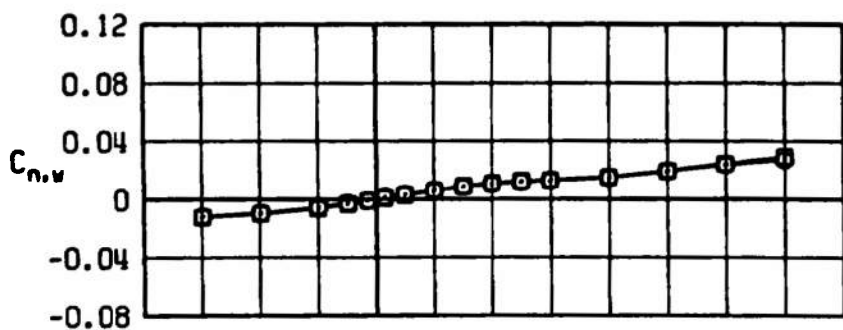
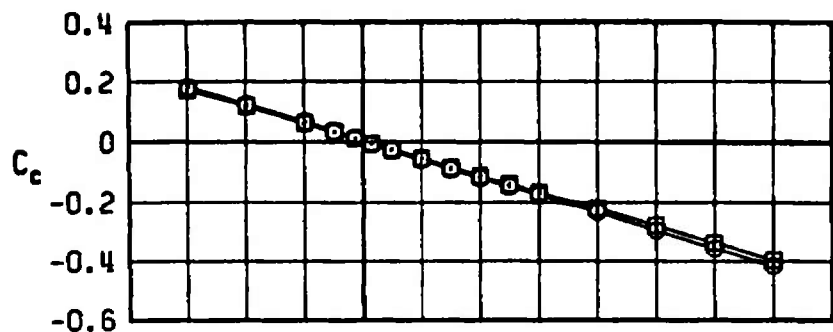
f. $M_\infty = 0.95$
Figure 24. Continued.

SYMBOL	CONFIG	M_∞	λ_H	ϵ^P	ϵ^Q	ϵ^R
\square	B2S1W2T5L1C2	1.00	30	0	0	0
\circ	B2S1W2T5L1C2	1.00	88	0	0	0



g. $M_\infty = 1.00$
Figure 24. Continued.

SYMBOL	CONFIG	M_∞	λ_M	δP	δQ	δR
\square	B2S1W2T5L1C2	1.10	30	0	0	0
\circ	B2S1W2T5L1C2	1.10	88	0	0	0

 $\alpha = 0$ 

h. $M_\infty = 1.10$
Figure 24. Continued.

SYMBOL	CONFIG	M_∞	λ_w	ϵ_P	ϵ_Q	ϵ_R
\square	B2S1W2T5L1C2	1.20	30	0	0	0
\circ	B2S1W2T5L1C2	1.20	88	0	0	0

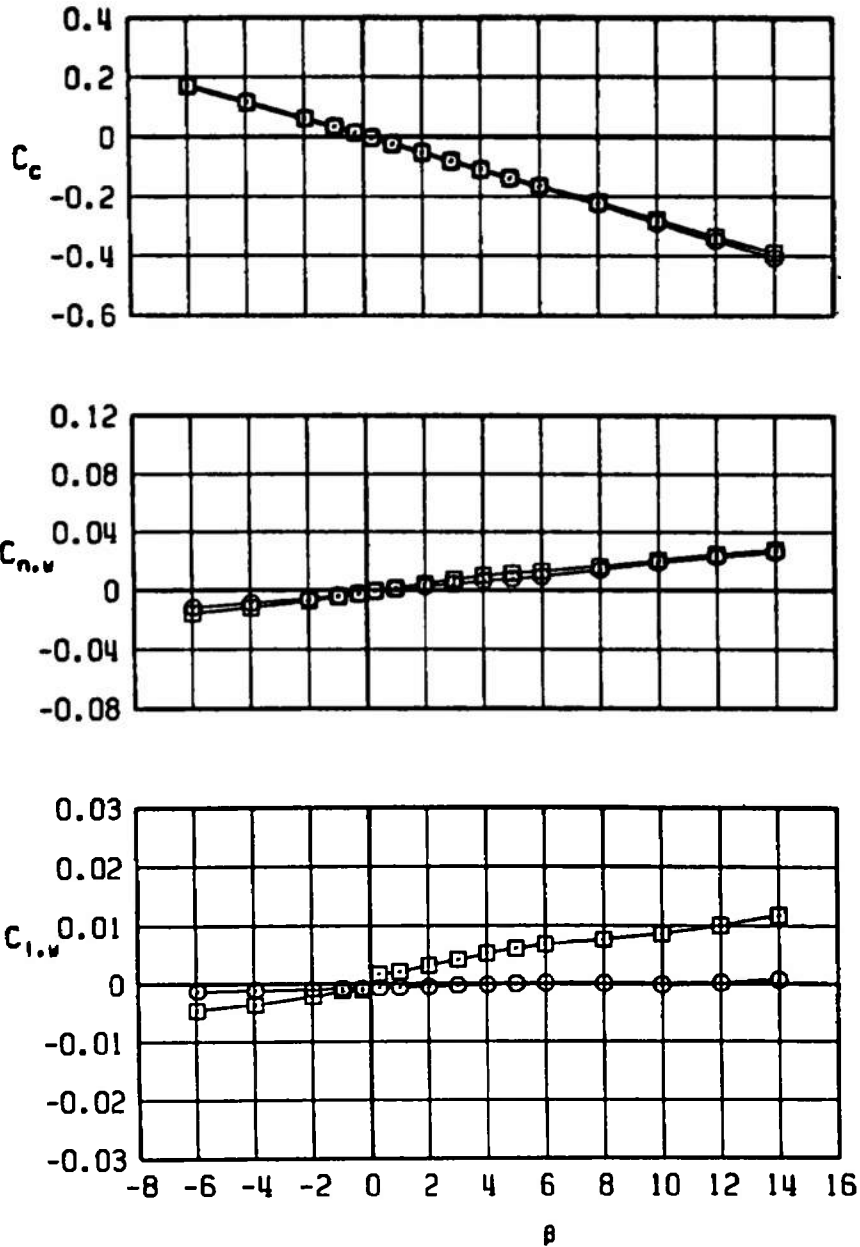
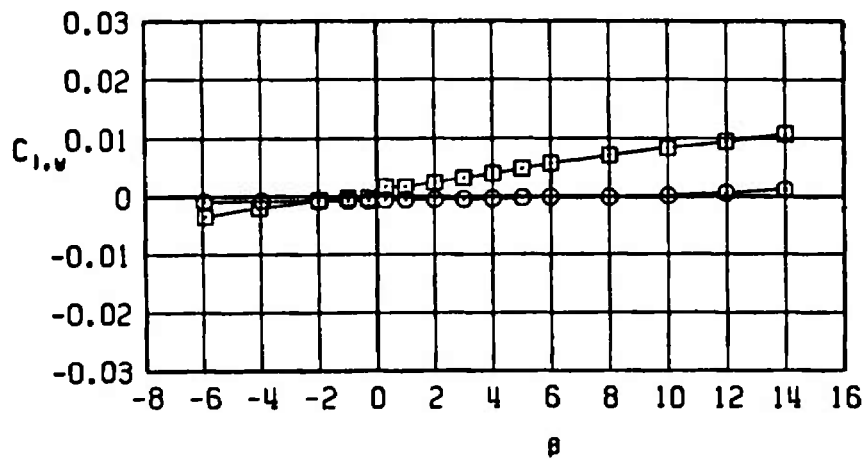
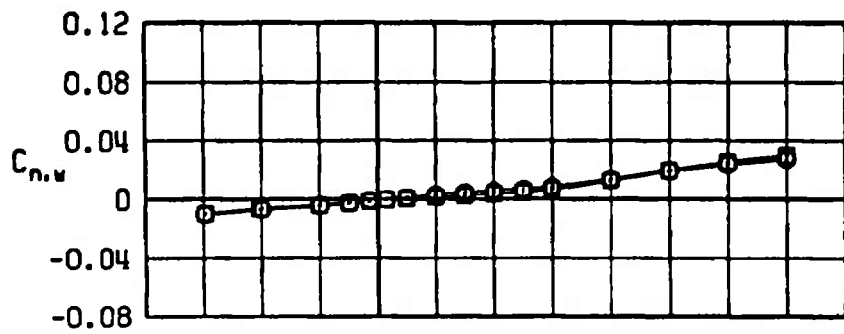
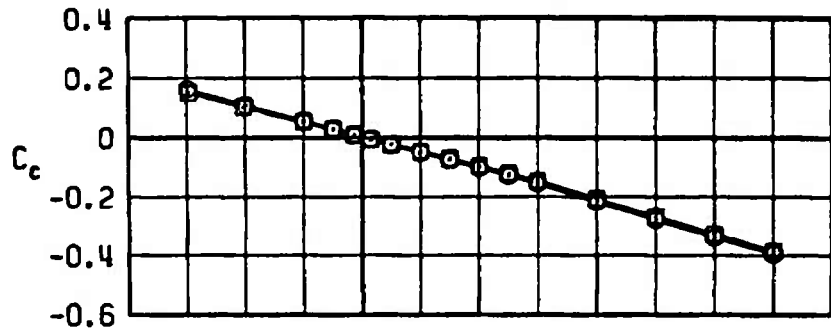
 $\alpha = 0$ i. $M_\infty = 1.20$

Figure 24. Continued.

SYMBOL	CONFIG	M_∞	λ_M	δP	δQ	δR
□	B2S1W2T5L1C2	1.30	30	0	0	0
○	B2S1W2T5L1C2	1.30	88	0	0	0

 $\alpha = 0$ 

j. $M_\infty = 1.30$
Figure 24. Concluded.

SYMBOL	CONFIG	M_∞	λ_w	ϕ_P	ϕ_D	ϕ_R
□	B2S1W2T5L1C2	0.50	30	0	0	0
○	B2S1W2T5L1C2	0.50	88	0	0	0

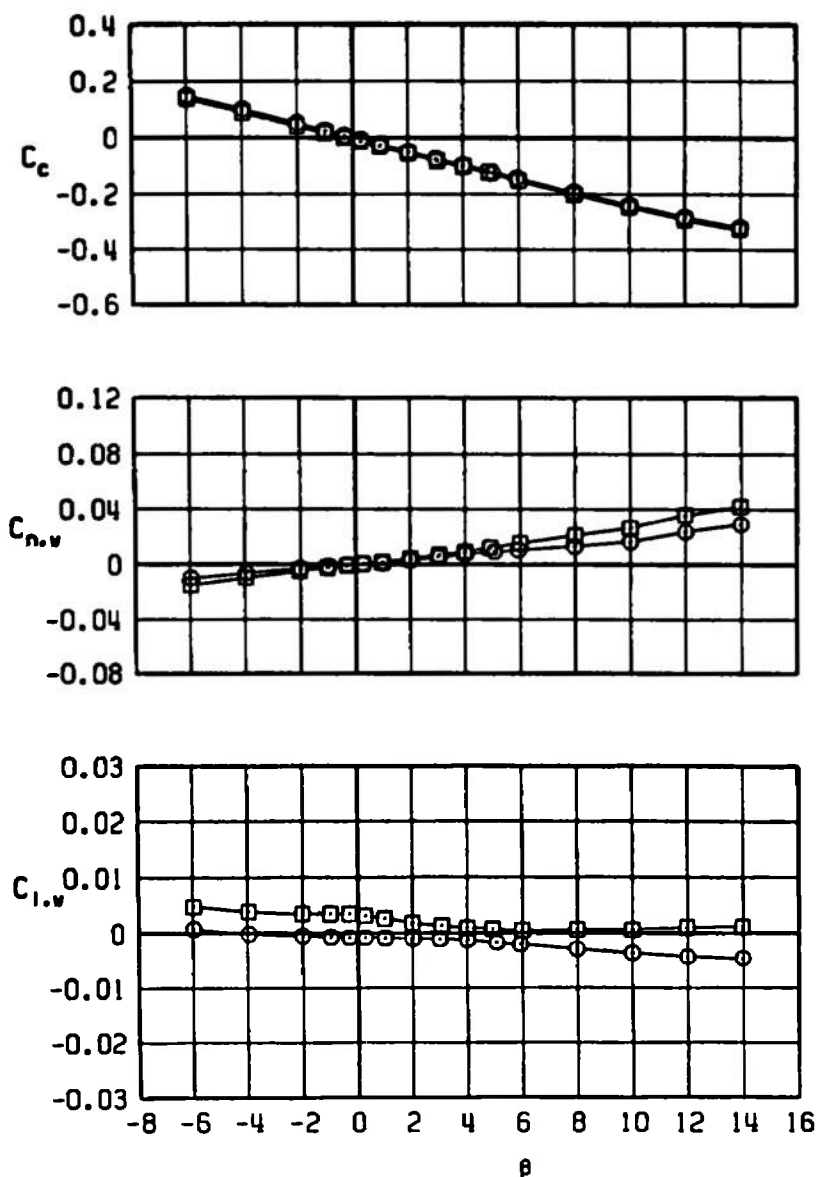
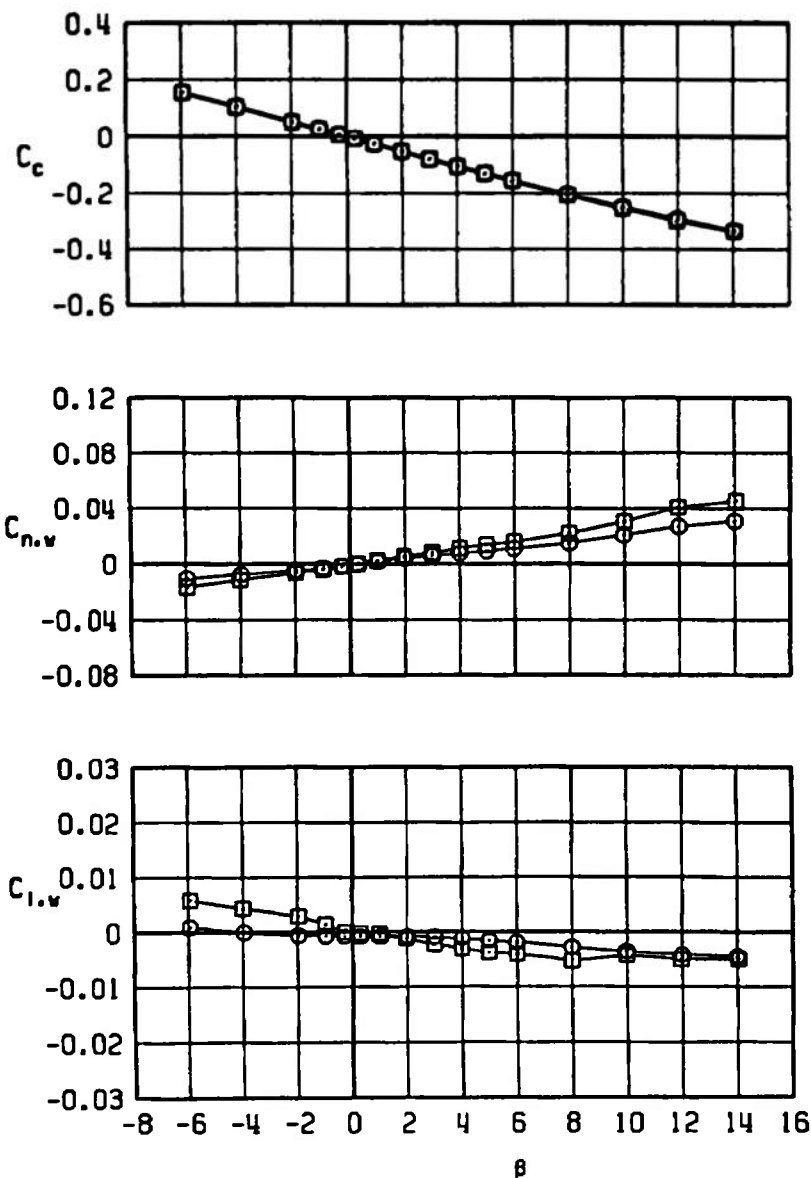
 $\alpha = 5$ a. $M_\infty = 0.50$

Figure 25. Effect of the wing sweep angle on the crosswind-force, yawing-moment, and rolling-moment coefficients of the MK-84 MGGB II configuration, $\alpha = 5$ deg.

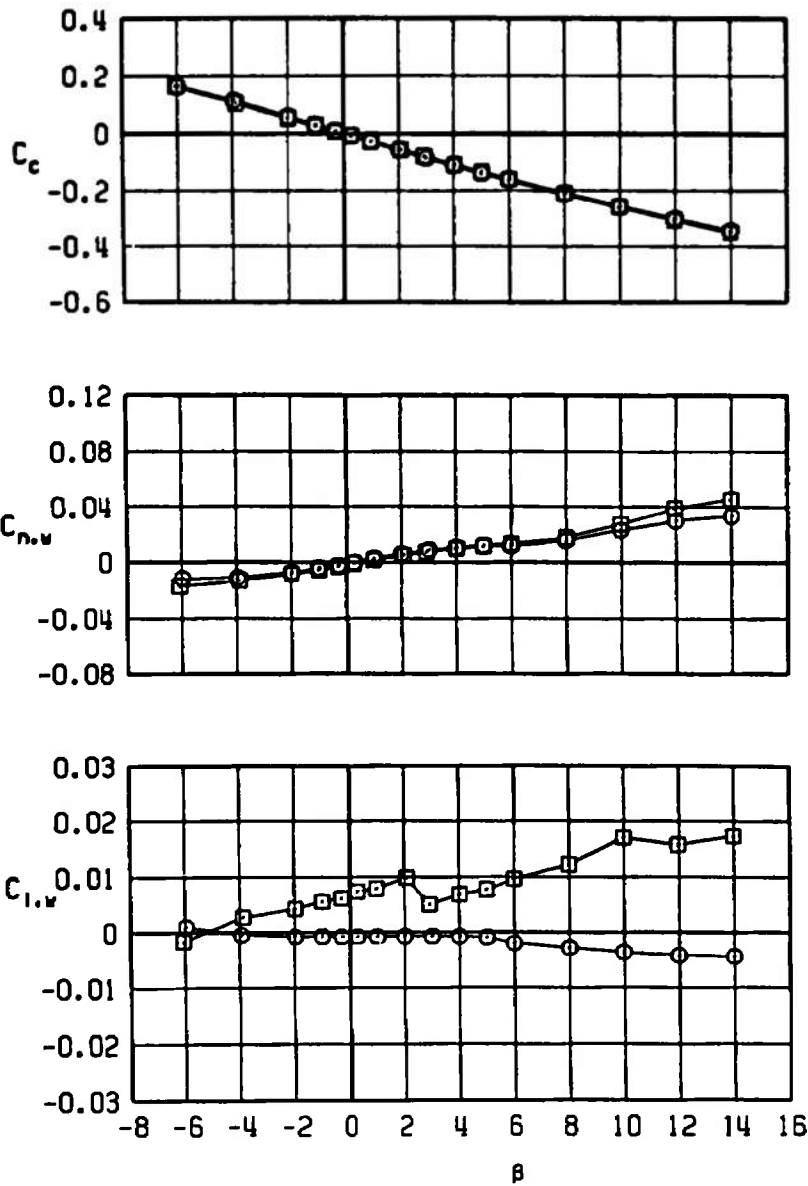
SYMBOL	CONFIG	M_∞	λ_H	δP	δQ	δR
\square	B2S1W2T5L1C2	0.75	30	0	0	0
\circ	B2S1W2T5L1C2	0.75	88	0	0	0

 $\alpha = 5$ 

b. $M_\infty = 0.75$
Figure 25. Continued.

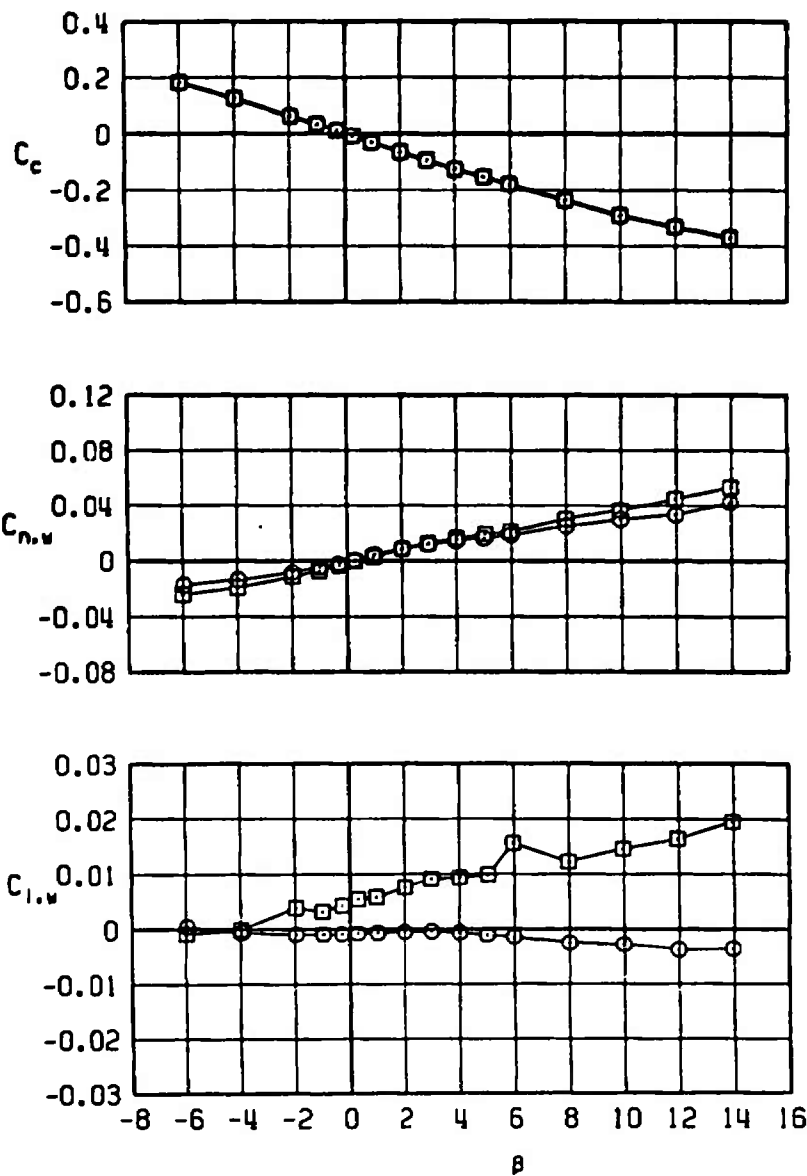
SYMBOL	CONFIG	M_∞	λ_M	δP	δQ	δR
\square	B2S1W2T5L1C2	0.85	30	0	0	0
\circ	B2S1W2T5L1C2	0.85	88	0	0	0

$\alpha = 5$



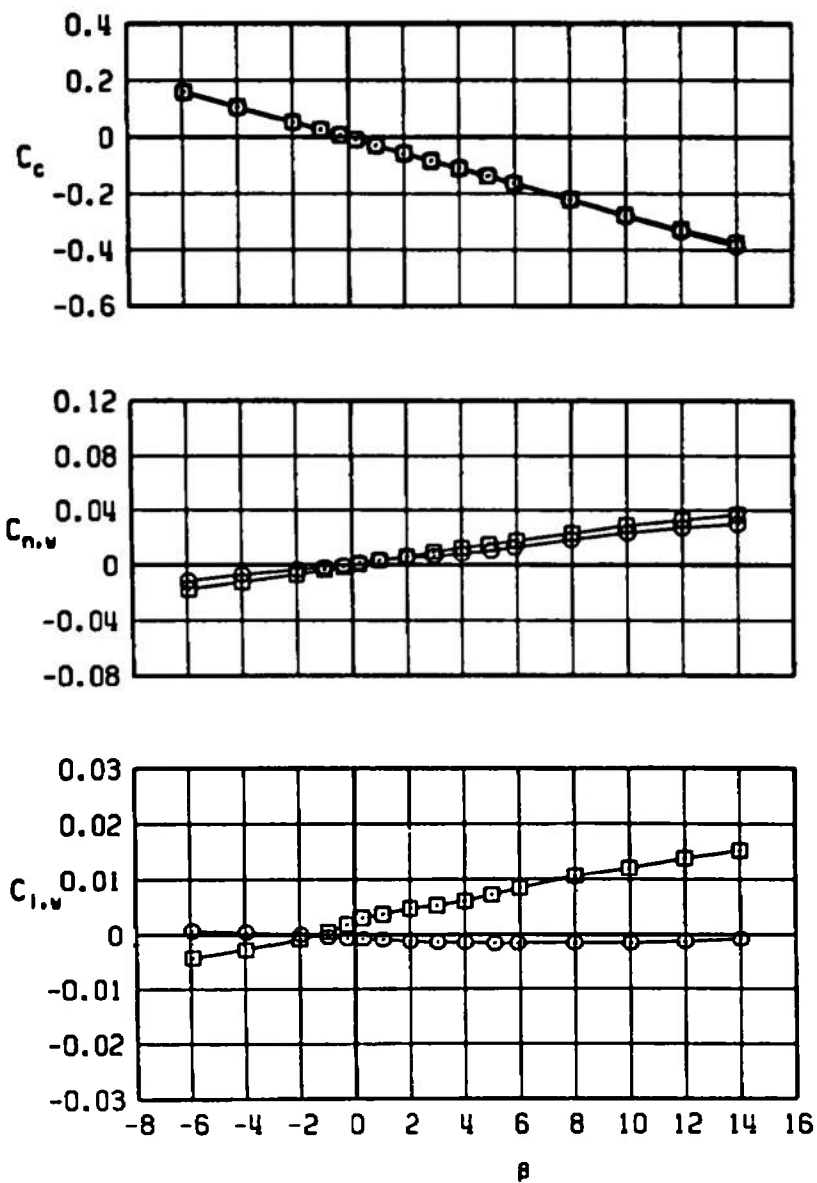
c. $M_\infty = 0.85$
Figure 25. Continued.

SYMBOL	CONFIG	M_∞	λ_W	δP	δQ	δR
□	B2S1W2T5L1C2	0.95	30	0	0	0
○	B2S1W2T5L1C2	0.95	88	0	0	0

 $\alpha = 5$ 

d. $M_\infty = 0.95$
Figure 25. Continued.

SYMBOL	CONFIG	M_∞	λ_M	δP	δQ	δR
□	B2S1W2T5L1C2	1.10	30	0	0	0
○	B2S1W2T5L1C2	1.10	88	0	0	0

 $\alpha = 5$ 

e. $M_\infty = 1.10$
Figure 25. Continued.

SYMBOL	CONFIG	M_∞	λ_W	δP	δQ	δR
\square	8251W2T5LIC2	1.30	30	0	0	0
\circ	8251W2T5LIC2	1.30	88	0	0	0

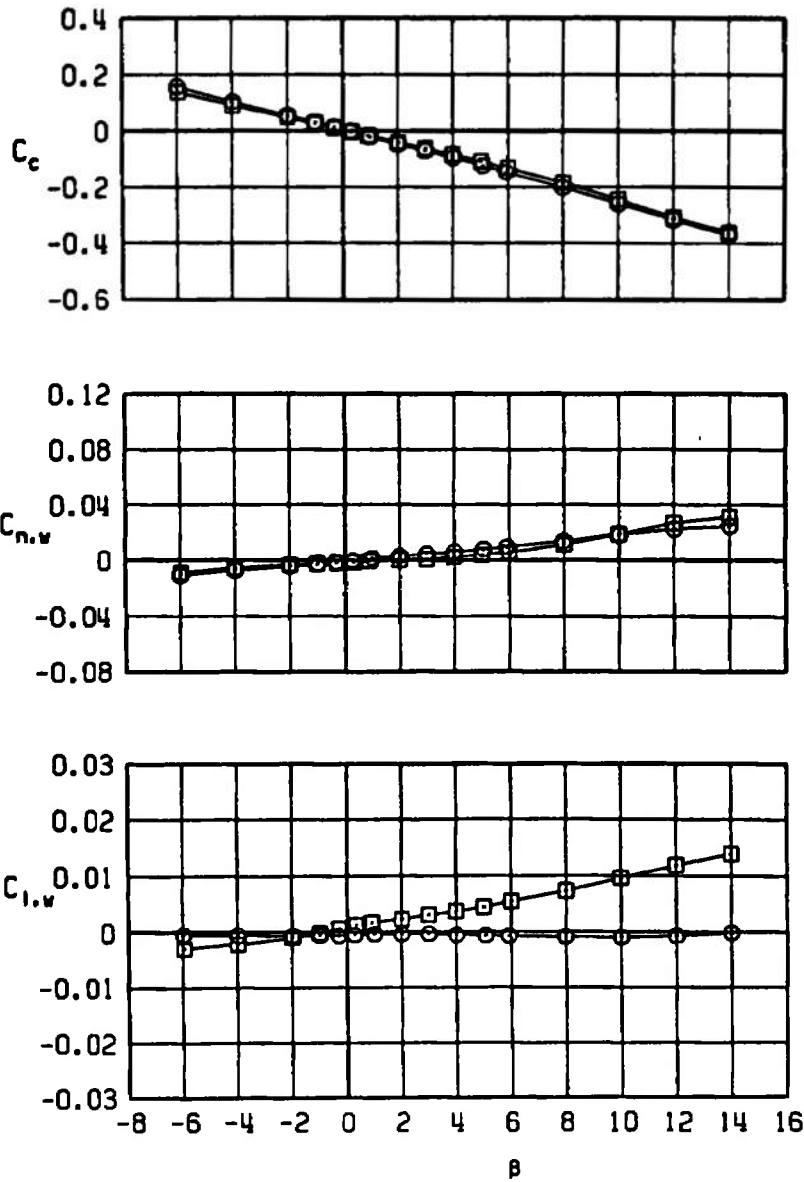
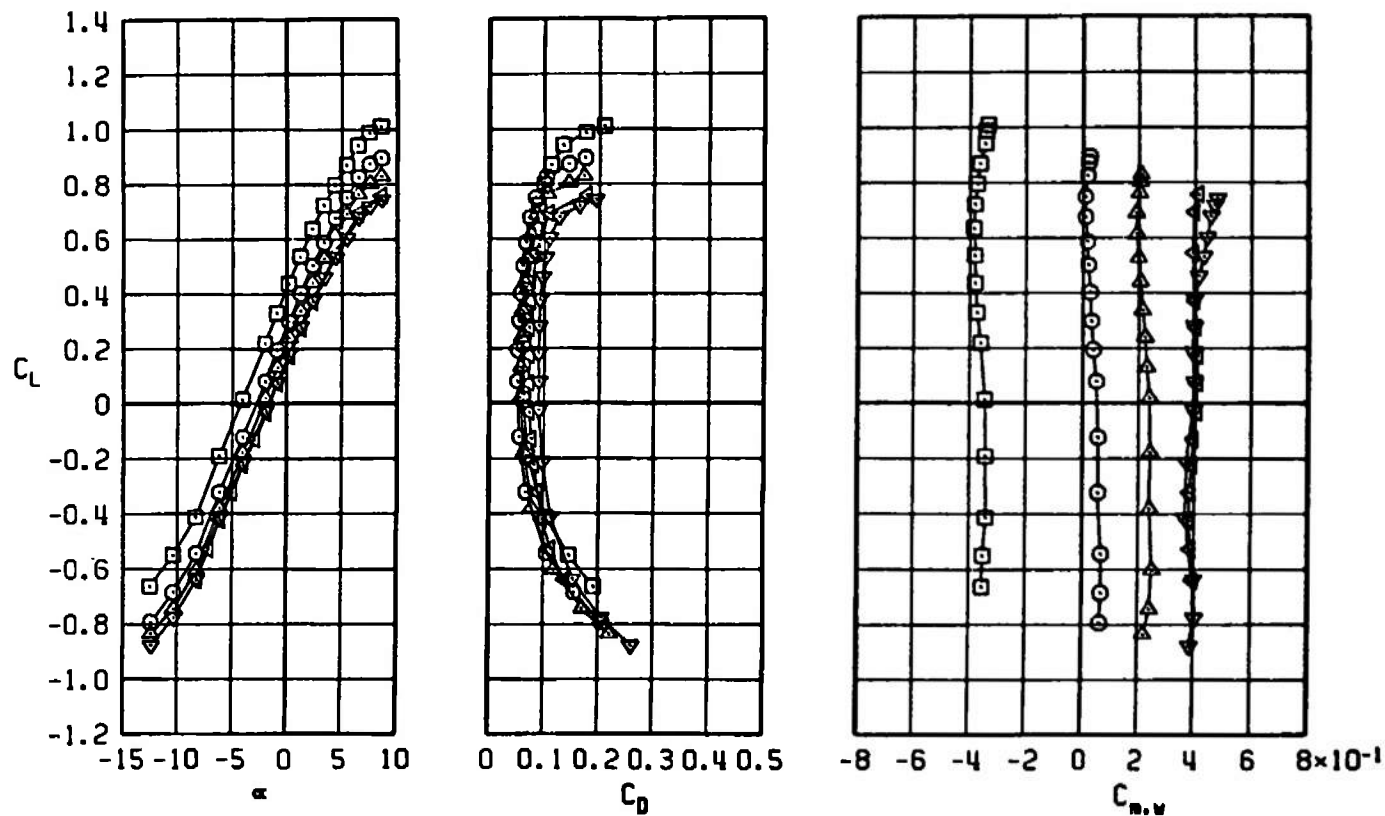
 $\alpha = 5$ f. $M_\infty = 1.30$

Figure 25. Concluded.

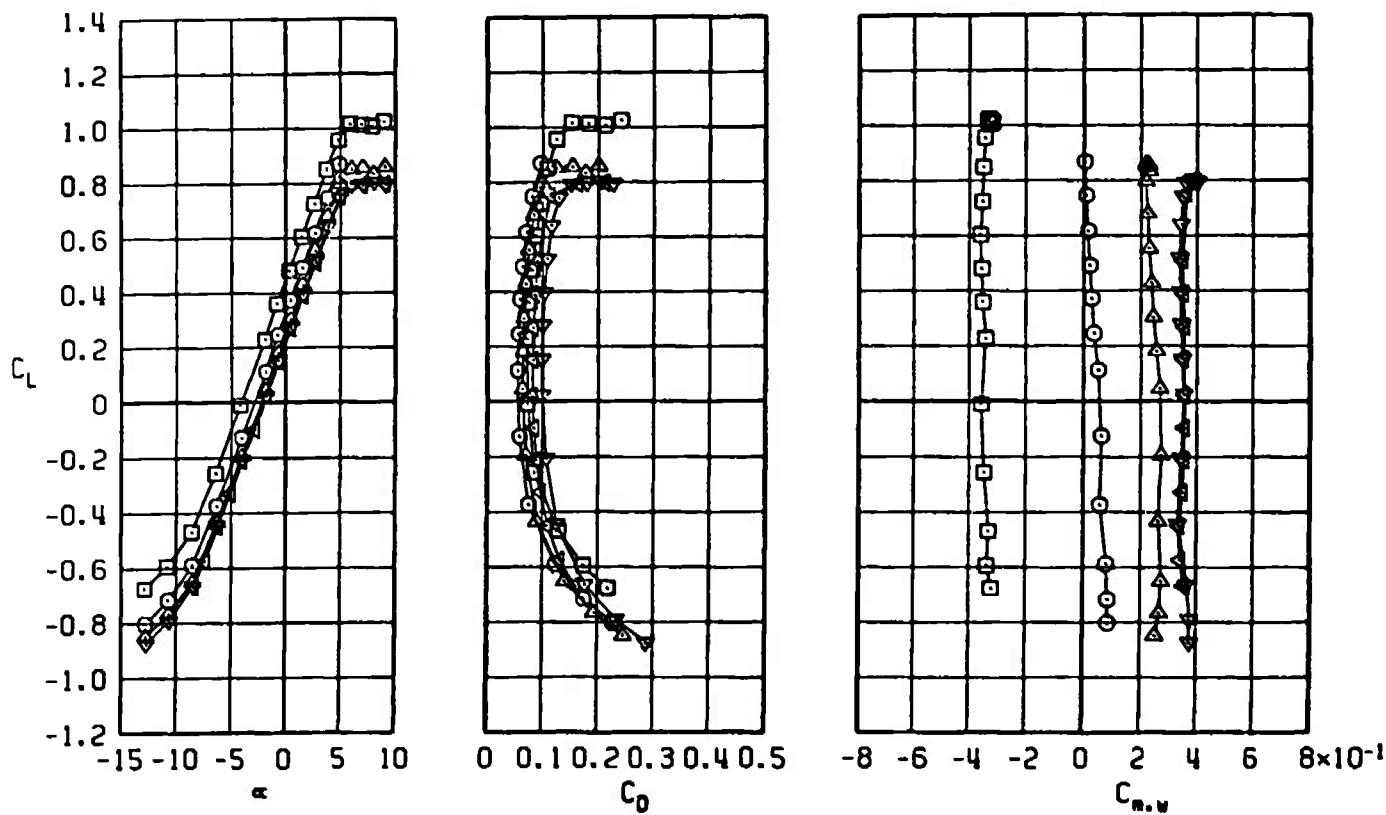
SYMBOL	CONFIG	M_∞	λ_M	δP	δQ	δR
□	B2S1W2T5L1C2	0.50	30	0	+10	0
○	B2S1W2T5L1C2	0.50	30	0	0	0
△	B2S1W2T5L1C2	0.50	30	0	-5	0
◀	B2S1W2T5L1C2	0.50	30	0	-10	0
▽	B2S1W2T5L1C2	0.50	30	0	-15	0



a. $M_\infty = 0.50$

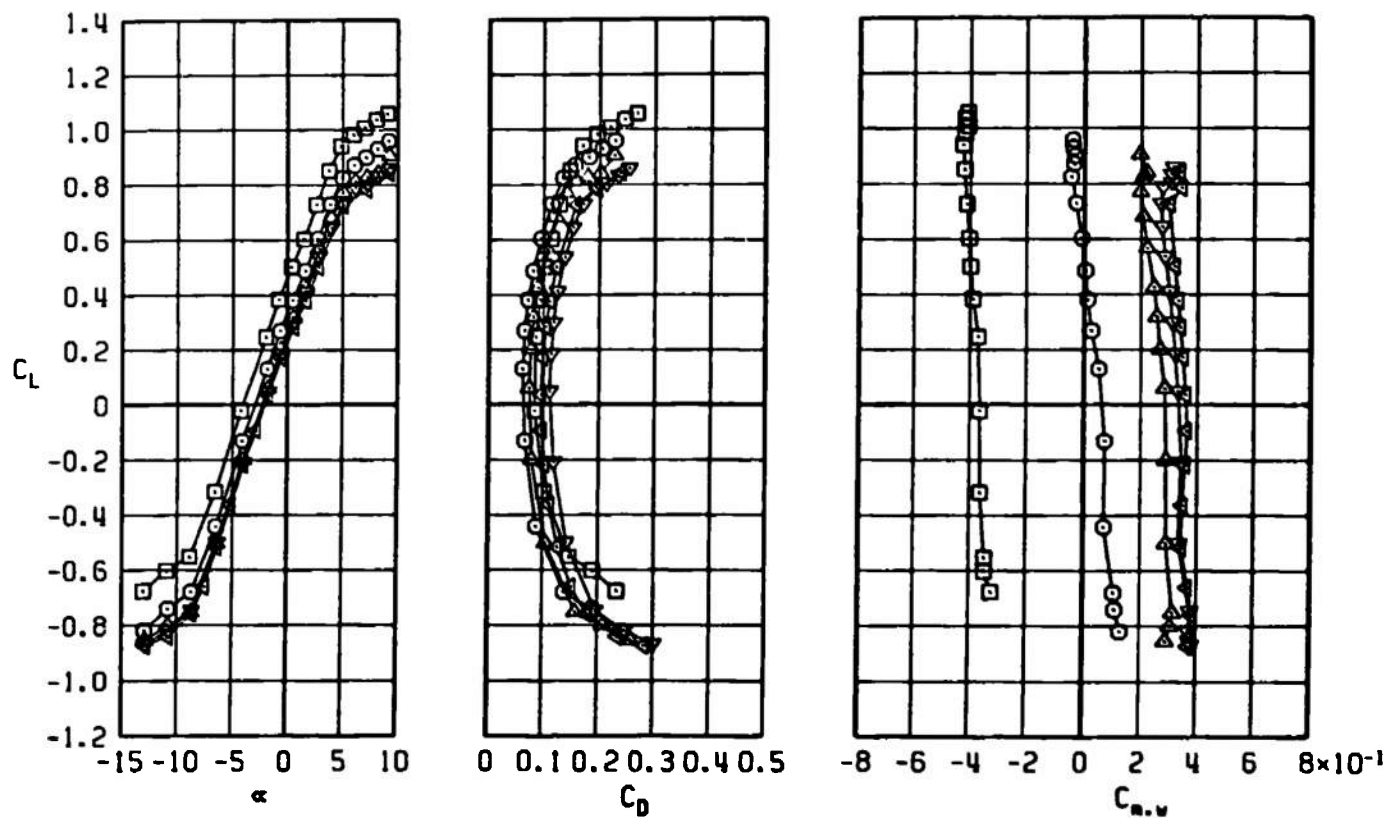
Figure 26. Effect of pitch control deflections on the lift, drag, and pitching-moment coefficients of the MK-84 MGGB II configuration.

SYMBOL	CONF1G	M_∞	λ_M	δP	δQ	δR
□	B2S1W2TSL1C2	0.75	30	0	+10	0
○	B2S1W2TSL1C2	0.75	30	0	0	0
△	B2S1W2TSL1C2	0.75	30	0	-5	0
◀	B2S1W2TSL1C2	0.75	30	0	-10	0
▼	B2S1W2TSL1C2	0.75	30	0	-15	0



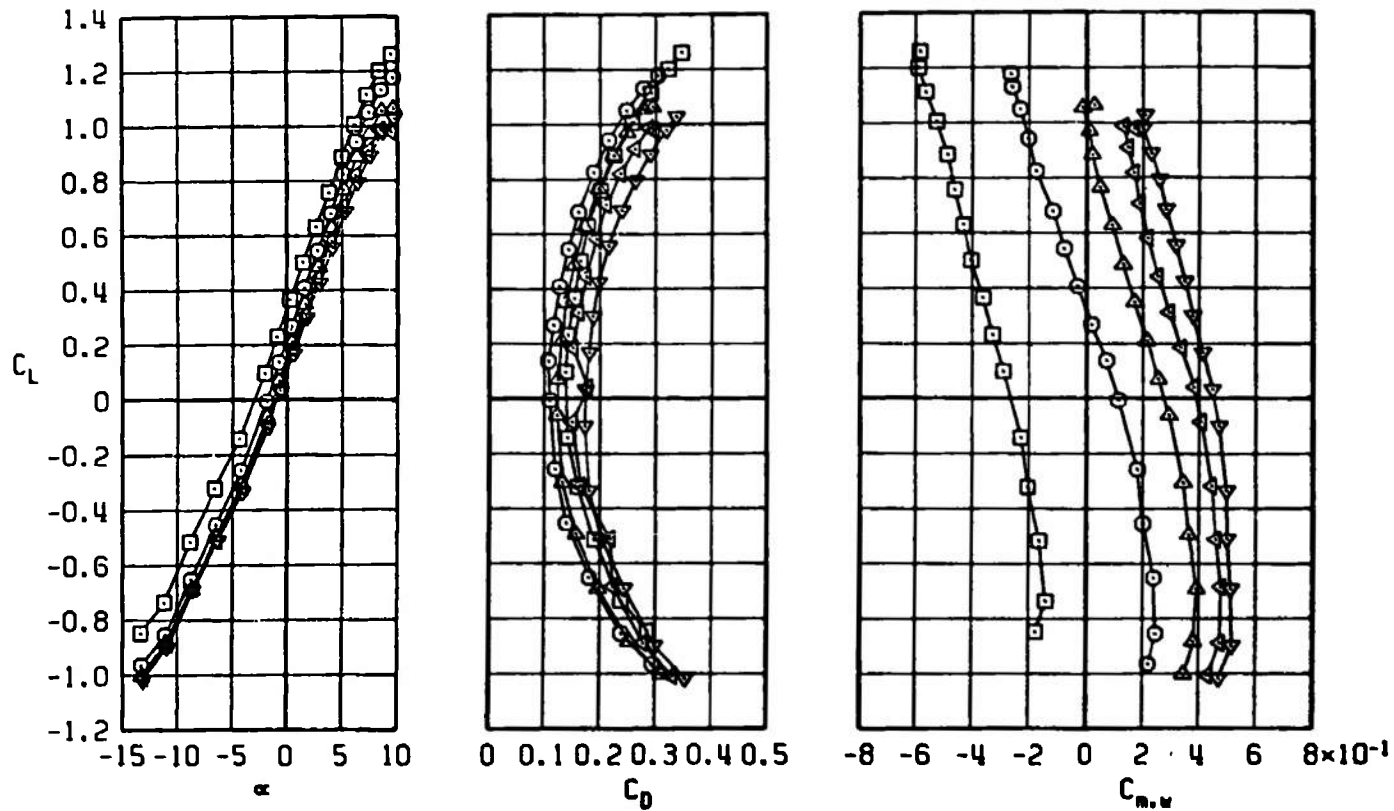
b. $M_\infty = 0.75$
Figure 26. Continued.

SYMBOL	CONFIG	M_∞	λ_N	δP	δQ	δR
□	B2S1W2T5L1C2	0.85	30	0	+10	0
○	B2S1W2T5L1C2	0.85	30	0	0	0
△	B2S1W2T5L1C2	0.85	30	0	-5	0
◀	B2S1W2T5L1C2	0.85	30	0	-10	0
▽	B2S1W2T5L1C2	0.85	30	0	-15	0



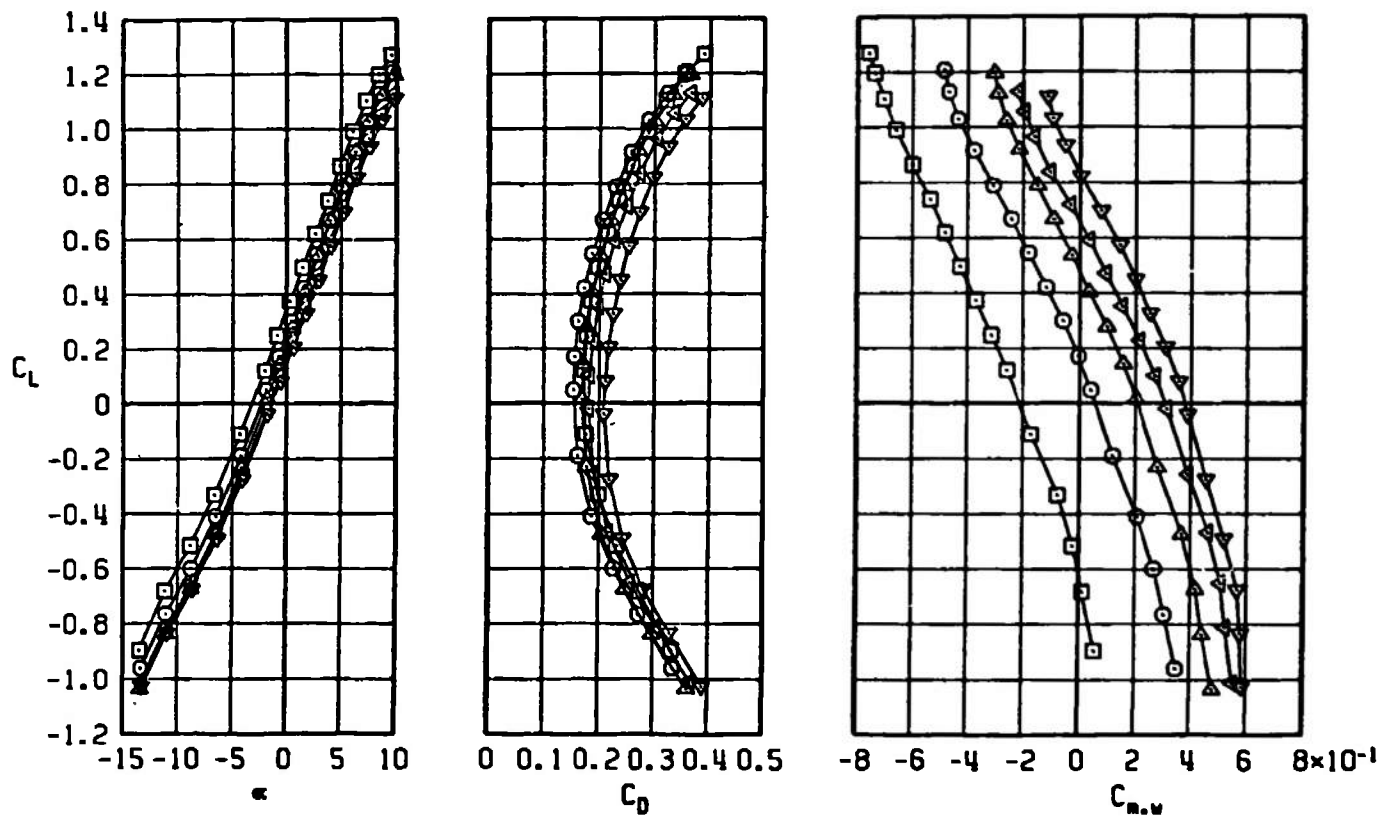
c. $M_\infty = 0.85$
Figure 26. Continued.

SYMBOL	CONFIG	M_∞	λ_H	δP	δQ	δR
□	B2S1W2T5L1C2	0.95	30	0	+10	0
○	B2S1W2T5L1C2	0.95	30	0	0	0
△	B2S1W2T5L1C2	0.95	30	0	-5	0
◀	B2S1W2T5L1C2	0.95	30	0	-10	0
▼	B2S1W2T5L1C2	0.95	30	0	-15	0



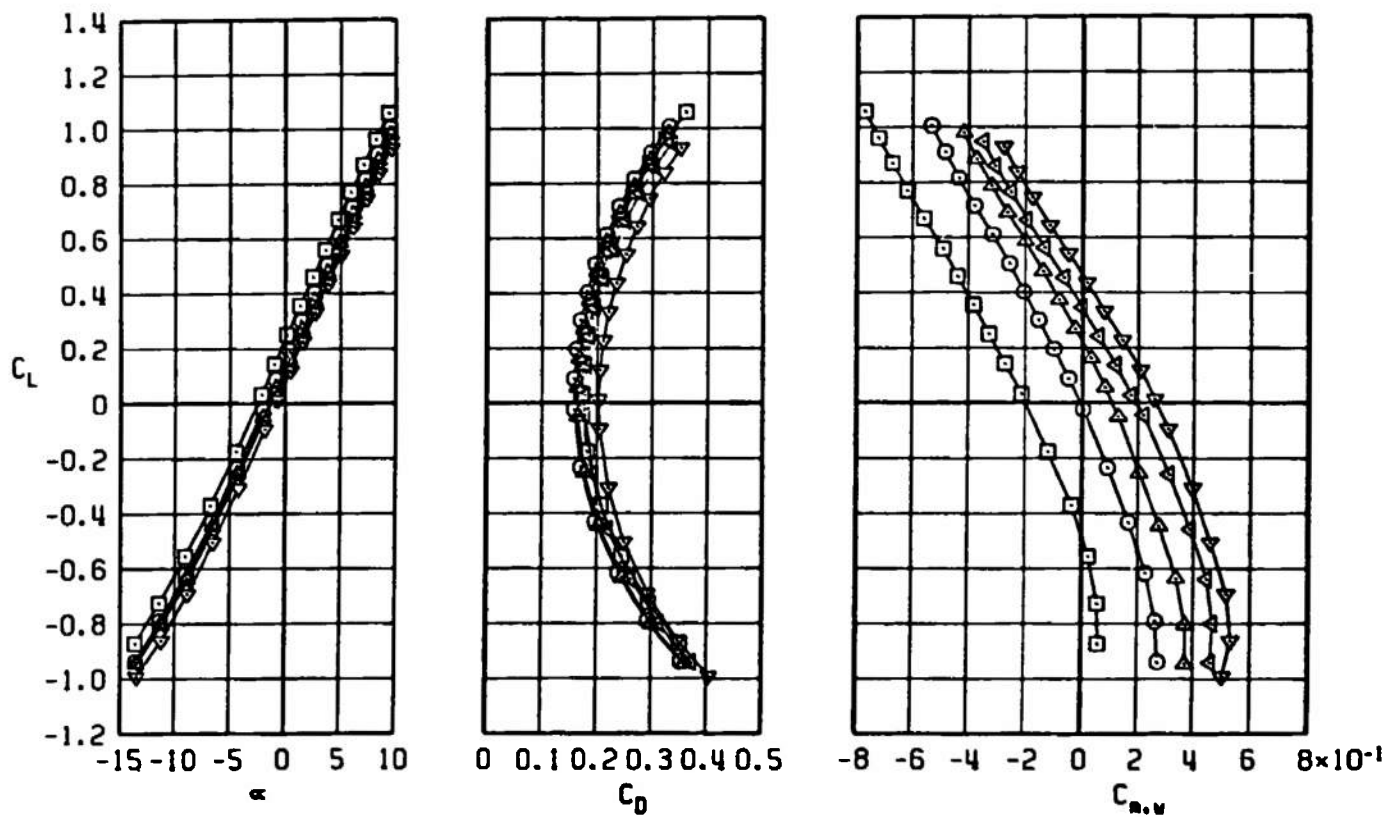
d. $M_\infty = 0.95$
Figure 26. Continued.

SYMBOL	CONFIG	M_∞	λ_∞	δP	δQ	δR
□	B2S1W2T5L1C2	1.10	30	0	+10	0
○	B2S1W2T5L1C2	1.10	30	0	0	0
△	B2S1W2T5L1C2	1.10	30	0	-5	0
▽	B2S1W2T5L1C2	1.10	30	0	-10	0
▽	B2S1W2T5L1C2	1.10	30	0	-15	0



e. $M_\infty = 1.10$
Figure 26. Continued.

SYMBOL	CONFIG	M_∞	λ_∞	δP	δQ	δR
□	B2S1W2T5L1C2	1.30	30	0	+10	0
○	B2S1W2T5L1C2	1.30	30	0	0	0
△	B2S1W2T5L1C2	1.30	30	0	-5	0
▽	B2S1W2T5L1C2	1.30	30	0	-10	0
▽	B2S1W2T5L1C2	1.30	30	0	-15	0



f. $M_\infty = 1.30$
Figure 26. Concluded.

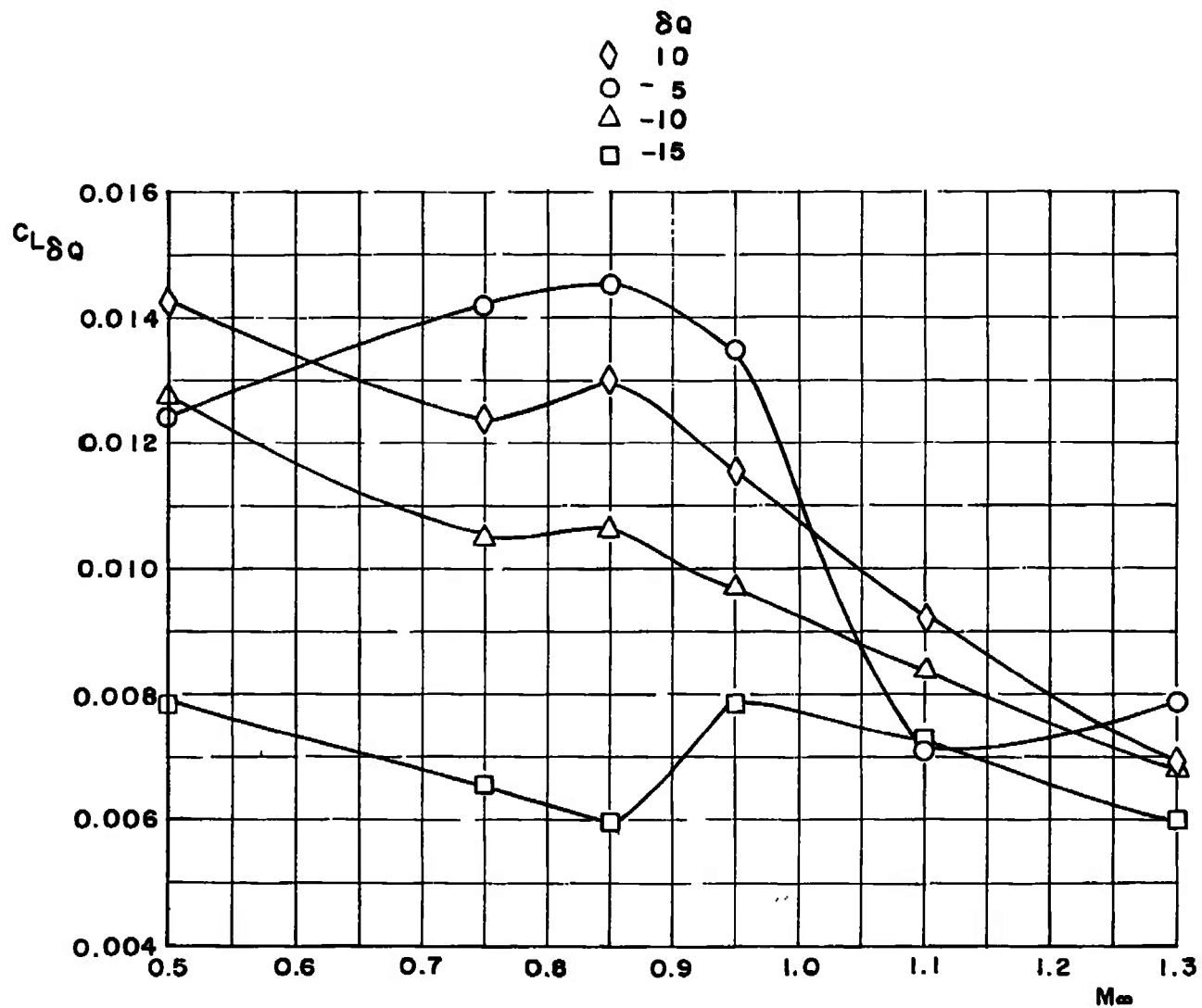


Figure 27. Effectiveness of the flap control surfaces in producing lift at zero angle of attack.

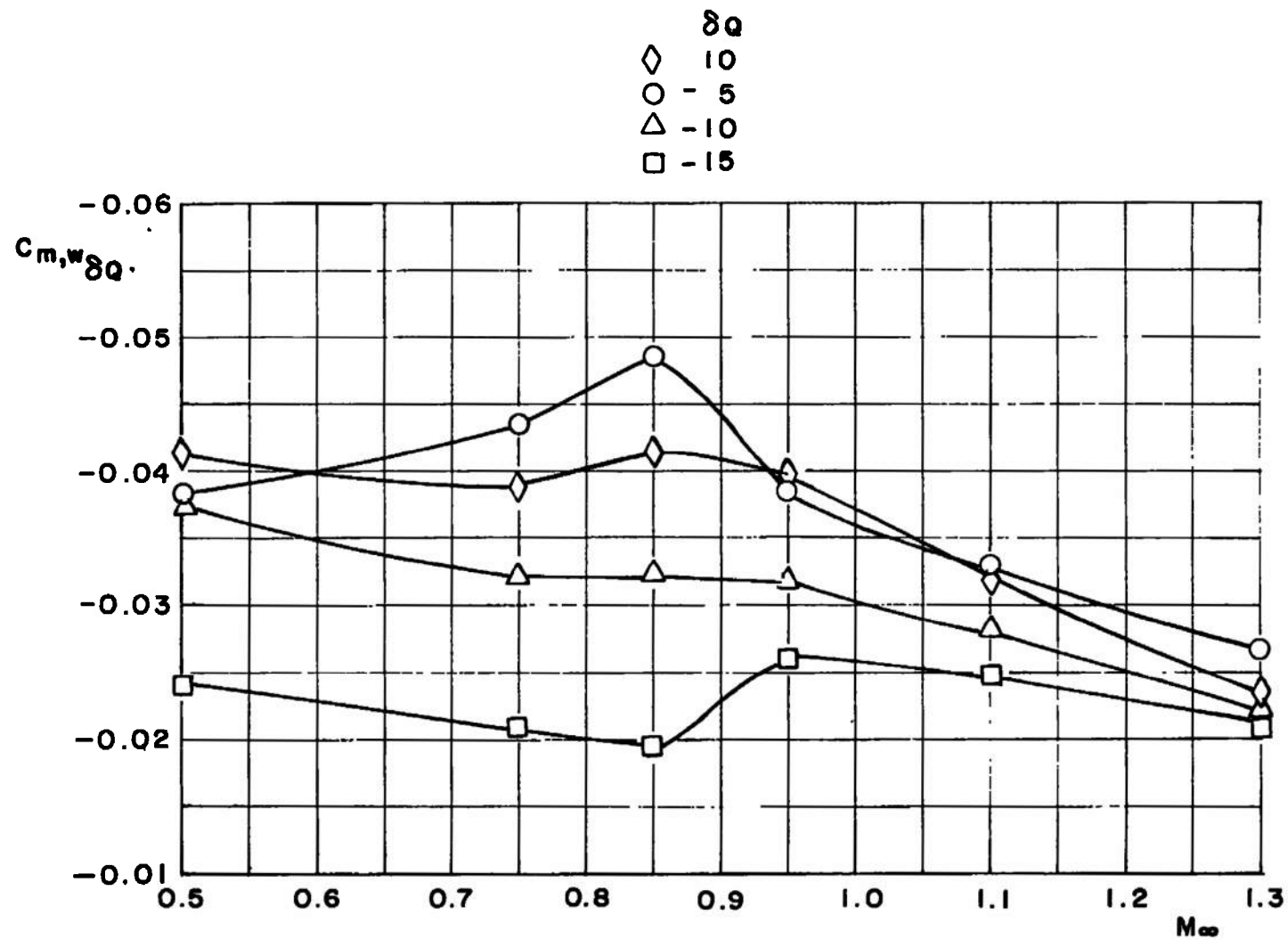


Figure 28. Pitch effectiveness of the flap control surfaces at zero angle of attack.

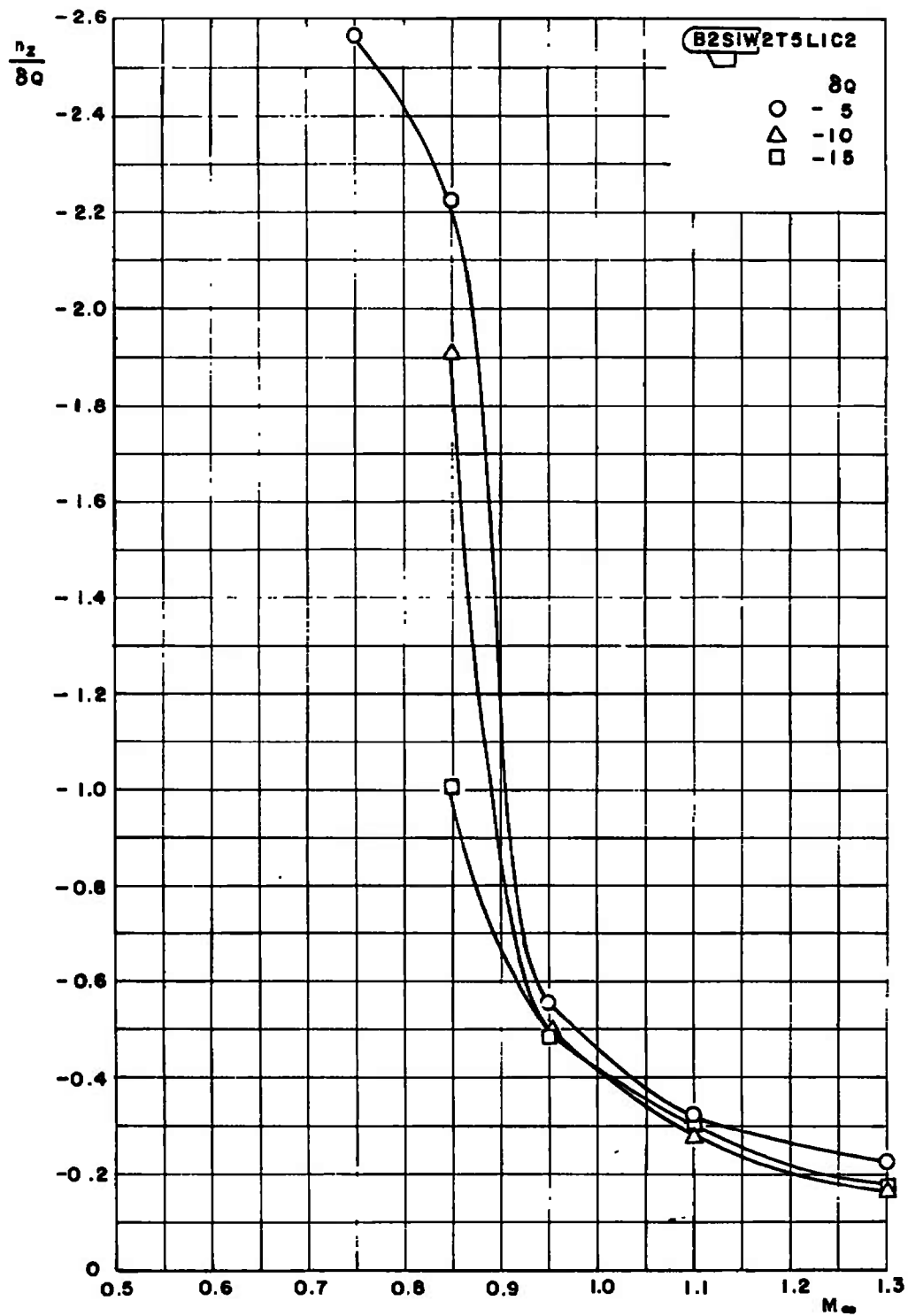


Figure 29. Longitudinal load factor per degree of pitch control deflection (δQ) versus Mach number.

SYMBOL	CONFIG	M_∞	λ_M	δP	δQ	δR
□	82S1W2T5L1C2	0.50	30	0	0	0
○	82S1W2T5L1C2	0.50	30	0	0	5
△	82S1W2T5L1C2	0.50	30	0	0	10
◀	82S1W2T5L1C2	0.50	30	0	0	15

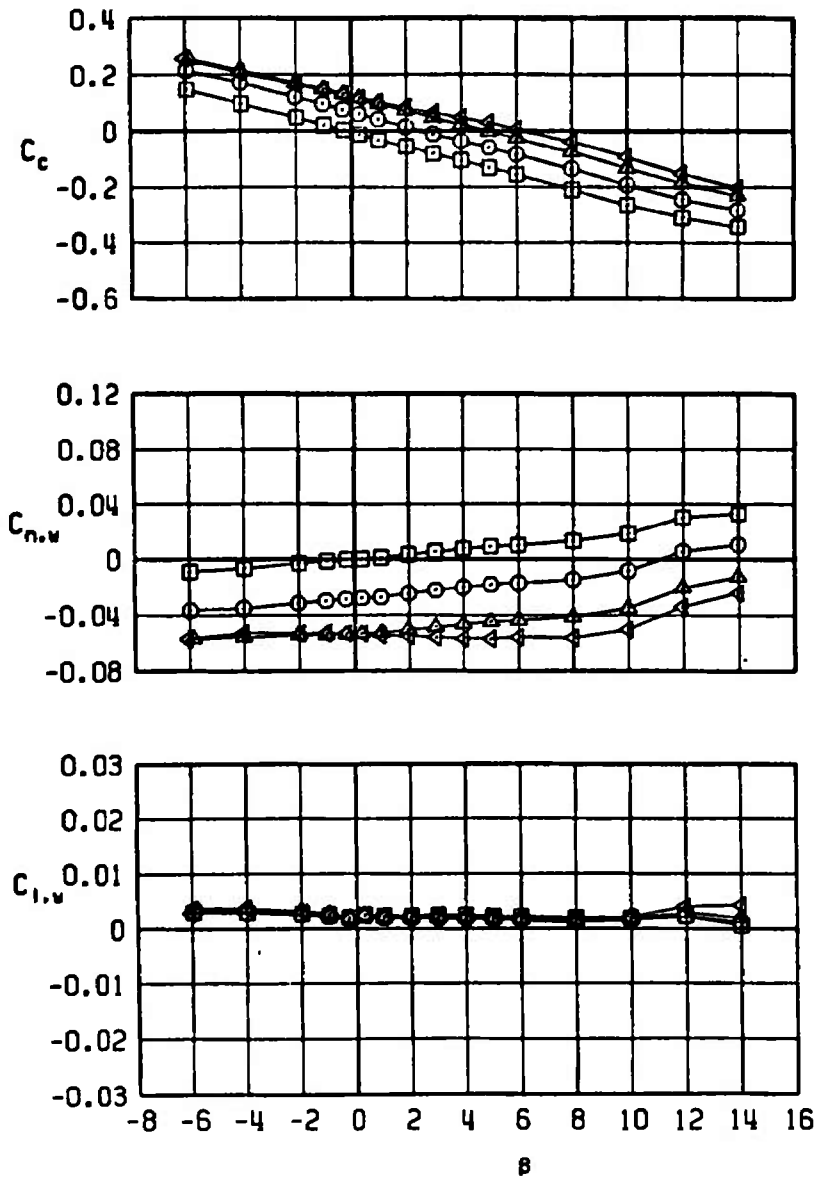
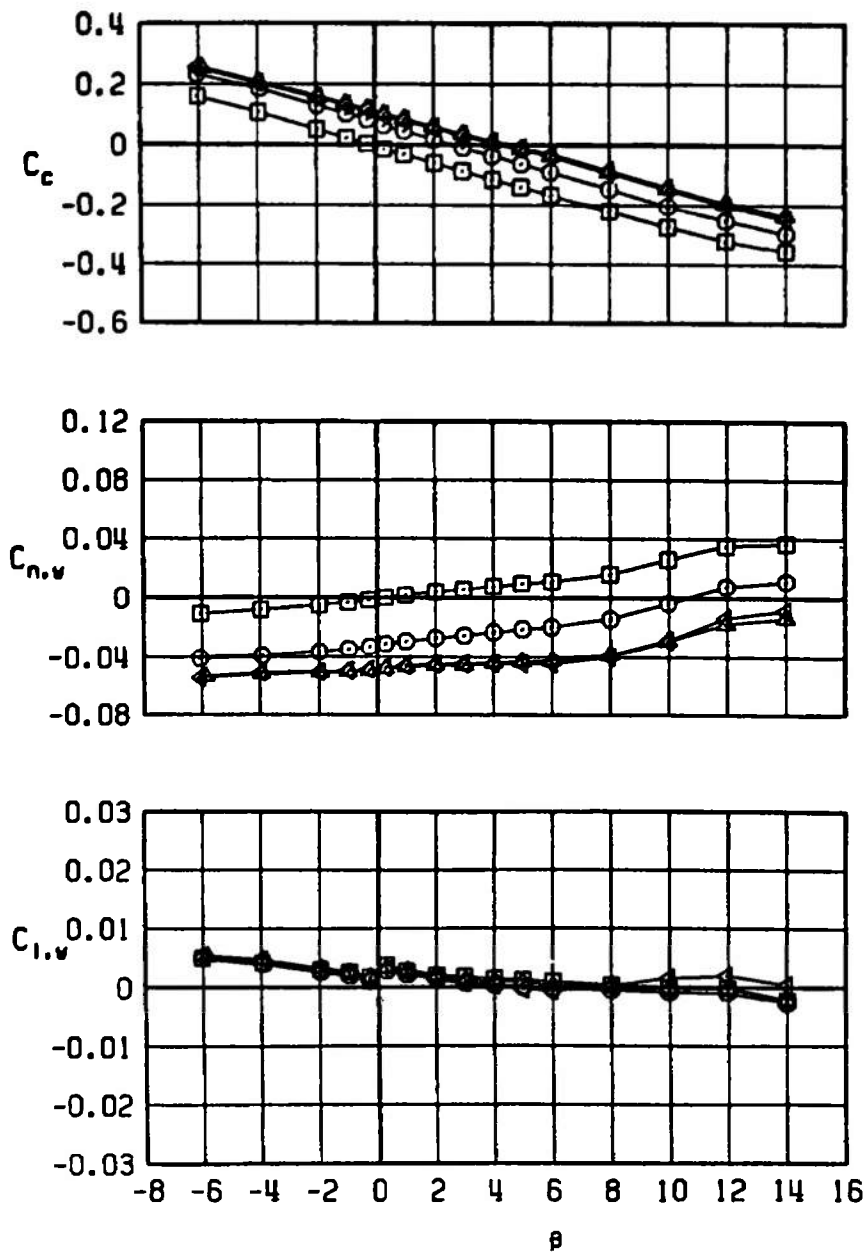
 $\alpha = 0$ a. $M_\infty = 0.50$

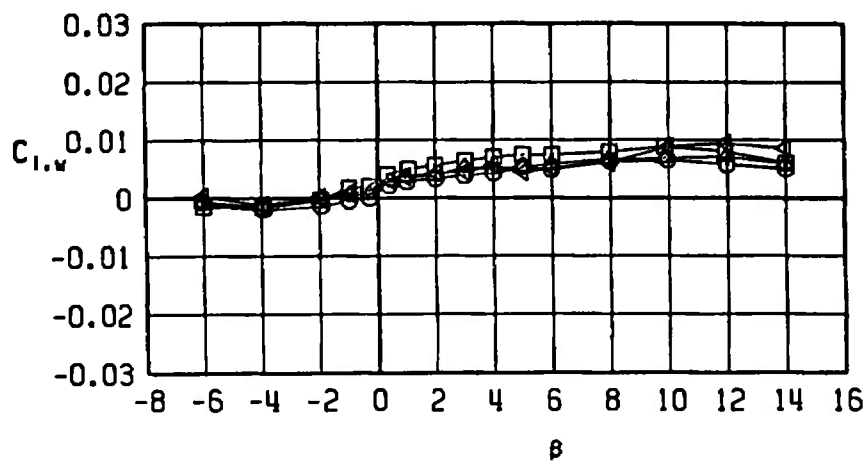
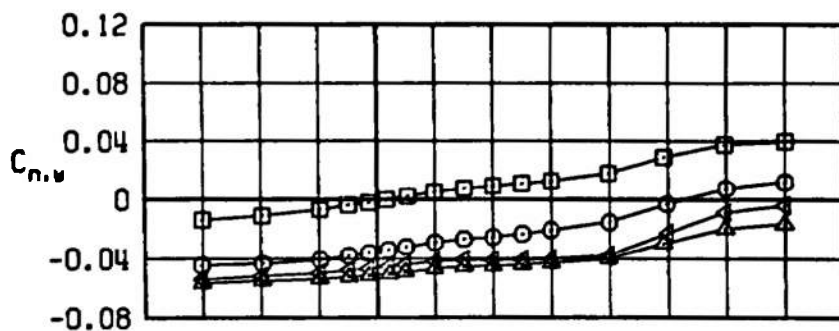
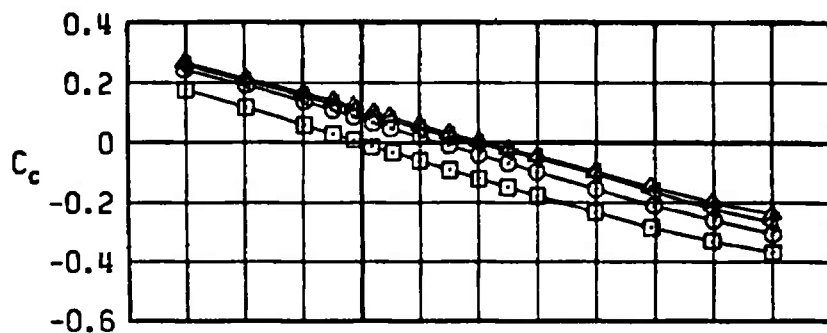
Figure 30. Effect of yaw control deflections on the crosswind-force, yawing-moment, and rolling-moment coefficients of the MK-84 MGBB II configuration.

SYMBOL	CONFIG	M_∞	λ_N	δP	δQ	δR
□	B2S1W2T5L1C2	0.75	30	0	0	0
○	B2S1W2T5L1C2	0.75	30	0	0	5
△	B2S1W2T5L1C2	0.75	30	0	0	10
◄	B2S1W2T5L1C2	0.75	30	0	0	15

 $\alpha = 0$ 

b. $M_\infty = 0.75$
Figure 30. Continued.

SYMBOL	CONFIG	M_∞	λ_M	δP	δQ	δR
□	B2S1W2T5L1C2	0.85	30	0	0	0
○	B2S1W2T5L1C2	0.85	30	0	0	5
△	B2S1W2T5L1C2	0.85	30	0	0	10
◀	B2S1W2T5L1C2	0.85	30	0	0	15

 $\alpha = 0$ 

c. $M_\infty = 0.85$
Figure 30. Continued.

SYMBOL	CONFIG	M_∞	λ_H	δP	δQ	δR
□	B2S1W2T5L1C2	0.95	30	0	0	0
○	B2S1W2T5L1C2	0.95	30	0	0	5
△	B2S1W2T5L1C2	0.95	30	0	0	10
◄	B2S1W2T5L1C2	0.95	30	0	0	15

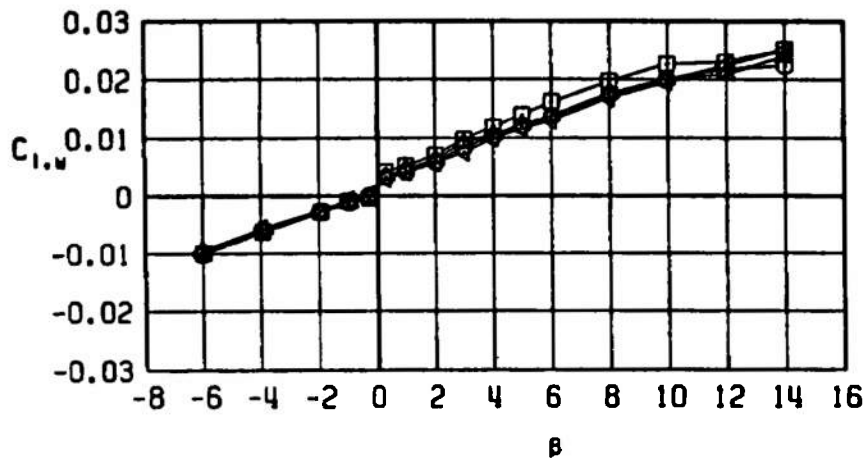
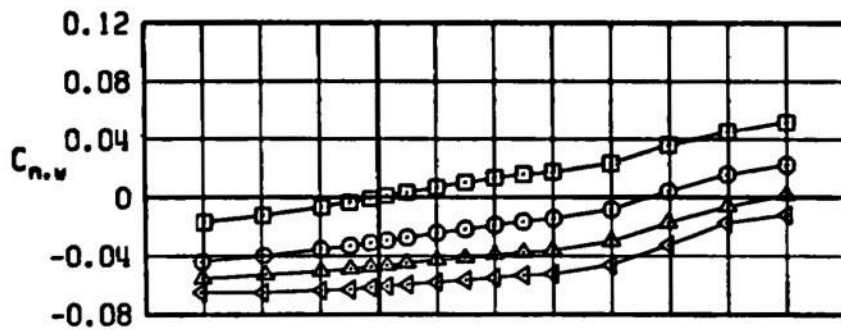
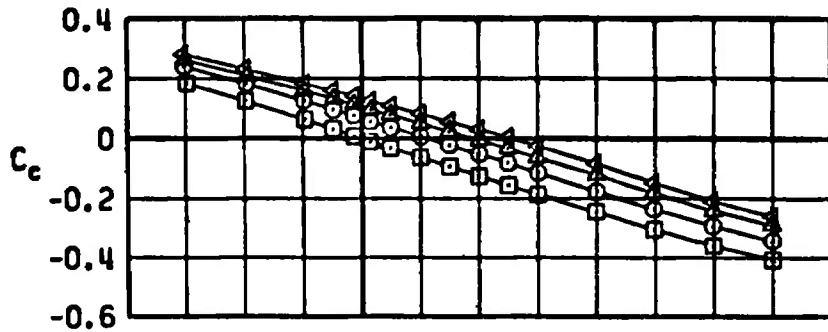
 $\alpha = 0$ d. $M_\infty = 0.95$

Figure 30. Continued.

SYMBOL	CONFIG	M_∞	λ_H	δP	δQ	δR
\square	B2S1W2T5L1C2	1.10	30	0	0	0
\circ	B2S1W2T5L1C2	1.10	30	0	0	5
\triangle	B2S1W2T5L1C2	1.10	30	0	0	10
\triangleleft	B2S1W2T5L1C2	1.10	30	0	0	15

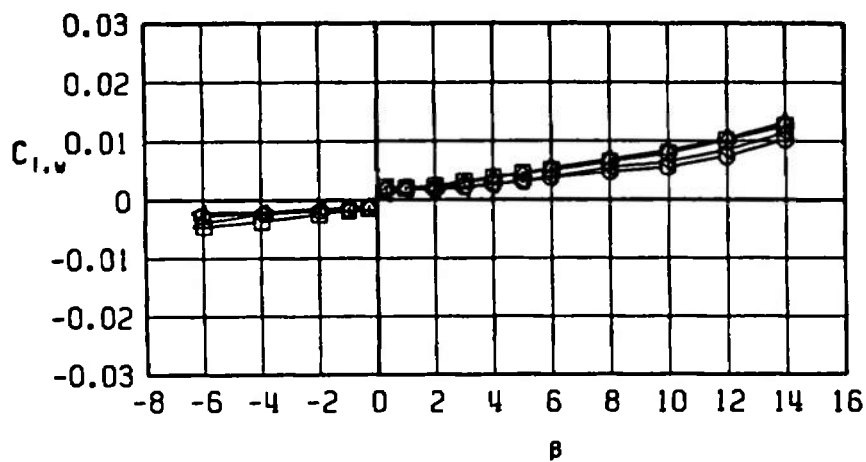
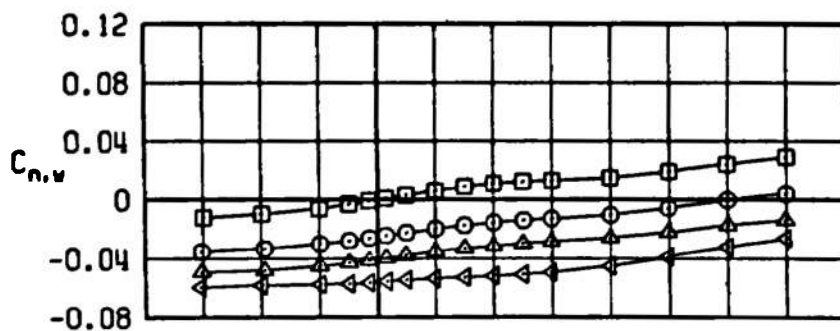
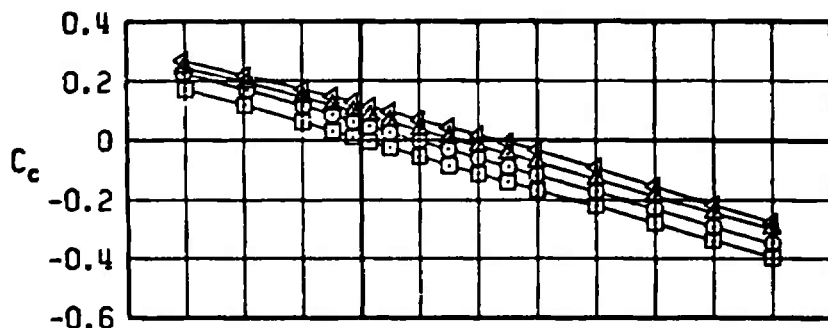
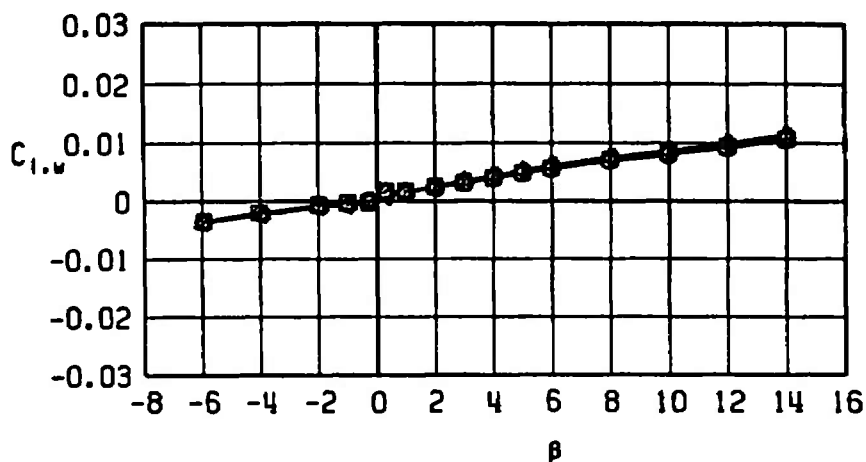
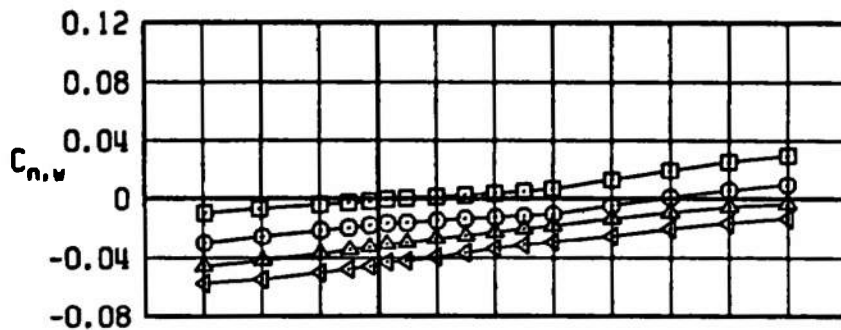
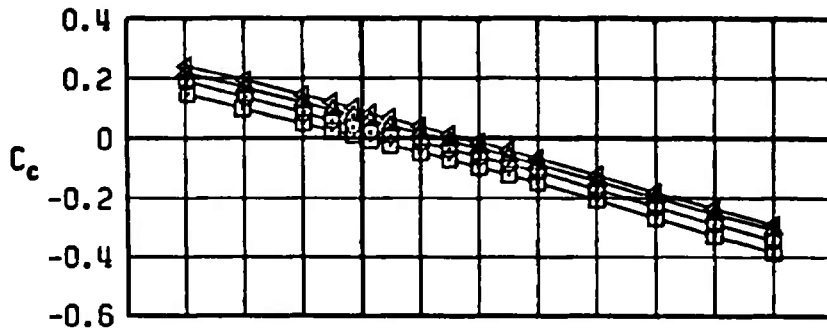
 $\alpha = 0$ e. $M_\infty = 1.10$

Figure 30. Continued.

SYMBOL	CONFIG	M_∞	λ_M	δP	δQ	δR
□	B2S1W2T5L1C2	1.30	30	0	0	0
○	B2S1W2T5L1C2	1.30	30	0	0	5
△	B2S1W2T5L1C2	1.30	30	0	0	10
◁	B2S1W2T5L1C2	1.30	30	0	0	15

 $\alpha = 0^\circ$ 

f. $M_\infty = 1.30$
Figure 30. Concluded.

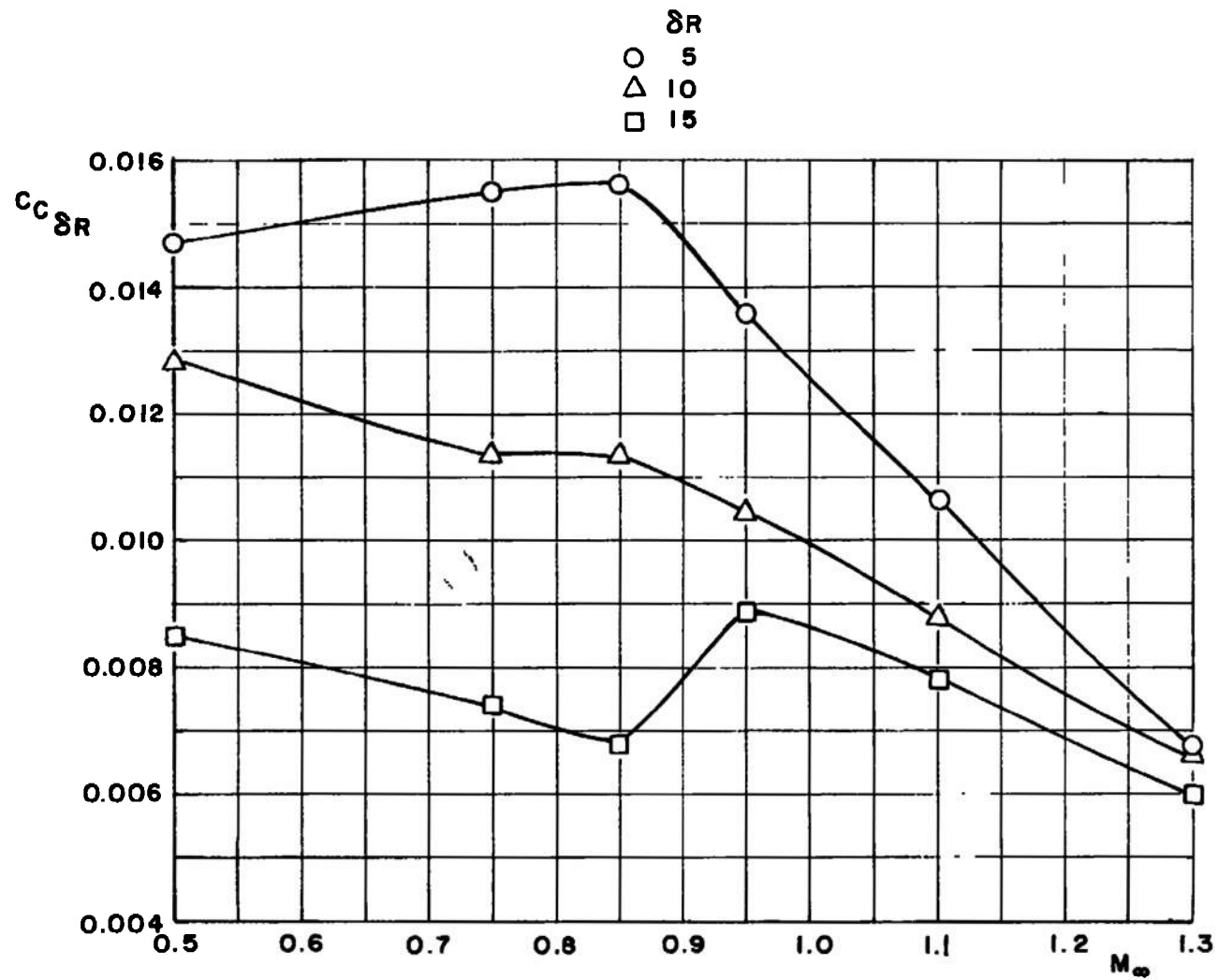


Figure 31. Effectiveness of the flap control surfaces in producing crosswind force at zero sideslip angle.

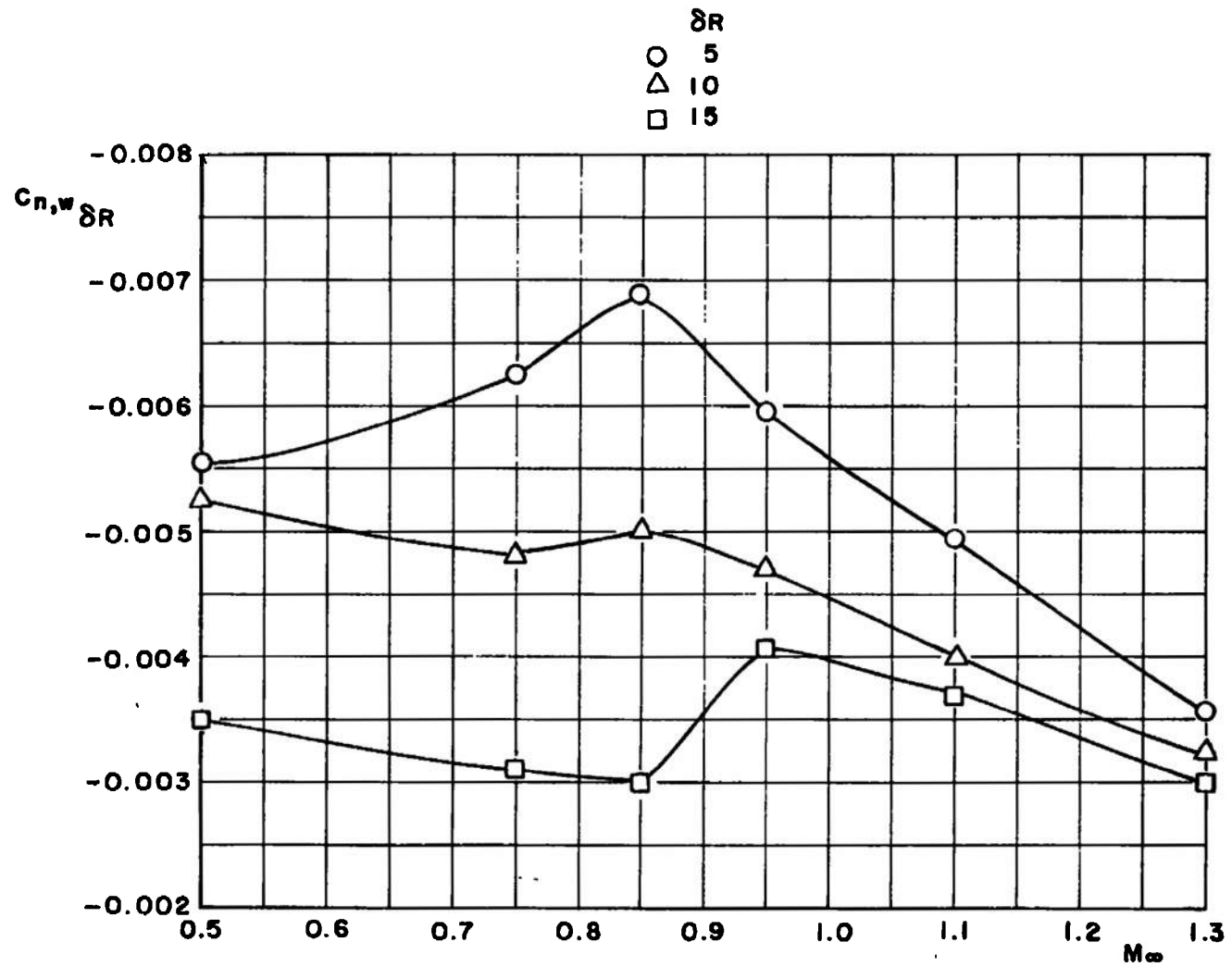


Figure 32. Yaw effectiveness of the flap control surfaces at zero angle of attack.

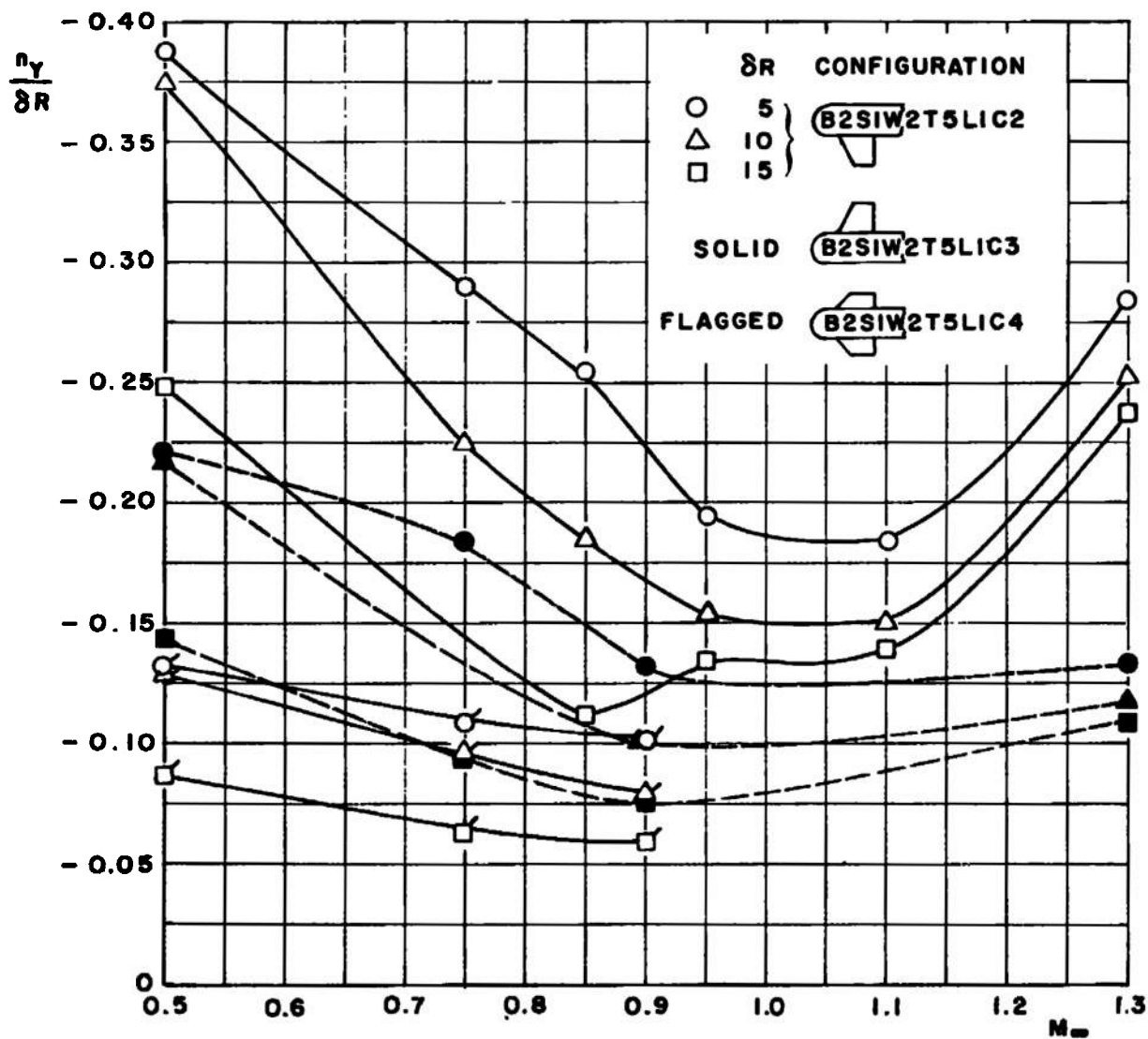
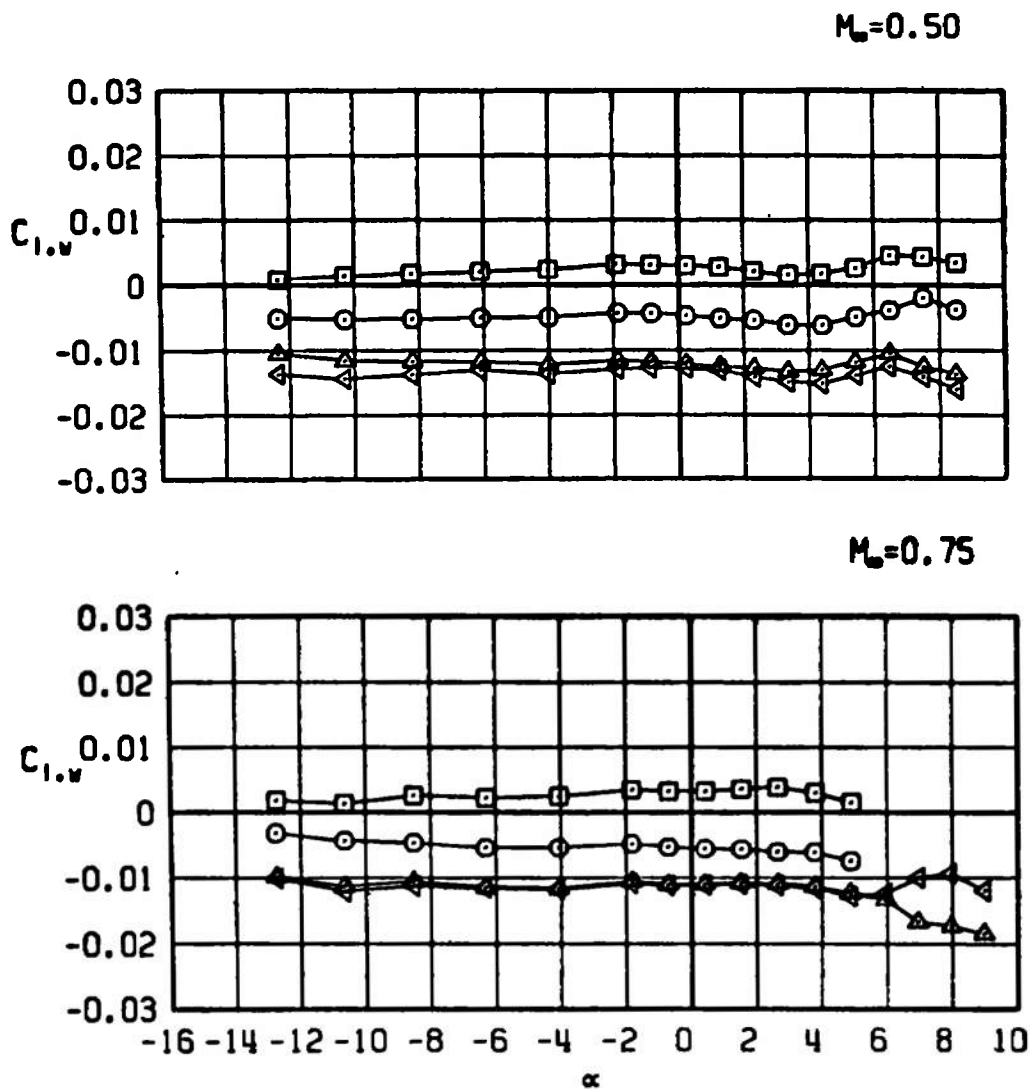


Figure 33. Lateral load factor per degree of yaw control deflection (δR) versus Mach number.

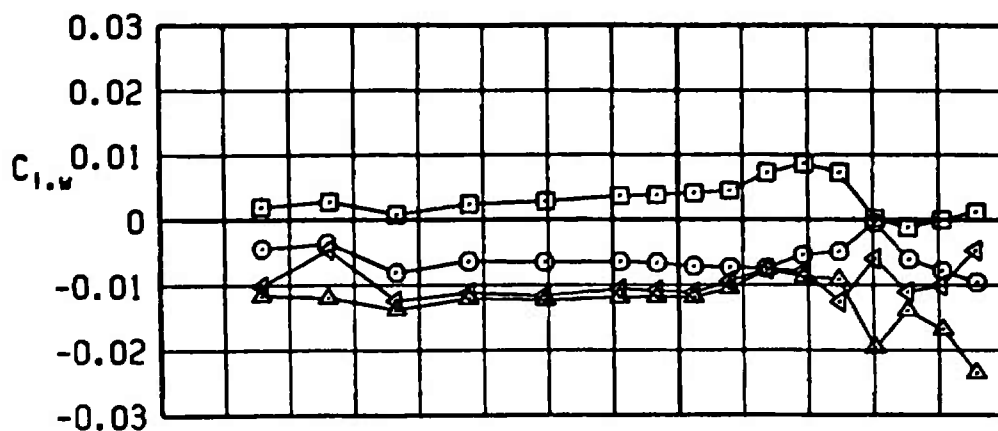
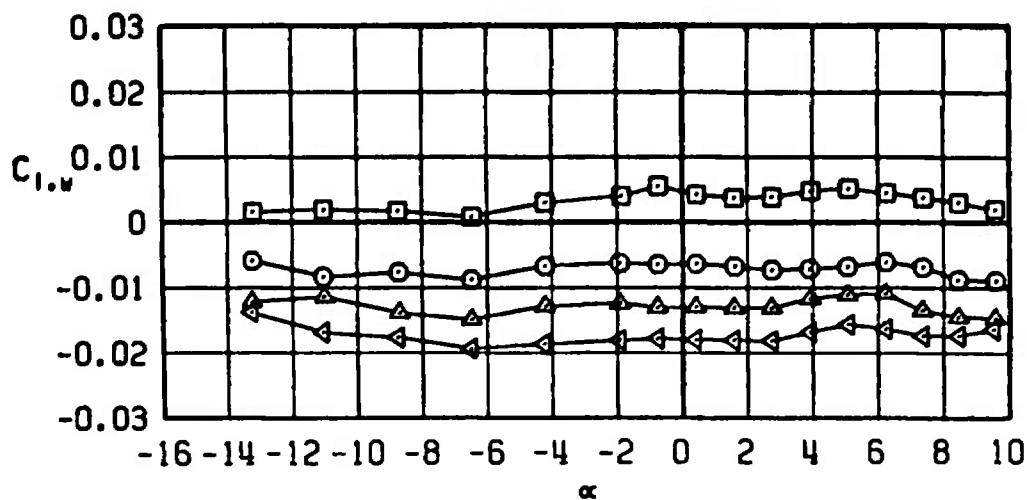
SYMBOL	CONFIG	λ_M	δP	δQ	δR
□	B2S1W2T5L1C2	30	0	0	0
○	B2S1W2T5L1C2	30	-5	0	0
△	B2S1W2T5L1C2	30	-10	0	0
◄	B2S1W2T5L1C2	30	-15	0	0



a. $M_\infty = 0.50$ and 0.75

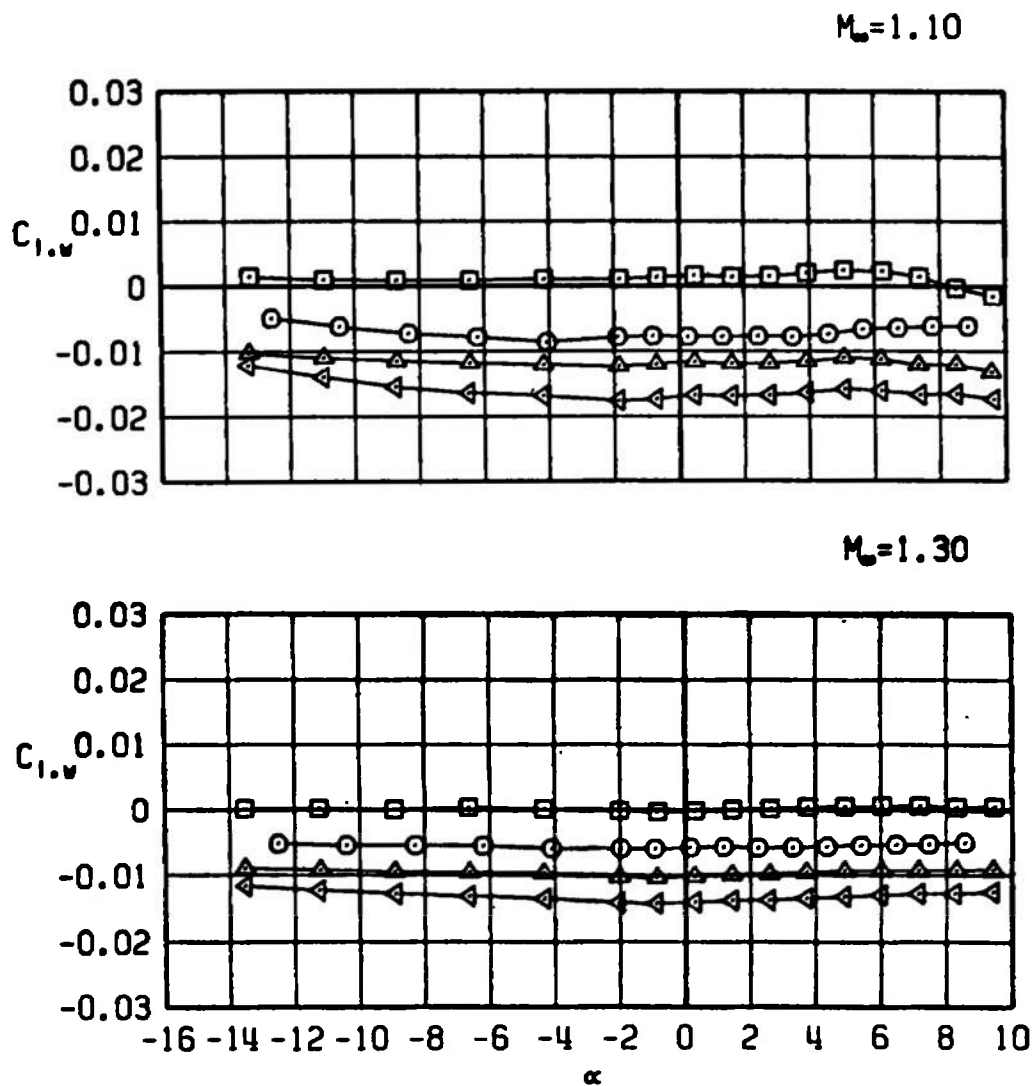
Figure 34. Effect of roll control deflections on the rolling-moment coefficients of the MK-84 MGGB II configuration.

SYMBOL	CONFIG	λ_w	δP	δQ	δR
□	B2S1W2T5L1C2	30	0	0	0
○	B2S1W2T5L1C2	30	-5	0	0
△	B2S1W2T5L1C2	30	-10	0	0
◄	B2S1W2T5L1C2	30	-15	0	0

 $M_\infty = 0.85$  $M_\infty = 0.95$ 

b. $M_\infty = 0.85$ and 0.95
Figure 34. Continued.

SYMBOL	CONFIG	λ_M	ϕ_P	ϕ_Q	ϕ_R
□	B2S1W2T5L1C2	30	0	0	0
○	B2S1W2T5L1C2	30	-5	0	0
△	B2S1W2T5L1C2	30	-10	0	0
◁	B2S1W2T5L1C2	30	-15	0	0



c. $M_\infty = 1.10$ and 1.30
Figure 34. Concluded.

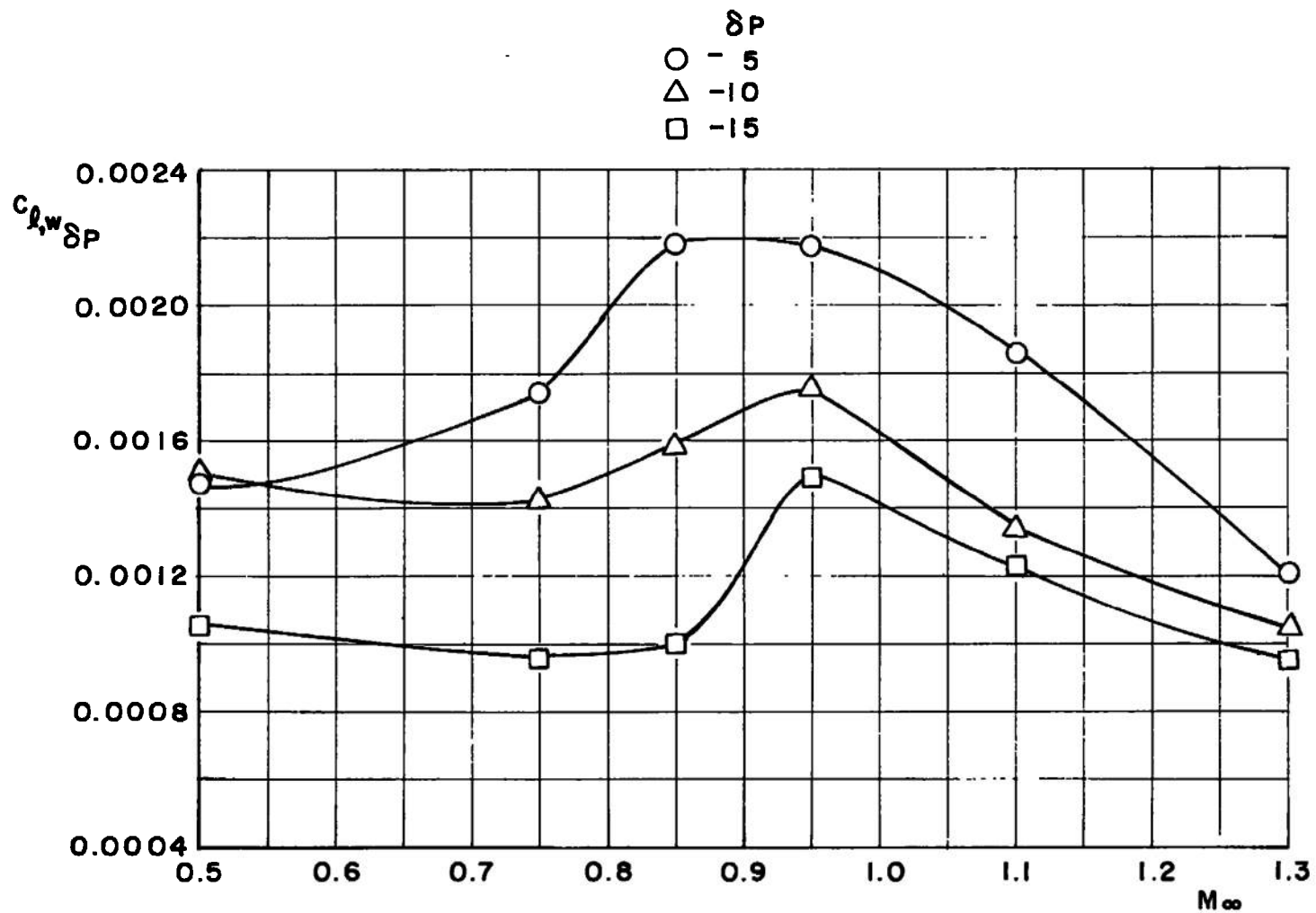
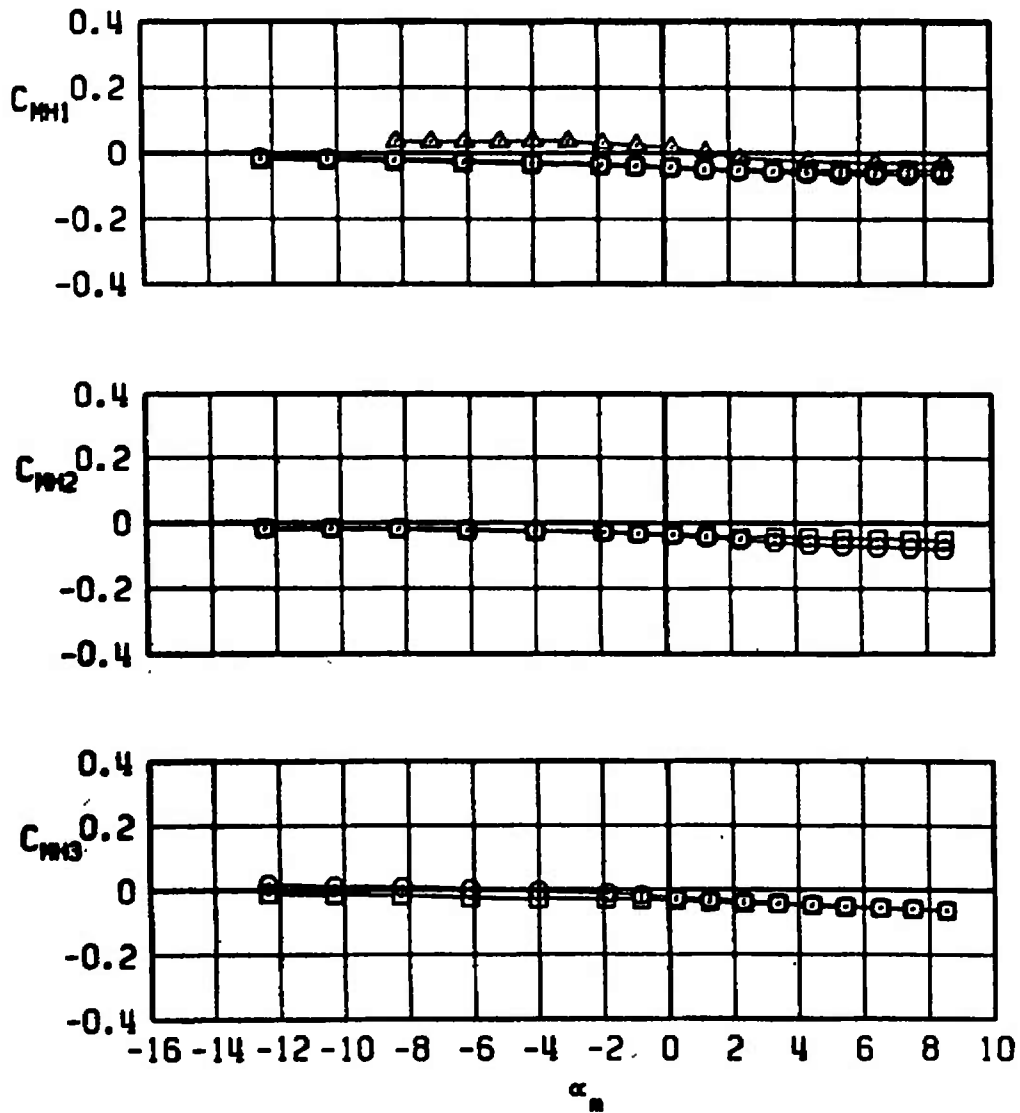


Figure 35. Roll effectiveness of the flap control surfaces at zero angle of attack.

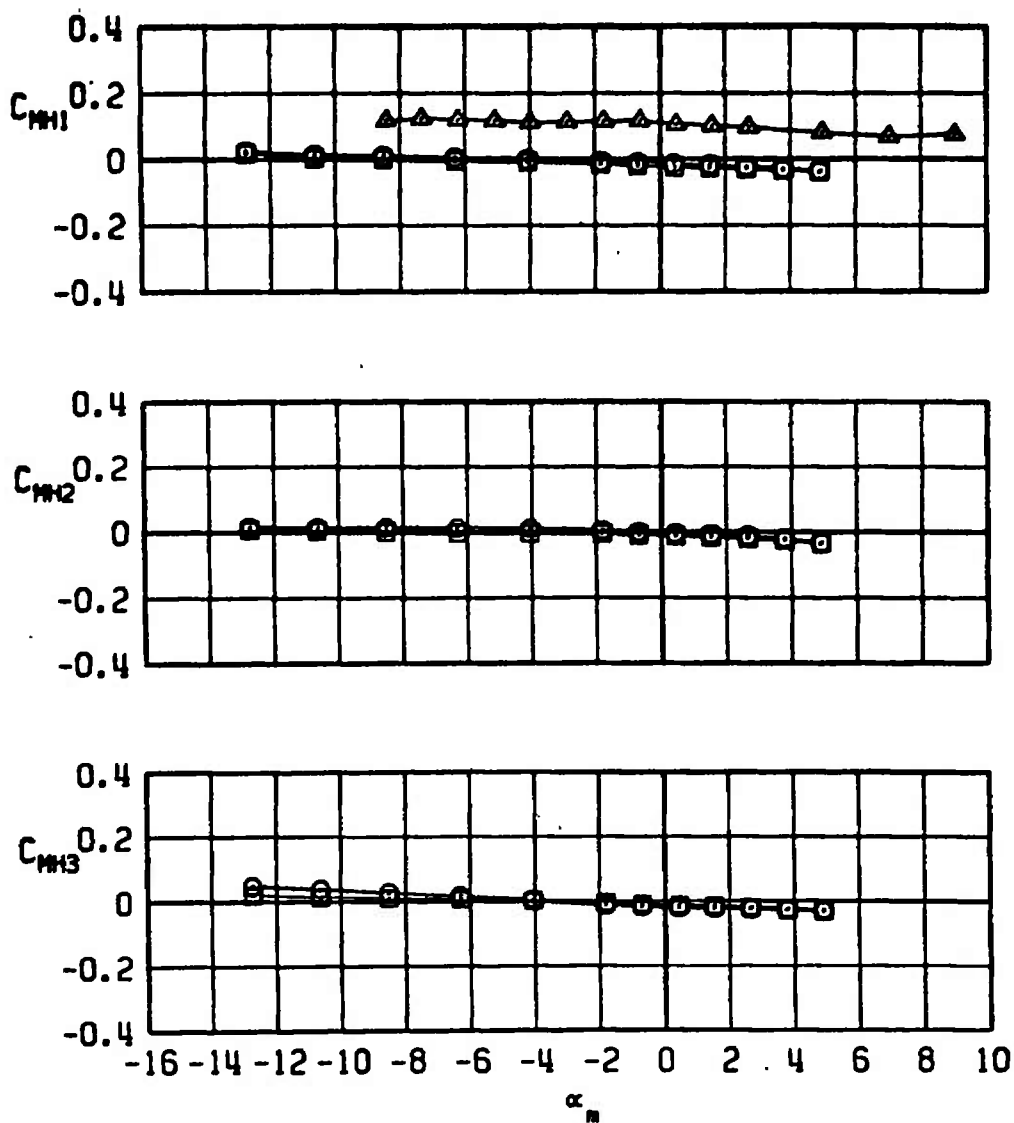
SYMBOL	CONFIG	M_∞	λ_M	δP	δQ	δR
□	B2S1W2T5L1C2	0.50	30	0	0	0
○	B2S1W2T5L1C2	0.50	30	-5	0	0
△	B2S1W2T5L1C2	0.50	30	0	-10	0



a. $M_\infty = 0.50$

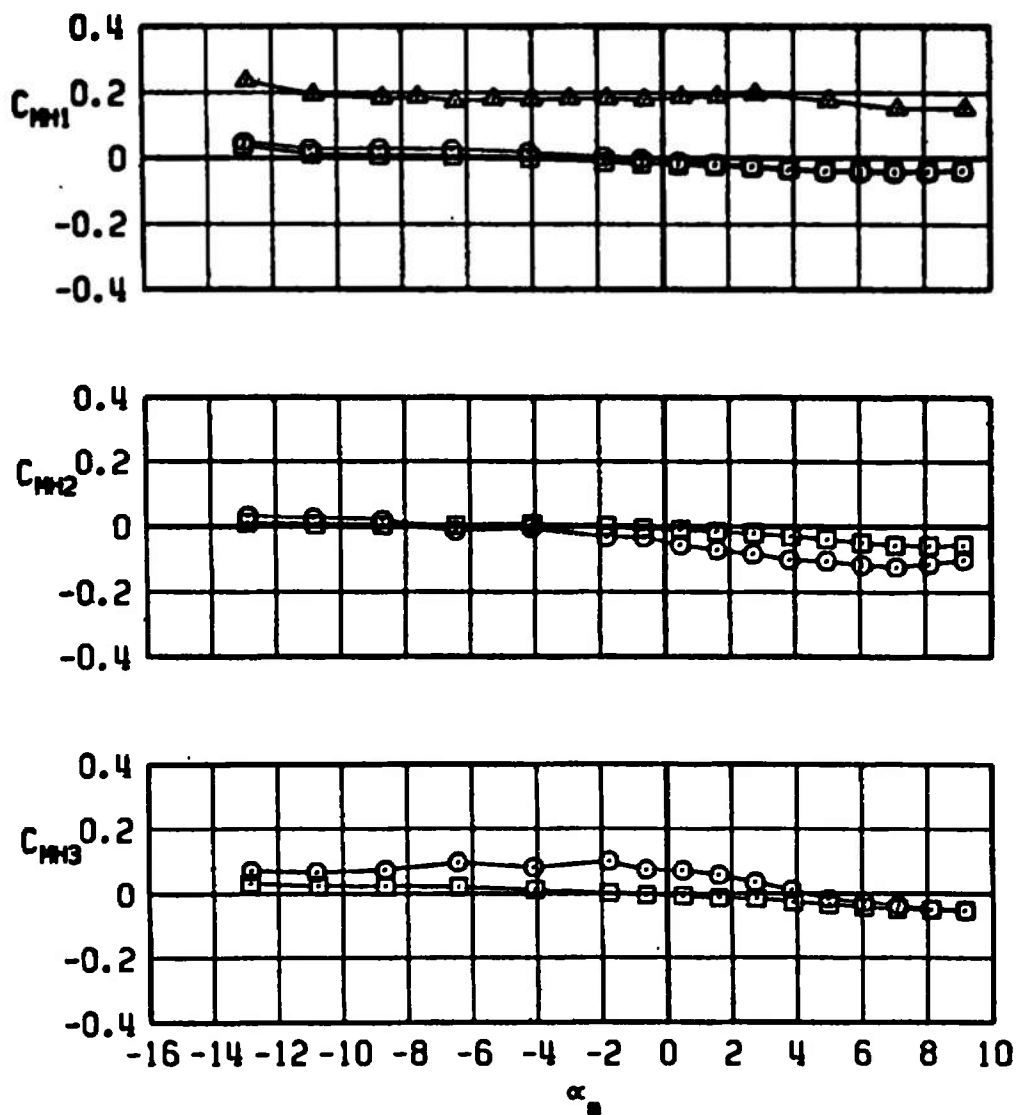
Figure 36. Control surface hinge-moment coefficients versus angle of attack for different control deflection angles.

SYMBOL	CONFIG	M_∞	λ_w	ϕ_P	ϕ_Q	ϕ_R
□	B2S1W2T5L1C2	0.75	30	0	0	0
○	B2S1W2T5L1C2	0.75	30	-5	0	0
△	B2S1W2T5L1C2	0.75	30	0	-10	0



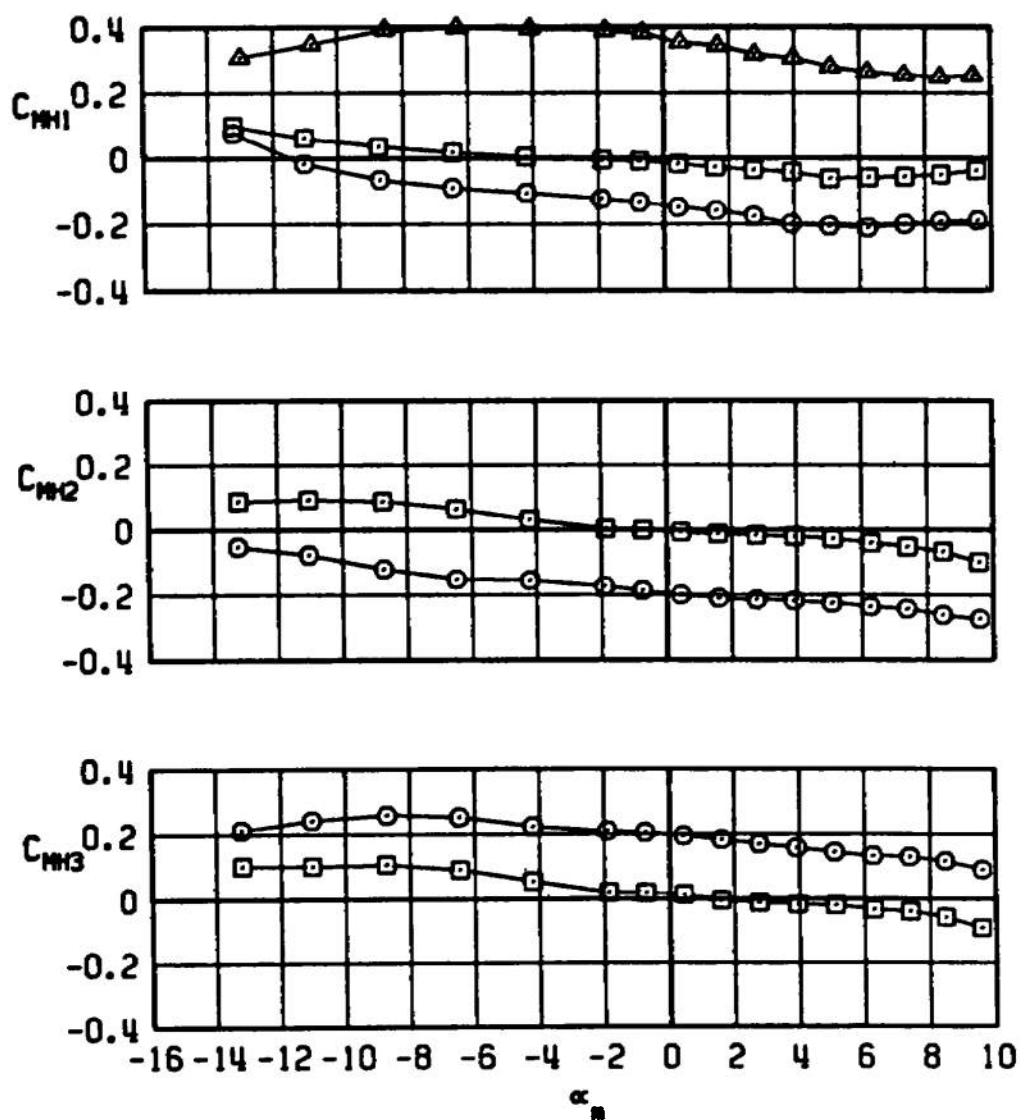
b. $M_\infty = 0.75$
Figure 36. Continued.

SYMBOL	CONFIG	M_∞	λ_H	λ_P	δO	δR
□	B2S1W2T5L1C2	0.85	30	0	0	0
○	B2S1W2T5L1C2	0.85	30	-5	0	0
△	B2S1W2T5L1C2	0.85	30	0	-10	0



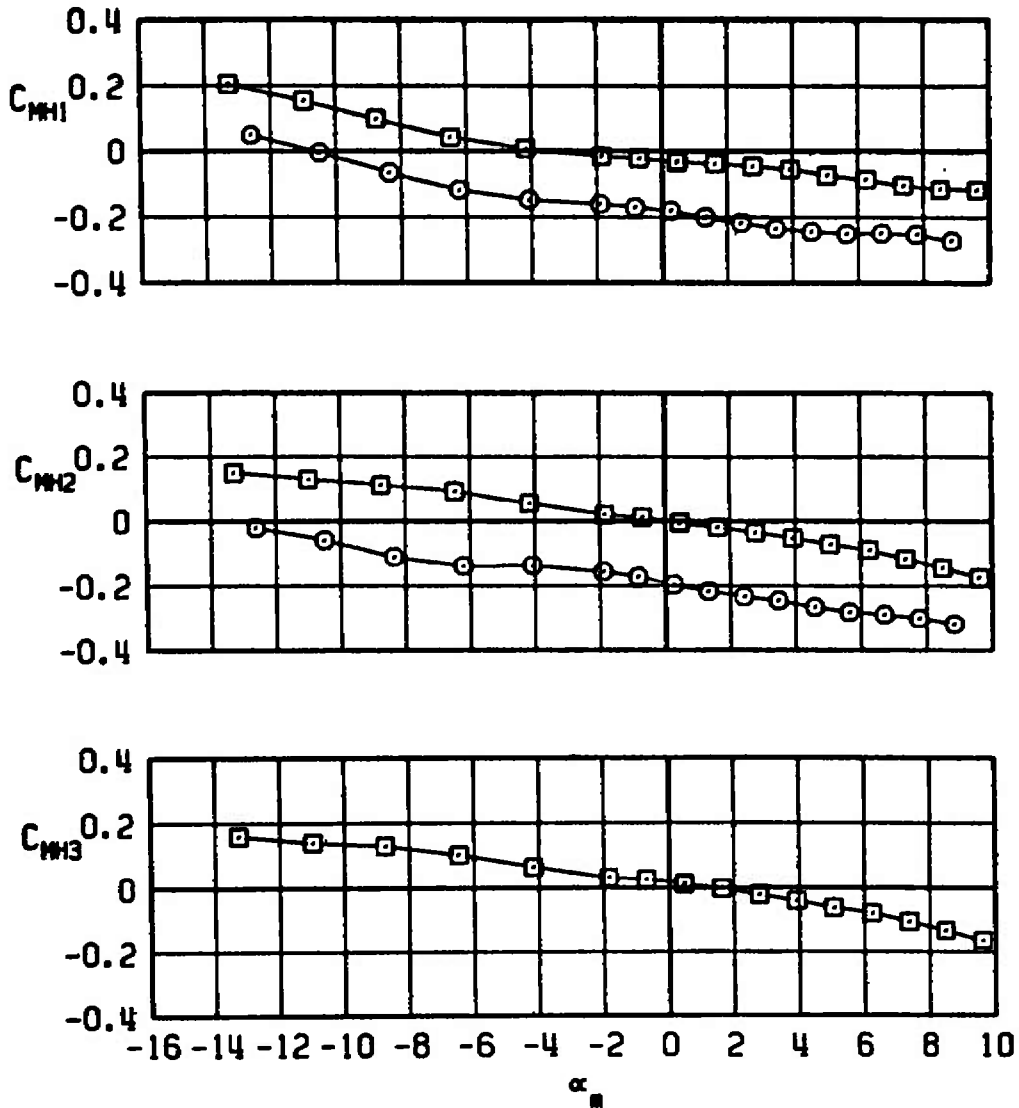
c. $M_\infty = 0.85$
Figure 36. Continued.

SYMBOL	CONFIG	M_∞	λ_M	δP	δQ	δR
□	B2S1W2T5L1C2	0.95	30	0	0	0
○	B2S1W2T5L1C2	0.95	30	-5	0	0
△	B2S1W2T5L1C2	0.95	30	0	-10	0



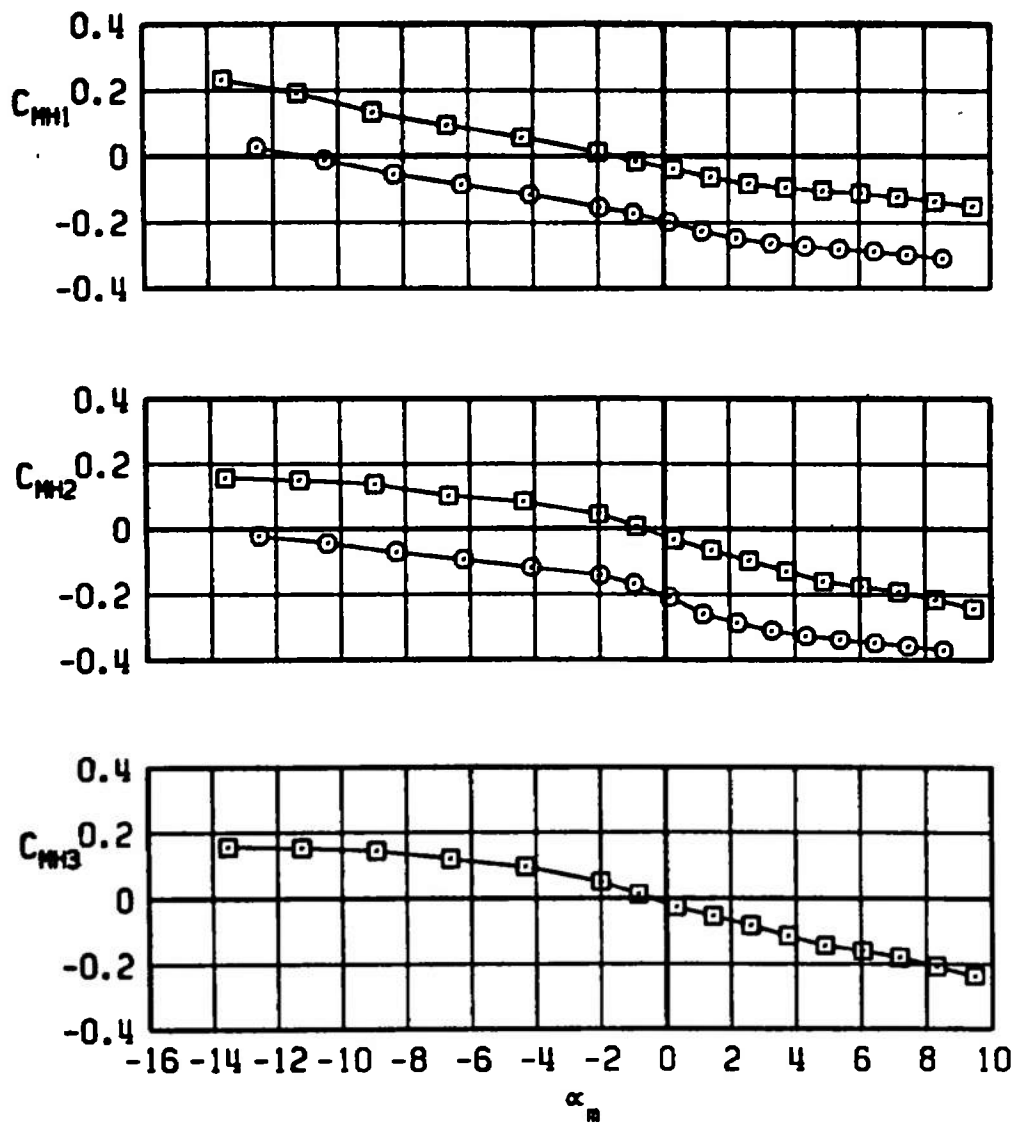
d. $M_\infty = 0.95$
Figure 36. Continued.

SYMBOL	CONFIG	M_∞	λ_M	δP	δQ	δR
□	B2S1W2T5L1C2	1.10	30	0	0	0
○	B2S1W2T5L1C2	1.10	30	-5	0	0



e. $M_\infty = 1.10$
Figure 36. Continued.

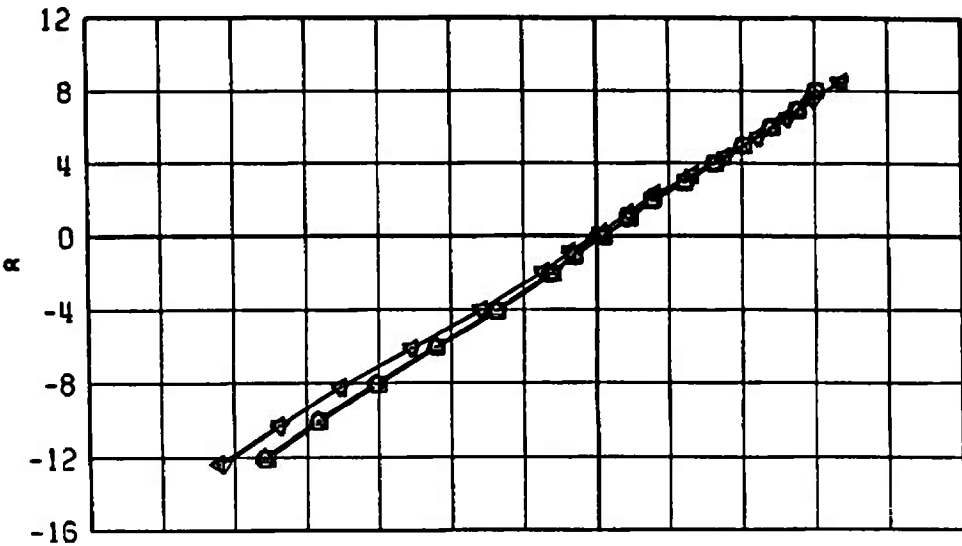
SYMBOL	CONFIG	M_∞	λ_M	δP	δQ	δR
\square	B2S1W2T5L1C2	1.30	30	0	0	0
\circ	B2S1W2T5L1C2	1.30	30	-5	0	0



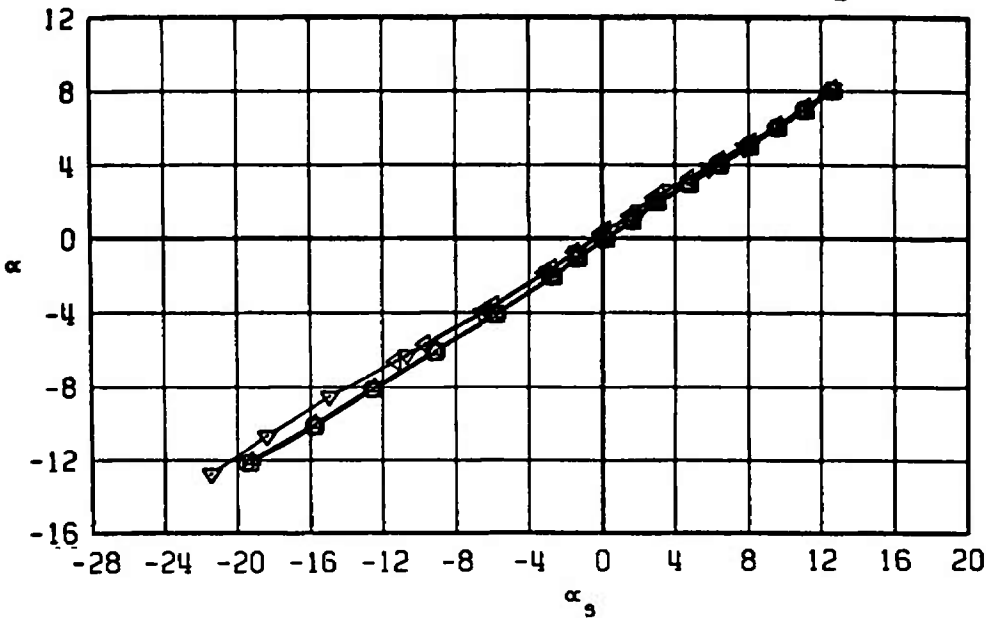
f. $M_\infty = 1.30$
Figure 36. Concluded.

SYMBOL	CONFIG	λ_H	δP	δQ	δR
□	B2	-	-	-	-
○	B2C2	-	-	-	-
△	B2T5C2	-	0	0	0
◁	B2S1W2T5L1	30	0	0	0
▽	B2S1W2T5L1C2	30	0	0	0

$M_\infty=0.50$



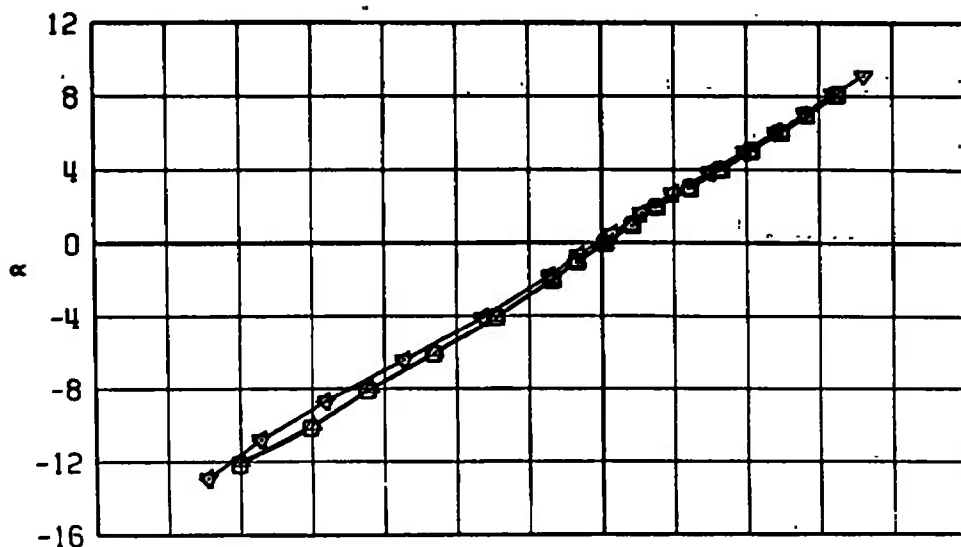
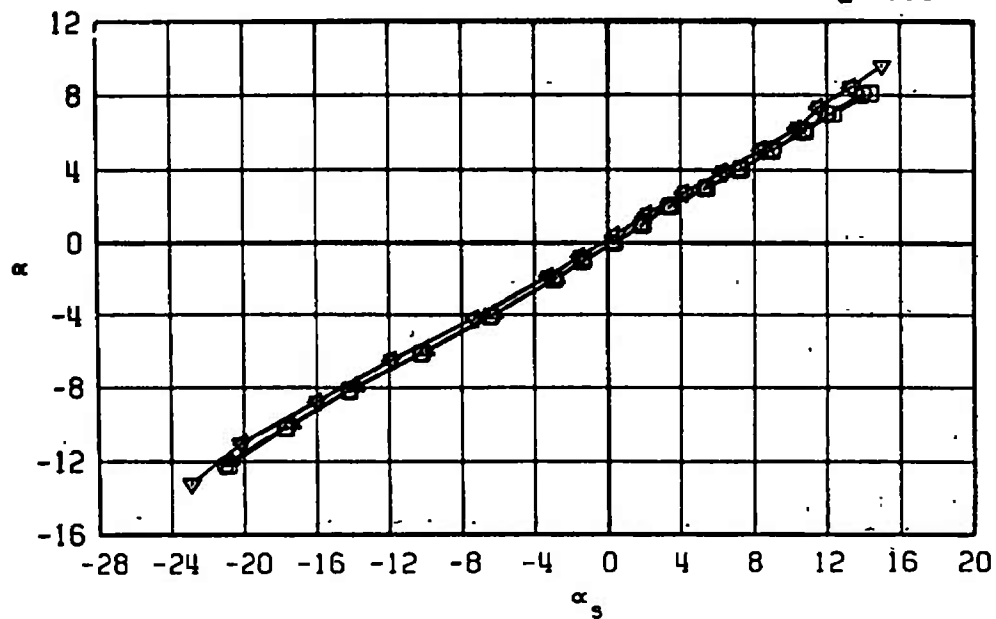
$M_\infty=0.75$



a. $M_\infty = 0.50$ and 0.75

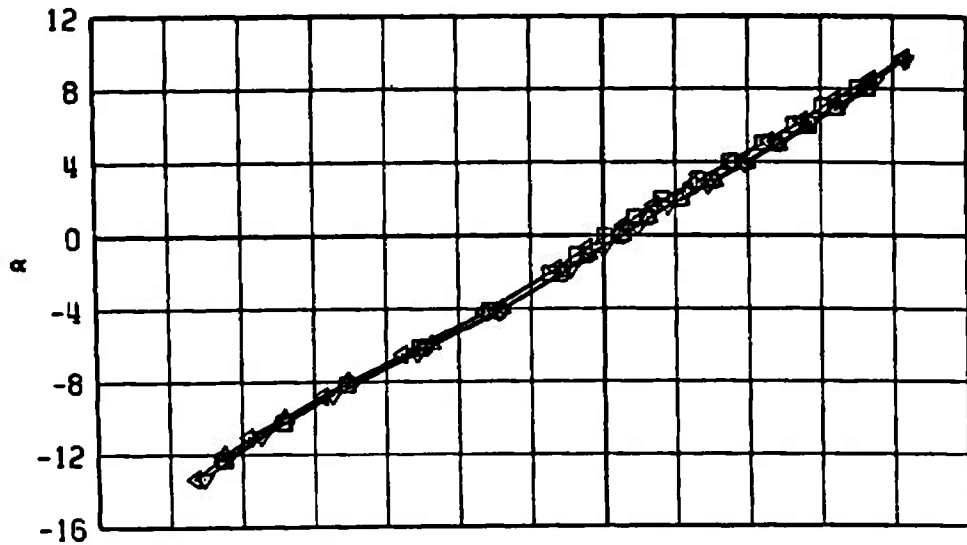
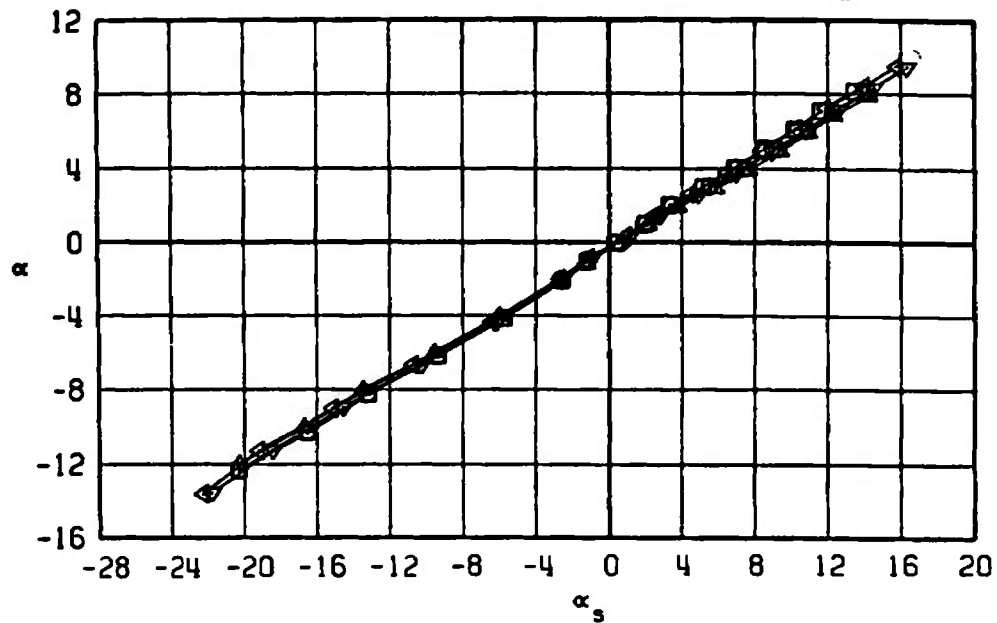
Figure 37. Vane calibration data, α versus α_s , comparing configurations B2, B2C2, B2T5C2, B2S1W2T5L1, and B2S1W2T5L1C2.

SYMBOL	CONFIG	λ_M	δP	δQ	δR
□	B2	-	-	-	-
○	B2C2	-	-	-	-
△	B2T5C2	-	0	0	0
◀	B2S1W2T5L1	30	0	0	0
▽	B2S1W2T5L1C2	30	0	0	0

 $M_\infty = 0.85$  $M_\infty = 0.95$ 

b. $M_\infty = 0.85$ and 0.95
Figure 37. Continued.

SYMBOL	CONFIG	λ_w	δP	δQ	δR
□	B2	-	-	-	-
○	B2C2	-	-	-	-
△	B2T5C2	-	0	0	0
◁	B2S1W2T5L1	30	0	0	0
▽	B2S1W2T5L1C2	30	0	0	0

 $M_\infty = 1.10$  $M_\infty = 1.30$ 

c. $M_\infty = 1.10$ and 1.30
Figure 37. Concluded.

Table 1. Summary of Test Conditions and Flap Control Surface Deflections

δP	δQ	δR	Mach No./ p_t									
			0.50	0.70	0.75	0.85	0.90	0.95	1.00	1.10	1.20	1.30
			1000	1000	1000	1000	1000	1100	1100	1100	1200	1200
0	0	0	x	x	x	x	x	x	x	x	x	x
-5	↓	↓	x		x	x		x		x		x
-10			x		x	x	x	x		x		x
-15			x		x	x		x		x		x
0	+10		x		x	x		x		x		x
	-5		x		x	x		x		x		x
	-10		x		x	x	x	x		x		x
	-15	↓	x		x	x		x		x		x
	0	+5	x		x	x		x		x		x
	0	+10	x		x	x	x	x		x		x
	0	+15	x		x	x		x		x		x
-5	+5	0	x		x	x		x		x		x
+5	0	+5	x		x	x		x		x		x
0	+5	+5	x		x	x		x		x		x

Table 2. Uncertainties in Aerodynamic and Hinge-Moment Coefficients

M_{∞}	ΔC_L	ΔC_D	$\Delta C_{m,w}$	ΔC_c	$\Delta C_{n,w}$	$\Delta C_{\ell,w}$	ΔC_{MH}
0.50	± 0.0180	± 0.0065	± 0.0049	± 0.0074	± 0.0011	± 0.0010	± 0.0088
0.75	± 0.0129	± 0.0038	± 0.0026	± 0.0051	± 0.0008	± 0.0006	± 0.0052
0.85	± 0.0117	± 0.0034	± 0.0023	± 0.0046	± 0.0007	± 0.0005	± 0.0054
0.95	± 0.0126	± 0.0035	± 0.0031	± 0.0046	± 0.0008	± 0.0004	± 0.0066
1.10	± 0.0119	± 0.0034	± 0.0050	± 0.0043	± 0.0007	± 0.0004	± 0.0056
1.30	± 0.0104	± 0.0031	± 0.0044	± 0.0038	± 0.0006	± 0.0003	± 0.0063

Table 3. Precision of Flap Control Surface Deflection Angle Settings

Nominal Angle, deg	Measured Angle, deg			
	Fin No. 1	Fin No. 2	Fin No. 3	Fin No. 4
0	+0.15	+0.31	-0.61	-0.23
-5	-5.36	-5.28	-4.59	-4.74
+5	+4.70	+4.60	+5.58	+5.20
-10	-10.37	-10.00	-9.67	-9.67
+10	+10.55	+10.76	+9.98	+10.84
-15	-15.70	-15.39	-14.67	-14.99
+15	+14.83	+14.52	+15.23	+15.39

NOMENCLATURE

b	Reference wing span, 2.267 ft
C_c	Crosswind-force coefficient, crosswind force/ $q_\infty S$
$C_{c\beta}$	Slope of C_c versus β curve, evaluated between sideslip angles from -2 to 2 deg, per deg
$C_{c\delta R}$	Crosswind-force control effectiveness parameter, per deg $\frac{(C_c)_{\delta R=x} - (C_c)_{\delta R=0}}{\delta R = x}$ at zero sideslip angle
C_D	Drag coefficient, drag/ $q_\infty S$
C_L	Lift coefficient, lift/ $q_\infty S$
$C_{L\alpha}$	Slope of C_L versus α curve, evaluated between angles of attack from -2 to 2 deg, per deg
$C_{L\delta Q}$	Lift control effectiveness parameter, per deg $\frac{(C_L)_{\delta Q=x} - (C_L)_{\delta Q=0}}{\delta Q = x}$ at zero angle of attack
$C_{\ell,w}$	Rolling-moment coefficient, rolling moment/ $q_\infty S b$
$C_{\ell,w\delta p}$	Roll control effectiveness parameter, per deg $\frac{(C_{\ell,w})_{\delta p=x} - (C_{\ell,w})_{\delta p=0}}{\delta p = x}$ at zero angle of attack and zero sideslip angle
C_{MH1}	Hinge-moment coefficient for fin control surface number 1, hinge moment/ $2\overline{MA} q_\infty$, positive moment tends to force trailing edge down
C_{MH2}	Hinge-moment coefficient for fin control surface number 2, hinge moment/ $2\overline{MA} q_\infty$, positive moment tends to force trailing edge down
C_{MH3}	Hinge-moment coefficient for fin control surface number 3, hinge moment/ $2\overline{MA} q_\infty$, positive moment tends to force trailing edge down
$C_{m,w}$	Pitching-moment coefficient, pitching moment/ $q_\infty S c$, moment reference point on bomb centerline at MS 15.745*

*Moment reference point on bomb centerline at MS 15.962 for the wings-folded ($\lambda_w = 88$ deg) configuration.

$C_{m,w\alpha}$	Slope of $C_{m,w}$ versus α curve, evaluated between angles of attack from -2 to 2 deg, per deg
$C_{m,w\delta Q}$	Pitch control effectiveness parameter, per deg $\frac{(C_{m,w})_{\delta Q=x} - (C_{m,w})_{\delta Q=0}}{\delta Q = x}$ at zero angle of attack
$C_{n,w}$	Yawing-moment coefficient, yawing moment/ $q_{\infty}S_b$, moment reference point at MS 15.745*
$C_{n,w\beta}$	Slope of $C_{n,w}$ versus β curve, evaluated between sideslip angles from -2 to 2 deg, per deg
$C_{n,w\delta R}$	Yaw control effectiveness parameter, per deg $\frac{(C_{n,w})_{\delta R=x} - (C_{n,w})_{\delta R=0}}{\delta R = x}$ at zero sideslip angle
c	Reference chord length, 0.3079 ft
c_{FS}	Full-scale reference chord length, 1.5395 ft
I_w	Wing incidence angle, deg
L/D	Lift-to-drag ratio
\overline{MA}	Flap control surface moment area, 0.0003825 ft ³
MS	Model station
M_{∞}	Free-stream Mach number
$n_Y/\delta R$	Directional load factor, $\left[C_{c\delta R} - C_{c\beta} \frac{C_{n,w\delta R}}{C_{n,w\beta}} \right] \frac{q_{FS} S_{FS}}{W}, \text{ per deg}$
$n_Z/\delta Q$	Longitudinal load factor, $\left[C_{L\delta Q} - C_L \frac{C_{m,w\delta Q}}{C_{m,w}} \right] \frac{q_{FS} S_{FS}}{W}, \text{ per deg}$
p_t	Free-stream total pressure, psfa

*Moment reference point on bomb centerline at MS 15.962 for the wings-folded ($\lambda_w = 88$ deg) configuration.

p_{∞}	Free-stream static pressure, psia
q_{FS}	Full-scale dynamic pressure, 778 psf
q_{∞}	Free-stream dynamic pressure, psf
Re	Free-stream unit Reynolds number, ft^{-1}
S	Wing area, 0.6638 ft^2
S_{FS}	Full-scale wing area, 16.595 ft^2
u, v, w	Velocity components along the body axes, ft/sec
V_{∞}	Free-stream velocity, ft/sec
W	Full-scale weight of the MK-84 MGGB II, 2650 lb
α	Angle of attack, $TAN^{-1} w/u$, deg
α_s	Angle of attack as indicated by a vane-type angle-of-attack indicator, deg
α_{trim}	Trim angle of attack, angle of attack for zero pitching moment, deg
β	Angle of sideslip, $SIN^{-1} v/V_{\infty}$, deg
Γ	Wing dihedral angle, deg
δP	Fin control surface deflection angle for roll control, $\delta P = (-\delta 1 - \delta 2 + \delta 3 + \delta 4)/4$
δQ	Fin control surface deflection angle for pitch control, $\delta Q = (\delta 1 + \delta 2 + \delta 3 + \delta 4)/4$
δR	Fin control surface deflection angle for yaw control, $\delta R = (-\delta 1 + \delta 2 - \delta 3 + \delta 4)/4$
$\delta 1-4$	Control deflection angles for the respective flap control surfaces 1 through 4 (see Fig. 13). positive when trailing edge is down, deg
λ_w	Wing sweep angle, deg

MODEL NOMENCLATURE

B2	MK-84 bomb with KMU-353X kit (less tail fins and flaps) and a vane-type angle-of-attack indicator
----	---

C2	2-in. vertical canard mounted on lower fuselage surface
C3	2-in. vertical canard mounted on upper fuselage surface
C4	0.80-in. vertical canards mounted on the upper and lower fuselage surfaces
L1	Launch lugs
S1	Basic strongback
T5	Cruciform tail and flap control surfaces, flap hinge line at MS 28.293
W2	Wing with NACA 65-410 airfoil section and sway brace slots